SUPRAMOLECULAR NUCLEIC ACID CHEMISTRY

EDITED BY: James Tucker and Janarthanan Jayawickramarajah
PUBLISHED IN: Frontiers in Chemistry

frontiers Research Topics

ISSN 1664-8714
ISBN 978-2-88966-110-7
DOI 10.3389/978-2-88966-110-7

About Frontiers

Frontiers is more than just an open-access publisher of scholarly articles: it is a pioneering approach to the world of academia, radically improving the way scholarly research is managed. The grand vision of Frontiers is a world where all people have an equal opportunity to seek, share and generate knowledge. Frontiers provides immediate and permanent online open access to all its publications, but this alone is not enough to realize our grand goals.

Frontiers Journal Series

The Frontiers Journal Series is a multi-tier and interdisciplinary set of open-access, online journals, promising a paradigm shift from the current review, selection and dissemination processes in academic publishing. All Frontiers journals are driven by researchers for researchers; therefore, they constitute a service to the scholarly community. At the same time, the Frontiers Journal Series operates on a revolutionary invention, the tiered publishing system, initially addressing specific communities of scholars, and gradually climbing up to broader public understanding, thus serving the interests of the lay society, too.

Dedication to Quality

Each Frontiers article is a landmark of the highest quality, thanks to genuinely collaborative interactions between authors and review editors, who include some of the world's best academicians. Research must be certified by peers before entering a stream of knowledge that may eventually reach the public - and shape society; therefore, Frontiers only applies the most rigorous and unbiased reviews.
Frontiers revolutionizes research publishing by freely delivering the most outstanding research, evaluated with no bias from both the academic and social point of view. By applying the most advanced information technologies, Frontiers is catapulting scholarly publishing into a new generation.

What are Frontiers Research Topics?

Frontiers Research Topics are very popular trademarks of the Frontiers Journals Series: they are collections of at least ten articles, all centered on a particular subject. With their unique mix of varied contributions from Original Research to Review Articles, Frontiers Research Topics unify the most influential researchers, the latest key findings and historical advances in a hot research area! Find out more on how to host your own Frontiers Research Topic or contribute to one as an author by contacting the Frontiers Editorial Office: researchtopics@frontiersin.org

SUPRAMOLECULAR NUCLEIC ACID CHEMISTRY

Topic Editors:
James Tucker, University of Birmingham, United Kingdom
Janarthanan Jayawickramarajah, Tulane University, United States

Citation: Tucker, J., Jayawickramarajah, J., eds. (2020). Supramolecular Nucleic Acid Chemistry. Lausanne: Frontiers Media SA. doi: 10.3389/978-2-88966-110-7

Table of Contents

frontiers in Chemistry

EDITORIAL
published: 31 August 2020
doi: 10.3389/fchem.2020.00749

Editorial: Supramolecular Nucleic Acid Chemistry

James H. R. Tucker[1]* *and Janarthanan Jayawickramarajah*[2]*

[1] School of Chemistry, University of Birmingham, Birmingham, United Kingdom, [2] Department of Chemistry, Tulane University, New Orleans, LA, United States

Keywords: supramolecular, nucleic acids, DNA, self-assembly, molecular assemblies

Editorial on the Research Topic

Supramolecular Nucleic Acid Chemistry

The reversible and non-covalent nature of the interactions governing the structure and binding properties of nucleic acids mean that the fields of supramolecular chemistry and nucleic acid chemistry are closely intertwined. Indeed, the high fidelity and programmable molecular recognition properties of DNA have long been the source of inspiration to many a supramolecular chemist in designing molecular assemblies that are both discrete in shape and dynamic in nature. However at the same time, researchers working in the field of nucleic acids can draw inspiration and rationale from concepts and approaches that are rooted in supramolecular chemistry. For example, many themes central to supramolecular chemistry such as sensing, switching, self-assembly, catalysis, and molecular motion can be successfully applied to nucleic acid systems. This Research Topic is a compilation of 12 original papers from 50 authors and nine different countries on nucleic acid chemistry that highlight the synergies and links with supramolecular chemistry.

The collection includes two topical reviews. Firstly there is an overview by Takezawa and Shionoya of DNA three-way-junction motifs that are bridged by interstrand metal complexes; such structures could lead to new, tuneable metal-responsive supramolecular architectures based on nucleic acids. The second by Michel et al. gives a broad and detailed account of the state-of-the-art on environment-sensitive fluorescent nucleic acid probes of relevance to sensing and cell imaging applications. Following on with the sensing theme, an electrochemical approach to detecting DNA is presented by Goodchild et al., who report a new surface-bound probe with a redox tag that can discriminate between closely-related sequences, down to changes at the single base level. Another study on tagged DNA comes from Burns et al. who report a novel molecular ruler system comprised of a series of DNA strands modified in two positions with metal-bound and metal-free porphyrin groups that enable the detection and monitoring of small changes in DNA structure.

Various non-canonical DNA structural motifs are the theme of several articles in this collection, including three-way junctions (vide supra), G-quadruplexes, and i-motifs. A report by Punt et al. describes how the covalent incorporation of different ligands into DNA and their binding of d block metals impart significant changes on G-quadruplex stability, with clear implications for the controlled design of functional metal-containing nucleic acid complexes. Molecules that interact with G-quadruplexes are the focus for Ranjan et al. and in particular dual-binding ligands with both groove binding and intercalating moieties that form strong and selective complexes with these structures. The i-motif and the possibility of it playing a role in biological processes is currently a topic of considerable interest in the field of nucleic acid chemistry. An important contribution to the discussion is the report by Abdelhamid and Waller, who show how kinetic effects such as annealing and equilibration times are important factors in determining the longevity at neutral pH and ambient temperature of an i-motif structure formed from a sequence in the human telomeric region. Meanwhile Pages et al. show that the length and position of thymine loops within an i-motif forming sequence affects its structure as well as the extent of its stabilization by enantiomers of an octahedral Ru(II) complex.

Edited and reviewed by:
Tony D. James,
University of Bath, United Kingdom

***Correspondence:**
James H. R. Tucker
j.tucker@bham.ac.uk
Janarthanan Jayawickramarajah
jananj@tulane.edu

Specialty section:
This article was submitted to Supramolecular Chemistry, a section of the journal Frontiers in Chemistry

Received: *06 July 2020*
Accepted: *20 July 2020*
Published: *31 August 2020*

Citation:
Tucker JHR and Jayawickramarajah J (2020) Editorial: Supramolecular Nucleic Acid Chemistry. Front. Chem. 8:749. doi: 10.3389/fchem.2020.00749

How genetic information might have been transferred prebiotically on earth in the absence of enzymes continues to fascinate chemists. An intriguing paper by Núñez-Pertíñez and Wilks considers the possibility of deep-eutectic solvents (DESs) as stabilizing media for prebiotic reactions, using nucleic acid-templated peptide synthesis as their model. Rather different DNA-templated systems are considered by Fritz and Wagenknecht. These authors reveal the important structural parameters required to form DNA-templated assemblies of perylene-nucleoside derivatives in aqueous solutions, which includes having an ethynylene linker between the nucleobase and the chromophore. The supramolecular assembly theme continues in work reported by Atchimnaidu et al., who prepared β-CD-functionalised DNA assemblies for the binding of star-shaped adamantyl PEG polymers, resulting in the formation of non-covalent crosslinked nanoparticles for capturing both hydrophobic and hydrophilic micropollutants in water. Finally, rather different cross-linked systems are reported by Cadoni et al., who demonstrate an effective method for immobilizing PNA strands onto maleimide-functionalized gold nanoparticles, via a double exchange Diels-Alder cycloaddition reaction. These immobilized strands retain their ability to interact with DNA, with the resulting duplexes able to be released through a retro-Diels-Alder reaction.

In summary, this Research Topic has highlighted how the fields of nucleic acids and supramolecular chemistry can be imbricated to generate hybrid systems (such as assemblies that harness canonical/non-canonical base-pairing as well as synthetic metal-ligand, host-guest, and aromatic stacking interactions) of fundamental scientific interest. Further, the Topic also illustrates the potential for developing exciting function, including detecting specific DNA sequences, binding to folded DNA structures for biomedical applications, and generating assemblies capable of environmental remediation. Although just a snap-shot of the diversity of research directions being pursued in Supramolecular Nucleic Acid Chemistry—it is clear that the field shows much promise in not only generating increasingly complex systems but also in addressing topical issues plaguing modern society.

AUTHOR CONTRIBUTIONS

All authors listed have made a substantial, direct and intellectual contribution to the work, and approved it for publication.

Conflict of Interest: The authors declare that the research was conducted in the absence of any commercial or financial relationships that could be construed as a potential conflict of interest.

frontiers in Chemistry

ORIGINAL RESEARCH
published: 22 October 2019
doi: 10.3389/fchem.2019.00659

Influences of Linker and Nucleoside for the Helical Self-Assembly of Perylene Along DNA Templates

*Yannic Fritz and Hans-Achim Wagenknecht**

Karlsruhe Institute of Technology, Institute of Organic Chemistry, Karlsruhe, Germany

Six different conjugates of perylene with 2′-deoxyuridine and with 2-amino-2′-deoxyadenosine were synthesized and applied for DNA-templated assembly in aqueous buffer solutions. They differ by the linkers ethynylene, phenylene, and phenylene–ethynylene between nucleoside and chromophore. The nucleosides were investigated as monomers in $CHCl_3$ and dimethyl sulfoxide by optical spectroscopy. The properties of the four phenylene-linked conjugates are similar to that of perylene as reference because these linkers separate both aromatic parts. The ethynylene linker electronically couples the chromophore with the respective nucleoside and thus red shifts the absorbance. The DNA-templated assembly properties were elucidated by mixing the templates in aqueous buffer with the perylene–nucleoside conjugates from a dimethyl sulfoxide stock solution. Specific binding of the nucleosides was probed by comparing the results with dA_{20} and T_{20} as single-stranded DNA templates. Our studies reveal the structural parameters that are important for the DNA-templated assembly of perylenes. First, perylene-2′-deoxyuridine conjugates do not form DNA-templated helical assemblies, regardless of the choice of linker. Second, the ethynylene linker is crucial for successful DNA-templated chromophore assemblies of perylene-2-amino-2′-deoxyadenosine conjugates. Third, in contrast, the phenylene linker inhibits self-assembly along single-stranded DNA templates. In conclusion, the 2-amino-2′-deoxyadenosin in combination with the ethynylene linker provides the best structural feature for specific and helical DNA-templated assembly of perylenes. This result is important for the design of future DNA-based supramolecular architectures with chromophores, in particular DNA-based light-harvesting systems and DNA systems for emitting or sensing circularly polarized luminescence.

Keywords: DNA, chromophor, assembly, template, fluorescence

OPEN ACCESS

Edited by:
Janarthanan Jayawickramarajah, Tulane University, United States

Reviewed by:
Milan Balaz, Underwood International College, Yonsei University, South Korea
Amparo Ruiz Carretero, Centre National de la Recherche Scientifique (CNRS), France

****Correspondence:***
Hans-Achim Wagenknecht
Wagenknecht@kit.edu

Specialty section:
This article was submitted to Supramolecular Chemistry, a section of the journal Frontiers in Chemistry

Received: *02 August 2019*
Accepted: *17 September 2019*
Published: *22 October 2019*

Citation:
Fritz Y and Wagenknecht H-A (2019) Influences of Linker and Nucleoside for the Helical Self-Assembly of Perylene Along DNA Templates. Front. Chem. 7:659. doi: 10.3389/fchem.2019.00659

INTRODUCTION

Supramolecular chemistry and supramolecular polymerization summarize the efforts to self-organize molecules through interactions in a precise and controllable way. Probably more than any other class of compounds, DNA provides a rather unexplored and groundbreaking new access to this challenge via bottom–up, programmed, and hierarchically ordered assembly of molecules, in particular organic chromophores, into designed supramolecular DNA architectures. The last two centuries have shown that—beyond their pure biological purpose—nucleic acids are able to serve as unique structural basis to create nanometer-sized two- and three-dimensional objects.

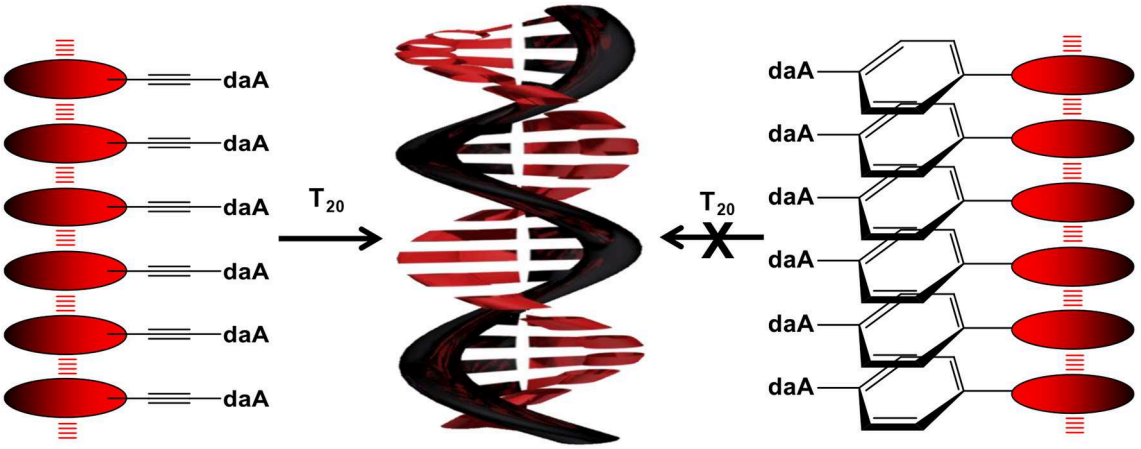

GRAPHICAL ABSTRACT | Illustration of the DNA-templated assembly of **Pe–Et–daA** and **Pe–Ph–daA**.

Representatively, the DNA nanostructures of Seeman (1982) and Kallenbach et al. (1983) and the DNA origami's by Rothemund (2006) are mentioned here. Since then, "DNA nanotechnology" has been established as the approach that applies self-assembly of DNA single strands to form molecular architectures in a highly organized manner (Yakovchuk et al., 2006; Lubrich et al., 2008; Wang et al., 2009; Chen et al., 2019). The sequence-defined recognition by canonical base pairing in DNA in combination with a perfectly coplanar stacking distance of 3.4 Å and a helical chirality should yield supramolecular architectures (Burge et al., 2006). Such architectures are difficult to be achieved by simple organic-chemical building blocks without DNA, neither covalently (polymers) nor non-covalently (supramolecular polymers). In a bottom–up approach, we follow herein the basic principle of chemistry research that "structure determines properties." Therefore, the controlled assembly of organic chromophores in supramolecular architectures based on nucleic acids holds the key potential for future functional materials with well-defined photochemical properties. In particular, the helical twist between the chromophores, which is induced by the DNA scaffold, controls electron transfer and energy transfer processes and thereby reduces the self-quenching that is typically observed in chromophore aggregates (Asanuma et al., 2003; Teo et al., 2009; Dutta et al., 2011; Kato et al., 2013; Li et al., 2013; Probst et al., 2014; Ishutkina et al., 2018).

In 2009, Kumar and Duff presented one of the first DNA-based light harvesting systems (Kumar and Duff, 2009). In the same year, our group published a temperature-controlled white-light-emitting DNA by covalent incorporation of pyrene- and Nile-red-modified nucleosides (Varghese and Wagenknecht, 2009). The combination with a perylene–nucleoside yielded a light-harvesting antenna, and thereby, any excitation in the range between 350 and 600 nm efficiently resulted in a charge-separated state (Ensslen et al., 2015a). Two years later, the influence of the template strand length on the energy transfer of attached naphthalene nucleosides was investigated by the group of Stevens (Ruiz-Carretero et al., 2011; Stevens et al., 2011). Balaz et al. created nanoassemblies with porphyrine-linked 2-aminoadenines and oligothymidine as DNA templates, which showed an adjustable helicity depending on temperature gradients (Sargsyan et al., 2014). With pyrene and Nile red attached to different nucleosides, a sequence-specific self-assembly along a template DNA strand was accomplished in 2018 (Hofsass et al., 2018). Pyrene was linked via ethynylene bridge to 2-amino-2′-deoxyadenosine (daA) and Nile red to 2′-deoxyuridine (dU), which are complementary to thymine (T) and adenine (A), respectively, as recognition units of the template. Moreover, fullerene–DNA–chromophore assemblies were integrated as photoactive layers in solar cells that showed charge carrier generation in the spectral regime of all three components (Ensslen et al., 2016). These recent examples demonstrate the significance and potential of supramolecular DNA architectures.

To get a closer insight into the influence of linker and nucleoside on the optical and self-assembly properties with DNA, six different perylene-conjugated nucleosides (**Figure 1**) are presented herein that differ (i) by the linker between the chromophore and the nucleoside, including ethynylene (Et), phenylene (Ph), and the combined phenylene–ethynylene (PhEt) linkers, and (ii) by the nucleoside, either dU that recognizes A in the DNA template, or daA that recognizes T in the DNA template. The Et linker yields a coplanar orientation of nucleoside and perylene parts in the conjugates, whereas the Ph linker introduces a rotational twist between the two parts. The PhEt linker combines the two extreme geometries and could potentially serve as compromise. We study the self-assembly of these nucleoside conjugates and the influence of the corresponding single-stranded DNA templates oligothymidine ($\mathbf{T_{20}}$) and oligo-2′-deoxyadenosine ($\mathbf{dA_{20}}$) in comparison by methods of optical spectroscopy to characterize their optical and chiroptical properties.

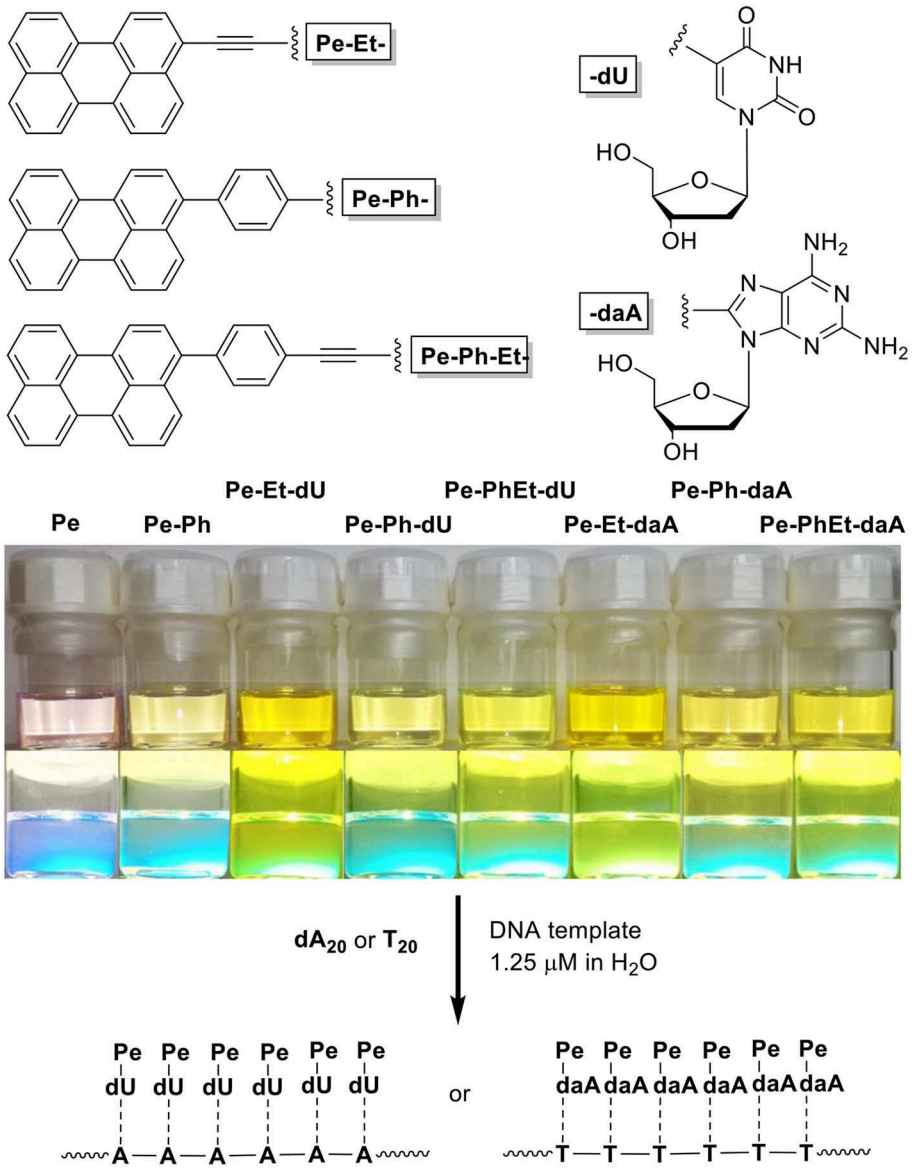

FIGURE 1 | (Top) Structure of the nucleoside conjugates **Pe–Et–dU**, **Pe–Ph–dU**, **Pe–Ph–Et–dU**, and **Pe–Et–daA**, **Pe–Ph–daA**, **Pe–Ph–Et–daA**. **(Bottom)** Image of solutions of perylene (**Pe**), 3-phenylperylene (**PePh**), and the nucleoside conjugates in $CHCl_3$/dimethyl sulfoxide (DMSO) = 4:1 (100 μM) and image of their fluorescence during excitation by a UV handheld lamp.

MATERIALS AND METHODS

All chemicals used for synthesis had at least the purification grade "for synthesis." Solvents used in synthesis, optical spectroscopy or analysis had the grade "HPLC" or "pro analysis." Water was deionized and ultra-filtrated by a Millipore Direct 8/16 from MERCK MILLIPORE. Unmodified DNA strands were bought from METABION, which were already HPLC-purified and lyophilized. The DNA was dissolved in water and concentrations were determined spectrometric with a NANODROP ND-100 spectrophotometer. All Pd-catalyzed reactions were performed under exclusion of oxygen and water (except for Suzuki-couplings, which used water as reagent). Reaction mixtures were treated by freezepump-thaw in three cycles before adding the catalyst or degassed with argon. Some reactions were performed in sealed glass vials (10 mL or 20 mL), which resulted in significantly higher yield compared to common round bottom flasks. The purity of all products were determined by NMR-spectroscopy and high-resolution mass spectrometry. NMR spectra were recorded on a BRUKER Advance 500 (500 MHz, 1H-NMR; 126 MHz, 13C-NMR). Chemical shifts were reported in parts per million (ppm), relative to the standard tetramethylsilane (δ = 0.00 ppm) and the spectrum was calibrated against the 1 H residues of the deuterated

solvents. Due to the bad solubility of most products, the use of deuterated pyridine was necessary. The mass-spectrometry was performed on a THERMOFISHER Scientientific Q Exactive (Orbitrap) by electron spray ionization (ESI) and reported in mass/charge (m/z). In case of daA-containing products, the protonated species was mostly found. For all spectroscopic experiments semi-micro quartz glass cuvettes from STARNA (width 10 mm, volume 1.4 mL) were used and all spectra were recorded at 20°C. Absorption spectra were recorded on a Lambda 750 from PERKIN ELMER with a PTP-6+6 Peltier System. Circular dichroism was measured with a JASCO J-810 Spectropolarimeter and the peltier-element PTC-423S (100 nm/min, 4 accumulations). Fluorescence was recorded on a Fluoromax-4 from HORIBA SCIENTIFIC with an AC 200 thermostat from THERMO SCIENTIFIC. All samples were excited at 420 nm and the spectra were divided by the absorbance at 420 nm for comparison. Absolute fluorescence quantum yields were determined with a Quantaurus QY C11347 from HAMAMATSU (measured in different concentrations between 40 and 60 μM and averaged). Self-assembly experiments were prepared as follows: Chromophore 45 mM, DNA template 1.5 μM, phosphate-buffer 10 mM (pH 7.0), 250 mM NaCl. Due to solubility issues, the chromophores were added from a 1 mM stock solution in DMSO, which causes a DMSO content of 4.5%. For CD and fluorescence experiments the Chromophore was added shortly before the measurement, to minimize the influence of precipitation.

RESULTS AND DISCUSSION

All nucleoside conjugates were synthesized as described in the **Supporting Information**. The key steps are Pd-catalyzed Sonogashira and Suzuki couplings between the halogenated nucleoside precursors and the perylene derivatives. We expected that the linker between chromophore and nucleoside has a strong impact on the photophysical properties. In principal, the ethynylene group connects the perylene chromophore with the nucleosides in a coplanar orientation and thereby yields π-conjugation between them, whereas the phenylene group electronically isolates the π-systems by rotation. Indeed, this structural influence is clearly observable by the ultraviolet–visible (UV/vis) absorbance (**Figure 2**): The characteristic perylene absorbance between 400 and 520 nm is nearly identical for all Ph- and Ph–Et-linked conjugates compared to 1-phenyl-perylene as reference (Kawasumi et al., 2013). In particular, both **Pe–Ph–dU** and **Pe–Ph–daA** show only very little absorbance differences to the reference, which is an advantage of the Ph linker that efficiently interrupts the π-conjugation with the nucleoside. Only the Et-linked conjugates **Pe–Et–dU** and **Pe–Et–daA** display an absorbance that is red shifted by 23 and 35 nm, respectively. This shows the π-conjugating effect of the Et linker.

In order to study the effect of the nucleosides and the linkers on the fluorescence, the spectra and quantum yields were recorded (**Table 1** and **Figure S1**). In $CHCl_3$ as solvent [with 6% dimethyl sulfoxide (DMSO) to ensure solubility], the four Ph- and Ph–Et-conjugated nucleosides yield higher quantum yields (77–84% for dU and 83% for daA conjugates) than **Pe–Et–dU** and **Pe–Et–daA** (58 and 78%, respectively). These results agree with the electronically separating character of the Ph linker, too. In contrast, the Et group enlarges the π-system and thus lowers the quantum yields. In conclusion, these results show the

TABLE 1 | Fluorescence quantum yields of perylene (**Pe**), 1-phenylperylene (**PePh**), and the perylene–nucleosides in DMSO and $CHCl_3$ with 6% DMSO (average of 40, 50, and 60 μM), $\lambda_{exc} = 420$ nm.

Nucleoside	Φ_F in DMSO	Φ_F in $CHCl_3$ (6% DMSO)
Pe–Et–dU	76 ± 0.97%	58 ± 1.1%
Pe–Ph–dU	96 ± 1.9%	84 ± 0.16%
Pe–Ph–Et–dU	90 ± 1.6%	77 ± 0.45%
Pe–Et–daA	6.7 ± 0.21%	78 ± 0.66%
Pe–Ph–daA	2.8 ± 0.08%	83 ± 0.21%
Pe–Ph–Et–daA	5.5 ± 0.16%	83 ± 0.21%
Pe	~100%	98 ± 0.60%
PePh	~100%	~100%

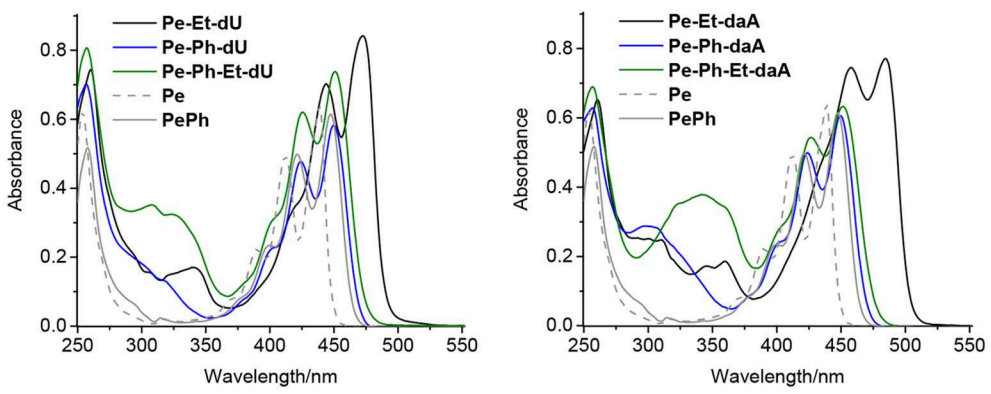

FIGURE 2 | Ultraviolet–visible (UV/vis) absorption spectra of perylene (**Pe**), 1-phenylperylene (**PePh**), and the perylene–nucleosides with dU **(Left)** and with daA **(Right)**, each 20 μM in $CHCl_3$ [2% dimethyl sulfoxide (DMSO)].

expected tuning of the optical properties of the chromophore–nucleoside conjugates by the choice of linker. Surprisingly, the emissions of the daA-modified chromophores are nearly quantitatively quenched in pure DMSO, while the emissions of the dU-modified ones give quantum yields from 76 to 96%. These striking fluorescence quantum yield differences in DMSO become plausible by photoinduced electron transfer in the daA conjugates that occurs only in the highly polar solvent DMSO. Based on redox potentials from literature, daA can be more easily oxidized ($E_{ox} = 1.1$ V vs. NHE in water) (Stockert et al., 2002) than dU ($E_{ox} = 1.34$ V) (Faraggi et al., 1996). Using the reduction potential for perylene of $E_{red} = -1.91$ V together with $E_{00} = 2.8$ eV (Rossetti et al., 2005), the Rehm–Weller equation for the driving forces $\Delta G = E_{ox} - E_{red} - E_{00} + E_C$ (Coulomb energy E_c) gives a small ΔG of -0.3 eV for the daA conjugates in favor of a photoinduced charge transfer, but a negligible ΔG for the dU conjugates (without consideration of E_C) that makes the photoinduced charge transfer very unlikely in the latter conjugates. Obviously, the different polarity of the solvents DMSO and $CHCl_3$ influence the Coulomb energy in the charge-separate state such that only in the highly polar solvent DMSO the photoinduced electron transfer in the daA conjugates is observable. In DMSO, the charge-separated state is stabilized and thereby the Coulomb energy is reduced.

To examine the self-assembling ability of the nucleoside conjugates, experiments with $\mathbf{T_{20}}$ and $\mathbf{dA_{20}}$, respectively, as single-stranded DNA templates were performed. The chromophore conjugates were characterized by their UV/vis absorbance, fluorescence, and circular dichroism in aqueous buffer at pH 7 to elucidate (i) their self-assembling properties and, more importantly (ii) the potential influence of the single-stranded DNA templates. Specific binding of the nucleoside conjugates was elucidated by comparing the results with $\mathbf{dA_{20}}$ and $\mathbf{T_{20}}$ as templates. Previous work in our group revealed that the assembly of nucleosides along DNA templates succeeded at room temperature with no annealing (Hofsass et al., 2018). We kept this method for the studies herein. The shapes of all absorption spectra in H_2O differ from those of the monomer reference spectra in DMSO. First, the absorbance of the assemblies of **Pe–Et–dU** (**Figure 3**, left) and **Pe–Et–daA** (**Figure 3**, middle) along the DNA templates were compared to DNA-free samples in aqueous buffer (with 4.5% DMSO from the perylene-nucleoside stock solutions). In case of **Pe–Et–dU**, the perylene-typical fine structure is significantly broadened, indicating self-assembly of the chromophores. There is only little influence of the complementary DNA template $\mathbf{dA_{20}}$, if at all, by a slightly increased absorbance compared to the non-complementary template $\mathbf{T_{20}}$ and compared to the absence of any DNA, too. For **Pe–Et–daA** in the presence of the complementary template $\mathbf{T_{20}}$, however, the perylene-typical fine structure is maintained but with an altered ratio of the included absorption bands. With the non-complementary template $\mathbf{dA_{20}}$ and without any DNA, this fine structure is completely lost, and the absorbance is significantly blue shifted to a broad absorbance from 350 to 550 nm with a maximum at 408 nm. Since this absorbance is similar to that without the template, we assign it to the non-templated self-assembly of **Pe–Et–daA**. The influence of the complementary DNA template $\mathbf{T_{20}}$ is significant and serves as first indication for a base pairing of the **Pe–Et–daA** monomers along this template and thus the formation of an ordered and helical assembly (*vide infra*). It is important to mention here that daA is, in principal, a modified 2′-deoxyadenosine with a second amino group to enhance the binding selectivity by a potential third hydrogen bond to thymidines as recognition unit in the DNA template $\mathbf{T_{20}}$ (Hofsass et al., 2018). The lacking third hydrogen bond between **Pe–Et–dU** and the DNA templates probably accounts for its lacking selectivity between $\mathbf{dA_{20}}$ and $\mathbf{T_{20}}$ (and

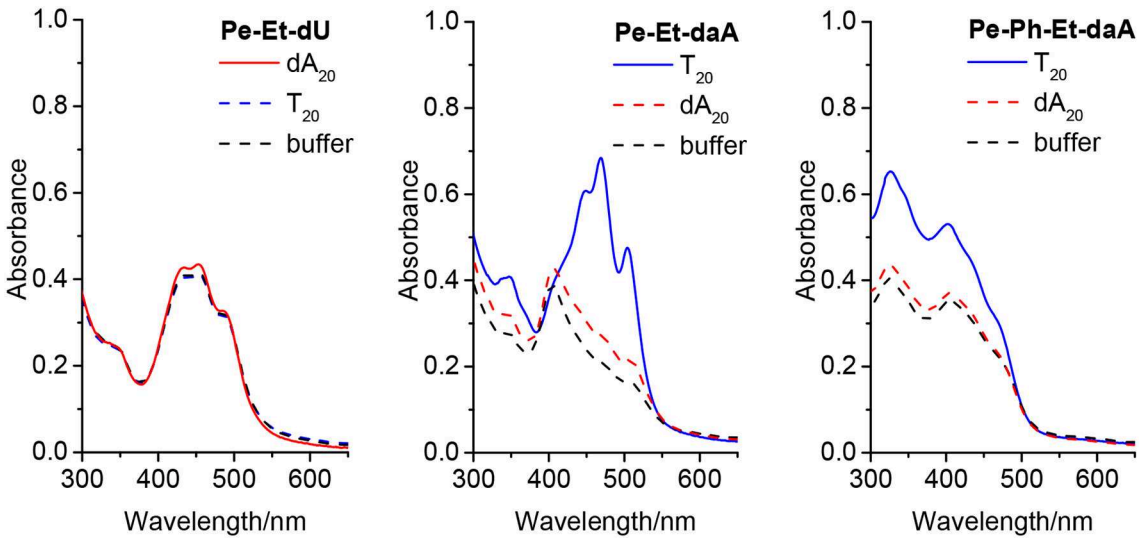

FIGURE 3 | Ultraviolet–visible (UV/vis) absorbance of **Pe–Et–dU (Left)**, **Pe–Et–daA (Middle)**, and **Pe–Ph–Et–daA (Right)**, each 45 μM in aqueous buffer (10 mM sodium phosphate, pH 7, 250 mM NaCl, with 4.5% DMSO) without and with DNA templates $\mathbf{T_{20}}$ and $\mathbf{dA_{20}}$ (1.5 μM), respectively.

without template). The UV/vis absorbances of the remaining four nucleosides with Ph- and Ph–Et linkers in water look all similar and do not allow to elucidate any influence of the single-stranded DNA templates on the formation of these chromophore assemblies (**Figure 3**, right and **Figure S3**). This indicates that the Ph linkers are not all suitable for DNA-templated assembly of perylenes. A careful look on the absorbances reveals, however, that only **Pe–Ph–Et–daA** shows an enhanced absorbance at 408 nm in the presence of the complementary template $\mathbf{T_{20}}$ compared to $\mathbf{dA_{20}}$ and to pure buffer (**Figure 3**, right), indicating that there might be a small structural influence of the DNA on this particular chromophore assembly.

The fluorescence further supports the elucidation of structural prerequisites for the assembly of perylene–nucleoside conjugates along single-stranded DNA templates that were indicated by their UV/vis absorbance. In all non-templated samples, an unstructured and broad fluorescence was observed at ∼600–650 nm, which we assign to perylene excimers as a result of the self-assembly of the perylene–nucleoside conjugates in water. In particular, both **Pe–Et–dU** and **Pe–Et–daA** without DNA templates show this unstructured and broad fluorescence at 600 and 650 nm, respectively (**Figure 4**, left and middle). If we assume a coplanar arrangement by π-π stacking between the perylene monomers and Watson–Crick or any similar base pairing between the nucleoside conjugates and the templates, a helical twist is introduced by the DNA to the perylene assembly in water. According to our previous results with pyrene conjugates, such helicity typically reduces excimer-like fluorescence (Trifonov et al., 2005). In fact, the assembly in the presence of the template $\mathbf{T_{20}}$ significantly changes the fluorescence readout of **Pe–Et–daA**. This sample shows mainly a blue-shifted and enhanced fluorescence at 590 nm, which we assign to the ordered and presumably helical assembly of these chromophores. This assignment supports the considerably different absorbance of **Pe–Et–daA** with $\mathbf{T_{20}}$ as described above. The assembly of **Pe–Et–dU** shows only fluorescence between 450 and 550 nm and only little excimer fluorescence intensity. The lacking influence of neither $\mathbf{dA_{20}}$ nor $\mathbf{T_{20}}$ as complementary or non-complementary templates on the fluorescence readout implies that **Pe–Et–dU** forms a stable non-templated self-assembly. This stands in contrast to **Pe–Et–daA** for which only the complementary DNA template $\mathbf{T_{20}}$ orders the chromophore assembly in such a way that the fluorescence is blue shifted. In contrast to the two Et-linked nucleosides, the fluorescence of **Pe–Ph–dU**, **Pe–Ph–daA,** and **Pe–Ph–Et–dU** show only excimer-like fluorescence of the non-templated and self-assembled perylene conjugates at 650 nm, which is not significantly altered by the DNA templates (**Figure S2**). Similar to the observations by UV/vis absorption spectroscopy, the DNA templates have no significant effect on the self-assembly of the Pe–Ph conjugates. Obviously, the twist introduced by the Ph in these nucleoside conjugates disturbs the coplanar orientation of nucleoside and perylene and thereby inhibits the templated assembly along the single-stranded DNA. Typical DNA double helix has a stacking distance of 0.34 nm between two base pairs, whereas the diameter of Ph is 0.43 nm; a rotational twist in the Ph-linked conjugates cannot be accepted by this type of assembly. A careful look onto the fluorescence of **Pe–Ph–Et–daA** reveals a small blue shift from 628 nm (with the non-complementary template $\mathbf{dA_{20}}$ and without any template) to 618 nm with the complementary template $\mathbf{T_{20}}$ (**Figure 4**, right) and thereby supports the small influence of this DNA template on this particular chromophore assembly similarly to the previously discussed UV/vis absorbance.

To get a closer look into the possible helical orientations of the perylene–nucleoside conjugates introduced by the single-stranded DNA template, circular dichroism (CD) was recorded for all samples. We do not interpret the CD in the range between 250 and 350 nm because the perylene–nucleoside absorbance overlaps with the template absorbance. All nucleoside conjugates without DNA template display only small chiroptical activity in DMSO but no sign for ordered helical arrangements (**Figure S4**). These signals mainly arise from the chromophores connected to the chiral β-D-ribofuranoside residue and in particular in DMSO as good solvent for both parts of the nucleoside conjugates, polar and non-polar. The CD spectra of **Pe–Et–dU** with $\mathbf{dA_{20}}$, with $\mathbf{T_{20}}$ and without any DNA template are similar to those of the monomers in DMSO (**Figure 5**, left). This result further supports our explanation that the stable, non-templated self-assemblies of **Pe–Et–dU** are not chiral and they are not significantly influenced by the DNA template. The intrinsic self-stacking of the perylenes overrules any template effect. Similarly, small CD signals are observed in the samples with **Pe–Ph–dU**, **Pe–Ph–daA**, and **Pe–Ph–Et–dU** (**Figure S5**). This makes conclusively clear that two potential hydrogen bonds, which are provided by the dU unit, are not sufficient for effective and specific assembly of perylenes along DNA templates. In contrast, both **Pe–Et–daA** and **Pe–PhEt–daA** show strong chiroptical signals, which are enhanced in presence of $\mathbf{T_{20}}$. The CD of **Pe–Et–daA** with $\mathbf{T_{20}}$ (**Figure 5**, middle) displays a clearly excitonically coupled signal in the perylene absorbance range between 350 and 550 nm by the combination of a negative Cotton effect followed by a positive Cotton effect. This indicates a left-handed chirality in these DNA-based assemblies with coplanarily stacked **Pe–Et–daA** chromophores. We previously observed this chirality for DNA-templated assemblies with pyrene- and Nile-red-modified nucleosides (Ensslen et al., 2015b; Hofsass et al., 2018). Even stronger CD signals were observed for the templated assemblies of **Pe–Ph–Et–daA** with $\mathbf{T_{20}}$ (**Figure 5**, right) but not for **Pe–Ph–Et–dU** with $\mathbf{dA_{20}}$ (**Figure S5**). Obviously, the Ph–Et linker still allows the chromophore assembly along $\mathbf{T_{20}}$, but the perylene orientation differs from that of the clearly excitonically couples and coplanarily stacked **Pe–Et–daA** assembly with $\mathbf{T_{20}}$ because the CD shows only a negative Cotton effect. Overall, there are two major results with respect to the structural parameters: (i) The structural influence of the DNA template is observed only with the daA conjugates but not with the dU conjugates, and (ii) while the Et-linked chromophores with daA selectively assemble along the complementary template strand with left-handed chirality, the Ph-linked chromophores do not form templated water-soluble assemblies. Only the conjugate of daA

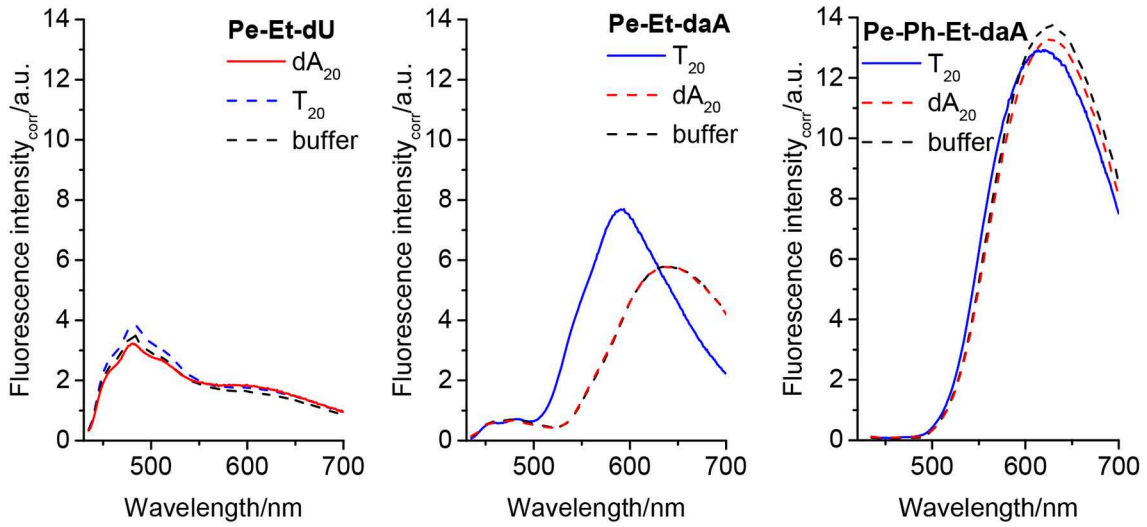

FIGURE 4 | Fluorescence of **Pe–Et–dU (Left)**, **Pe–Et–daA (Middle)**, and **Pe–Et–daA (Right)**, each 45 μM in aqueous buffer (10 mM sodium phosphate, pH 7, 250 mM NaCl, with 4.5% DMSO) without and with DNA templates $\mathbf{T_{20}}$ and $\mathbf{dA_{20}}$ (1.5 μM), respectively. Excitation at 420 nm. The fluorescence intensity was corrected by the absorbance at 420 nm.

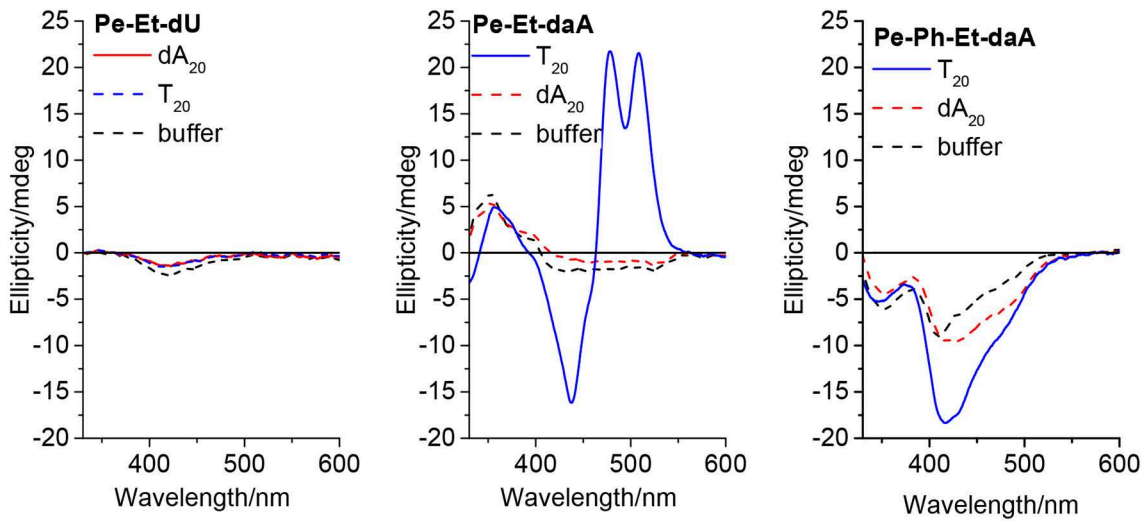

FIGURE 5 | Circular dichroism of **Pe–Et–dU (Left)**, **Pe–Et–daA (Middle)**, and **Pe–Ph–Et–daA (Right)**, each 45 μM in aqueous buffer (10 mM sodium phosphate, pH 7, 250 mM NaCl, with 4.5% DMSO) without and with DNA templates $\mathbf{T_{20}}$ and $\mathbf{dA_{20}}$ (1.5 μM), respectively.

with both linkers (Ph–Et) interact with the DNA templates in a different type of chiral assembly.

CONCLUSIONS

Six different conjugates of perylene with dU and with daA were synthesized and applied for DNA-templated assembly in aqueous solutions. The perylene conjugates differ by the linkers between the perylene chromophore and by the aromatic nucleoside heterocycle. The photophysical properties of the nucleoside monomers and their self-assemblies were investigated by optical spectroscopy methods. The Ph linker as well as the combined Ph–Et linker separate both aromatic parts. Accordingly, the optical properties of the Pe–Ph and Pe–Ph–Et conjugates with dU and daA are similar to that of perylene and 1-phenylperylene as reference chromophores. In comparison, the Et linker electronically couples the chromophores and thus red shifts the absorbance. The DNA assemblies were formed by mixing the templates in water with the perylene–nucleoside conjugates from a DMSO stock solution. Important structural

parameters for the DNA-templated assembly of perylenes were elucidated: (i) Perylene–dU conjugates do form stable, non-templated assemblies and overrule the DNA template effect. dU can base pair only by two hydrogen bonds with the nucleotides in the DNA template, whereas daA provides the donors and acceptor for three hydrogen bonds. Although we do not provide direct experimental evidenced for base pairing via hydrogen bonding similar to Watson–Crick base pairing, this difference seems to be striking in particular for the comparison of the assemblies with **Pe–Et–dU** vs. with **Pe–Et–daA**. (ii) The Et linker is required for successful DNA-templated chromophore assemblies of the conjugate with daA. It orientates both aromatic parts in a coplanar orientation. Obviously, this facilitates the formation of a helical DNA-templated assembly with presumably π-π-stacked coplanarily arranged perylenes, which was evidenced in particular by the assemblies of **Pe–Et–daA** in comparison with **Pe–Ph–daA**. (iii) The Ph linker twists both aromatic parts and thus completely inhibits self-assembly along single-stranded DNA templates in aqueous solutions. Accordingly, the conjugate **Pe–Et–daA** shows the strongest selectivity to the complementary DNA templates, while the Ph-linked one did not form templated assemblies. The assembly of **Pe–Et–daA** with $\mathbf{T_{20}}$ shows a left-handed chirality and excitonic coupling. The conjugate **Pe–Ph–Et–daA** with both linkers shows also a structural influence by $\mathbf{T_{20}}$ as DNA template in particular according to the chiroptical properties; however, the structure of this perylene assembly significantly differs from the coplanar and excitonically coupled **Py–Et–daA** assembly. Overall, the daA nucleoside in combination with the Et linker provides the two structural prerequisites for specific and helical DNA-templated assembly that were identified by our study. This result is in agreement with other DNA-templated chromophore arrangements by us and others (Stevens et al., 2011; Sargsyan et al., 2014; Hofsass et al., 2018). Such investigations are important for the design of DNA-based supramolecular architectures with chromophores, in particular DNA-based light-harvesting systems and DNA architectures for emitting or sensing circularly polarized luminescence.

DATA AVAILABILITY STATEMENT

All datasets generated for this study are included in the manuscript/**Supplementary Files**.

AUTHOR CONTRIBUTIONS

YF did all experiments and wrote parts of the manuscript. H-AW supervised the research and wrote the manuscript.

ACKNOWLEDGMENTS

Financial support by the Deutsche Forschungsgemeinschaft (Wa 1386/20-1) and KIT was gratefully acknowledged.

EXPERIMENTAL PART

All experimental procedures are described in the **Supporting Information**.

SUPPLEMENTARY MATERIAL

The Supplementary Material for this article can be found online at: https://www.frontiersin.org/articles/10.3389/fchem.2019.00659/full#supplementary-material

REFERENCES

Asanuma, H., Kashida, H., Liang, X., and Komiyama, M. (2003). DNA–Naphthyl Red conjugate as a visualizing probe of DNA hybridization. *Chem. Commun.* 1536–1537. doi: 10.1039/B302875E

Burge, S., Parkinson, G. N., Hazel, P., Todd, A. K., and Neidle, S. (2006). Quadruplex DNA: sequence, topology and structure. *Nucl. Acids Res.* 34, 5402–5415. doi: 10.1093/nar/gkl655

Chen, K., Kong, J., Zhu, J., Ermann, N., Predki, P., and Keyser, U. F. (2019). Digital data storage using DNA nanostructures and solid-state nanopores. *Nano Lett.* 19, 1210–1215. doi: 10.1021/acs.nanolett.8b04715

Dutta, P. K., Varghese, R., Nangreave, J., Lin, S., Yan, H., and Liu, Y. (2011). DNA-directed artificial light-harvesting antenna. *J. Am. Chem. Soc.* 133, 11985–11993. doi: 10.1021/ja1115138

Ensslen, P., Brandl, F., Sezi, S., Varghese, R., Kutta, R. J., Dick, B., et al. (2015a). DNA-based oligochromophores as light-harvesting systems. *Chem. Eur. J.* 21, 9349–9354. doi: 10.1002/chem.201501213

Ensslen, P., Fritz, Y., and Wagenknecht, H. A. (2015b). Mixed non-covalent assemblies of ethynyl nile red and ethynyl pyrene along oligonucleotide templates. *Org. Biomol. Chem.* 13, 487–492. doi: 10.1039/C4OB01860E

Ensslen, P., Gartner, S., Glaser, K., Colsmann, A., and Wagenknecht, H. A. (2016). A DNA-fullerene conjugate as a template for supramolecular chromophore assemblies: towards DNA-based solar cells. *Angew. Chem. Int. Ed. Engl.* 55, 1904–1908. doi: 10.1002/anie.201509332

Faraggi, M., Broitman, F., Trent, J. B., and Klapper, M. H. (1996). One-electron oxidation reactions of some purine and pyrimidine bases in aqueous solutions. electrochemical and pulse radiolysis studies. *J. Phys. Chem.* 100, 14751–14761. doi: 10.1021/jp960590g

Hofsass, R., Sinn, S., Biedermann, F., and Wagenknecht, H. A. (2018). Programmable and sequence-selective supramolecular assembly of two different chromophores along DNA templates. *Chem. Eur. J.* 24, 16257–16261. doi: 10.1002/chem.201804314

Ishutkina, M. V., Berry, A. R., Hussain, R., Khelevina, O. G., Siligardi, G., and Stulz, E. (2018). Self-assembled porphyrazine nucleosides on DNA templates: highly fluorescent chromophore arrays and sizing forensic tandem repeat sequences. *Eur. J. Org. Chem.* 2018, 5054–5059. doi: 10.1002/ejoc.201800683

Kallenbach, N. R., Ma, R.-I., and Seeman, N. C. (1983). An immobile nucleic acid junction constructed from oligonucleotides. *Nature* 305, 829–831. doi: 10.1038/305829a0

Kato, T., Kashida, H., Kishida, H., Yada, H., Okamoto, H., and Asanuma, H. (2013). Development of a robust model system of FRET using base surrogates tethering fluorophores for strict control of their position and orientation within DNA duplex. *J. Am. Chem. Soc.* 135, 741–750. doi: 10.1021/ja309279w

Kawasumi, K., Mochida, K., Segawa, Y., and Itami, K. (2013). Palladium-catalyzed direct phenylation of perylene: struvtural and optical properties of 3,4,9-triphenylperylene and 3,4,9,10-tetraphenylperylene. *Tetrahedron* 69, 4371–4374. doi: 10.1016/j.tet.2013.01.037

Kumar, C. V., and Duff, M. R. Jr. (2009). DNA-based supramolecular artificial light harvesting complexes. *J. Am. Chem. Soc.* 131, 16024–16026. doi: 10.1021/ja904551n

Li, S., Langenegger, S. M., and Häner, R. (2013). Control of aggregation-induced emission by DNA hybridization. *Chem. Commun.* 49, 5835–5837. doi: 10.1039/c3cc42706d

Lubrich, D., Lin, J., and Yan, J. (2008). A contractile DNA machine. *Angew. Chem. Int. Ed.* 47, 7026–7028. doi: 10.1002/anie.200800476

Probst, M., Langenegger, S. M., and Häner, R. (2014). A modular LHC built on the DNA three-way junction. *Chem. Commun.* 50, 159–161. doi: 10.1039/C3CC47490A

Rossetti, L., Franceschin, M., Schirripa, S., Bianco, A., Ortaggi, G., and Savino, M. (2005). Selective interactions of perylene derivatives having different side chains with inter- and intramolecular G-quadruplex DNA structures. A correlation with telomerase inhibition. *Bioorg. Med. Chem. Lett.* 2005, 413–420. doi: 10.1016/j.bmcl.2004.10.061

Rothemund, P. W. (2006). Folding DNA to create nanoscale shapes and patterns. *Nature* 440, 297–302. doi: 10.1038/nature04586

Ruiz-Carretero, A., Janssen, P. G. A., Stevens, A. L., Surin, M., Herz, L. M., and Schenning, A. P. H. J. (2011). Directing energy transfer in discrete one-dimensional oligonucleotide-templated assemblies. *Chem. Commun.* 47, 884–886. doi: 10.1039/C0CC04128A

Sargsyan, G., Leonard, B. M., Kubelka, J., and Balaz, M. (2014). Supramolecular ssDNA templated porphyrin and metalloporphyrin nanoassemblies with tunable helicity. *Chem. Eur. J.* 20, 1878–1892. doi: 10.1002/chem.201304153

Seeman, N. C. (1982). Nucleic acid junctions and lattices. *J. Theor. Biol.* 99, 237–247. doi: 10.1016/0022-5193(82)90002-9

Stevens, A. L., Janssen, P. G. A., Ruiz-Carretero, A., Surin, M., Schenning, A. P. H. J., and Herz, L. M. (2011). Energy transfer in single-stranded DNA-templated stacks of naphthalene chromophores. *J. Phys. Chem. C* 115, 10550–10560. doi: 10.1021/jp2036444

Stockert, A. L., Shinde, S. S., Anderson, R. F., and Hille, R. (2002). The reaction mechanism of xanthine oxidase: evidence for two-electron chemistry rather than sequential one-electron steps. *J. Am. Chem. Soc.* 124, 14554–14555. doi: 10.1021/ja027388d

Teo, Y. N., Wilson, J. N., and Kool, E. T. (2009). Polyfluorophores on a DNA backbone: a multicolor set of labels excited at one wavelength. *J. Am. Chem. Soc.* 131, 3923–3933. doi: 10.1021/ja805502k

Trifonov, A., Raytchev, M., Buchvarov, I., Rist, M., Barbaric, J., Wagenknecht, H. A., et al. (2005). Ultrafast energy transfer and structural dynamics in DNA. *J. Phys. Chem. B* 109, 19490–19495. doi: 10.1021/jp052108c

Varghese, R., and Wagenknecht, H. A. (2009). White-light-emitting DNA (WED). *Chem. Eur. J.* 15, 9307–9310. doi: 10.1002/chem.200901147

Wang, R., Liu, W., and Seeman, N. C. (2009). Prototyping nanorod control: a DNA double helix sheathed within a DNA six-helix bundle. *Chem. Biol.* 16, 862–867. doi: 10.1016/j.chembiol.2009.07.008

Yakovchuk, P., Protozanova, E., and Frank-Kamenetskii, M. D. (2006). Base-stacking and base-pairing contributions into thermal stability of the DNA double helix. *Nucl. Acids Res.* 34, 564–574. doi: 10.1093/nar/gkj454

Conflict of Interest: The authors declare that the research was conducted in the absence of any commercial or financial relationships that could be construed as a potential conflict of interest.

frontiers in Chemistry

ORIGINAL RESEARCH
published: 05 November 2019
doi: 10.3389/fchem.2019.00744

Stabilization of Long-Looped i-Motif DNA by Polypyridyl Ruthenium Complexes

*Benjamin J. Pages[1], Sarah P. Gurung[2,3], Kane McQuaid[2,3], James P. Hall[1,3], Christine J. Cardin[2] and John A. Brazier[1]**

[1] School of Pharmacy, University of Reading, Reading, United Kingdom, [2] Department of Chemistry, University of Reading, Reading, United Kingdom, [3] Diamond Light Source, Didcot, United Kingdom

A spectroscopic study of the interactions of Λ- and Δ-$[Ru(phen)_2(dppz)]^{2+}$ with i-motif DNA containing thymine loops of various lengths. In the presence of i-motifs, the luminescence of the Λ enantiomer was enhanced much more than the Δ. Despite this, the effect of each enantiomer on i-motif thermal stability was comparable. The sequences most affected by $[Ru(phen)_2(dppz)]^{2+}$ were those with long thymine loops; this suggests that long-looped i-motifs are attractive targets for potential transition metal complex drugs and should be explored further in drug design.

Keywords: i-motif, DNA, ruthenium, melting, stabilization, luminescence

OPEN ACCESS

Edited by:
Janarthanan Jayawickramarajah, Tulane University, United States

Reviewed by:
Robert Elmes, Maynooth University, Ireland
Qionghua Jin, Capital Normal University, China

***Correspondence:**
John A. Brazier
j.a.brazier@reading.ac.uk

Specialty section:
This article was submitted to Supramolecular Chemistry, a section of the journal Frontiers in Chemistry

Received: *14 August 2019*
Accepted: *17 October 2019*
Published: *05 November 2019*

Citation:
Pages BJ, Gurung SP, McQuaid K, Hall JP, Cardin CJ and Brazier JA (2019) Stabilization of Long-Looped i-Motif DNA by Polypyridyl Ruthenium Complexes. Front. Chem. 7:744. doi: 10.3389/fchem.2019.00744

INTRODUCTION

The intercalated motif (i-motif) is a DNA structure containing intercalated cytosine$^+$-cytosine base pairs between four strands (**Figures 1A,B**) (Gehring et al., 1993; Školáková et al., 2019). I-motifs were originally thought to only form in acidic pH due to the protonation of cytosine required; however, stable i-motif formation has been reported at alkaline (Zhou et al., 2010) and neutral pH (Day et al., 2013; Fujii and Sugimoto, 2015; Wright et al., 2017), as well as conditions mimicking physiological molecular crowding (Rajendran et al., 2010). Moreover, recent demonstrations of the presence of i-motifs in the nuclei of human cells (Dzatko et al., 2018; Zeraati et al., 2018), and their ability to inhibit DNA polymerase (Takahashi et al., 2017) has increased interest in their biological function (Abou assi et al., 2018). Sequences that are complementary to those that form G-quadruplexes have been shown to form i-motif structures in the promoter regions of several cancer genes (Brooks et al., 2010; Brazier et al., 2012; Li et al., 2016). These include the transcription factors that code the cellular myelocytomatosis (c-Myc) (Mathur et al., 2004) and B-cell lymphoma-2 (Bcl-2) oncogenes, the latter of which is overexpressed in some cancers and may be underexpressed in some neurodegenerative diseases (Bar-Am et al., 2005; Knight et al., 2019). The transcription factor hnRNP LL reportedly binds to i-motifs, which suggests that the i-motif acts as a recognition site for the activation of transcription of Bcl-2(Kang et al., 2014).

The unique structure and potential biological roles of the i-motif makes it an attractive binding target for small molecules, particularly if the binding results in stabilization. For example, the porphyrin TMPyP4 reportedly binds to i-motifs similar in structure to the human telomeric sequence [5′-$(C_3TAA)_3C_3$-3′] (Fedoroff et al., 2000). A variety of other i-motif-binding ligands have been reported, including carbon nanotubes (Li et al., 2006), bis-acridines (Alberti et al., 2001), mitoxantrone (Wright et al., 2016), crystal violet (Ma et al., 2011), and derivatives of thiazole orange (Sheng et al., 2017) and coumarin (Satpathi et al., 2019). An under-researched family of ligands in the field of i-motifs is transition metal complexes, of which i-motif binding studies are limited

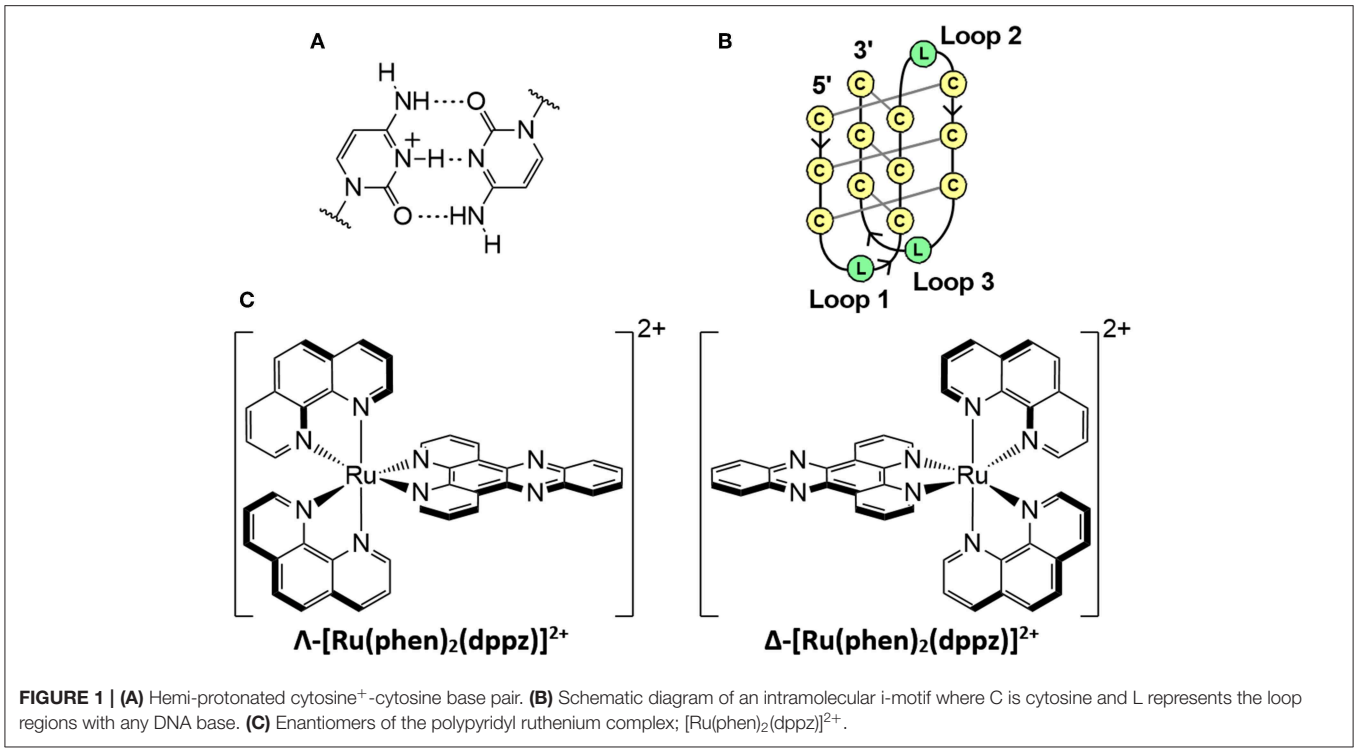

FIGURE 1 | (A) Hemi-protonated cytosine^{+}-cytosine base pair. **(B)** Schematic diagram of an intramolecular i-motif where C is cytosine and L represents the loop regions with any DNA base. **(C)** Enantiomers of the polypyridyl ruthenium complex; $[Ru(phen)_2(dppz)]^{2+}$.

(Shi et al., 2010a,b; Lu et al., 2015). Metal complexes have been studied as DNA binders for decades due to their uses as therapeutic and diagnostic agents (Metcalfe and Thomas, 2003; Pages et al., 2015; Deo et al., 2016). In particular, polypyridyl ruthenium complexes have been extensively researched for medicinal purposes due to their high stability, affinity for DNA, and luminescence properties (Gill and Thomas, 2012; Deo et al., 2016; Poynton et al., 2017). The complex $[Ru(phen)_2(dppz)]^{2+}$ (**Figure 1C**, where phen = 1,10-phenanthroline; dppz = dipyrido[3,2-*a*:2′3′-*c*]phenazine) and derivatives demonstrate a DNA "light switch" effect, in which luminescence is greatly enhanced when bound to DNA (Friedman et al., 1990; Cardin et al., 2017). The equilibrium between dark and emissive states is influenced by both changes in solvent environment around the ancillary phen ligands and changes in the hydrogen bonding of solvent molecules with the pyrazine nitrogen atoms of the dppz ligand (Chantzis et al., 2013; Véry et al., 2014). The emissive state occurs during intercalative binding of $[Ru(phen)_2(dppz)]^{2+}$ with DNA (Hartshorn and Barton, 1992; Olofsson et al., 2004). Solution and crystallographic studies have revealed that this complex and its derivatives bind to duplex and G-quadruplex DNA (Wilson et al., 2013; Hall et al., 2016; McQuaid et al., 2019a), and can inhibit telomerase activity (Yu et al., 2012). Preliminary work has demonstrated non-specific binding between i-motifs and *rac*-$[Ru(phen)_2(dppz)]^{2+}$ (*rac*-Ru) (Shi et al., 2010a,b).

We have previously demonstrated that the stability of i-motifs is influenced by loop length, with longer loops resulting in lower overall stability and vice-versa; this is likely due to the differences in flexibility of the loop regions (Gurung et al., 2015). We speculate that these regions are more desirable binding sites as they aren't as tightly packed as the intercalated cytosine core. In fact, the nature of the lateral loops of the Bcl-2 i-motif was determined to be vital to the binding potency of IMC-48 (Kang et al., 2014). Here we report the first study of interactions between enantiomerically resolved ruthenium complexes and i-motifs with various loop lengths. We have used synchrotron radiation circular dichroism (SRCD), UV, and luminescence spectroscopy to probe the binding of Λ-$[Ru(phen)_2(dppz)]^{2+}$ (Λ-Ru) and Δ-$[Ru(phen)_2(dppz)]^{2+}$ (Δ-Ru) to a series of i-motif sequences. These consisted of a block of three paired cytosines and combinations of long and short thymine loops. Loop lengths were either uniform (C_3T_X, e.g., C_3T_4) or combinations of 3 and 8 thymines (C_3T_{XXX} e.g., C_3T_{383}), with C_3T_3/C_3T_{333}, and C_3T_8/C_3T_{888} being in both "groups" (**Table 1**).

MATERIALS AND METHODS

Materials

Λ- and Δ-$[Ru(phen)_2dppz]^{2+}$ were synthesized and resolved through our previously reported methods; full details are included in the Supporting Information (Ortmans et al., 2004; McQuaid et al., 2019a). Unless otherwise stated, all materials and chemicals were sourced from Sigma-Aldrich (Merck) or Honeywell research chemicals. Oligonucleotides were obtained from Eurogentec (RP-HPLC purified) and used without further purification. All solvents were obtained at HPLC grade and used without further purification.

TABLE 1 | DNA melting temperatures (T_M) of the C_3T_X and C_3T_{XXX} sequences (1 μM ss) with and without 1 equiv. Λ-Ru or Δ-Ru.

Label	Sequence 5′ → 3′	Native	Λ-Ru		Δ-Ru	
		T_M	T_M	ΔT_M	T_M	ΔT_M
$C_3T_{3/333}$	$(CCCTTT)_3CCC$	60.0	60.3	+0.3	60.3	+0.3
C_3T_4	$(CCCTTTT)_3CCC$	59.6	58.9	−0.7	58.7	−0.9
C_3T_5	$(CCCTTTTT)_3CCC$	51.7	51.4	−0.3	51.4	−0.3
C_3T_6	$(CCCTTTTTT)_3CCC$	47.0	48.4	+1.4	48.2	+1.2
C_3T_7	$(CCCTTTTTTT)_3CCC$	41.9	45.8	+3.9	45.7	+3.8
$C_3T_{8/888}$	$(CCCTTTTTTTT)_3CCC$	37.8	44.1	+6.3	43.2	+5.4
C_3T_{338}	CCCTTTCCCTTTCCCTTTTTTTCCC	49.1	50.8	+1.7	50.5	+1.4
C_3T_{383}	CCCTTTCCCTTTTTTTCCCTTTCCC	55.3	55.2	−0.1	55.0	−0.3
C_3T_{388}	CCCTTTCCCTTTTTTTCCCTTTTTTTCCC	46.1	48.1	+2.0	47.2	+1.1
C_3T_{833}	CCCTTTTTTTCCCTTTCCCTTTCCC	49.5	51.0	+1.5	50.8	+1.3
C_3T_{838}	CCCTTTTTTTCCCTTTCCCTTTTTTTCCC	39.8	45.7	+6.0	45.6	+5.9
C_3T_{883}	CCCTTTTTTTCCCTTTTTTTCCCTTTCCC	46.6	48.8	+2.2	47.8	+1.2

Values are in degrees Celsius with a standard deviation of ±∼0.1–0.6°C. Standard deviation for individual measurements are shown in ***Table S3.1****.*

Solution Preparation and Annealing

Initial stock solutions of the ruthenium complexes and oligonucleotides were made in water and checked for concentration using the extinction coefficient of 20 000 M^{-1} cm^{-1} at 440 nm for the former, and for the latter, the Eurogentec-provided extinction coefficients at 260 nm, calculated using the nearest-neighbor model. The stocks were then diluted with buffer and combined to form solutions with either a 1:0 or 1:1 ratio of DNA strand to ruthenium complex. Annealing of the oligonucleotides, both with and without ruthenium complex present, was achieved by incubating the buffered solution at 90°C for 5 min, and then allowing it to cool to room temperature overnight. Preliminary experiments showed that adding ruthenium complex before or after i-motif annealing did not affect the melting temperature (**Figure S3.1**), and so all ruthenium additions in this study were done pre-annealing.

Synchrotron Radiation Circular Dichroism

Samples consisted of the oligonucleotide [100 μM single stranded (ss)] and ruthenium complex (100 μM) in 20 mM sodium cacodylate buffer at pH 5. The concentration of buffer was lowered relative to other experiments to obtain the lowest data resolution cut-off. CD spectra were recorded at 20 °C between 195 and 350 nm with a 1 nm increment. Experiments were performed in a 0.01 cm pathlength cuvette, on beamline B23 at Diamond Light Source Ltd.

UV Melting

UV melting experiments were carried out using Agilent Cary 100 with a temperature controlled six-cell changer. Samples consisted of the oligonucleotide (1 μM ss) and either 0 or 1 molar equivalent of the ruthenium complex. The buffer consisted of 50 mM sodium cacodylate at a pH of either 5 or 8. Absorption was recorded at 260 and 295 nm at 1 °C intervals between 20–90°C, with a temperature change rate of 0.5 °C/min in a 1 cm pathlength quartz cuvette. Melting curves were generated from this data. To determine the melting temperature, the curves were fitted with a sigmoidal function: $y = \frac{H}{1+\exp[-St\times(T-T_M)]} + S$ where the constants are H, St, S and T_M: the height, steepness, starting point and inflexion point (melting temperature) of the function, respectively, and the variable is T, the temperature. This function was generated for each curve through minimization of the sum of residuals between the raw data and model. The fit was applied to the region that best represented a sigmoid. Experiments were performed in triplicate and the results averaged.

Luminescence Spectroscopy

Luminescence spectroscopy measurements were performed using a 1 cm pathlength quartz cell at room temperature. Samples consisted of oligonucleotides and ruthenium complex with a final concentration of 20 μM each (ss DNA), dissolved in 50 mM sodium cacodylate buffer (pH 5 or 8). Emission spectra were measured between 550 and 875 nm with an excitation wavelength of 440 nm.

RESULTS AND DISCUSSION

Synchrotron Radiation Circular Dichroism

SRCD spectra of the C_3T_X sequences were obtained with and without the presence of *rac*-Ru at pH 5 (**Figure S2.1**). *Rac*-Ru had to be used here as the CD signal of Λ-Ru and Δ-Ru would obscure that of the i-motif. Only minor changes in CD spectra were observed with addition of *rac*-Ru, demonstrating that the i-motif structure still forms in the presence of ruthenium complexes. This is supported by the UV melting profiles of both native and ruthenium-bound C_3T_X and C_3T_{XXX}, which show characteristic hyperchromicity at 260 nm and hypochromicity at 295 nm (**Figures S3.2–5**) (Phan and Mergny, 2002).

UV Melting

UV melting experiments revealed that for C_3T_X sequences with loops of 6 thymines or less, there was no appreciable difference

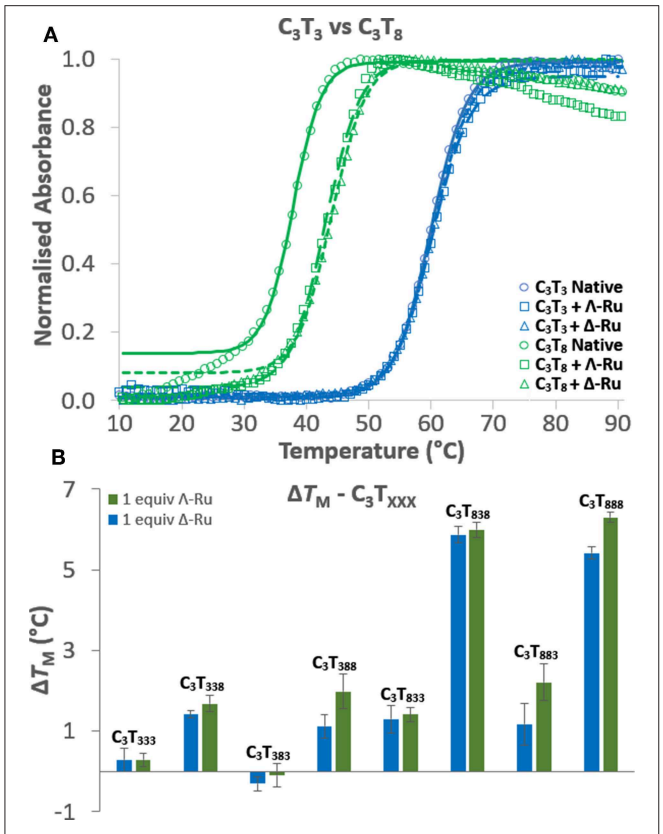

FIGURE 2 | (A) UV melting curves of C_3T_3 (blue) and C_3T_8 (green) in their native forms (circles) and in the presence of Λ-Ru (squares) or Δ-Ru (triangles). **(B)** Comparison of the ΔT_M induced by Λ-Ru (green) and Δ-Ru (blue) for C_3T_{XXX}.

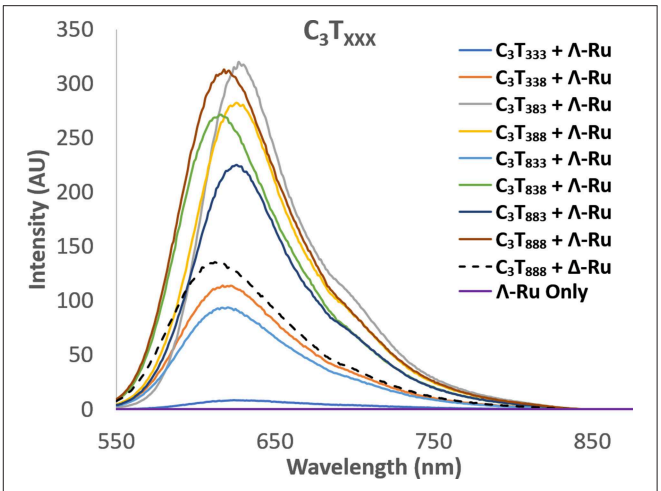

FIGURE 3 | Luminescence spectra of Λ-Ru (20 μM) with C_3T_{XXX} (20 μM ss). The spectrum of Δ-Ru with C_3T_{888} is also shown for comparison (broken line).

(<1.5°C) in melting temperature (T_M) with one equivalent of Λ-Ru or Δ-Ru, while stabilization of ~4°C occurred for C_3T_7 and ~6°C for C_3T_8 (**Table 1**, **Figure 2A**, and **Figure S3.7**). This result suggests that the longer loops have cavities that allow binding of ruthenium complexes, resulting in stabilization. For C_3T_{XXX}, sequences with longer loops 1 and 3 experienced the most stabilization with ruthenium, while a long loop 2 did not affect stabilization (**Figure 2B**, **Table 1**). For example, the ΔT_M of C_3T_{838} was ~6°C, while C_3T_{383} was not stabilized. Interestingly, the sequences with the lowest native stability were those that were stabilized by Λ-Ru and Δ-Ru the most. There was little difference in the effect of Λ-Ru and Δ-Ru on sequence stability, although Λ-Ru did occasionally produce higher ΔT_M values. These experiments were repeated at pH 8 for C_3T_3 and C_3T_8; a melting curve was not observed, implying an absence of i-motif structure (**Figure S3.6**).

Luminescence

Enhancement of luminescence was observed for Λ-Ru and Δ-Ru when bound to all i-motif sequences, aside from C_3T_3, for which little enhancement occurred (**Figure 3**, **Figure S4.1**). For non-C_3T_3 sequences, emission was much higher for Λ-Ru than for Δ-Ru, meaning that the solvent environment and pyrazine nitrogen exposure were more favorable for luminescence of Λ-Ru. Without the presence of DNA, the emission of each complex was very low (**Figure 3**, **Figure S4.1**). For C_3T_X, emission generally increased with loop length, with a large increase for C_3T_7 and C_3T_8 (**Figure S4.1**). For C_3T_{XXX}, trends differed between Λ-Ru and Δ-Ru. For Δ-Ru, C_3T_{838} and C_3T_{888} produced the highest emission (>300x Ru alone), C_3T_{333} showed relatively little enhancement (20x Ru alone), and the other sequences showed relatively moderate enhancement (100-140x Ru alone). For Λ-Ru, emission was more varied per sequence and was correlated with loop length (**Figure 3**). A long loop 2 resulted in more than double the emission of a long loop 1 or 3, as evidenced by the higher emission of C_3T_{383}– (600x Ru alone) relative to C_3T_{338}, C_3T_{833} (200-250x Ru alone), and C_3T_{838} (550x Ru alone).

In addition to luminescence enhancement, the emission maxima shifted depending on the sequence. For Δ-Ru, λ_{max} was generally blue-shifted with increasing loop length (**Table S4.1**, **Figure S4.3**). This correlated positively with emission intensity, which has been observed for ruthenium complexes that undergo stacking with G-quadruplex DNA (Wilson et al., 2010). However, for Λ-Ru, there are few trends relating λ_{max} to loop length, or to intensity (**Figure S4.3**); this overall suggests while Δ-Ru is likely to undergo base stacking with i-motif loops, Λ-Ru may also interact through different modes. The luminescence of Λ-Ru and Δ-Ru with C_3T_3 and C_3T_8 was also recorded at pH 8; interestingly, emission enhancement still occurred despite the lack of i-motif structure. Relative to their i-motif forms, C_3T_3 and C_3T_8 produced higher and lower enhancement, respectively (**Figure S4.2**). Luminescence enhancement of $[Ru(phen)_2(dppz)]^{2+}$ due to interactions with single stranded sequences without tertiary structure has been previously reported (Coates et al., 2001), and could explain this phenomenon.

Melting vs. Luminescence

When comparing the UV melting and luminescence data for these complexes, some trends do emerge. For C_3T_X, the binding of Λ-Ru and Δ-Ru to longer-looped sequences resulted in both

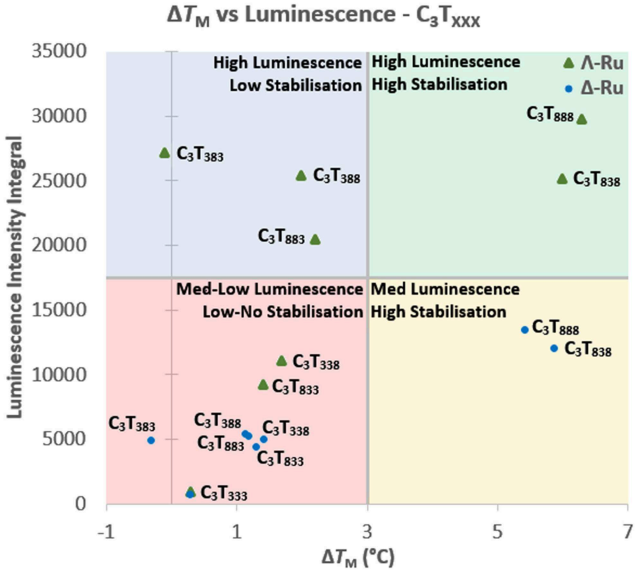

FIGURE 4 | Comparison of the integrated luminescence intensity and ΔT_M of Λ-Ru (green triangles) and Δ-Ru (blue circles) when bound with C_3T_{XXX}. The graph is quartered into sections based upon the relative luminescence enhancement and thermal stabilization for each i-motif-ruthenium combination.

higher ΔT_M and higher ruthenium emission (**Figure S5.1**). For shorter loops, luminescence generally increased with increasing length, but melting stabilization did not. For the C_3T_{XXX} series, there are some trends relating emission, T_M and the position of the long loops (**Figure 4**). The luminescence of Λ-Ru indicates that it binds to longer loops irrespective of where they are positioned, but the T_M data only shows stabilization when bound to loops 1 or 3. Λ-Ru demonstrated high luminescence with C_3T_{383}, but no stabilization, whereas interaction with C_3T_{838} and C_3T_{888} resulted in high luminescence and stabilization. C_3T_{333} was not stabilized and did not enhance luminescence. The other sequences were slightly stabilized and produced medium-low luminescence enhancement (**Figure 4**). Overall, the presence of Λ-Ru with longer loops 1 and 3 resulted in increased stability and luminescence, while only luminescence was increased with a long loop 2. Δ-Ru did not follow the same C_3T_{XXX} trends as Λ-Ru, aside from low luminescence and ΔT_M for C_3T_{333} (**Figure 4**). Luminescence and ΔT_M were only notable for C_3T_{888} and C_3T_{838}, while these values were medium-low for the remaining sequences. Unlike Λ-Ru, the interactions of Δ-Ru with a long loop 2 did not increase luminescence relative to loops 1 or 3, despite resulting in approximately the same thermal stabilization as Λ-Ru.

CONCLUSION

In this study we have demonstrated that the length and position of i-motif thymine loops not only impacts the native structure, but also the degree of stabilization by Λ-Ru and Δ-Ru. These complexes do not stabilize short-looped sequences, but do stabilize the relatively less stable, long-looped i-motifs. It is possible that the longer loops are more flexible, and that they may form T-T hairpins; we recently reported binding of Λ-[Ru(tetraazaphenanthrene)$_2$(dppz)]$^{2+}$ to mismatched T-T base pairs and speculate something similar may be occurring here in the longer i-motif loops (McQuaid et al., 2019b). The luminescence blue-shifting implies that base stacking and perhaps other modes may contribute to ruthenium-loop interactions, but further spectroscopic and crystallographic experiments are required to elucidate the true binding behavior. Overall, these results demonstrate that i-motif sequences with longer loops are potential transition metal drug targets for therapeutic and diagnostic purposes.

DATA AVAILABILITY STATEMENT

The raw data supporting the conclusions of this manuscript will be made available by the authors, without undue reservation, to any qualified researcher.

AUTHOR CONTRIBUTIONS

BP led the writing of the manuscript and performed UV and luminescence experiments. SG performed the SRCD experiments, supported by JH. BP and SG each were responsible for analysis of their collected data. KM synthesized and resolved the ruthenium enantiomers. CC and JB conceived the project and supervised the work. All authors contributed to the writing of the manuscript.

FUNDING

This work was supported by the Biotechnology and Biological Sciences Research Council grant BB/M004635/1 and BB/P021328/1 (to JH, CC, and JB). The authors are also grateful to Diamond Light Source for provision of beamtime on beamline B23 (SM19962 and SM16002).

ACKNOWLEDGMENTS

The authors are grateful to the University of Reading for access to instruments in the Chemical Analysis Facility. BP was supported by the BBSRC grant BB/P021328/1. SG was supported by a joint Ph.D. studentship between the University of Reading and Diamond Light Source. KM was supported by a joint Ph.D. studentship between the Engineering and Physical Sciences Research Council and Diamond Light Source.

SUPPLEMENTARY MATERIAL

The Supplementary Material for this article can be found online at: https://www.frontiersin.org/articles/10.3389/fchem.2019.00744/full#supplementary-material

REFERENCES

Abou assi, H., Garavís, M., González, C., and Damha, M. J. (2018). i-Motif DNA: structural features and significance to cell biology. *Nucleic Acids Res.* 46, 8038–8056. doi: 10.1093/nar/gky735

Alberti, P., Ren, J., Teulade-Fichou, M. P., Guittat, L., Riou, J.-F., Chaires, J. B., et al. (2001). Interaction of an acridine dimer with DNA quadruplex structures. *J. Biomol. Struct. Dyn.* 19, 505–513. doi: 10.1080/07391102.2001.10506758

Bar-Am, O., Weinreb, O., Amit, T., and Youdim, M. B. H. (2005). Regulation of Bcl-2 family proteins, neurotrophic factors, and APP processing in the neurorescue activity of propargylamine. *FASEB J.* 19, 1899–1901. doi: 10.1096/fj.05-3794fje

Brazier, J. A., Shah, A., and Brown, G. D. (2012). I-Motif formation in gene promoters: unusually stable formation in sequences complementary to known G-quadruplexes. *Chem. Commun.* 48, 10739–10741. doi: 10.1039/C2CC30863K

Brooks, T. A., Kendrick, S., and Hurley, L. (2010). Making sense of G-quadruplex and i-motif functions in oncogene promoters. *FEBS J.* 277, 3459–3469. doi: 10.1111/j.1742-4658.2010.07759.x

Cardin, C. J., Kelly, J. M., and Quinn, S. J. (2017). Photochemically active DNA-intercalating ruthenium and related complexes – insights by combining crystallography and transient spectroscopy. *Chem. Sci.* 8, 4705–4723. doi: 10.1039/c7sc01070b

Chantzis, A., Very, T., Daniel, C., Monari, A., and Assfeld, X. (2013). Theoretical evidence of photo-induced charge transfer from DNA to intercalated ruthenium (II) organometallic complexes. *Chem. Phys. Lett.* 578, 133–137. doi: 10.1016/j.cplett.2013.05.068

Coates, C. G., Mcgarvey, J. J., Callaghan, P. L., Coletti, M., and Hamilton, J. G. (2001). Probing the Interaction of [Ru(phen)2(dppz)]2+ with single-stranded DNA what degree of protection is required for operation of the "Light-Switch Effect"? *J. Phys. Chem. B.* 105, 730–735. doi: 10.1021/jp002856w

Day, H. A., Huguin, C., and Waller, Z. A. E. (2013). Silver cations fold i-motif at neutral pH. *Chem. Commun.* 49, 7696–7698. doi: 10.1039/C3CC43495H

Deo, K. M., Pages, B. J., Ang, D. L., Gordon, C. P., and Aldrich-Wright, J. R. (2016). Transition metal intercalators as anticancer agents—recent advances. *Int. J. Mol. Sci.* 17, 1818. doi: 10.3390/ijms17111818

Dzatko, S., Krafcikova, M., Hänsel-Hertsch, R., Fessl, T., Fiala, R., Loja, T., et al. (2018). Evaluation of the stability of DNA i-motifs in the nuclei of living mammalian cells. *Angew. Chem. Int. Ed.* 57, 2165–2169. doi: 10.1002/anie.201712284

Fedoroff, O. Y., Rangan, A., Chemeris, V. V., and Hurley, L. H. (2000). Cationic porphyrins promote the formation of i-Motif DNA and bind peripherally by a nonintercalative mechanism. *Biochemistry* 39, 15083–15090. doi: 10.1021/bi001528j

Friedman, A. E., Chambron, J. C., Sauvage, J. P., Turro, N. J., and Barton, J. K. (1990). A molecular light switch for DNA: Ru(bpy)2(dppz)2+. *J. Am. Chem. Soc.* 112, 4960–4962. doi: 10.1021/ja00168a052

Fujii, T., and Sugimoto, N. (2015). Loop nucleotides impact the stability of intrastrand i-motif structures at neutral pH. *Phys. Chem. Chem. Phys.* 17, 16719–16722. doi: 10.1039/C5CP02794B

Gehring, K., Leroy, J.-L., and Guéron, M. (1993). A tetrameric DNA structure with protonated cytosine-cytosine base pairs. *Nature* 363, 561–565. doi: 10.1038/363561a0

Gill, M. R., and Thomas, J. A. (2012). Ruthenium(ii) polypyridyl complexes and DNA-from structural probes to cellular imaging and therapeutics. *Chem. Soc. Rev.* 41, 3179–3192. doi: 10.1039/C2CS15299A

Gurung, S. P., Schwarz, C., Hall, J. P., Cardin, C. J., and Brazier, J. A. (2015). The importance of loop length on the stability of i-motif structures. *Chem. Commun.* 51, 5630–5632. doi: 10.1039/C4CC07279K

Hall, J. P., Keane, P. M., Beer, H., Buchner, K., Winter, G., Sorensen, T. L., et al. (2016). Delta chirality ruthenium 'light-switch' complexes can bind in the minor groove of DNA with five different binding modes. *Nucleic Acids Res.* 44, 9472–9482. doi: 10.1093/nar/gkw753

Hartshorn, R. M., and Barton, J. K. (1992). Novel dipyridophenazine complexes of ruthenium(II): exploring luminescent reporters of DNA. *J. Am. Chem. Soc.* 114, 5919–5925. doi: 10.1021/ja00041a002

Kang, H.-J., Kendrick, S., Hecht, S. M., and Hurley, L. H. (2014). The transcriptional complex between the BCL2 i-Motif and hnRNP LL is a molecular switch for control of gene expression that can be modulated by small molecules. *J. Am. Chem. Soc.* 136, 4172–4185. doi: 10.1021/ja4109352

Knight, T., Luedtke, D., Edwards, H., Taub, J. W., and Ge, Y. (2019). A delicate balance – The BCL-2 family and its role in apoptosis, oncogenesis, and cancer therapeutics. *Biochem. Pharmacol.* 162, 250–261. doi: 10.1016/j.bcp.2019.01.015

Li, H., Hai, J., Zhou, J., and Yuan, G. (2016). The formation and characteristics of the i-motif structure within the promoter of the c-myb proto-oncogene. *J. Photochem. Photobiol., B* 162, 625–632. doi: 10.1016/j.jphotobiol.2016.07.035

Li, X., Peng, Y., Ren, J., and Qu, X. (2006). Carboxyl-modified single-walled carbon nanotubes selectively induce human telomeric i-motif formation. *Proc. Nat. Acad. Sci. U.S.A.* 103:19658. doi: 10.1073/pnas.0607245103

Lu, L., Wang, M., Liu, L.-J., Wong, C.-Y., Leung, C.-H., and Ma, D.-L. (2015). A luminescence switch-on probe for terminal deoxynucleotidyl transferase (TdT) activity detection by using an iridium(iii)-based i-motif probe. *Chem. Commun.* 51, 9953–9956. doi: 10.1039/C5CC02790J

Ma, D.-L., Kwan, M. H.-T., Chan, D. S.-H., Lee, P., Yang, H., Ma, V. P.-Y., et al. (2011). Crystal violet as a fluorescent switch-on probe for i-motif: label-free DNA-based logic gate. *Analyst* 136, 2692–2696. doi: 10.1039/C1AN15091J

Mathur, V., Verma, A., Maiti, S., and Chowdhury, S. (2004). Thermodynamics of i-tetraplex formation in the nuclease hypersensitive element of human c-myc promoter. *Biochem. Biophys. Res. Commun.* 320, 1220–1227. doi: 10.1016/j.bbrc.2004.06.074

McQuaid, K., Abell, H., Gurung, S. P., Allan, D. R., Winter, G., Sorensen, T., et al. (2019a). Structural studies reveal enantiospecific recognition of a DNA G-quadruplex by a ruthenium polypyridyl complex. *Angew. Chem. Int. Ed.* 58, 9881–9885. doi: 10.1002/anie.201814502

McQuaid, K., Hall, J. P., Baumgaertner, L., Cardin, D. J., and Cardin, C. J. (2019b). Three thymine/adenine binding modes of the ruthenium complex Λ-[Ru(TAP)2(dppz)]2+ to the G-quadruplex forming sequence d(TAGGGTT) shown by X-ray crystallography. *Chem. Commun.* 55, 9116–9119. doi: 10.1039/C9CC04316K

Metcalfe, C., and Thomas, J. A. (2003). Kinetically inert transition metal complexes that reversibly bind to DNA. *Chem. Soc. Rev.* 32, 215–224. doi: 10.1039/B201945K

Olofsson, J., Önfelt, B., and Lincoln, P. (2004). Three-State Light Switch of [Ru(phen)2dppz]2+: Distinct Excited-State Species with Two, One, or No Hydrogen Bonds from Solvent. *J. Phys. Chem. A* 108, 4391–4398. doi: 10.1021/jp037967k

Ortmans, I., Elias, B., Kelly, J. M., Moucheron, C., and Kirsch-Demesmaeker, A. (2004). [Ru(TAP)2(dppz)]2+: a DNA intercalating complex, which luminesces strongly in water and undergoes photo-induced proton-coupled electron transfer with guanosine-5′-monophosphate. *Dalton Trans.* 2004, 668–676. doi: 10.1039/B313213G

Pages, B. J., Ang, D. L., Wright, E. P., and Aldrich-Wright, J. R. (2015). Metal complex interactions with DNA. *Dalton Trans.* 44, 3505–3526. doi: 10.1039/C4DT02700K

Phan, A. T., and Mergny, J. L. (2002). Human telomeric DNA: G-quadruplex, i-motif and Watson–Crick double helix. *Nucleic Acids Res.* 30, 4618–4625. doi: 10.1093/nar/gkf597

Poynton, F. E., Bright, S. A., Blasco, S., Williams, D. C., Kelly, J. M., and Gunnlaugsson, T. (2017). The development of ruthenium(ii) polypyridyl complexes and conjugates for *in vitro* cellular and *in vivo* applications. *Chem. Soc. Rev.* 46, 7706–7756. doi: 10.1039/C7CS00680B

Rajendran, A., Nakano, S.-I., and Sugimoto, N. (2010). Molecular crowding of the cosolutes induces an intramolecular i-motif structure of triplet repeat DNA oligomers at neutral pH. *Chem. Commun.* 46, 1299–1301. doi: 10.1039/B922050J

Satpathi, S., Sappati, S., Das, K., and Hazra, P. (2019). Structural characteristics requisite for the ligand-based selective detection of i-motif DNA. *Org. Biomol. Chem.* 17, 5392–5399. doi: 10.1039/C9OB01020C

Sheng, Q., Neaverson, J. C., Mahmoud, T., Stevenson, C. E. M., Matthews, S. E., and Waller, Z. A. E. (2017). Identification of new DNA i-motif binding ligands through a fluorescent intercalator displacement assay. *Org. Biomol. Chem.* 15, 5669–5673. doi: 10.1039/C7OB00710H

Shi, S., Geng, X., Zhao, J., Yao, T., Wang, C., Yang, D., et al. (2010a). Interaction of [Ru(bpy)2(dppz)]2+ with human telomeric DNA:

Preferential binding to G-quadruplexes over i-motif. *Biochim.* 92, 370–377. doi: 10.1016/j.biochi.2010.01.003

Shi, S., Zhao, J., Geng, X., Yao, T., Huang, H., Liu, T., et al. (2010b). Molecular "light switch" for G-quadruplexes and i-motif of human telomeric DNA: [Ru(phen)2(dppz)]2+. *Dalton Trans.* 39, 2490–2493. doi: 10.1039/B916094A

Školáková, P., Renčiuk, D., Palacký, J., Krafčík, D., Dvoráková, Z., Kejnovská, I., et al. (2019). Systematic investigation of sequence requirements for DNA i-motif formation. *Nucleic Acids Res.* 47, 2177–2189. doi: 10.1093/nar/gkz046

Takahashi, S., Brazier, J. A., and Sugimoto, N. (2017). Topological impact of noncanonical DNA structures on Klenow fragment of DNA polymerase. *Proc. Nat. Acad. Sci.* 114, 9605–9610. doi: 10.1073/pnas.1704258114

Véry, T., Ambrosek, D., Otsuka, M., Gourlaouen, C., Assfeld, X., Monari, A., et al. (2014). Photophysical properties of ruthenium(II) Polypyridyl DNA intercalators: effects of the molecular surroundings investigated by theory. *Chem. Eur. J.* 20, 12901–12909. doi: 10.1002/chem.201402963

Wilson, T., Costa, P. J., Félix, V., Williamson, M. P., and Thomas, J. A. (2013). Structural Studies on Dinuclear ruthenium(II) complexes that bind diastereoselectively to an antiparallel folded human telomere sequence. *J. Med. Chem.* 56, 8674–8683. doi: 10.1021/jm401119b

Wilson, T., Williamson, M. P., and Thomas, J. A. (2010). Differentiating quadruplexes: binding preferences of a luminescent dinuclear ruthenium(ii) complex with four-stranded DNA structures. *Org. Biomol. Chem.* 8, 2617–2621. doi: 10.1039/B924263E

Wright, E. P., Day, H. A., Ibrahim, A. M., Kumar, J., Boswell, L. J. E., Huguin, C., et al. (2016). Mitoxantrone and analogues bind and stabilize i-Motif forming DNA sequences. *Sci. Rep.* 6:39456. doi: 10.1038/srep39456

Wright, E. P., Huppert, J. L., and Waller, Z. A. E. (2017). Identification of multiple genomic DNA sequences which form i-motif structures at neutral pH. *Nucleic Acids Res.* 45, 2951–2959. doi: 10.1093/nar/gkx090

Yu, Q., Liu, Y., Wang, C., Sun, D., Yang, X., Liu, Y., et al. (2012). Chiral Ruthenium(II) polypyridyl complexes: stabilization of G-Quadruplex DNA, inhibition of telomerase activity and cellular uptake. *PLoS ONE* 7:e50902. doi: 10.1371/journal.pone.0050902

Zeraati, M., Langley, D. B., Schofield, P., Moye, A. L., Rouet, R., Hughes, W.E., et al. (2018). I-motif DNA structures are formed in the nuclei of human cells. *Nat. Chem.* 10, 631–637. doi: 10.1038/s41557-018-0046-3

Zhou, J., Wei, C., Jia, G., Wang, X., Feng, Z., and Li, C. (2010). Formation of i-motif structure at neutral and slightly alkaline pH. *Mol. Biosyst.* 6, 580–586. doi: 10.1039/B919600E

Conflict of Interest: The authors declare that the research was conducted in the absence of any commercial or financial relationships that could be construed as a potential conflict of interest.

frontiers in Chemistry

MINI REVIEW
published: 15 January 2020
doi: 10.3389/fchem.2019.00925

Supramolecular DNA Three-Way Junction Motifs With a Bridging Metal Center

*Yusuke Takezawa and Mitsuhiko Shionoya**

Department of Chemistry, Graduate School of Science, The University of Tokyo, Tokyo, Japan

Various nano-sized supramolecular architectures have been constructed from DNA molecules via sequence-dependent self-assembly. A DNA three-way junction (3WJ), consisting of three oligonucleotides that are partially complementary to each other, is one of the simplest DNA supramolecular structures. This minireview covers studies on DNA 3WJ motifs bridged by an interstrand metal complex with some related works. The incorporation of interstrand metal complexes into DNA has attracted increasing attention because it potentially allows for metal-dependent regulation of the thermal stability and the structure of DNA supramolecules. Metal-bridged DNA 3WJs were synthesized from three DNA strands containing a bipyridine (bpy)-modified nucleotide in the presence of appropriate metal ions. The bpy-modified DNA strands were crosslinked by an interstrand 3:1 metal complex [$Ni^{II}(bpy)_3$ etc.] at the junction core. As a result, the thermal stability of the 3WJs was significantly enhanced upon metal complexation. Furthermore, metal-mediated structural transformation between DNA duplexes and 3WJs was demonstrated by using the same bpy-modified DNA strands. A mixture of bpy-modified strands and their natural complementary strands were self-assembled exclusively into duplexes in the absence of any transition metal ions. In contrast, addition of Ni^{II} ions induced the formation of 3WJs through the formation of an interstrand $Ni^{II}(bpy)_3$ complex, which served as a template for the 3WJ assembly. Because DNA 3WJ structures are essential structural motifs for DNA-based nanoarchitectures, the metal-mediated stabilization and structural induction of metal-locked 3WJs would lead to many potential applications to artificial DNA architectures.

Keywords: DNA, metal complex, artificial DNA, structural conversion, supramolecular chemistry, DNA nanotechnology

OPEN ACCESS

Edited by:
Janarthanan Jayawickramarajah, Tulane University, United States

Reviewed by:
Guido H. Clever, Technical University Dortmund, Germany
Miguel Vázquez López, University of Santiago de Compostela, Spain

****Correspondence:***
Mitsuhiko Shionoya
shionoya@chem.s.u-tokyo.ac.jp

Specialty section:
This article was submitted to Supramolecular Chemistry, a section of the journal Frontiers in Chemistry

Received: *05 November 2019*
Accepted: *18 December 2019*
Published: *15 January 2020*

Citation:
Takezawa Y and Shionoya M (2020) Supramolecular DNA Three-Way Junction Motifs With a Bridging Metal Center. Front. Chem. 7:925. doi: 10.3389/fchem.2019.00925

INTRODUCTION

A large variety of nano-sized supramolecular architectures have been constructed from DNA molecules via self-assembly, which can be precisely programmed by deliberate sequence design (Stulz and Clever, 2015). The sequence-dependent DNA self-assembly results in not only naturally-occurring duplex structures but also artificial supramolecular architectures including junctions, polyhedra, and DNA origami structures (Seeman, 2016). A DNA three-way junction

(3WJ), consisting of three oligonucleotides that are partially complementary to each other, is one of the simplest DNA supramolecular structures. As three double helices are emanating from its branching point, 3WJ motifs serve as nodes or vertices of 2D and 3D DNA architectures. While the assembly of linear DNA duplexes yields only one-dimensional structures, the assembly of 3WJ motifs offers a versatile means to construct two-dimensional lattices, three-dimensional networks, polyhedra, dendrimers, and diverse intricate architectures.

In this minireview, studies on DNA 3WJ motifs bridged by an interstrand metal complex are thoroughly overviewed. The incorporation of interstrand metal complexes into DNA has attracted growing attention because it potentially allows for metal-dependent regulation of the thermal stability and the structure of DNA supramolecules. The most studied approach is the replacement of natural hydrogen-bonded base pairs in DNA duplexes by artificial metal-mediated base pairs, which are formed through coordination bonding between two ligand-type nucleosides and a bridging metal ion (Takezawa and Shionoya, 2012; Takezawa et al., 2017a,b; Müller, 2019). As metal coordination bonds are stronger than hydrogen bonds in general, incorporation of metal-mediated base pairs most often results in significant duplex stabilization (Tanaka et al., 2002a). Multiple incorporation of metal-mediated base pairs provides discrete metal arrays along DNA helices, exhibiting characteristic physical properties (Tanaka et al., 2003, 2006; Takezawa and Shionoya, 2014). Some metallo-base pairs are also used to induce conformational changes of DNA structures such as duplex–hairpin transformation (Kuklenyik and Marzilli, 1996; Böhme et al., 2007; Johannsen et al., 2010). Furthermore, a hydroxypyridone-based Cu^{II}-mediated base pair is applied for the switching of the electrical conductivity of DNA devices (Liu et al., 2011) and of the catalytic activity of DNAzyme (Takezawa et al., 2019). The concept of interstrand metal complexation has been also applied to other higher-order DNA structures (Takezawa et al., 2015; Naskar et al., 2019), such as triple helices (Tanaka et al., 2002b; Takezawa et al., 2009) and G-quadruplex structures (Engelhard et al., 2013). Recently, DNA 3WJ structures bridged by an interstrand metal complex have been constructed in a manner analogous to the metal-bridged DNA helices mentioned above (Duprey et al., 2013; Stubinitzky et al., 2014; Takezawa et al., 2016). In addition to metal-dependent thermal stabilization of 3WJs, metal-mediated structural transformation between DNA duplexes and 3WJs was demonstrated. Since DNA 3WJ structures are essential structural motifs for DNA-based nanoarchitectures, the metal-mediated stabilization and structural induction of 3WJ motifs have many potential applications to artificial DNA architectures.

STABILIZATION OF DNA THREE-WAY JUNCTION MOTIFS

Figure 1A shows a typical structure of DNA 3WJs, which was revealed by X-ray analysis (Woods et al., 2001). A DNA 3WJ has a trigonal hydrophobic cavity at the center, which can be modified either covalently or non-covalently. Recent researches also focus on the development of molecules that bind to a central cavity of 3WJ through non-covalent interactions. Hannon et al. reported that a unique supramolecular metallo-helicate, $[Fe^{II}_2L_3]^{4+}$, binds to a 3WJ cavity, and revealed its binding structure by X-ray structural analysis (Oleksi et al., 2006). The size and shape of the helicate fit well with the 3WJ cavity. Intermolecular interactions between the helicate and the 3WJ, electrostatic interactions and π-stacking, synergistically contributed to the binding. Vázquez and Vázquez López synthesized a chiral peptide helicate having two tris(bipyridine)–Fe^{II} complexes, which was conjugated to a foldon protein afterward (Gamba et al., 2014; Gómez-González et al., 2018). The ΛΛ-isomer of the helical metallopeptide was found to bind to a DNA 3WJ more strongly than the enantiomeric ΔΔ-isomer. Chenoweth et al. have synthesized triptycene-based 3WJ binders bearing positively charged side chains (Barros and Chenoweth, 2014). The binding of triptycene derivatives resulted in the significant enhancement of the thermal stability of 3WJs. More recently, a cationic azacryptand (Novotna et al., 2015) and a fluorescent calix[3]carbazole (Yang et al., 2018) have been developed as 3WJ binding compounds. A tetrahedral supramolecular metallo-cage, $[Fe^{II}_4L_4]^{8+}$, was also reported to bind to 3WJs as well as mismatched DNA duplexes (Zhu et al., 2019). These 3WJ binders would be potential drug candidates because target 3WJ structures are found in the DNA replication fork as well as RNA secondary structures (Ducani et al., 2010; Barros et al., 2016). In the context of supramolecular nucleic acid chemistry, the 3WJ binding molecules are of great interest due to their future application as chemical inputs to stabilize or induce 3WJ-based supramolecular DNA architectures.

Covalent chemical modification is a promising way to functionalize 3WJ structures. Through covalent incorporation of functional units, the central cavity of 3WJs were utilized as a scaffold for chromophore assembly (Probst et al., 2012) and as a space for reactions (Hansen et al., 2009). Chemical modification also led to the thermal stabilization of 3WJs. Incorporation of pyrene-modified nucleotides into one of the three strands increased the stability of 3WJs (Filichev and Pedersen, 2003; Kumar et al., 2012). The 3WJ stabilization was also achieved by introducing a double-headed nucleoside having an additional nucleobase at the 2′-position (Jørgensen et al., 2011). These stabilization effects can be explained by the additional stacking interaction with the base pairs facing the central cavity. Stabilization based on the hydrophobic effect was also demonstrated by the incorporation of lipophilic spacers or side chains into three strands forming 3WJs (Laing and Juliano, 2015).

Interstrand metal complexation is another efficient strategy to stabilize 3WJ structures. A metal ligand can be incorporated into each strand so that the addition of appropriate metal ions leads to interstrand 3:1 ligand–metal complexation. As the ligand-modified 3WJs are stabilized only in the presence of appropriate metal ions, the thermal stability of the 3WJ can be tuned in a metal-responsive manner. Thus, the metal-dependent 3WJ stabilization is more advantageous in terms of applicability in supramolecular DNA chemistry. The design and properties of metal-bridged DNA 3WJs will be described in the following sections.

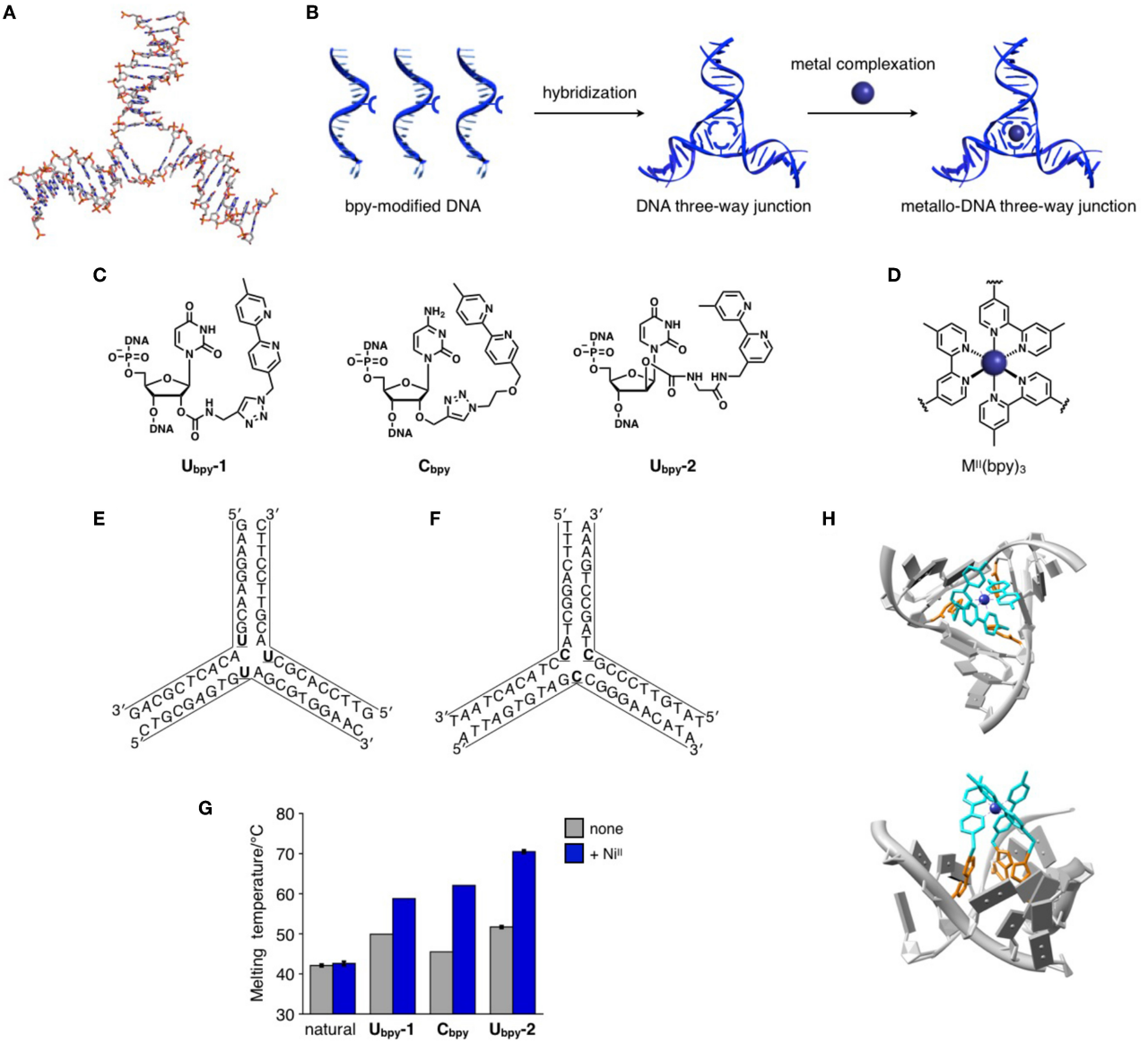

FIGURE 1 | (A) An ideal structure of an unmodified DNA three-way junction (3WJ) motif. Drawn based on a crystal structure (PDB ID: 1DRG) reported by Baldwin et al. **(B)** Construction of a DNA three-way junction motif bridged by a metal complex. **(C)** Molecular design of bipyridine (bpy)-modified nucleotides. **(D)** The structure of a representative metal complex formed at the core of the 3WJ. **(E,F)** Base sequences of DNA strands forming metal-bridged 3WJs. **U** represents $\mathbf{U}_{bpy}$**-1** or $\mathbf{U}_{bpy}$**-2**. **C** represents $\mathbf{C}_{bpy}$. **(G)** Melting temperatures of the 3WJs in the absence and in the presence of Ni^{II} ions. $[Ni^{II}]/[3WJ] = 1.1$ (for $\mathbf{C}_{bpy}$) or 1.0 (for the others). Note that the measurement conditions were slightly different form each other. For the details, see the original papers (Duprey et al., 2013; Stubinitzky et al., 2014; Takezawa et al., 2016). **(H)** Proposed structure of the $Ni^{II}(bpy)_3$ complex at the core of the $\mathbf{U}_{bpy}$**-1**-containing 3WJ. Only Λ-isomer is shown. Reproduced from a literature (Duprey et al., 2013) with permission from Wiley-VCH.

METAL-DEPENDENT STABILIZATION OF MODIFIED DNA THREE-WAY JUNCTIONS

The basic concept of the construction of metal-bridged DNA three-way junction (3WJ) structures is depicted in **Figure 1B**. Each DNA strand constituting a 3WJ motif can be modified with a metal-ligand, which forms a 3:1 ligand–metal complex at the branching point. As the three strands are additionally bridged by metal coordination bonds, the resulting metallo-DNA 3WJ was expected to be thermally stabilized. As a proof-of-concept example, we have chosen a bidentate bipyridine ligand (bpy), which is known to form stable complexes with various transition metal ions, for the construction of 3WJ structures bridged by an interstrand tris(bipyridine) metal complex. The bpy ligand was attached to the 2′-position of the ribose moiety because the reported crystal structures of natural 3WJs showed

that the 2′-hydrogen atoms are directed to the center of the junction (Woods et al., 2001; Oleksi et al., 2006). Thus, the chemical modification at the 2′-position was thought to be most appropriate for the interstrand metal complexation at the junction core.

The structures of designed bpy-modified nucleosides and a representative tris(bipyridine) metal complex are shown in **Figures 1C,D**, respectively. We firstly designed **U_{bpy}-1**, in which a bpy ligand was post-synthetically introduced via azide–alkyne Huisgen cycloaddition (Duprey et al., 2013). An analogous nucleoside **C_{bpy}**, derivatized from 2′-propargyl cytidine, was reported by Wagenknecht (Stubinitzky et al., 2014). We also synthesized an improved version of bpy-modified nucleosides, **U_{bpy}-2**, which has a bpy ligand at the 2′-position but on the opposite side (i.e., 2′-α position) through a carbamate linkage (Takezawa et al., 2016). These nucleosides were introduced in the middle of the DNA strands. When annealed, three bpy-modified strands self-assembled into 3WJ structures in which three bpy ligands are pre-organized in the junction core (**Figures 1E,F**). The formation of the 3WJ structures was confirmed by native polyacrylamide gel electrophoresis (PAGE) analysis (Takezawa et al., 2016). The metal complexation of $M(bpy)_3$ complexes ($M = Ni^{II}$ and Fe^{III}) was confirmed based on UV spectroscopic analysis, showing a characteristic π-π* transition absorption (Duprey et al., 2013; Stubinitzky et al., 2014). Electrospray ionization (ESI) mass spectrometry also provided evidence for the 1:1 binding of a metal ion and a bpy-modified 3WJ (Takezawa et al., 2016). All these analyses proved that each desired metal-bridged DNA 3WJ was formed with an appropriate transition metal ion.

UV-melting analysis clearly showed that the thermal stability of the bpy-modified 3WJs were significantly enhanced upon addition of metal ions (**Figure 1G**). In the presence of one equivalent of Ni^{II} ions, the melting temperature (T_m) of a 3WJ possessing **U_{bpy}-1** nucleosides (**Figure 1E**, $\underline{U} = U_{bpy}$**-1**) was increased from 49.9°C to 58.8°C ($\Delta T_m = +8.9$°C) (Duprey et al., 2013). Titration of Ni^{II} ions showed that the highest stability was reached at a ratio $[Ni^{II}]:[3WJ] = 1:1$. In contrast, Ni^{II} addition did not stabilize a natural 3WJ possessing T nucleosides instead of **U_{bpy}-1** (**Figure 1E**, $\underline{U} =$ **T**) at all. Consequently, the Ni^{II}-dependent stabilization was ascribed to the formation of an interstrand $Ni^{II}(bpy)_3$ complex at the junction core.

In the above-mentioned structure, **U_{bpy}-1** nucleosides formally replaced thymidines (Ts) in a full-match 3WJ. On the other hand, when unpaired **C_{bpy}** nucleosides were additionally inserted into the branching point of the 3WJ (**Figure 1F**, $\underline{C} =$ **C_{bpy}**), the 3WJ was stabilized by as much as +16.6°C upon addition of 1.1 equivalent of Ni^{II} ions (Stubinitzky et al., 2014). This larger stabilization compared with the case with **U_{bpy}-1** could be attributed to its more flexible 3WJ scaffold.

A bpy-modified nucleoside more recently we reported, **U_{bpy}-2**, further achieved increased metal-dependent 3WJ stabilization (Takezawa et al., 2016). A 3WJ containing three **U_{bpy}-2** (**Figure 1D**, $\underline{U} = U_{bpy}$**-2**) showed sharper sigmoidal melting curves. While the 3WJ melted at 51.7°C under a metal-free condition, the melting temperature was drastically increased up to 70.5°C in the presence of Ni^{II} ions ($\Delta T_m = +18.8$°C). The 3WJ stabilization observed here ranks as particularly large one even compared to the duplex stabilization caused by metal-mediated base paring (Takezawa et al., 2017a). It is worth to note that 3WJs containing only one or two bpy ligands showed no or less stabilization effects by Ni^{II} addition ($\Delta T_m = +0.7$°C and +5.8°C, respectively). This result proved that all the three bpy ligands were involved in the metal complexation to form an interstrand $Ni^{II}(bpy)_3$ complex which provides the highest T_m.

A modeling structure of the metal-bridged DNA 3WJ consisting of **U_{bpy}-1** nucleosides is shown in **Figure 1H**. Due to the longer linker between the bpy ligand and the ribose moiety, the $Ni^{II}(bpy)_3$ complex resided just above the cavity. Thus, there is room for improving the degree of the stabilization through further optimization by linker design as well as by the use of other metal ligands.

Some of other divalent transition metal ions were found to stabilize the bpy-modified 3WJs. We have reported that the **U_{bpy}-1**-modified 3WJ was stabilized by addition of equimolar amount of Fe^{II} ($\Delta T_m = +5.0$°C) or Co^{II} ions (+3.3°C) (Duprey et al., 2013). In a similar fashion, the **C_{bpy}**-modified 3WJ was stabilized by addition of Fe^{III} ions ($\Delta T_m = +16.7$°C with 6 equiv. Fe^{III}) or Zn^{II} ions ($\Delta T_m = +6.4$°C with 1.1 equiv. Zn^{II}) (Stubinitzky et al., 2014). The degree of the metal-dependent stabilization is reflected by the overall stability constants (β_3) of the $M^{II}(bpy)_3$ complexes in aqueous media. For instance, the metal addition increased the melting temperatures of the **U_{bpy}-1**-modified 3WJ in the order $Ni^{II} > Fe^{II} > Co^{II}$, which agrees with the order of the β_3 values reported for a simple bipyridine ligand ($\log \beta_3 =$ 20.2, 17.2, and 15.9 for Ni^{II}, Fe^{II}, and Co^{II}, respectively) (Smith and Martell, 1975). This result indicates that the thermal stability of the metal-bridged DNA 3WJ structures would be modulated according to the standard coordination thermodynamics.

Metal-bridged DNA 3WJs would be utilized as building blocks of higher-order DNA structures. Wagenknecht et al. attached perylene diimides (PDI) molecules at the termini of **C_{bpy}**-modified 3WJs and investigated further DNA self-assembly (Stubinitzky et al., 2014). Thus, the strategy of metal-dependent 3WJ stabilization will be applied to metal-responsive regulation of the stability of DNA supramolecules and to the construction of stable DNA materials.

METAL-TRIGGERED STRUCTURAL CONVERSION OF MODIFIED DNA THREE-WAY JUNCTIONS

Metal-triggered structural conversion has been a principal pillar of supramolecular chemistry. A number of stimuli-responsive supramolecules as well as molecular machines have been invented based on the dynamic metal–ligand coordination. This is also the case with supramolecular nucleic acid chemistry. Metal-mediated base pairs, especially those consisting of natural bases (i.e., T–Hg^{II}-T and C–Ag^{I}-C pairs), have been utilized for triggering structural changes in DNA duplexes, and further applied to the operation of DNA-based molecular switches and nanomachines (Liu et al., 2014; Wang et al., 2015; Lu et al.,

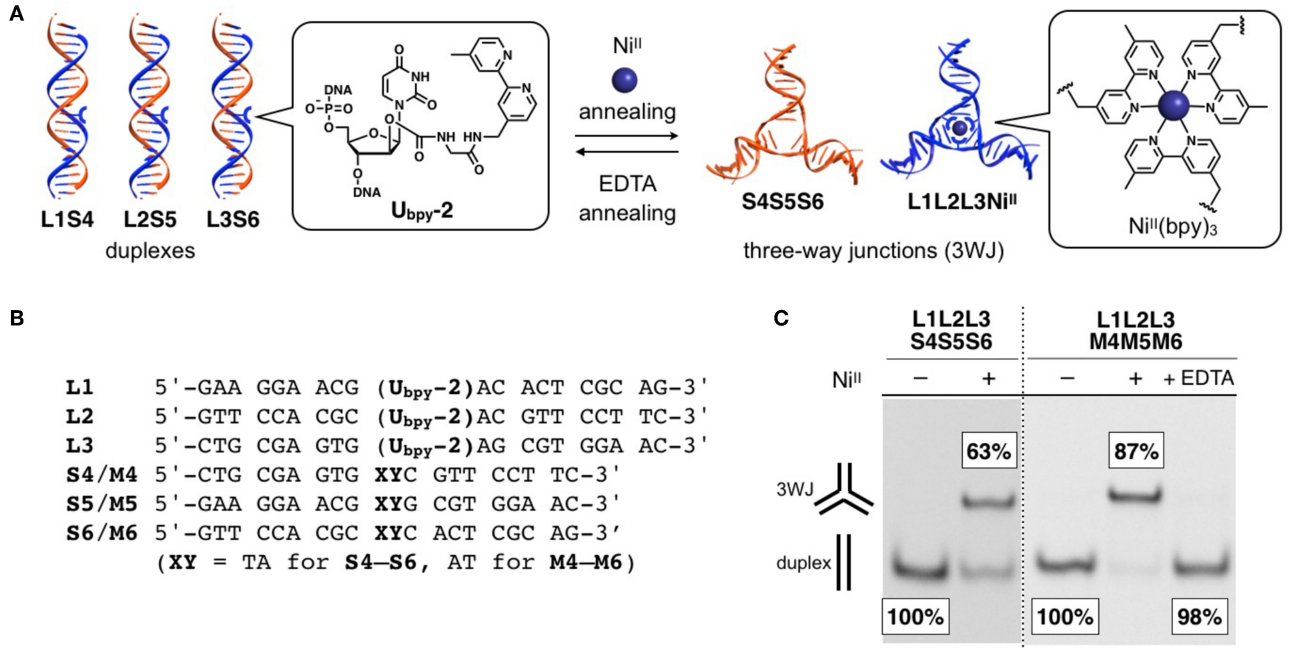

FIGURE 2 | (A) Schematic representation of metal-triggered structural transformation between DNA duplexes and three-way junctions (3WJs). **(B)** Sequences of the DNA strands used for the metal-triggered structural conversion. **(C)** Native polyacrylamide gel electrophoresis (PAGE) analysis of the mixture of DNA strands in the absence and in the presence of one equivalent of Ni^{II} ions. "+EDTA" indicates the result after the removal of Ni^{II} ions by EDTA. Adapted from a literature (Takezawa et al., 2016) published by The Royal Society of Chemistry under the Creative Commons CCBY license.

2016). Metal-triggered structural conversion of DNA three-way junction (3WJ) motifs has been also of great interest in this field because 3WJs are pivotal components of DNA nanoarchitectures. The bipyridine (bpy)-modified DNA strands described above were utilized for Ni^{II}-triggered duplex−3WJ conversion (**Figure 2A**) (Takezawa et al., 2016).

The system was comprised of three bpy-modified strands (**L1**, **L2**, and **L3**) and their complementary strands (**S4**, **S5**, and **S6**) (**Figure 2B**). Native PAGE analysis, in which one of the natural strands was labeled with a fluorophore for quantification, showed that the six DNA strands were self-assembled into three DNA duplexes (**L1S4**, **L2S5**, and **L3S6**) in the absence of transition metal ions. When one equivalent of Ni^{II} ions was added, two 3WJ structures, i.e., a metal-bridged 3WJ (**L1L2L3**·Ni^{II}) and an unmodified 3WJ (**S4S5S6**), were formed in 63% yield (**Figure 2C**), showing Ni^{II}-mediated transformation from duplexes to 3WJs. This structural conversion occurred as a result of the formation of an interstrand $Ni^{II}(bpy)_3$ complex, which served as a template for the 3WJ assembly. The maximum transformation efficiency was observed when 1.2 equiv. of Ni^{II} was added. This stoichiometry roughly corresponds to the 3:1 complexation of three bpy ligands and a Ni^{II} ion. Other transition metal ions such as Co^{II} also induced the 3WJ formation albeit in a substantially lower yield. Among late first-row transition metal ions, Ni^{II} showed the highest conversion efficiency. This result correlates with the largest overall stability constant (log β_3 = 20.2), as is the case with the Ni^{II}-dependent 3WJ stabilization discussed in the previous section.

More efficient duplex−3WJ transformation was demonstrated with mutated strands (**M4**, **M5**, and **M6** shown in **Figure 2B**). While these strands form a fully complementary 3WJ (**M4M5M6**), they form duplexes containing two mismatch pairs (**L1M4**, **L2M5**, and **L3M6**) with the bpy-modified strands. As a consequence, the thermal stabilities of the duplexes were lowered. The alteration in the relative stabilities resulted in the Ni^{II}-mediated 3WJ formation in a sufficiently higher yield (**Figure 2C**). In addition, the subsequent removal of Ni^{II} ions by a chelating agent (EDTA) led to the quantitative regeneration of the duplexes. Accordingly, the metal-responsive reversible structural transformation was demonstrated between the duplexes and the 3WJs.

The efficiency of the metal-mediated 3WJ structural induction can be potentially improved by redesigning the interstrand metal complexes based on past achievements. Construction of 3WJ systems that are responsive to other types of metal ions may be also possible in theory. Thus, the metal-triggered 3WJ transformation would be a promising methodology to develop controllable DNA-based materials.

CONCLUSIONS AND PERSPECTIVES

DNA supramolecular architectures have been constructed conventionally based on the sequence-dependent hybridization. DNA self-assembly is programmable with the aid of theoretical prediction of the thermodynamic stability. The incorporation of interstrand metal complexes into DNA expands the scope

of DNA-based supramolecular chemistry because metal coordination offers thermodynamic and kinetic characteristics different from hydrogen bonding-based DNA self-assembly. This minireview overviewed the development of DNA three-way junction (3WJ) structures bridged by an interstrand metal complex. Three types of bipyridine (bpy)-modified 3WJs have been reported and all of them were thermally stabilized by addition of transition metal ions such as Ni^{II}. The metal-dependent stabilization was attributed to the formation of an interstrand complex ($Ni^{II}(bpy)_3$ etc.), which crosslinked the three oligonucleotides forming the 3WJ. Structural conversion between duplexes and 3WJs was further demonstrated in a Ni^{II}-responsive manner. During the structural rearrangement, the formation of a $Ni^{II}(bpy)_3$ complex served as a trigger for the 3WJ assembly.

The design concept of the metal-bridged DNA 3WJs would have broad utility. The metal selectivity can be altered by selecting an appropriate metal ligand, and the efficiency of the stabilization and the structural conversion are in principle tunable based on the thermodynamics of the metal complex formation. Interstrand metal complexation may lead to the rigidification of the 3WJ structures, which will change the properties of 3WJ-based materials such as dendrimers and hydrogels (Yang et al., 2014; Wang et al., 2017). Chirality induction of interstrand metal complexes is also expected (Duprey et al., 2013). Furthermore, the strategy of metallo-DNA 3WJ formation with the use of 3:1 ligand–metal complexation would be employed for other types of DNA branched structures such as four-way junctions.

DNA junction structures are essential structural motifs for DNA-based nanoarchitectures. Therefore, the metal-mediated stabilization and structural induction of 3WJs would be applied to the development of metal-responsive DNA supramolecules and coordination-driven DNA molecular machines. Accordingly, the idea of the metal-bridged DNA 3WJs has many potential applications and provides a new insight in the field of supramolecular nucleic acid chemistry.

AUTHOR CONTRIBUTIONS

YT performed data analysis and prepared the manuscript. MS finalized the manuscript.

FUNDING

This research was supported by JSPS KAKENHI Grant Nos. 21225003, JP26248016, and JP16H06509 (Coordination Asymmetry) to MS, and No. JP18H02081 to YT. YT also acknowledges financial supports from the Foundation Advanced Technology Institute (ATI) and Foundation for Interaction in Science and Technology (FIST).

REFERENCES

Barros, S. A., and Chenoweth, D. M. (2014). Recognition of nucleic acid junctions using triptycene-based molecules. *Angew. Chem. Int. Ed.* 53, 13746–13750. doi: 10.1002/anie.201407061

Barros, S. A., Yoon, I., and Chenoweth, D. M. (2016). Modulation of the *E. coli rpoH* temperature sensor with triptycene-based small molecules. *Angew. Chem. Int. Ed.* 55, 8258–8261. doi: 10.1002/anie.201601626

Böhme, D., Düpre, N., Megger, D. A., and Müller, J. (2007). Conformational change induced by metal-ion-binding to DNA containing the artificial 1,2,4-triazole nucleoside. *Inorg. Chem.* 46, 10114–10119. doi: 10.1021/ic700884q

Ducani, C., Leczkowska, A., Hodges, N. J., and Hannon, M. J. (2010). Noncovalent DNA-binding metallo-supramolecular cylinders prevent DNA transactions *in vitro*. *Angew. Chem. Int. Ed.* 49, 8942–8945. doi: 10.1002/anie.201004471

Duprey, J.-L., Takezawa, Y., and Shionoya, M. (2013). Metal-locked DNA three-way junction. *Angew. Chem. Int. Ed.* 52, 1212–1216. doi: 10.1002/anie.201207338

Engelhard, D. M., Pievo, R., and Clever, G. H. (2013). Reversible stabilization of transition-metal-binding DNA G-quadruplexes. *Angew. Chem. Int. Ed.* 52, 12843–12847. doi: 10.1002/anie.201307594

Filichev, V. V., and Pedersen, E. B. (2003). Intercalating nucleic acids (INAs) with insertion of *N*-(pyren-1-ylmethyl)-(3*R*,4*R*)-4-(hydroxymethyl)pyrrolidin-3-ol. DNA (RNA) duplex and DNA three-way junction stabilities. *Org. Biomol. Chem.* 1, 100–103. doi: 10.1039/b210335b

Gamba, I., Rama, G., Ortega-Carrasco, E., Maréchal, J.-D., Martínez-Costas, J., Vázquez, M. E., et al. (2014). Programmed stereoselective assembly of DNA-binding helical metallopeptides. *Chem. Commun.* 50, 11097–11100. doi: 10.1039/C4CC03606A

Gómez-González, J., Peña, D. G., Barka, G., Sciortino, G., Maréchal, J.-D., Vázquez López, M., et al. (2018). Directed self-assembly of trimeric DNA-binding chiral miniprotein helicates. *Front. Chem.* 6:520. doi: 10.3389/fchem.2018.00520

Hansen, M. H., Blakskjær, P., Petersen, L. K., Hansen, T. H., Højfeldt, J. W., Gothelf, K. V., et al. (2009). A yoctoliter-scale DNA reactor for small-molecule evolution. *J. Am. Chem. Soc.* 131, 1322–1327. doi: 10.1021/ja808558a

Johannsen, S., Megger, N., Böhme, D., Sigel, R. K. O., and Müller, J. (2010). Solution structure of a DNA double helix with consecutive metal-mediated base pairs. *Nat. Chem.* 2, 229–234. doi: 10.1038/nchem.512

Jørgensen, A. S., Shaikh, K. I., Enderlin, G., Ivarsen, E., Kumar, S., and Nielsen, P. (2011). The synthesis of double-headed nucleosides by the CuAAC reaction and their effect in secondary nucleic acid structures. *Org. Biomol. Chem.* 9, 1381–1388. doi: 10.1039/c0ob00438c

Kuklenyik, Z., and Marzilli, L. G. (1996). Mercury(II) site-selective binding to a DNA hairpin. Relationship of sequence-dependent intra- and interstrand cross-linking to the hairpin-duplex conformational transition. *Inorg. Chem.* 35, 5654–5662. doi: 10.1021/ic960260a

Kumar, P., Shaikh, K. I., Jørgensen, A. S., Kumar, S., and Nielsen, P. (2012). Three pyrene-modified nucleotides: synthesis and effects in secondary nucleic acid structures. *J. Org. Chem.* 77, 9562–9573. doi: 10.1021/jo301571s

Laing, B. M., and Juliano, R. L. (2015). DNA three-way junctions stabilized by hydrophobic interactions for creation of functional nanostructures. *ChemBioChem* 16, 1284–1287. doi: 10.1002/cbic.201500034

Liu, S., Clever, G. H., Takezawa, Y., Kaneko, M., Tanaka, K., Guo, X., et al. (2011). Direct conductance measurement of individual metallo-DNA duplexes within single-molecule break junctions. *Angew. Chem. Int. Ed.* 50, 8886–8890. doi: 10.1002/anie.201102980

Liu, X., Lu, C.-H., and Willner, I. (2014). Switchable reconfiguration of nucleic acid nanostructures by stimuli-responsive DNA machines. *Acc. Chem. Res.* 47, 1673–1680. doi: 10.1021/ar400316h

Lu, C.-H., Cecconello, A., and Willner, I. (2016). Recent advances in the synthesis and functions of reconfigurable interlocked DNA nanostructures. *J. Am. Chem. Soc.* 138, 5172–5185. doi: 10.1021/jacs.6b00694

Müller, J. (2019). Nucleic acid duplexes with metal-mediated base pairs and their structures. *Coord. Chem. Rev.* 393, 37–47. doi: 10.1016/j.ccr.2019.05.007

Naskar, S., Guha, R., and Müller, J. (2019). Metal-modified nucleic acids: metal-mediated base pairs, triples and tetrads. *Angew. Chem. Int. Ed.* doi: 10.1002/anie.201905913. [Epub ahead of print].

Novotna, J., Laguerre, A., Granzhan, A., Pirrotta, M., Teulade-Fichou, M.-P., and Monchaud, D. (2015). Cationic azacryptands as selective three-way DNA junction binding agents. *Org. Biomol. Chem.* 13, 215–222. doi: 10.1039/C4OB01846J

Oleksi, A., Blanco, A. G., Boer, R., Usón, I., Aymamí, J., Rodger, A., et al. (2006). Molecular recognition of a three-way DNA junction by a metallosupramolecular helicate. *Angew. Chem. Int. Ed.* 45, 1227–1231. doi: 10.1002/anie.200503822

Probst, M., Wenger, D., Biner, S. M., and Häner, R. (2012). The DNA three-way junction as a mould for tripartite chromophore assembly. *Org. Biomol. Chem.* 10, 755–759. doi: 10.1039/C1OB06400B

Seeman, N. C. (2016). *Structural DNA Nanotechnology*. Cambridge: Cambridge University Press.

Smith, R. M., and Martell, A. E. (1975). *Critical Stability Constants*, Vol. 2. New York, NY: Plenum Press.

Stubinitzky, C., Bijeljanin, A., Antusch, L., Ebeling, D., Hölscher, H., and Wagenknecht, H.-A. (2014). Bifunctional DNA architectonics: three-way junctions with sticky perylene bisimide caps and a central metal lock. *Chem. Eur. J.* 20, 12009–12014. doi: 10.1002/chem.201402956

Stulz, E., and Clever, G. H. (2015). (eds.). *DNA in Supramolecular Chemistry and Nanotechnology*. Chichester: Wiley-Blackwell.

Takezawa, Y., Duprey, J.-L., and Shionoya, M. (2015). "Metal-Aided Construction of Unusual DNA Structural Motifs," in *DNA in Supramolecular Chemistry and Nanotechnology*, ed. E. Stulz, G. H. Clever (Chichester: Wiley), 65–77.

Takezawa, Y., Maeda, W., Tanaka, K., and Shionoya, M. (2009). Discrete self-assembly of iron(III) ions inside triple-stranded artificial DNA. *Angew. Chem. Int. Ed.* 48, 1081–1084. doi: 10.1002/anie.200804654

Takezawa, Y., Müller, J., and Shionoya, M. (2017a). Artificial DNA base pairing mediated by diverse metal ions. *Chem. Lett.* 46, 622–633. doi: 10.1246/cl.160985

Takezawa, Y., Nakama, T., and Shionoya, M. (2019). Enzymatic synthesis of Cu(II)-responsive deoxyribozymes through polymerase incorporation of artificial ligand-type nucleotides. *J. Am. Chem. Soc.* 141, 19342–19350. doi: 10.1021/jacs.9b08955

Takezawa, Y., and Shionoya, M. (2012). Metal-mediated DNA base pairing: alternatives to hydrogen-bonded Watson–Crick base pairs. *Acc. Chem. Res.* 45, 2066–2076. doi: 10.1021/ar200313h

Takezawa, Y., and Shionoya, M. (2014). "DNA inspired self-assembled metal arrays," in *Handbook of Biomimetics and Bioinspiration*, Vol. 1, ed. E. Jabbari, D.-H. Kim, L. P. Lee, A. Ghaemmaghami, and *A. Khademhosseini (Singapore: World Scientific Publishing)*, 217–245.

Takezawa, Y., Shionoya, M., and Müller, J. (2017b). "Self-assemblies based on metal-mediated artificial nucleobase pairing," in *Comprehensive Supramolecular Chemistry II*, Vol. 4, ed. J. L. Atwood (Oxford: Elsevier Ltd.), 259–293.

Takezawa, Y., Yoneda, S., Duprey, J.-L., Nakama, T., and Shionoya, M. (2016). Metal-responsive structural transformation between artificial DNA duplexes and three-way junctions. *Chem. Sci.* 7, 3006–3010. doi: 10.1039/C6SC00383D

Tanaka, K., Clever, G. H., Takezawa, Y., Yamada, Y., Kaul, C., Shionoya, M., et al. (2006). Programmable self-assembly of metal ions inside artificial DNA duplexes. *Nat. Nanotechnol.* 1, 190–194. doi: 10.1038/nnano.2006.141

Tanaka, K., Tengeiji, A., Kato, T., Toyama, N., and Shionoya, M. (2003). A discrete self-assembled metal array in artificial DNA. *Science* 299, 1212–1213. doi: 10.1126/science.1080587

Tanaka, K., Tengeiji, A., Kato, T., Toyama, N., Shiro, M., and Shionoya, M. (2002a). Efficient incorporation of a copper hydroxypyridone base pair in DNA. *J. Am. Chem. Soc.* 124, 12494–12498. doi: 10.1021/ja027175o

Tanaka, K., Yamada, Y., and Shionoya, M. (2002b). Formation of silver(I)-mediated DNA duplex and triplex through an alternative base pair of pyridine nucleobases. *J. Am. Chem. Soc.* 124, 8802–8803. doi: 10.1021/ja020510o

Wang, D., Hu, Y., Liu, P., and Luo, D. (2017). Bioresponsive DNA hydrogels: beyond the conventional stimuli responsiveness. *Acc. Chem. Res.* 50, 733–739. doi: 10.1021/acs.accounts.6b00581

Wang, F., Liu, X., and Willner, I. (2015). DNA switches: from principles to applications. *Angew. Chem. Int. Ed.* 54, 1098–1129. doi: 10.1002/anie.201404652

Woods, K. C., Martin, S. S., Chu, V. C., and Baldwin, E. P. (2001). Quasi-equivalence in site-specific recombinase structure and function: crystal structure and activity of trimeric cre recombinase bound to a three-way lox DNA junction. *J. Mol. Biol.* 313, 49–69. doi: 10.1006/jmbi.2001.5012

Yang, D., Hartman, M. R., Derrien, T. L., Hamada, S., An, D., Yancey, K. G., et al. (2014). DNA materials: bridging nanotechnology and biotechnology. *Acc. Chem. Res.* 47, 1902–1911. doi: 10.1021/ar5001082

Yang, Z., Chen, Y., Li, G., Tian, Z., Zhao, L., Wu, X., et al. (2018). Supramolecular recognition of three way junction DNA by a cationic calix[3]carbazole. *Chem. Eur. J.* 24, 6087–6093. doi: 10.1002/chem.201705564

Zhu, J., Haynes, C. J. E., Kieffer, M., Greenfield, J. L., Greenhalgh, R. D., Nitschke, J. R., et al. (2019). $Fe^{II}_4L_4$ tetrahedron binds to nonpaired DNA bases. *J. Am. Chem. Soc.* 141, 11358–11362. doi: 10.1021/jacs.9b03566

Conflict of Interest: The authors declare that the research was conducted in the absence of any commercial or financial relationships that could be construed as a potential conflict of interest.

frontiers in Chemistry

ORIGINAL RESEARCH
published: 23 January 2020
doi: 10.3389/fchem.2020.00004

Exploiting Double Exchange Diels-Alder Cycloadditions for Immobilization of Peptide Nucleic Acids on Gold Nanoparticles

Enrico Cadoni[1,2], *Daniele Rosa-Gastaldo*[2], *Alex Manicardi*[1], *Fabrizio Mancin*[2] *and Annemieke Madder*[1]*

[1] Organic and Biomimetic Chemistry Research Group, Department of Organic and Macromolecular Chemistry, Ghent University, Ghent, Belgium, [2] Dipartimento di Scienze Chimiche, Università di Padova, Padova, Italy

The generation of PNA-decorated gold nanoparticles (AuNPs) has revealed to be more difficult as compared to the generation of DNA-functionalized ones. The less polar nature of this artificial nucleic acid system and the associated tendency of the neutral poly-amidic backbone to aspecifically adsorb onto the gold surface rather than forming a covalent bond through gold-thiol interaction, combined with the low solubility of PNAs itself, form the main limiting factors in the functionalization of AuNP. Here, we provide a convenient methodology that allows to easily conjugate PNAs to AuNP. Positively charged PNAs containing a masked furan moiety were immobilized via a double exchange Diels-Alder cycloaddition onto masked maleimide-functionalized AuNPs in a one-pot fashion. Conjugated PNA strands retain their ability to selectively hybridize with target DNA strands. Moreover, the duplexes resulting from hybridization can be detached through a retro-Diels-Alder reaction, thus allowing straightforward catch-and-release of specific nucleic acid targets.

Keywords: PNA, gold nanoparticles, AuNP, gold nanocluster, reversible diels-alder, controlled release, peptide nucleic acids

OPEN ACCESS

Edited by:
Janarthanan Jayawickramarajah, Tulane University, United States

Reviewed by:
Andrew J. Surman, King's College London, United Kingdom
Yi Yan, Northwestern Polytechnical University, China

***Correspondence:**
Annemieke Madder
annemieke.madder@ugent.be

Specialty section:
This article was submitted to Supramolecular Chemistry, a section of the journal Frontiers in Chemistry

Received: *15 November 2019*
Accepted: *06 January 2020*
Published: *23 January 2020*

Citation:
Cadoni E, Rosa-Gastaldo D, Manicardi A, Mancin F and Madder A (2020) Exploiting Double Exchange Diels-Alder Cycloadditions for Immobilization of Peptide Nucleic Acids on Gold Nanoparticles. Front. Chem. 8:4. doi: 10.3389/fchem.2020.00004

INTRODUCTION

The use of DNA-decorated gold nanoparticles (AuNP) of various shape and size has been gradually established over the years, gaining a central role in the realization of a wide range of applications including DNA-based biosensing, gene delivery and *in vivo* imaging to name just a few examples (Ghosh et al., 2008; Homola, 2008; Boisselier and Astruc, 2009; Song et al., 2016). As a result, several methodologies for realizing DNA-AuNP complexes are available (Liu and Liu, 2017). On the other hand, alternative AuNP constructs with non-natural DNA mimics have not been explored so widely. The use of peptide nucleic acids (PNAs) can provide several advantages over the use of standard DNA, such as the formation of more stable and selective complexes with natural DNA and RNA targets which are less affected by experimental conditions (i.e., ionic strength, solvent polarity, presence of chaotropic agents, and pH) and improved resistance to chemical and biological degradation (Demidov et al., 1994; Nielsen, 2004). These characteristics endow PNAs with superior properties for the construction of AuNP based nucleic acid probes. AuNP-DNA assemblies typically require carefully tuned conditions to achieve hybridization with complementary strands, such as high ionic strength in order to overcome the high charge repulsion between the strongly negatively

charged DNA nanoparticles and the complementary strands (Liu and Liu, 2017; Madsen and Gothelf, 2019). However, these high ionic strengths conditions, at the same time, can destabilize charged nanoparticles, causing them to aggregate (Behrens et al., 1998; Pamies et al., 2014).

Despite the aforementioned advantages, only few examples of well-described procedures for functionalization of AuNP with PNA are reported. One of the principal reasons is connected to the tendency of the neutral PNAs to randomly adsorb onto the gold surface, rendering a covalent functionalization through standard thiol-gold bond formation more difficult. In a first example from 2003, Chakrabarti et al. already reported on the difficulties encountered in conjugating standard PNAs to gold nanostructures (Chakrabarti and Klibanov, 2003). In fact, the use of uncapped N-terminal cysteine for the decoration of citrate-stabilized AuNPs, caused an immediate and irreversible aggregation as a consequence of the decreased surface negative charge density, but it was reported that this destabilization could be reduced by adding a poly-Glu tail at the C-terminus. Using this methodology, they were later able to synthesize PNA-decorated nanoparticles, but the functionality of PNA was compromised and no clear evidence of hybridization to complementary DNA was detected (Murphy et al., 2004). An effective approach for the preparation of fully functional PNA-decorated nanoparticles was finally reported by Duy et al., who employed the TWEEN-20 surfactant to prevent nanoparticle aggregation during the exchange between the citrate anions on the surface of the gold nanoparticles and thiolated PNA strands (Duy et al., 2010). In a more recent work a long chain, PEG-based, ω-mercapto carboxylic acid was used to create a monolayer providing both steric and electrostatic stabilization to the AuNPs. In a second step PNA strands, containing a variety of mono- and trithiol linkers conjugated at the N-terminus, could be covalently attached to the surface by thiol exchange in the presence of TWEEN-20 and a triphenyl phosphine as antioxidant, achieving the synthesis of stable PNA-AuNPs (Anstaett et al., 2013). The above examples suggest that the best strategy to obtain stable AuNP-PNA systems is the co-functionalization of the nanoparticle surface with stabilizing surfactants, either thiolated or not. Thiol exchange-based strategies, however, are difficult to control in terms of degree of substitution, and typically require large excesses of the entering species. In addition, special care is needed to avoid dimerization or oxidation of thiol-containing PNAs.

An alternative and elegant approach to overcome this problem is the use of click chemistry (Chen et al., 2017): either Huisgen 1,3-cycloadditions, or concerted reactions, such as Diels-Alder (DA) reactions, which have found numerous applications. In this context, bio-conjugation of nanomaterials, often exploits these approaches because of the tolerance of aqueous solutions and the high reaction selectivity (Sapsford et al., 2013). Diels-Alder-based approaches were previously exploited in NP context as a means to protect maleimide-containing thiols prior to their surface decoration, for the realization of NP-NP dimers, for biopolymer NP functionalization with antibodies and in stimuli-responsive drug release systems (Zhu et al., 2006; Liu et al., 2010; Ghiassian et al., 2015; Oluwasanmi et al., 2017).

In the context of our previous work on furan-oxidation based nucleic acid interstrand crosslinking (Manicardi et al., 2016), we recently developed a Diels-Alder/retro-Diels-Alder (DA/rDA) approach for the protection of furan moieties during their incorporation in PNA strands to avoid C5 alkylation of the aromatic ring during cleavage of the furan-modified PNAs from the solid support (Elskens et al., 2017). These studies have inspired us to exploit such furan-modified PNA strands for the realization of a simple methodology for AuNP functionalization (**Figure 1**). Here we report on the one-pot conjugation of a maleimide-protected furan-PNA to furan-protected maleimide-AuNPs and demonstrate the capability of this system to retain selective recognition of the target DNA as well as the possibility to release the resulting duplex system from the nanoparticle.

RESULTS AND DISCUSSION

Synthesis of Gold Nanoparticles and Maleimide Linker

As evident on the basis of the examples discussed in the introduction, thiol protected nanoparticles have certain advantages over citrate stabilized ones. Indeed, the relatively strong covalent binding of thiol-based coating molecules and the steric stabilization they provide, guarantee better stability during the purification steps after PNA functionalization, compared to the weak binding and electrostatic stabilization provided by citrate anions. In addition, thiols grant the possibility to prepare overall neutral monolayers, which helps to minimize electrostatic interactions between the monolayer and PNA or DNA molecules. Finally, using thiols as coating agents it is possible to prepare ultrasmall (about 2 nm core size) nanoparticles. We chose this specific size for two reasons: first of all, by using 2 nm AuNPs it is possible to investigate in detail the composition of the monolayer by using solution NMR spectroscopy (in the case of larger nanoparticles the use of NMR spectroscopy is hampered by the massive signal broadening due to the slow tumbling). Secondly, the chosen size ensures the absence of a plasmonic band in the UV-Vis spectrum, that could limit the possibility for optical characterization of the AuNP-PNA complex.

AuNPs were synthesized using a well-established two-phase two-step solution procedure (Manea et al., 2008). This involves the reduction of $AuCl_4^-$ in toluene (tetraoctylammonium bromide was used for phase transfer) by dioctylamine at first and then by $NaBH_4$. The amount of dioctylamine present in the reaction mixture also determines the size of the gold core, since this molecule weakly binds to the particle surface. For this exploratory study, we chose to use 20 eq of dioctylamine to obtain AuNPs with an average gold core around 1.6 nm diameter (average formula $Au_{127}SR_{38}$). Dioctylamine-coated nanoparticles so obtained were then functionalized by the simple addition of the desired thiol. In this case, the nanoparticles were passivated with a zwitterionic thiol (**ZW-SH**) featuring a phosphorylcholine moiety (**Figure 2C**). We chose this thiol since it is well-known to give readily soluble and stable nanoparticles, and it has been already used to make biocompatible and bioconjugated nanoparticles with mixed monolayers (Jha et al., 2017). In order to be able to perform

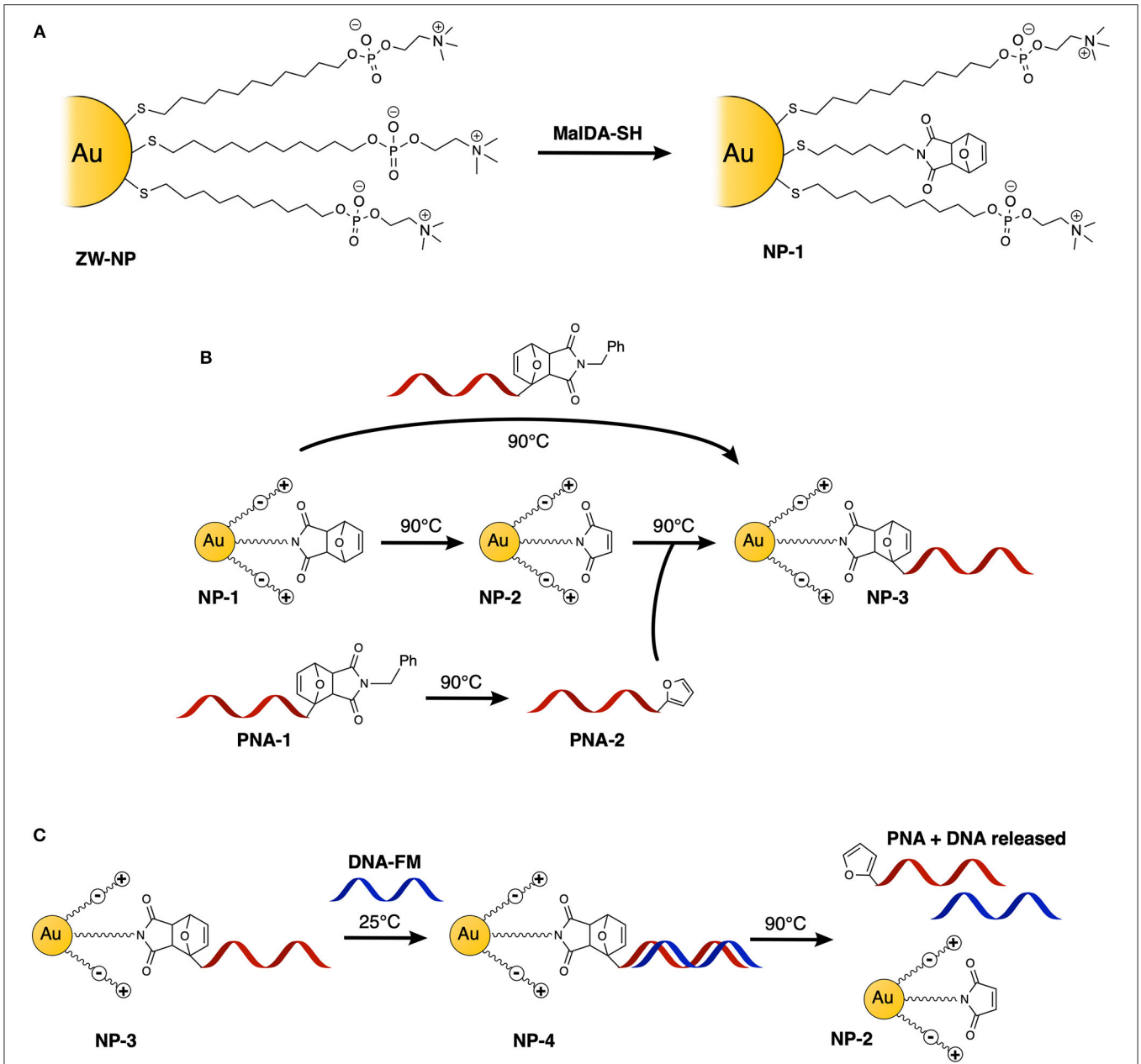

FIGURE 1 | Schematic representation of the experiments performed in this study: **(A)** schematic representation of Diels-Alder protected maleimide containing nanoparticle **(NP-1)** synthesis starting from its precursor **ZW-NP**; **(B)** functionalization of AuNPs with PNA, via direct one-step double-exchange Diels-Alder and two-step Diels-Alder methodologies; **(C)** hybridization and release experiments with DNA.

the PNA functionalization, a second thiol, bearing a furan-protected maleimide moiety (**MalDA-SH**, shown in **Figure 2C**), was inserted in the AuNPs via a thiol exchange reaction. The reaction simply required the addition of 0.5 eq of thiol (with respect to the overall amount of **ZW-SH**) to a solution of **ZW-NP** in methanol, followed by overnight stirring at 35°C. A 14% substitution of **ZW-SH** with **MalDA-SH** was estimated by ^{1}H-NMR (**NP-1**, see **Figure S11**). The substitution achieved is optimal to guarantee the solubility of the nanoparticle and the coupling of the PNA. By changing the equivalents of thiol added, it is possible to tune the degree of substitution, however, when performing the exchange reaction with 1 eq of thiol (leading to a potential exchange of 25–30%), the resulting monolayer is too hydrophobic and the NPs were not completely soluble in water (data not shown). Finally, the possibility to free the maleimide group was demonstrated by heating the AuNPs at 90 °C for 16 h, affording **NP-2**. The deprotection can be followed by ^{1}H-NMR spectroscopy: after 7 h a 50% conversion could be concluded from the spectrum, while after 24 h almost quantitative disappearance of **MalDA-SH** signal was noticed

A

Name	Sequence (N to C-Terminus)
PNA-1	**FurDA**-$(AEEA)_2$-CGTGTGATCAG-Lys(TAMRA)Arg_2-NH_2
PNA-2	**Fur**-$(AEEA)_2$-CGTGTGATCAG-Lys(TAMRA)Arg_2-NH_2

Name	Sequence (5'-3')
DNA-FM	5'-(6-FAM)-CTGATCACACG-3'
DNA-MM	5'-(6-FAM)-CTGCTCAAACG-3'

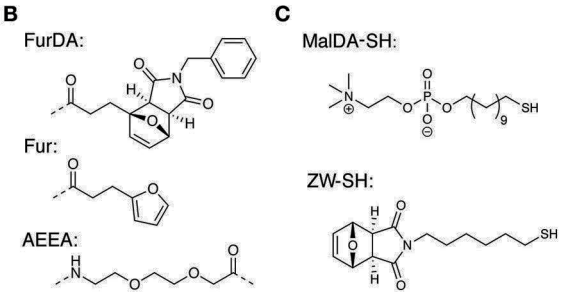

FIGURE 2 | Sequences and small molecule building blocks used in this work. **(A)** PNA and complementary DNA sequences. **(B)** Structures of the monomers and spacers incorporated in the PNA sequences. **(C)** Thiols used for AuNP synthesis.

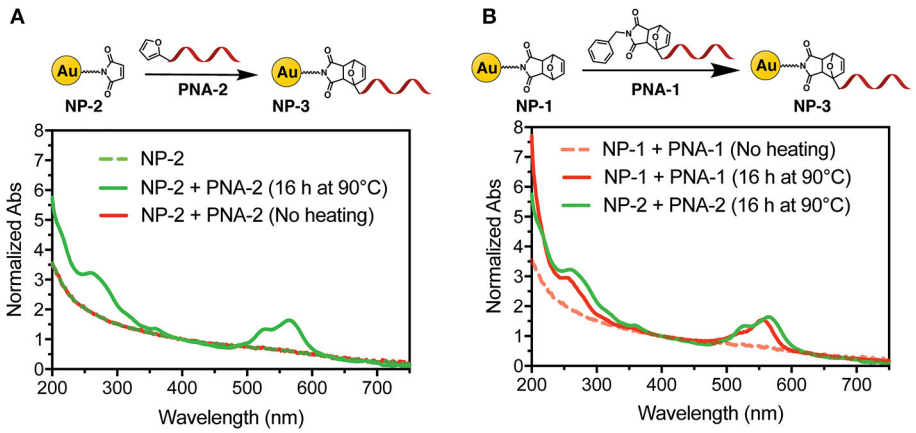

FIGURE 3 | UV-Vis spectra of **NP-3** (normalized at 400 nm). **(A) NP-3** obtained via a two-step Diels-Alder approach; **(B)** comparison of **NP-3** obtained via the one-step double exchange Diels-Alder (red line) vs. the two-step approach (green line), after heating at 90°C for 16 h.

together with the appearance of unknown degradation products (see **Figure S12**). Therefore, an intermediate deprotection time was chosen, leading to a composition of the coating monolayer of **NP-2** containing both **Mal-SH** and a small amount of residual **MalDA-SH** (for the sake of simplicity in **Figure 1A** only the most abundant form is reported). However, this is not affecting the PNA coupling.

PNA Synthesis

Although **ZW-SH** does not present a net charge, **NP-1** have a slightly positive ζ-potential (2.4 ± 0.9 mV). For this reason, two arginine residues were placed at the C-terminus of the PNA probes, which, besides guaranteeing improved PNA solubility, should allow to maintain the PNA tails oriented toward the solution (Biscaglia et al., 2017), and further favored DNA attraction via electrostatic interaction. Furthermore, a lysine residue carrying a 5-carboxytetramethylrhodamine (TAMRA) was included to facilitate monitoring of the nanoparticle functionalization. Finally, to enable Diels-Alder conjugation, a N-benzylmaleimide masked furan moiety was included in the N-terminal position following two 2-(2-(2-aminoethoxy)ethoxy)acetic acid (AEEA) spacers (**PNA-1**, see **Figure 2A**). The required **FurDA-OH** building block (structure shown in **Figure 2B**) could be conveniently synthesized in a single step by heating 2-furanpropionic acid in presence of an excess of maleimide in ethyl acetate (see **Supplementary Material**). The pure exo-adduct then precipitates from the solution driving the reaction to completion and allowing purification by simple filtration and re-crystallization.

In order to test the feasibility of the DA functionalization approach, a PNA bearing an unprotected furan (**PNA-2**) was also synthesized by removing the maleimide moiety of **PNA-1** under rDA conditions. Given the instability of the AEEA spacer when heated in the acidic solution resulting from the PNA cleavage, a new protocol for rDA under basic conditions was developed (see **Supplementary Material**), differing from rDA-based furan deprotection conditions previously reported (Elskens et al., 2017).

Conjugation of the Probe via Diels-Alder Cycloaddition

To first demonstrate the possibility to decorate AuNP with PNA using a DA approach, direct adduct formation between **NP-2** and **PNA-2** was tested. A buffered solution (PBS pH 7.4) of **NP-2** containing 50 μM maleimide and 100 μM **PNA-2** was heated at 90°C for 16 h. After purification by filtration on a 10 k Da cut-off filter the system was characterized by UV spectroscopy. As

shown in **Figure 3A** the characteristic absorption of the PNA and of the TAMRA, 260 and 550 nm respectively, were clearly visible on top of the AuNP scattering, while they were absent in a similar experiment that was maintained at room temperature for the same time.

Next, we tested the possibility to uncage the required functional groups on **NP-1** and **PNA-1** and form the desired **NP-3** in a one-pot fashion. In this setup, formation of the DA adduct in **NP-3** is enthalpy driven by the higher stability of the adduct deriving from 2-alkyl furan as compared to those deriving from furan (Boutelle and Northrop, 2011), while, at the same time, the adduct formed by the two other counterparts should show reduced solubility in aqueous media and precipitate.

Interestingly, the absorption spectrum of **NP-3** obtained via double exchange DA reaction does not shown significant differences as compared with the same product deriving from the two-step DA approach. To validate the results, a negative control experiment was performed without heating the solution, and the resulting UV spectrum lacks the characteristic absorption peaks of the PNA (**Figure 3B**). Finally, once the feasibility of the methodology was established, we focused our attention on the kinetics of the functionalization process. As shown in **Figure S1**, after 2 h of heating, the conjugation with the PNA appears to have reached half of the maximum value, which is observed after 4 h.

DNA Hybridization and Release

In order to confirm the ability of the attached PNA probe to be radially exposed to the solution and thus maintain its ability to recognize target sequences, hybridization experiments were performed. For this purpose, a 5′-fluorescein (FAM) labeled DNA designed to be complementary to the PNA sequence was employed (see **Figure 2A** for the DNA sequences). UV analysis of **NP-4** obtained after overnight hybridization with **DNA-FM** in PBS pH 7.4 clearly shows the presence of the characteristic absorption of the FAM peak at 490 nm, as shown in **Figure 4A**.

To exclude the possibility of non-specific adsorption of the negatively charged DNA to the positively charged **NP-3** we performed overnight hybridization experiments in presence of the mismatched **DNA-MM** sequence. In this case the FAM peak was not present in the UV spectrum of the purified sample, thus confirming the selectivity of the hybridization (**Figure 4A**). Similar UV profiles were also obtained after 1-h hybridization See **Figure S2**, indicating that the time allowed for hybridization under these conditions can be shortened.

As a final step, we also wanted to show the possibility to thermally release the attached probes from the AuNP. A **NP-4** solution was therefore heated overnight at 90°C to release the duplex via rDA, then quickly cooled in an ice bath, and filtered through a 10 kDa cut-off filter. As shown in **Figure 4B** the released solution (yellow curve) clearly shows both FAM (490 nm) and TAMRA (550 nm) components. Although the DNA release from the system could also result from melting the PNA:DNA complex, the presence of the TAMRA peak in the filtered solution is a clear evidence of the release of the PNA probe from the AuNP. MALDI-TOF analysis of the filtrate also confirmed this hypothesis (see **Figure S4**). A second rDA treatment was carried out to achieve an almost complete release from the AuNP surface. However, in addition to the PNA release, aggregation of the AuNPs was suspected from the observation of a broad band around 520 nm (see **Figure S3B**).

MATERIALS AND METHODS

Retro Diels-Alder on AuNP

NP-2 are prepared by heating the desired volume (typical 1 mL, 500 μM concentration in maleimide linkers) of an aqueous **NP-1** solution for 16 h at 95 °C in a glass vial. The solvent is then removed under reduced pressure to remove the furan. The nanoparticles are finally re-suspended in the initial volume of water.

PNA-AuNP Conjugation

In a typical experiment, 100 μL of a PBS solution (pH 7.4) containing PNA (50 μM) and AuNP (concentration adjusted to provide 25 μM maleimide-containing linker) is heated for 4 h at 90°C. This solution is then diluted with 20 μL of PBS buffer and purified by filtration over Amicon 10 kDa ultracentrifuge

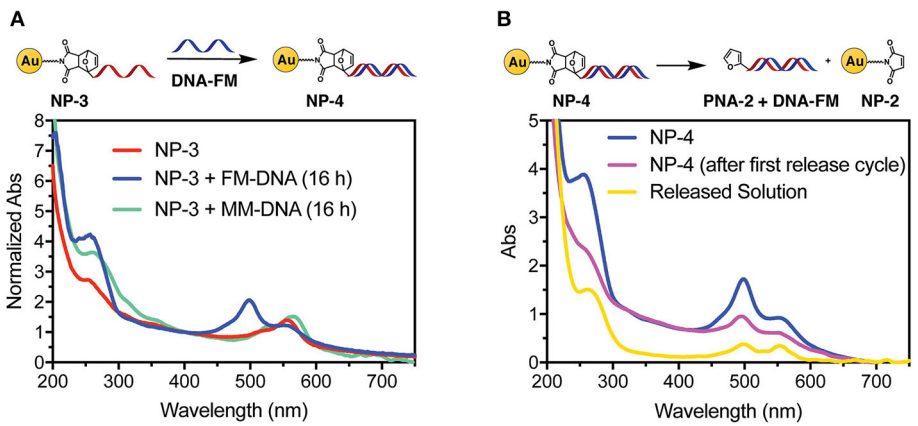

FIGURE 4 | UV-vis spectra of **NP-4** after hybridization with target DNA **(A)** and after thermal release **(B)**.

filters (14000 rcf, 5 min). The remaining solution is re-diluted by adding 200 μL of PBS and filtrated again to remove impurities (unreacted PNA, DA byproducts). The concentrated solution of **NP-3** is then recovered and analyzed via UV spectrometry.

Hybridization Experiments

In a typical hybridization experiment, a 100 μL PBS solution (pH 7.4) containing **NP-3** at 10 μM and 5′-FAM-labeled DNA at 20 μM, was allowed to hybridize under shaking for at least 1 h at 25°C. The hybridized solution was then diluted to 200 μL with PBS and purified by filtration over Amicon 10 kDa ultracentrifuge filters (14000 rcf, 10 min). The remaining solution was washed twice by adding 200 μL of PBS and filtrated again to remove impurities (unhybridized DNA). The concentrated solution of **NP-4** was finally recovered and analyzed via UV spectrometry.

Release Experiments

In a typical release experiment, 50 μL of **NP-4** solution obtained from the previous step were placed in an Eppendorf tube, shaken overnight at 90°C. The solution was thereafter placed in an ice-cold bath for 10 min (to avoid re-attachment) and purified by filtration over Amicon 10 kDa ultracentrifuge filters (14000 rcf, 10 min). The obtained filtrate was analyzed via UV before washing. Afterwards, the nanoparticles were washed adopting the same procedure of the previous paragraph. The final concentrated nanoparticle solution was finally recovered and analyzed via UV spectrometry.

CONCLUSIONS

In conclusion, we reported on a convenient methodology that allows conjugating peptide nucleic acids to gold nanoparticles, exploiting the reversibility of the Diels-Alder cycloaddition. This conjugation approach permits to overcome the problems related to the use of thiolated PNAs, making synthesis, handling, and purification of the probes easier, increasing the yields, and prolonging their shelf-life. In principle, varying the maleimide content of the precursor nanoparticle, allows modifying the PNA content without employing a large excess of PNA probe. The possibility to perform this functionalization via a one-pot double exchange Diels Alder protocol without affecting the outcome of the reaction further expands the applicability of this methodology, extending the shelf-life of the nanoparticle system given the increased stability of the protected maleimide **NP-1** as compared to its unprotected version **NP-2**. The simplicity of the protocol together with the robustness of the reactive moieties will also permit to expand this methodology to the functionalization of other nanosystems or surfaces. In addition, we demonstrated the ability of the attached system to retain its recognition abilities toward target DNA sequences as well as the possibility to use this type of connection for the realization of catch-and-release systems. We strongly believe that further optimization of the final release step will permit the application of this methodology to stimuli-responsive nanosystems.

DATA AVAILABILITY STATEMENT

All datasets generated for this study are included in the article/**Supplementary Material**.

AUTHOR CONTRIBUTIONS

EC, AMan, Amad, and FM designed the project and the experiments. AMan, AMad, and FM supervised the project overall. EC and AMan performed the synthesis of the PNA probes and building blocks, DR-G and EC synthesized the nanoparticles and thiolated linkers. The manuscript was prepared by EC, DR-G, and AMan and revised by all the authors.

FUNDING

FWO, European Union's Horizon 2020 (Skłodowska-Curie grant agreement Nos. 665501 and 721613).

ACKNOWLEDGMENTS

AMan has received funding from the FWO and European Union's Horizon 2020 research and innovation programme under the Marie Skłodowska-Curie grant agreement No. 665501. This project has received funding from the European Union's Horizon 2020 research and innovation programme under the Marie Skłodowska-Curie grant agreement No. 721613.

SUPPLEMENTARY MATERIAL

The Supplementary Material for this article can be found online at: https://www.frontiersin.org/articles/10.3389/fchem.2020.00004/full#supplementary-material

REFERENCES

Anstaett, P., Zheng, Y., Thai, T., Funston, A. M., Bach, U., and Gasser, G. (2013). Synthesis of stable peptide nucleic acid-modified gold nanoparticles and their assembly onto gold surfaces. *Angew. Chem. Int. Ed.* 52, 4217–4220. doi: 10.1002/anie.201209684

Behrens, S. H., Borkovec, M., and Schurtenberger, P. (1998). Aggregation in charge-stabilized colloidal suspensions revisited. *Langmuir* 14, 1951–1954. doi: 10.1021/la971237k

Biscaglia, F., Rajendran, S., Conflitti, P., Benna, C., Sommaggio, R., Litti, L., et al. (2017). Enhanced EGFR targeting activity of plasmonic nanostructures with engineered GE11 peptide. *Adv. Healthc. Mater.* 6:1700596. doi: 10.1002/adhm.201700596

Boisselier, E., and Astruc, D. (2009). Gold nanoparticles in nanomedicine: preparations, imaging, diagnostics, therapies and toxicity. *Chem. Soc. Rev.* 38, 1759–1782. doi: 10.1039/b806051g

Boutelle, R. C., and Northrop, B. H. (2011). Substituent effects on the reversibility of furan - Maleimide cycloadditions. *J. Org. Chem.* 76, 7994–8002. doi: 10.1021/jo201606z

Chakrabarti, R., and Klibanov, A. M. (2003). Nanocrystals modified with peptide nucleic acids (PNAs) for selective self-assembly and DNA detection. *J. Am. Chem. Soc.* 125, 12531–12540. doi: 10.1021/ja035399g

Chen, Y., Xianyu, Y., and Jiang, X. (2017). Surface modification of gold nanoparticles with small molecules for biochemical analysis. *Acc. Chem. Res.* 50, 310–319. doi: 10.1021/acs.accounts.6b00506

Demidov, V. V., Potaman, V. N., Frank-Kamenetskil, M. D., Egholm, M., Buchard, O., Sönnichsen, S. H., et al. (1994). Stability of peptide nucleic acids in human serum and cellular extracts. *Biochem. Pharmacol.* 48, 1310–1313. doi: 10.1016/0006-2952(94)90171-6

Duy, J., Connell, L. B., Eck, W., Collins, S. D., and Smith, R. L. (2010). Preparation of surfactant-stabilized gold nanoparticle-peptide nucleic acid conjugates. *J. Nanoparticle Res.* 12, 2363–2369. doi: 10.1007/s11051-010-9996-0

Elskens, J., Manicardi, A., Costi, V., Madder, A., and Corradini, R. (2017). Synthesis and improved cross-linking properties of C5-modified furan bearing PNAs. *Molecules* 22:2010. doi: 10.3390/molecules22112010

Ghiassian, S., Gobbo, P., and Workentin, M. S. (2015). Water-soluble maleimide-modified gold nanoparticles (AuNPs) as a platform for cycloaddition reactions. *Eur. J. Org. Chem.* 2015, 5438–5447. doi: 10.1002/ejoc.201500685

Ghosh, P., Han, G., De, M., Kim, C. K., and Rotello, V. M. (2008). Gold nanoparticles in delivery applications. *Adv. Drug Deliv. Rev.* 60, 1307–1315. doi: 10.1016/j.addr.2008.03.016

Homola, J. (2008). Surface plasmon resonance sensors for detection of chemical and biological species. *Chem. Rev.* 108, 462–493. doi: 10.1021/cr068107d

Jha, S., Ramadori, F., Quarta, S., Biasiolo, A., Fabris, E., Baldan, P., et al. (2017). Binding and uptake into human hepatocellular carcinoma cells of peptide-functionalized gold nanoparticles. *Bioconjug. Chem.* 28, 222–229. doi: 10.1021/acs.bioconjchem.6b00441

Liu, B., and Liu, J. (2017). Methods for preparing DNA-functionalized gold nanoparticles, a key reagent of bioanalytical chemistry. *Anal. Methods* 9, 2633–2643. doi: 10.1039/C7AY00368D

Liu, X., Liu, H., Zhou, W., Zheng, H., Yin, X., Li, Y., et al. (2010). Thermoreversible covalent self-assembly of oligo(p-phenylenevinylene) bridged gold nanoparticles. *Langmuir* 26, 3179–3185. doi: 10.1021/la903838w

Madsen, M., and Gothelf, K. V. (2019). Chemistries for DNA Nanotechnology. *Chem. Rev.* 119, 6384–6458. doi: 10.1021/acs.chemrev.8b00570

Manea, F., Bindoli, C., Polizzi, S., Lay, L., and Scrimin, P. (2008). Expeditious synthesis of water-soluble, monolayer-protected gold nanoparticles of controlled size and monolayer composition. *Langmuir* 24, 4120–4124. doi: 10.1021/la703558y

Manicardi, A., Gyssels, E., Corradini, R., and Madder, A. (2016). Furan-PNA: a mildly inducible irreversible interstrand crosslinking system targeting single and double stranded DNA. *Chem. Commun.* 52, 6930–6933. doi: 10.1039/C6CC02062C

Murphy, D., Redmond, G., De La Torre, B. G., and Eritja, R. (2004). Hybridization and melting behavior of Peptide Nucleic Acid (PNA) oligonucleotide chimeras conjugated to gold nanoparticles. *Helv. Chim. Acta* 87, 2727–2734. doi: 10.1002/hlca.200490245

Nielsen, P. E. (2004). PNA Technology. *Mol. Biotechnol.* 26, 233–248. doi: 10.1385/MB:26:3:233

Oluwasanmi, A., Al-Shakarchi, W., Manzur, A., Aldebasi, M. H., Elsini, R. S., Albusair, M. K., et al. (2017). Diels Alder-mediated release of gemcitabine from hybrid nanoparticles for enhanced pancreatic cancer therapy. *J. Control. Release* 266, 355–364. doi: 10.1016/j.jconrel.2017.09.027

Pamies, R., Cifre, J. G. H., Espín, V. F., Collado-González, M., Baños, F. G. D., and De La Torre, J. G. (2014). Aggregation behaviour of gold nanoparticles in saline aqueous media. *J. Nanoparticle Res.* 16:2376. doi: 10.1007/s11051-014-2376-4

Sapsford, K. E., Algar, W. R., Berti, L., Gemmill, K. B., Casey, B. J., Oh, E., et al. (2013). Functionalizing nanoparticles with biological molecules: developing chemistries that facilitate nanotechnology. *Chem. Rev.* 113, 1904–2074. doi: 10.1021/cr300143v

Song, Y., Luo, Y., Zhu, C., Li, H., Du, D., and Lin, Y. (2016). Recent advances in electrochemical biosensors based on graphene two-dimensional nanomaterials. *Biosens. Bioelectron.* 76, 195–212. doi: 10.1016/j.bios.2015.07.002

Zhu, J., Kell, A. J., and Workentin, M. S. (2006). A retro-Diels-Alder reaction to uncover maleimide-modified surfaces on monolayer-protected nanoparticles for reversible covalent assembly. *Org. Lett.* 8, 4993–4996. doi: 10.1021/ol0615937

Conflict of Interest: The authors declare that the research was conducted in the absence of any commercial or financial relationships that could be construed as a potential conflict of interest.

frontiers in Chemistry

ORIGINAL RESEARCH
published: 28 January 2020
doi: 10.3389/fchem.2020.00002

Efficient Capturing of Polycyclic Aromatic Micropollutants From Water Using Physically Crosslinked DNA Nanoparticles

*Siriki Atchimnaidu, Hari Veera Prasad Thelu, Devanathan Perumal, Kaloor S. Harikrishnan and Reji Varghese**

School of Chemistry, Indian Institute of Science Education and Research (IISER) Thiruvananthapuram, Thiruvananthapuram, India

Design and synthesis of physically (non-covalently) cross-linked nanoparticles through host-guest interaction between β-CD and adamantane is reported. Specific molecular recognition between β-CD functionalized branched DNA nanostructures (host) and a star-shaped adamantyl-terminated 8-arm poly(ethylene glycol) polymer (guest) is explored for the design of the nanoparticles. The most remarkable structural features of DNA nanoparticles include their excellent biocompatibility and the possibility of various non-covalent interactions with both hydrophobic and hydrophilic organic molecules. Potential of DNA nanoparticles for the rapid and efficient capture of various micropollutants typically present in water including carcinogens (hydrophobic micropollutants), organic dyes (hydrophilic), and pharmaceutical molecules (hydrophilic) is also demonstrated. The capture of micropollutants by DNA nanoparticles is attributed to the various non-covalent interactions between DNA nanoparticles and the micropollutants. Our results clearly suggest that DNA based nanomaterials would be an ideal candidate for the capturing and removal of both hydrophilic and hydrophobic micropollutants typically present in water.

Keywords: DNA nanostructures, self-assembly, micropollutants, water purification, host-guest interactions

OPEN ACCESS

Edited by:
Janarthanan Jayawickramarajah, Tulane University, United States

Reviewed by:
Apurba Lal Koner, Indian Institute of Science Education and Research, Bhopal, India
Bang-Jing Li, Chengdu Institute of Biology, (CAS), China

****Correspondence:***
Reji Varghese
reji@iisertvm.ac.in

Specialty section:
This article was submitted to Supramolecular Chemistry, a section of the journal Frontiers in Chemistry

Received: *25 October 2019*
Accepted: *06 January 2020*
Published: *28 January 2020*

Citation:
Atchimnaidu S, Thelu HVP, Perumal D, Harikrishnan KS and Varghese R (2020) Efficient Capturing of Polycyclic Aromatic Micropollutants From Water Using Physically Crosslinked DNA Nanoparticles. Front. Chem. 8:2. doi: 10.3389/fchem.2020.00002

INTRODUCTION

One of the major threats to human health is the occurrence of organic micropollutants such as pesticides, polycyclic aromatic hydrocarbons (carcinogens), pharmaceuticals etc. in drinking water, and hence their detection, capture, and removal from drinking water is extremely vital (Schwarzenbach et al., 2006). Micropollutants typically present in drinking water include both hydrophobic and hydrophilic organic molecules. Activated charcoal was traditionally used as sorbent for the capture and removal of micropollutants from drinking water (Órfão et al., 2006). Though activated charcoal is efficient and successful in removing hydrophobic micropollutants, they often fail in capturing the hydrophilic micropollutants. Nanomaterials offer an alternative and convenient substrate for the capture and removal of micropollutants from water. For example, carbon-based nanostructures such as multi-walled carbon nanotubes (Kuo, 2009), graphene (Xu et al., 2012), and graphene oxide (Gao et al., 2012) were proven to be remarkable adsorbents for organic micropollutants. In the case of carbonaceous nanomaterials, since the adsorption is

mainly achieved through the π-π stacking interactions, they were shown to be very efficient for the capturing of polycyclic aromatic hydrocarbons. However, carbonaceous nanomaterials were found not to be a superior adsorbent for hydrophilic micropollutants. Similarly, metal nanoparticles were also found to be promising substrate for the removal of micropollutant from water (Wang et al., 2018). However, the toxicity associated with the metal nanoparticle is a concern. Very recently, supramolecular approaches were also reported for the capture of micropollutants. For example, hydrophobic cavity of β-cyclodextrin (β-CD) was explored for the rapid capturing of different organic micropollutants using a porous β-cyclodextrin-based polymer (Alsbaiee et al., 2016). In another report, charge-transfer interaction was used for the capturing of polycyclic aromatic hydrocarbons using a semi-rigid cationic cyclophane as the host (Barnes et al., 2012). Even though there are few elegant strategies are reported in the literature, there is always a growing demand for the design of new nanomaterials for the capturing of organic micropollutants that exhibit (i) excellent biocompatibility, (ii) efficient capturing (interaction) toward both hydrophobic and hydrophilic micropollutants, and (iii) non-toxicity.

The unique structural characteristics of DNA such as nanoscale dimensions, predictable secondary structure, ease of synthesis and molecular recognition-directed self-assembly have fascinated scientists to use DNA as a molecular building block for the construction of DNA nanostructures (Seeman, 1982, 2010; Gothelf and LaBean, 2005; Aldaye et al., 2008; Pinheiro et al., 2011; Tørring et al., 2011). Recent years have seen the emergence of extremely complex one-dimensional (1D), 2D, and 3D nanostructures made of DNA, which have found potential applications in various fields ranging from material science to medicine (Walsh et al., 2011; Jiang et al., 2012; Modi et al., 2013) to nanotechnology (Seeman, 2003; Feldkamp and Niemeyer, 2006; Song et al., 2013; Jones et al., 2015). More interestingly, DNA is known to have efficient non-covalent (physical) interactions with both hydrophilic and hydrophobic organic molecules through various non-covalent interactions such as hydrogen bonding, π-π stacking, electrostatic interactions etc. (Hannah and Armitage, 2004). Hydrophobic molecules prefers to bind to DNA through intercalation within the nucleobases through hydrophobic interactions. Whereas hydrophilic cationic molecules binds to the phosphate backbone of DNA through electrostatic interaction. The remarkable structural features of DNA including the excellent biocompatibility, efficient non-covalent interactions with hydrophobic and hydrophilic molecules and non-toxicity indisputably suggest that DNA based nanomaterials would be a promising candidate for the capture of organic micropollutants from water. Among the various classes of nanomaterials, nanogels, particularly physically cross-linked, are unique owing to their nanosize, porosity, and high guest encapsulation ability (Yu et al., 2006). Moreover, physically

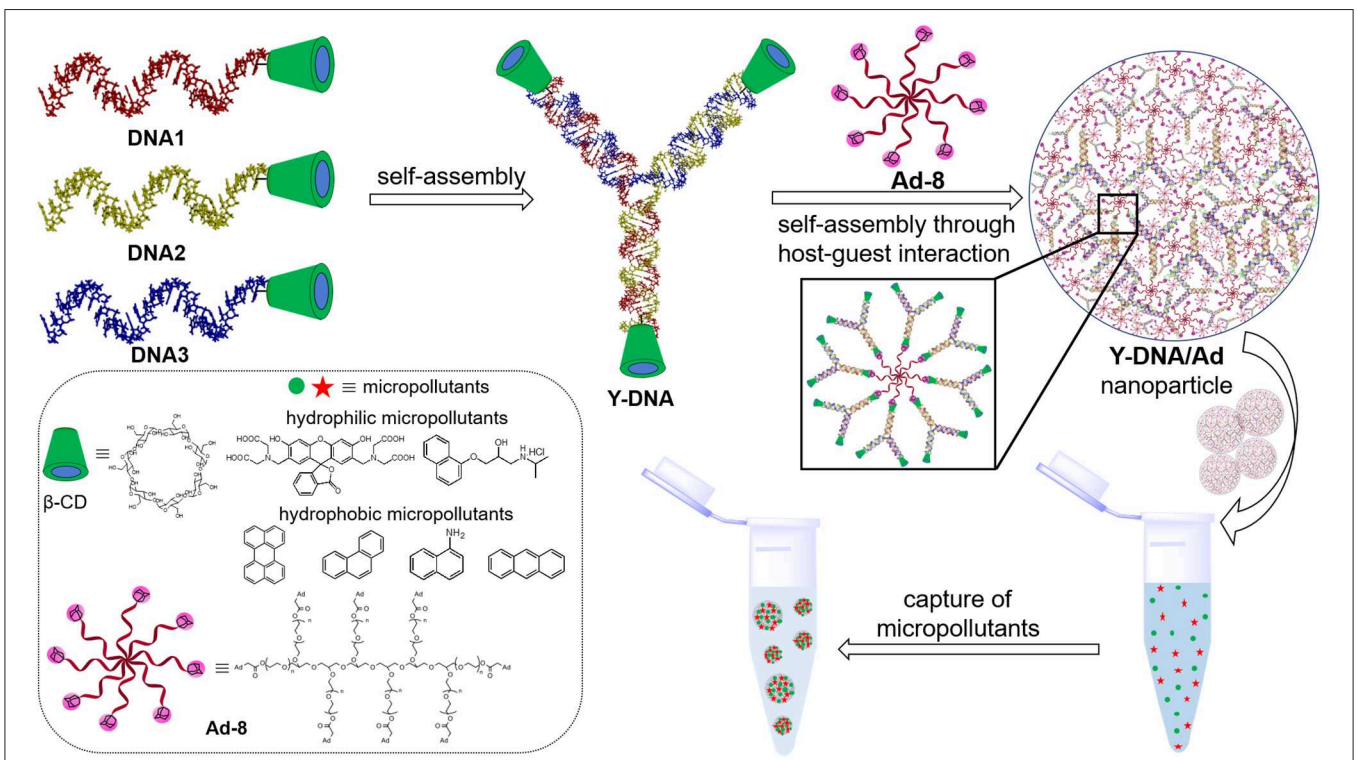

SCHEME 1 | Pictorial representation showing the structures of **DNA1–3** and their self-assembly into β-CD tethered branched Y-DNA (**Y-DNA**). Self-assembly of **Y-DNA** with **Ad-8** through multivalent host–guest interactions between β-CD and adamantane to **Y-DNA/Ad-8** nanoparticle and the capture of hydrophilic and hydrophobic micropollutants by DNA nanogel are also shown. Chemical structures of β-CD, **Ad-8** and micropollutants investigated in this study are shown in the box.

cross-linked nanogels are far superior over the chemically cross-linked counterparts because of their ease of synthesis, reversible and stimuli responsive nature (Mishra et al., 2018). Hence physically cross-linked DNA-based nanogel would be the most ideal candidate for the capture of organic micropollutants from water. Though chemically cross-linked DNA hydrogels have successfully explored for the removal of organic micropollutants from water, there is no report on the use of physically cross-linked DNA nanogels for the capture of micropollutants from water.

Supramolecular interactions have been extensively explored for the design of various soft nanomaterials with remarkable optical and electronic properties (Rest et al., 2014; Taniguchi et al., 2016; Mishra et al., 2018; Zhou et al., 2018). Very recently, we have explored the molecular recognition between β-CD and adamantane for the design of DNA-based physically cross-linked nanogel (Thelu et al., 2018). We have demonstrated the synthesis of DNA-based nanogel with controllable size using the multivalent host–guest interaction between β-CD functionalized branched DNA nanostructures as the host and a star-shaped adamantyl-terminated 8-arm poly(ethylene glycol) polymer as the guest. The potential of the nanogel as a nanocarrier for targeted drug delivery was also demonstrated. Herein, we report the potential of DNA-based nanogel for the capture of organic micropollutants, both hydrophobic and hydrophilic, from water (**Scheme 1**). The design of nanogel was already reported by us, and the same strategy was followed for the synthesis of DNA nanogel. This was achieved by self-assembly between multivalent host–guest interaction between β-CD functionalized branched DNA nanostructures as the host and a star-shaped adamantyl-terminated 8-arm poly(ethylene glycol) (PEG) polymer as the guest. The size of the nanogel could be controlled by appropriate modulation of the concentration of the guest and host. The potential of the nanogel to capture a series of hydrophobic molecules and hydrophilic molecules are demonstrated. The capture of the molecules into the DNA nanogel network is due to the non-covalent interactions of the micropollutants with the backbone and bases of DNA. Our results clearly show that the DNA based nanogels are promising nanomaterials for the capture of micropollutants.

TABLE 1 | Sequences of **DNA1–3**.

DNA	Sequence (5′→ 3′)
DNA1	β-CD-TTGGATCCGCATGACATTCGCCGTAAGA
DNA2	β-CD-TCTTACGGCGAATGACCGAATCAGCCTA
DNA3	β-CD-TAGGCTGATTCGGTTCATGCGGATCCAA

RESULTS AND DISCUSSIONS

The synthesis of the 8-arm star PEG polymer, **Ad-8** (guest molecule) was achieved by following our previously reported procedure (Thelu et al., 2018). The β-CD-tethered oligonucleotides (**DNA1–3**) are complementary to each to form β-CD-tethered Y-shaped DNA (**Y-DNA**) and the sequences

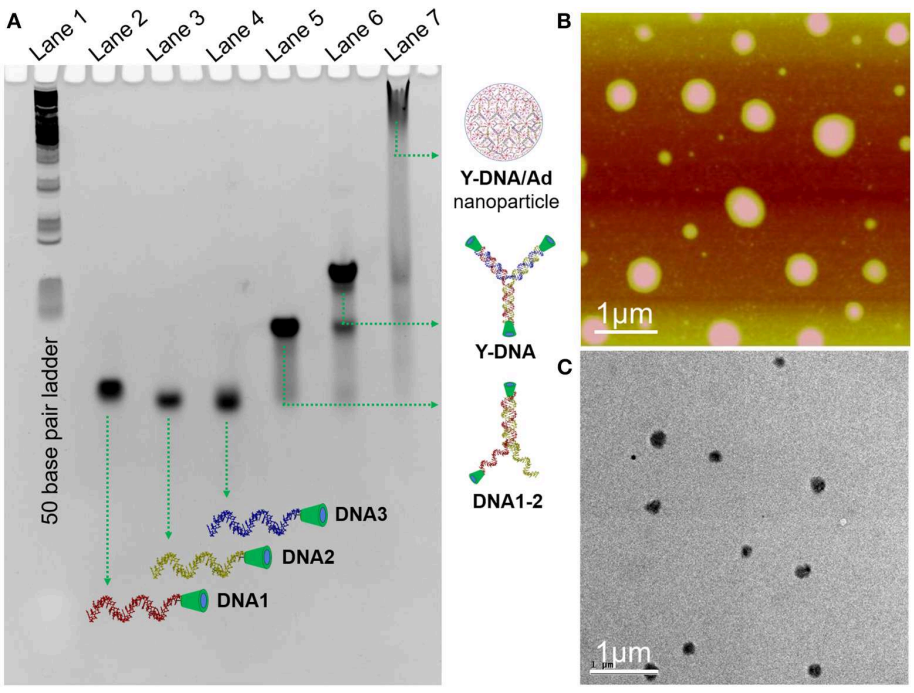

FIGURE 1 | (A) Native PAGE (14%) analysis of the self-assembly of **Y-DNA/Ad-8**. L1 for 50 base pair ladder, L2–L4 for **DNA1–3**, respectively, L5 for the assembly of **DNA1** and **DNA2**, L6 for the assembly of **DNA1**, **DNA2** and **DNA3**, L7 for the assembly of **Y-DNA** and **Ad-8**. **(B)** Tapping-mode AFM height and **(C)** TEM images of **Y-DNA/Ad-8** nanoparticles, respectively.

of the DNAs are provided in **Table 1**. The self-assembly of the oligonucleotides was initially studied using native polyacrylamide gel electrophoresis (PAGE) analyses (**Figure 1** and **Figure S1**). The self-assembly of the β-CD-tethered Y-shaped DNA (host) was achieved by the self-assembly of equimolar quantities of **DNA1–3** in PBS buffer containing NaCl (100 mM) by annealing from 90°C to room temperature following a reported procedure (Um et al., 2006). Native PAGE analyses clearly show that the sequential addition of complementary DNAs leads to the formation of host β-CD-tethered Y-shaped DNA (**Y-DNA**) as it is evident from the reduced electrophoretic mobility of the resultant DNA nanostructure compared with the corresponding individual complementary DNA strands. Further reduction in the electrophoretic mobility was observed with the addition of **Ad-8** to **Y-DNA**, which clearly reveals that the self-assembly between **Ad-8** and **Y-DNA** through host-guest interaction between β-CD and adamantane resulted in the formation of nanoaggregates for **Ad-8/Y-DNA** supramolecular complex. Dynamic light scattering (DLS) analyses of **Ad-8/Y-DNA** show the formation of aggregated species in solution with diameter in the range of 140–290 nm. Zeta potential (ζ) measurement reveals a value of −16.6 mV, which suggest the formation of aggregated species decorated with negatively charged DNA. Better insights into the morphology of the aggregates were provided by atomic force microscopy (AFM) and transmission electron microscopy (TEM) analyses. Atomic force microscopic height image of **Y-DNA/Ad-8** shows the formation of spherical nanoparticle with diameters in the range of 150–300 nm. The section analyses of the nanoparticle reveal that the average height of the nanoparticle is ∼18 nm, which is significantly lower than the corresponding average diameter of the nanoparticles. This indicates significant flattening of the nanoparticles occurs on the mica surface due to their soft nature, which is in accordance with similar soft nanoparticles. In accordance with AFM observations, TEM analyses also show the formation of nanoparticles with diameters in the range of ∼250 nm. Microscopic analyses are in good agreement with the DLS data. Microscopic, DLS and PAGE data collectively confirm that hierarchical assembly of **Y-DNA** and **Ad-8** through multivalent host-guest interaction between β-CD and adamantane leads to the formation of **Y-DNA/Ad-8** nanoparticles in water (nanogel).

The most striking features of the nanoparticles include: (i) excellent biocompatibility, (ii) non-toxicity, (iii) hydrophobic pockets, and (iv) anionic DNA backbone, which are ideal for their application as an adsorbent for the capturing of hydrophobic and hydrophilic molecules dissolved in water. This motivated us to explore the potential of the DNA nanoparticles for the capturing of micropollutants typically present in water. We have taken few representative examples for hydrophilic and hydrophobic molecules to demonstrate the potential of the nanogel to capture them from water. Hydrophobic molecules investigated in this study include carcinogenic aromatic hydrocarbon such as perylene, anthracene, phenanthrene, and 1-naphthyl amine. The hydrophilic molecules selected in our study include calcein (organic dye) and propranolol hydrochloride (pharmaceutical). Typically, concentration of the micropollutants present in drinking water is in the range of nanomolar to micromolar concentrations. Hence, we have artificially contaminated the water with different micropollutants with a final concentration of 100 nM. Final concentration of DNA nanoparticles used in our study was 500 nM. Typically, **Y-DNA/Ad-8** nanoparticle in PBS buffer (100 μL) containing NaCl (100 mM) was added into water containing micropollutant solution (400 μL), shaken for 1 min and kept undisturbed for about 10 min. In the cases of hydrophobic micropollutants, they were initially dissolved in acetone and diluted with water to 400 μL. Since the concentration of the micropollutants present in all these cases is 100 nM, we have used very sensitive fluorescence spectroscopy as the tool to follow the capture of micropollutants. This was studied by comparing florescence intensity changes of the micropollutants before and after DNA nanoparticle addition to their solution.

Initially, the biocompatibility of the nanogel was analyzed with two different cancer cell lines (HeLa and A549) by means of 3-(4,5-dimethylthiazol-2-yl)-2,5-diphenyltetrazolium

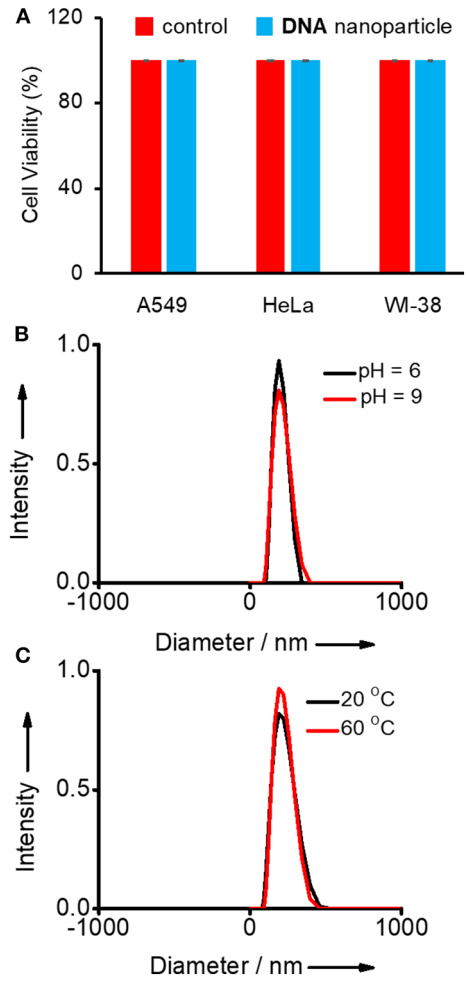

FIGURE 2 | (A) Comparison of viability of A549, HeLa (cancer cells), and WI-38 (normal cell) cell lines treated with **Y-DNA/Ad-8** nanoparticles. Size distribution of nanoparticle obtained from the DLS analyses **(B)** at two different pH and **(C)** at two different temperatures.

bromide (MTT) assay. The viability of untreated HeLa, A549, and WI-38 cells were taken as 100%. In order to assess the biocompatibility of **Y-DNA/Ad-8** nanoparticle, A549, HeLa (cancer cells), and WI-38 (normal cell) cells were incubated with **Y-DNA/Ad-8** nanoparticles for 24 h. The concentration of **Y-DNA/Ad-8** nanoparticle used for MTT assay was 500 nM. As expected, MTT assay reveals cell viability above 95% for all cell lines demonstrating excellent biocompatibility of **Y-DNA/Ad-8** nanoparticles (**Figure 2A**). Furthermore, thermal and pH stabilities of the nanoparticles under different experimental conditions were studied by DLS analyses. DLS analyses of the nanoparticle at pH 6 and 9 show no difference in the size distribution of the nanoparticle, which clearly show the pH stability of the nanoparticle (**Figure 2B**). Similarly, thermal stability of the nanoparticle was studied at 20 and 60°C and in this case also no noticeable change was observed for the size distribution of the nanoparticles (**Figure 2C**). These results reveal the thermal and pH stability of **Y-DNA/Ad-8** nanoparticles.

After confirming the biocompatibility and stability of **Y-DNA/Ad-8** nanoparticles, we have carried out the micropollutant capture experiments with the nanoparticles. It is to be mentioned that the hydrophobic micropollutants selected in our study showed very poor solubility in water. Emission spectrum of perylene in water shows its characteristic emission with emission maximum centered at 440 nm (λ_{exc} = 400 nm) (**Figure 3A** and **Figure S2**). Very interestingly, a significant enhancement in emission intensity (9 fold) was observed with the addition of **Y-DNA/Ad-8** nanoparticles, which can be attributed to the capturing of feebly water-soluble perylene into the hydrophobic cavities of the nanoparticle. It is also to be noted that a red-shift of 3 nm was observed for the emission peak at 440 nm. These results collectively suggest that perylene binds efficiently to the nucleobases through π-stacking interactions as reported in similar systems (Sezi and Wagenknecht, 2013; Gershberg et al., 2015). The red-shift in the emission peak suggest that the perylene reside in the hydrophobic environments after their capture from water. The possibility of non-covalent trapping of perylene in the hydrophobic pockets of the nanoparticle cannot be completely ruled out. From the fluorescence titration experiments we have calculated the capture efficiency of the nanoparticle as 500 nM of **Y-DNA/Ad-8** nanoparticle was able to capture 1 μM of perylene. Anthracene was nearly insoluble in water as evident from its fluorescence spectrum (λ_{exc} = 400 nm) in water. However, efficient capturing of anthracene by the nanoparticles caused a dramatic increase in the fluorescence intensity (**Figure 3B**). In this case as well, π-stacking with the nucleobases and hydrophobic interactions are responsible for the capturing of anthracene by the DNA nanoparticles. It is also to be noted that the excimer emission with maximum centered at 410 nm dominates in the emission spectrum due to the aggregation of anthracene in the hydrophobic environment of the nanoparticle (Neelakandan and Ramaiah, 2008). Fluorescence spectrum of phenanthrene in water clearly reveals that it is nearly insoluble in water. However, a significant enhancement in emission intensity was observed with the addition of nanoparticle into the solution due to the efficient capture of phenanthrene by the nanoparticles (**Figure 3C**). It is also worth noting that phenanthrene shows mainly excimer-like emission centered at 408 nm (λ_{exc} = 280 nm) after their capture (Haynes et al., 1990), which clearly suggest that phenanthrene exists as aggregated species in the nanogel assembly. This observation is in good agreement with other hydrophobic molecules. We have also

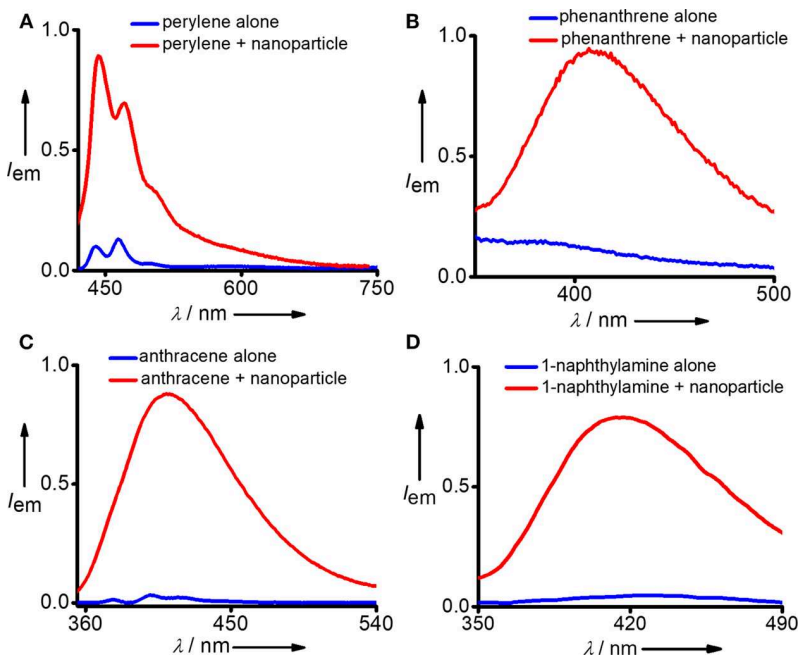

FIGURE 3 | Comparison of fluorescence spectra of **(A)** perylene, **(B)** phenanthrene, **(C)** anthracene, and **(D)** 1-naphthylamine before and after the addition of **Y-DNA/Ad-8** nanoparticles.

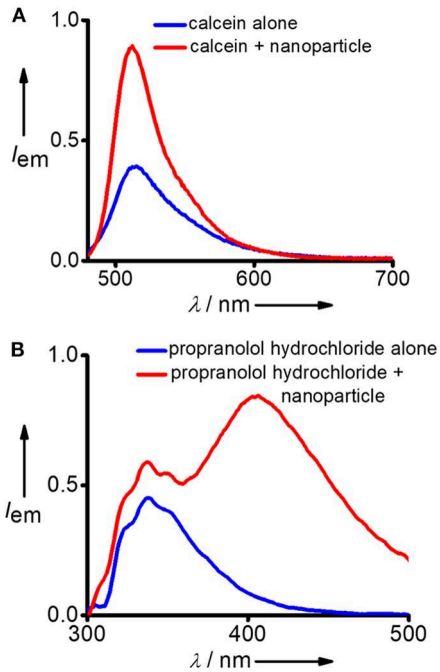

FIGURE 4 | Comparison of fluorescence spectra of **(A)** calcein and **(B)** propranolol hydrochloride before and after the addition of **Y-DNA/Ad-8** nanoparticles.

demonstrated the capture of 1-naphthylamine (**Figure 3D**). A dramatic increase in fluorescence intensity was observed with the capture of poorly water soluble 1-naphthylamine by the nanoparticles. In this case as well, only excimer-like red-shifted peak centered at 415 nm (λ_{exc} = 270 nm) was observed due to the aggregation of 1-naphthylamine in **Y-DNA/Ad-8** nanoparticle network.

After successful demonstration of the capture of hydrophobic micropollutants, we have extended our study toward the capture of hydrophilic micropollutants in water. We have taken calcein as a representative hydrophilic organic dye. Calcien is water soluble and it exhibits the characteristic emission spectrum with maximum centered at 512 nm (λ_{exc} = 470 nm). Interestingly, an increase in emission intensity was observed after the incubation with DNA nanoparticles (**Figure 4A**). This observation suggests that though calcien is water soluble, it is weakly aggregated in water and upon binding with the **Y-DNA/Ad-8** nanoparticle through non-covalent interactions dissociate the weakly assembled calcien aggregated species into the corresponding monomeric species, which resulted in an increase in emission intensity. Another hydrophilic molecule we have investigated in this study is propranolol hydrochloride, which is a pharmaceutical molecule. Propranolol hydrochloride is cationic molecule and is water soluble. This molecule shows its characteristic emission centered at 335 nm (λ_{exc} = 270 nm) in water (**Figure 4B**). Interestingly, in addition to the characteristic emission of propranolol hydrochloride at 335 nm, a new red-shifted peak centered at 405 nm also emerges after its incubation with **Y-DNA/Ad-8** nanoparticles. This suggest that positively charged propranolol hydrochloride efficiently binds to the negatively charged DNA backbone through electrostatic interactions with its hydrophobic naphthalene residue interact with the nucleobases through π-π stacking interactions. The emergence of red-shifted excimer-like peak suggest that the molecule is getting aggregated inside the nanogel network after their capture by the **Y-DNA/Ad-8** nanoparticles.

CONCLUSIONS

In summary, we have reported the synthesis of physically cross-linked DNA nanoparticles through multivalent host-guest interaction between β-CD functionalized branched DNA nanostructures as the host and a star-shaped adamantyl-terminated 8-arm poly(ethylene glycol) polymer as the guest. The most remarkable structural features of DNA nanoparticles include their excellent biocompatibility and the possibility of various non-covalent interactions with both hydrophobic and hydrophilic organic molecules. We have demonstrated the potential of DNA nanoparticles for the rapid and efficient capture of various micropollutants typically present in water including carcinogens (hydrophobic micropollutants), organic dyes (hydrophilic), and pharmaceutical molecules (hydrophilic). The capture of micropollutants by DNA nanoparticles was attributed to the various non-covalent interactions between DNA nanoparticles and the micropollutants. The excellent biocompatibility of the DNA nanoparticles and their potential as an efficient capture of both poorly water soluble hydrophobic micropollutants and highly water soluble hydrophilic micropollutants may motivate other researches to explore DNA-based nanomaterials as an adsorbent for the removal and purification of micropollutants from drinking water.

DATA AVAILABILITY STATEMENT

All datasets generated for this study are included in the article/**Supplementary Material**.

AUTHOR CONTRIBUTIONS

RV designed the project. SA, HT, DP, and KH performed all the experiments. RV and SA co-wrote the manuscript. All authors analyzed the data and commented on the manuscript.

FUNDING

Financial supports from DBT (BT/PR30172/NNT/28/1593/2018) and KSCSTE (KSYSA) are gratefully acknowledged.

ACKNOWLEDGMENTS

We thank UGC and CSIR for research fellowships.

SUPPLEMENTARY MATERIAL

The Supplementary Material for this article can be found online at: https://www.frontiersin.org/articles/10.3389/fchem.2020.00002/full#supplementary-material

REFERENCES

Aldaye, F. A., Palmer, A. L., and Sleiman, H. F. (2008). Assembling materials with DNA as the guide. *Science* 321, 1795–1799. doi: 10.1126/science.1154533

Alsbaiee, A., Smith, B. J., Xiao, L., Ling, Y., Helbling, D. E., and Dichtel, W. R. (2016). Rapid removal of organic micropollutants from water by a porous β-cyclodextrin polymer. *Nature* 529, 190–194. doi: 10.1038/nature16185

Barnes, J. C., Jurícek, M., Strutt, N. L., Frasconi, M., Sampath, S., Giesener, M. A., et al. (2012). ExBox: a polycyclic aromatic hydrocarbon scavenger. *J. Am. Chem. Soc*. 135, 183–192. doi: 10.1021/ja307360n

Feldkamp, U., and Niemeyer, C. M. (2006). Rational design of DNA nanoarchitectures. *Angew. Chem. Int. Ed.* 45, 1856–1876. doi: 10.1002/anie.200502358

Gao, Y., Li, Y., Zhang, L., Huang, H., Hu, J., Shah, S. M., et al. (2012). Adsorption and removal of tetracycline antibiotics from aqueous solution by graphene oxide. *J. Colloid Interface Sci.* 368, 540–546. doi: 10.1016/j.jcis.2011.11.015

Gershberg, J., Stojkovic', M. R., Škugor, M., Tomic', S., Rehm, T. H., Rehm, S., et al. (2015). Sensing of double-stranded DNA/RNA secondary structures by water soluble homochiral perylene bisimide dyes. *Chem. Eur. J*. 21, 7886–7895. doi: 10.1002/chem.201500184

Gothelf, K. V., and LaBean, T. H. (2005). DNA-programmed assembly of nanostructures. *Org. Biomol. Chem*. 3, 4023–4037. doi: 10.1039/b510551j

Hannah, K. C., and Armitage, B. A. (2004). DNA-Templated assembly of helical cyanine dye aggregates: a supramolecular chain polymerization. *Acc. Chem. Res*. 37, 845–853. doi: 10.1021/ar030257c

Haynes, D. R., Helwig, K. R., Tro, N. J., and George, S. M. (1990). Fluorescence quenching of the phenanthrene excimer on AI20 3(0001): coverage and distance dependence. *J. Chem. Phys.* 93, 2836–2847. doi: 10.1063/1.458869

Jiang, Q., Song, C., Nangreave, J., Liu, X., Lin, L., Qiu, D., et al. (2012). DNA Origami as a carrier for circumvention of drug resistance. *J. Am. Chem. Soc.* 134, 13396–13403. doi: 10.1021/ja304263n

Jones, M. R., Seeman, N. C., and Mirkin, C. A. (2015). Nanomaterials. Programmable materials and the nature of the DNA bond. *Science* 347, 1260901–1260911. doi: 10.1126/science.1260901

Kuo, C. Y. (2009). Comparison with as-grown and microwave modified carbon nanotubes to removal aqueous bisphenol A. *Desalination* 249, 976–982. doi: 10.1016/j.desal.2009.06.058

Mishra, A., Korlepara, D. B., Kumar, M., Jain, A., Jonnalagadda, N., Bejagam, K., et al. (2018). Biomimetic temporal self-assembly via fuel-driven controlled supramolecular polymerization. *Nat Commun.* 9:1295. doi: 10.1038/s41467-018-03542-z

Modi, S., Nizak, C., Surana, S., Halder, S., and Krishnan, Y. (2013). Two DNA nanomachines map pH changes along intersecting endocytic pathways inside the same cell. *Nat. Nanotechnol*. 8, 459–467. doi: 10.1038/nnano.2013.92

Neelakandan, P. P., and Ramaiah, D. (2008). DNA-Assisted long-lived excimer formation in a cyclophane. *Angew. Chem. Int. Ed.* 47, 8407–8411. doi: 10.1002/anie.200803162

Órfão, J. J. M., Silva, A. I. M., Pereira, J. C. V., Barata, S. A., Fonseca, I. M., Faria, P. C. C., et al. (2006). Adsorption of a reactive dye on chemically modified activated carbons–influence of pH. *J. Colloid Interf. Sci*. 296, 480–489. doi: 10.1016/j.jcis.2005.09.063

Pinheiro, A. V., Han, D., Shih, W. M., and Yan, H. (2011). Challenges and opportunities for structural DNA nanotechnology. *Nat. Nanotechnol.* 6, 763–772. doi: 10.1038/nnano.2011.187

Rest, C., Mayoral, M. J., Fucke, K., Schellheimer, J., Stepanenko, V., and Fernandez, G. (2014). Self-assembly and (Hydro)gelation triggered by cooperative π-π and Unconventional C–H· · ·X hydrogen bonding interactions. *Angew. Chem. Int. Ed.* 53, 700–705. doi: 10.1002/anie.201307806

Schwarzenbach, R. P., Escher, B. I., Fenner, K., Hofstetter, T. B., Johnson, C. A., Gunten von, U., et al. (2006). The challenge of micropollutants in aquatic systems. *Science* 313, 1072–1077. doi: 10.1126/science.1127291

Seeman, N. C. (1982). Nucleic acid junctions and lattices *J. Theor. Biol*. 99, 237–247. doi: 10.1016/0022-5193(82)90002-9

Seeman, N. C. (2003). DNA in a material world. *Nature* 421, 427–431. doi: 10.1038/nature01406

Seeman, N. C. (2010). Nanomaterials based on DNA. *Annu. Rev. Biochem*. 79, 65–87. doi: 10.1146/annurev-biochem-060308-102244

Sezi, S., and Wagenknecht,. H.-A. (2013). DNA-templated formation of fluorescent self-assembly of ethynyl pyrenes. *Chem. Commun*. 49, 9257–9259. doi: 10.1039/c3cc44733b

Song, C., Wang, Z.-G., and Ding, B. (2013). Smart nanomachines based on DNA self-assembly. *Small* 9, 2382–2392. doi: 10.1002/smll.201300824

Taniguchi, Y., Takishita, T., Kawai, T., and Nakashima, T. (2016). End-to-end self-assembly of semiconductor nanorods in water by using an amphiphilic surface design. *Angew. Chem. Int. Ed.* 55, 2083–2086. doi: 10.1002/anie.201509833

Thelu, H. V. P., Albert, S. K., Golla, M., Krishnan, N., Ram, D., Srinivasula, S. M., et al. (2018). Size controllable DNA nanogels from the self-assembly of DNA nanostructures through multivalent host–guest interactions. *Nanoscale* 10, 222–230. doi: 10.1039/C7NR06985E

Tørring, T., Voigt, N. V., Nangreave, J., Yan, H., and Gothelf, K. V. (2011). DNA origami: a quantum leap for self-assembly of complex structures. *Chem. Soc. Rev*. 40, 5636–5646. doi: 10.1039/c1cs15057j

Um, S. H., Lee, J. B., Park, N., Kwon, S. Y., Umbach, C. C., and Luo, D. (2006). Enzyme-catalysed assembly of DNA hydrogel. *Nat. Mater*. 5, 797–801. doi: 10.1038/nmat1741

Walsh, A. S., Yin, H., Erben, C. M., Wood, M. J. A., and Turberfield, A. J. (2011). DNA cage delivery to mammalian cells. *ACS Nano* 5, 5427–5432. doi: 10.1021/nn2005574

Wang, W., Xu, Z., Zhang, X., Wimmer, A., Shi, E., Qin, Y., et al. (2018). Rapid and efficient removal of organic micropollutants from environmental water using a magnetic nanoparticles-attached fluorographene-based sorbent. *Chem. Eng. J.* 343, 61–68. doi: 10.1016/j.cej.2018.02.101

Xu, J., Wang, L., and Zhu, Y. (2012). Decontamination of Bisphenol A from aqueous solution by graphene adsorption. *Langmuir* 28, 8418–8425. doi: 10.1021/la301476p

Yu, S., Hu, J., Pan, X., Yao, P., and Jiang, M. (2006). Stable and pH-sensitive nanogels prepared by self-assembly of chitosan and ovalbumin. *Langmuir* 22, 2754–2759. doi: 10.1021/la053158b

Zhou, X., Pathak, P., and Jayawickramarajah, J. (2018). Design, synthesis, and applications of DNA–macrocyclic host conjugates. *Chem. Commun*. 54, 11668–11680. doi: 10.1039/C8CC06716C

Conflict of Interest: The authors declare that the research was conducted in the absence of any commercial or financial relationships that could be construed as a potential conflict of interest.

frontiers in Chemistry

ORIGINAL RESEARCH
published: 29 January 2020
doi: 10.3389/fchem.2020.00026

Heteroleptic Coordination Environments in Metal-Mediated DNA G-Quadruplexes

*Philip M. Punt†, Lukas M. Stratmann†, Sinem Sevim, Lena Knauer, Carsten Strohmann and Guido H. Clever**

Faculty of Chemistry and Chemical Biology, TU Dortmund University, Dortmund, Germany

The presence of metal centers with often highly conserved coordination environments is crucial for roughly half of all proteins, having structural, regulatory, or enzymatic function. To understand and mimic the function of metallo-enzymes, bioinorganic chemists pursue the challenge of synthesizing model compounds with well-defined, often heteroleptic metal sites. Recently, we reported the design of tailored homoleptic coordination environments for various transition metal cations based on unimolecular DNA G-quadruplex structures, templating the regioselective positioning of imidazole ligandosides $\mathbf{L}^{\mathrm{I}}$. Here, we expand this modular system to more complex, heteroleptic coordination environments by combining $\mathbf{L}^{\mathrm{I}}$ with a new benzoate ligandoside $\mathbf{L}^{\mathrm{B}}$ within the same oligonucleotide. The modifications still allow the correct folding of parallel tetramolecular and antiparallel unimolecular G-quadruplexes. Interestingly, the incorporation of $\mathbf{L}^{\mathrm{B}}$ results in strong destabilization expressed in lower thermal denaturation temperatures T_m. While no transition metal cations could be bound by G-quadruplexes containing only $\mathbf{L}^{\mathrm{B}}$, heteroleptic derivatives containing both $\mathbf{L}^{\mathrm{I}}$ and $\mathbf{L}^{\mathrm{B}}$ were found to complex Cu^{II}, Ni^{II}, and Zn^{II}. Especially in case of Cu^{II} we found strong stabilizations of up to $\Delta T_m = +34°C$. The here shown system represents an important step toward the design of more complex coordination environments inside DNA scaffolds, promising to culminate in the preparation of functional metallo-DNAzymes.

Keywords: bioinorganic chemistry, coordination chemistry, DNA, G-quadruplex, DNAzymes

OPEN ACCESS

Edited by:
James Tucker, University of Birmingham, United Kingdom

Reviewed by:
Sriram Kanvah, Indian Institute of Technology Gandhinagar, India
Miguel Angel Aleman Garcia, Eindhoven University of Technology, Netherlands

****Correspondence:***
Guido H. Clever
guido.clever@tu-dortmund.de

†These authors have contributed equally to this work

Specialty section:
This article was submitted to Supramolecular Chemistry, a section of the journal Frontiers in Chemistry

Received: *14 November 2019*
Accepted: *09 January 2020*
Published: *29 January 2020*

Citation:
Punt PM, Stratmann LM, Sevim S, Knauer L, Strohmann C and Clever GH (2020) Heteroleptic Coordination Environments in Metal-Mediated DNA G-Quadruplexes. Front. Chem. 8:26. doi: 10.3389/fchem.2020.00026

INTRODUCTION

Proteins are involved in a vast number of processes ranging from structural and regulatory functions to enzymatic reactions. Roughly half of all proteins depend on metal cations helping to maintain a desired folding or serving as catalytic centers or redox cofactors (Raven et al., 1999; Lu et al., 2009; Rubino and Franz, 2012). Which function the respective metal ion adopts is strongly dependent on its properties, including accessible spin states, oxidation potential, Lewis-acidity, and bioavailability (Holm et al., 1996; Waldron et al., 2009). These properties are further fine-tuned by a well-defined first and second coordination sphere. The former is directly involved in metal coordination and usually consists of mixtures of different donor functionalities. Typically involved in coordination are the amino acids histidine, glutamic/aspartic acid, methionine, cysteine, or the backbone amide groups (Holm et al., 1996; Degtyarenko, 2000; Shook and Borovik, 2010; Valdez et al., 2014). In contrast, the second coordination sphere is not directly involved in metal binding but regulates catalytic processes, proton or electron shuttling, substrate transport, and

effects selectivity (Colquhoun et al., 1986; Degtyarenko, 2000; Waldron et al., 2009; Shook and Borovik, 2010; Zhao et al., 2013; Valdez et al., 2014; Cornish et al., 2016).

The design of artificial metallo-enzyme mimics with improved or novel properties is attracting increasing interest, but remains challenging. In the area of preparative bioinorganic chemistry, focus is set on small, multidentate chelate complexes, often requiring tedious multistep syntheses and only covering effects of the first coordination sphere (Samuel et al., 2010; Kanady et al., 2011; Anderson et al., 2013; Dicke et al., 2018). More biologically oriented approaches involve the replacement of natural metal cofactors with metal centers not known in nature. An example is the replacement of hemin in myoglobin with an iridium or rhodium porphyrin complex for enantioselective cyclopropanation reactions (Key et al., 2016; Litman et al., 2018). Another approach is embedding metal cofactors by covalent or non-covalent interactions into empty cavities of usually metal-free proteins. This was successfully applied in a series of examples enabling catalysis of the asymmetric transfer hydrogenation of imines (Wu et al., 2019), ring-closing metathesis (Jeschek et al., 2016), oxime (Drienovská et al., 2018), and hydrazine (Drienovská et al., 2018; Mayer et al., 2019) formation and hydration of alkenes (Drienovská et al., 2017). In contrast to the aforementioned examples, a more bottom up approach is the *de novo* design of new metallo-proteins by the precise arrangement of certain structural motifs to create a metal binding site (Raven et al., 1999; Lu et al., 2009; Rubino and Franz, 2012). In recent years, a more efficient alternative was developed based on small artificial peptoid structures. Due to their simple accessibility by solid phase synthesis and their capability to form well-ordered secondary structures, many examples were shown for selective metal binding and catalytic applications (Baskin and Maayan, 2016; Knight et al., 2017; Baskin et al., 2018; Ghosh et al., 2018).

Another type of biopolymers forming well-ordered secondary structures are oligonucleotides. In contrast to peptides, RNA and DNA only consist of four nucleotide building blocks, thus reducing the possibilities to create diverse coordination environments for a range of metal cations. To overcome this limitation, different strategies were developed to covalently or non-covalently anchor metal-chelating ligands inside DNA. Roelfes and co-workers pioneered the design of various oligonucleotides capable of Michael-Additions, Carbene transfer, *syn*-hydrations of alkenes or Diels-Alder reactions (Roelfes and Feringa, 2005; Coquière et al., 2007; Boersma et al., 2010a,b; Rioz-Martínez et al., 2016). Other groups used modified quadruplexes for sequence-specific DNA cleavage, light controlled thrombin catalysis or peroxidase mimicking DNAzymes (Xu et al., 2009; Ali et al., 2019; Wang et al., 2019). A difficulty of this approach lies in the largely unknown exact position and coordination environment of the catalytic centers. This difficulty could be overcome in the field of metal-mediated base pairing, where the hydrogen bonding interaction of canonical base pairs is replaced by metal coordination, leading to highly stabilized DNA structures (Mandal and Müller, 2017). While first examples included only the involvement of canonical bases (Katz, 1963), the field was later expanded by the incorporation of a variety of artificial nucleobases culminating in the development of programmable metal wires inside DNA duplexes (Tanaka et al., 2006; Clever et al., 2007; Mandal et al., 2016; Sandmann et al., 2019). Later, the concept was expanded from duplex to triplex DNA (Tanaka et al., 2002) and i-motifs (Abdelhamid et al., 2018), while we and others started to focus on G-quadruplexes (Miyoshi et al., 2007; Smith et al., 2012; Engelhard et al., 2013). The latter ones form from guanine-rich sequences where four G-residues cyclize to planar G-tetrads *via* Hoogsteen base pairing. Multiple G-tetrads form a G-quadruplex *via* π-π stacking interactions. Key to their high stability is the incorporation of a central cation—typically Na^+ or K^+ (Hänsel-Hertsch et al., 2017; Neidle, 2017). Our group was the first to report Cu^{II}-mediated tetramolecular G-quadruplexes based on pyridine and imidazole ligands (Engelhard et al., 2013, 2018b; Punt and Clever, 2019a), aimed at a range of applications. For example, dinuclear systems were employed as Cu^{II}-based EPR-rulers for accurate distance measurements (Engelhard et al., 2018a). We later expanded this concept to unimolecular G-quadruplexes, equipped with oligonucleotide loops which form cavities above the G-quadruplex stem in which the metal complexes are embedded (Engelhard et al., 2017). In a recent study, we further showed that these G-quadruplexes can act as robust templates to arrange different numbers of imidazole ligandosides, leading to fine-tuned affinities for a range of transition metal cations with respect to their preferred coordination environments (Punt and Clever, 2019b). While only homoleptic systems were investigated in that study, we herein expand the modular concept to heteroleptic systems with different donor functionalities. We introduce the design of mixed systems with imidazole and benzoate ligands, inspired by metallo-proteins, where the combination of imidazoles and carboxylate is often involved in metal coordination (e.g., in the 2-His-1-carboxylate facial triad) (Greenblatt et al., 1998; Koehntop et al., 2005). We show how this combination affects both, G-quadruplex stability and metal complexation.

RESULTS

In this study we report the incorporation of a new benzoate ligandoside $\mathbf{L}^{\mathbf{B}}$ in combination with the known imidazole ligandoside $\mathbf{L}^{\mathbf{I}}$. Both were incorporated in the (*S*) configuration as GNA (glycol nucleic acid) building blocks (Zhang et al., 2005, 2006) by solid phase synthesis into tetramolecular and unimolecular G-quadruplexes. The phosphoramidite of $\mathbf{L}^{\mathbf{I}}$ was synthesized as previously described (Punt and Clever, 2019b). For the new benzoate ligand $\mathbf{L}^{\mathbf{B}}$, a literature procedure was adopted (Engelhard et al., 2017). Accordingly, an initial nucleophilic attack of deprotonated solketal to methyl 4-(bromomethyl)benzoate followed by acidic deprotection reaction led to protected benzoate ligandoside (*R*)-**4**. Its structure and absolute configuration were confirmed by single-crystal X-ray diffraction (**Figure 1**). The primary hydroxyl group was DMT-protected (DMT = dimethoxytrityl) followed by a phosphorylation reaction yielding phosphoramidite building block (*S*)-**6**. DNA solid phase synthesis was then performed according to standard literature procedures with

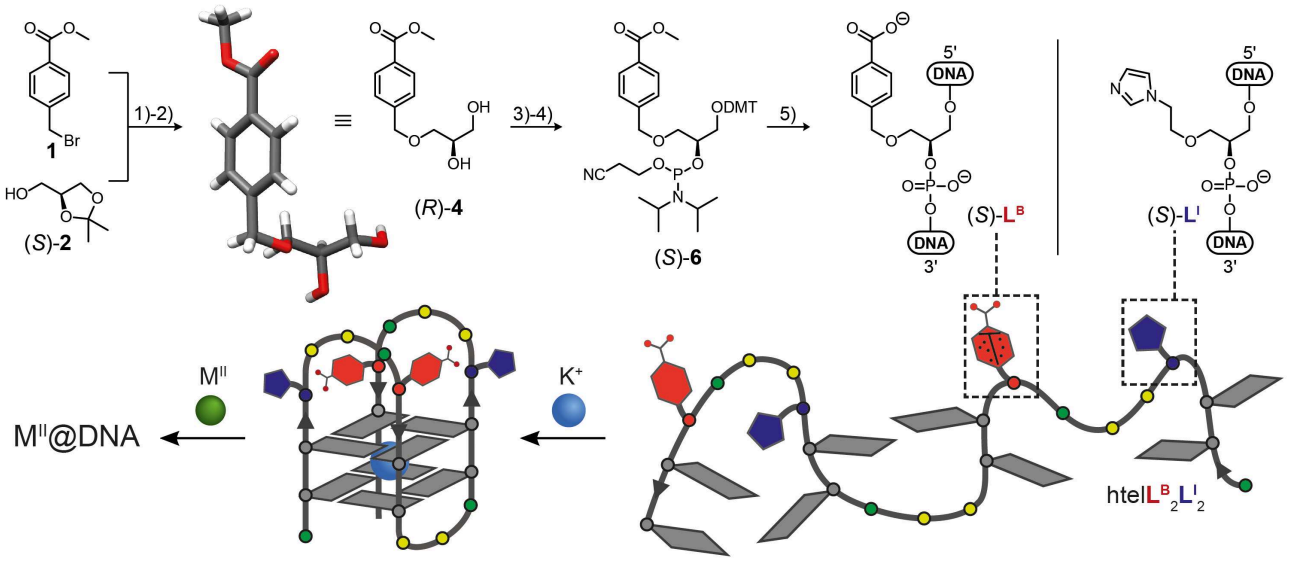

FIGURE 1 | Synthesis of benzoate ligandoside $\mathbf{L}^{B}$ and molecular structure of ligandoside $\mathbf{L}^{I}$ (**top**). (1) NaH, CH_3CN; (2) CH_3COOH, THF/H_2O; (3) DMT-Cl, DIPEA, DMAP, THF; (4) CEDIP-Cl, DIPEA, CH_2Cl_2; (5) automated solid-phase DNA synthesis. The single-crystal X-ray structure of the protected ligandoside (*R*)-**4** is shown. G-quadruplex formation (**bottom**) of htel$\mathbf{L}^{B}{}_2\mathbf{L}^{I}{}_2$ creates a heteroleptic coordination environment for transition metal ions (M = Co, Ni, Cu, Zn). Gray tiles: guanosine; red: ligandoside $\mathbf{L}^{B}$; blue: ligandoside $\mathbf{L}^{I}$; green circles: adenosine; yellow circles: thymidine. DMT = dimethoxytrityl; DIPEA = N,N-diisopropylethylamine; DMAP = N,N-dimethylaminopyridin; CEDIP-Cl = 2-cyanoethyl N,N-diisopropylchlorophosphoramidite.

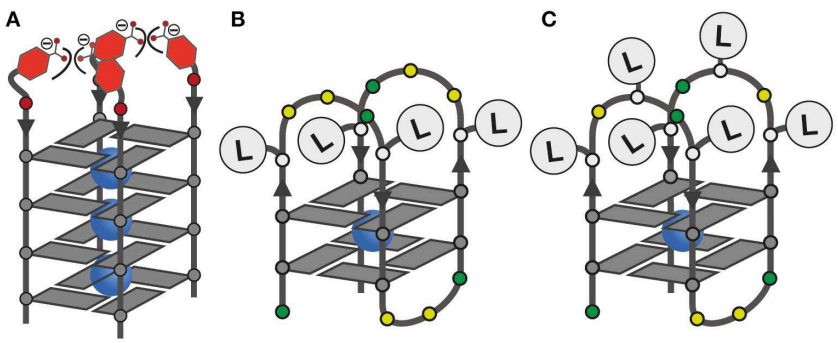

FIGURE 2 | (A) Schematic representation of the tetramolecular G-quadruplex $(\mathbf{L}^{B}G_4)_4$ with the proposed repulsive effect of negatively charged $\mathbf{L}^{B}$; **(B,C)** ligand positions in unimolecular G-quadruplexes with four or six incorporated ligands.

extended coupling times for the ligandosides $\mathbf{L}^{I}$ and $\mathbf{L}^{B}$ (see **Supplementary Material** for details). Coupling efficiencies for $\mathbf{L}^{B}$ and $\mathbf{L}^{I}$ were typically >99% per step. After solid phase synthesis, oligonucleotides were cleaved from the solid support and deprotected in 0.4 M NaOH in methanol/water (4:1) at 55°C for 16 h. Standard deprotection with concentrated ammonium hydroxide was avoided due to the risk of forming amides instead of carboxylates from the benzoate esters. After reversed-phase HPLC purification, oligonucleotides were desalted and DMT-groups removed using C18 *SepPak* cartridges and aq. TFA (2%). The oligonucleotides were then lyophilized at stored at −20°C.

Since $\mathbf{L}^{I}$ had already been established in tetramolecular and unimolecular G-quadruplexes, we first investigated the influence of $\mathbf{L}^{B}$ in the tetramolecular G-quadruplex $(\mathbf{L}^{B}G_4)_4$. Clear formation of a parallel G-quadruplex was observed by CD spectroscopy with a positive Cotton effect around ∼260 nm (see **Figure S25**). Thermal denaturation experiments showed a melting temperature T_m of 27°C which was significantly lower compared to previously reported $(\mathbf{L}^{I}G_4)_4$ (T_m = 36°C; Punt and Clever, 2019b). Since $\mathbf{L}^{B}$ and $\mathbf{L}^{I}$ are sharing the same backbone modification, we ascribe this destabilization to a repulsive effect between the negatively charged benzoates and phosphates (**Figure 2**). Next, the interaction of $(\mathbf{L}^{B}G_4)_4$ with a series of transition metal cations was investigated. In contrast to $(\mathbf{L}^{I}G_4)_4$ which was shown to complex Cu^{II}, Ni^{II}, Co^{II}, and Zn^{II}, no signs for metal complexation in $(\mathbf{L}^{B}G_4)_4$ were observed (see **Figures S3, S4**). This may be explained by the harder character

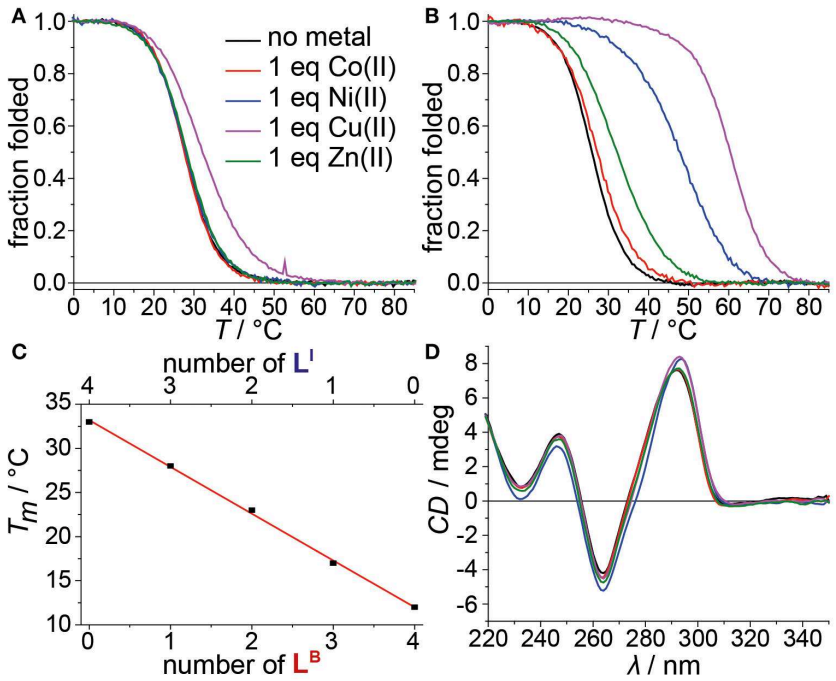

FIGURE 3 | Melting curves of **(A)** htel$\mathbf{L}^{B}\mathbf{L}^{I}{}_3$ and **(B)** htel$\mathbf{L}^{B}{}_2\mathbf{L}^{I}{}_4$ in absence or presence of different transition metal cations. **(C)** Linear dependence of thermal stabilities of htel$\mathbf{L}^{I}{}_4$, htel$\mathbf{L}^{B}\mathbf{L}^{I}{}_3$, htel$\mathbf{L}^{B}{}_2\mathbf{L}^{I}{}_2$, htel$\mathbf{L}^{B}{}_3\mathbf{L}^{I}$, and htel$\mathbf{L}^{B}{}_4$ depending on the number of incorporated $\mathbf{L}^{B}$. **(D)** CD spectra of htel$\mathbf{L}^{B}{}_2\mathbf{L}^{I}{}_4$ in absence or presence of different transition metal cations.

of the benzoate ligand, competing with hard ligands such as the contained chloride, cacodylate buffer or phosphate backbones. However, even for hard and oxophilic transition metal cations, including Gd^{III} and Ce^{III}, no interactions were found.

Mixing ligands in tetramolecular G-quadruplexes leads to statistical mixtures, which makes it challenging to design distinct heteroleptic coordination environments (see **Supplementary Material** for details). On the other hand, the folding of unimolecular G-quadruplexes into discrete topologies enables programmable ligand arrangements. Consequently, we moved forward to incorporate $\mathbf{L}^{B}$ in unimolecular G-quadruplexes. At first, $\mathbf{L}^{B}$ was incorporated four times in htel$\mathbf{L}^{B}{}_4$. Similar to $(\mathbf{L}^{B}G_4)_4$, incorporation of $\mathbf{L}^{B}$ caused strong destabilization (T_m = 12°C) compared to htel$\mathbf{L}^{I}{}_4$ (T_m = 33°C). Successive replacement of $\mathbf{L}^{B}$ with $\mathbf{L}^{I}$ was accompanied with a linear increase in stabilization for each replacement (htel$\mathbf{L}^{B}{}_3\mathbf{L}^{I}$ T_m = 17°C, htel$\mathbf{L}^{B}{}_2\mathbf{L}^{I}{}_2$ T_m = 23°C, htel$\mathbf{L}^{B}\mathbf{L}^{I}{}_3$ T_m = 28°C), highlighting the additive destabilizing effect of $\mathbf{L}^{B}$ (**Figure 3**). CD spectroscopy of htel$\mathbf{L}^{B}{}_4$, htel$\mathbf{L}^{B}{}_3\mathbf{L}^{I}$, htel$\mathbf{L}^{B}{}_2\mathbf{L}^{I}{}_2$, and htel$\mathbf{L}^{B}\mathbf{L}^{I}{}_3$ showed clear signatures corresponding to an antiparallel G-quadruplex topology with a positive Cotton effect around ~294 nm in all cases (see **Figures S26, S27**). This is consistent with the previous observations for homoleptic G-quadruplexes containing only $\mathbf{L}^{I}$. Next, the interaction with different transition metal cations was investigated. As for $(\mathbf{L}^{B}G_4)_4$, for htel$\mathbf{L}^{B}{}_4$, htel$\mathbf{L}^{B}{}_3\mathbf{L}^{I}$, and htel$\mathbf{L}^{B}{}_2\mathbf{L}^{I}{}_2$, thermal denaturation experiments showed no signs for interaction with the examined transition metal cations (Cu^{II}, Ni^{II}, Zn^{II}, Co^{II}, $V^{IV}O$). Pleasingly, this changed for htel$\mathbf{L}^{B}\mathbf{L}^{I}{}_3$ that showed a weak but distinct stabilization after addition of 1 equiv. of Cu^{II} (ΔT_m = + 4°C). Additional equivalents resulted in no further stabilization consistent with a specific binding of Cu^{II}. CD spectroscopy further confirmed retention of a clear antiparallel topology (see **Figures S6, S7, S11–S16**).

After we could show that at least three imidazole ligands are required to complex Cu^{II}, we moved forward to a new series of sequences with six incorporated ligands (htel$\mathbf{L}^{B}{}_4\mathbf{L}^{I}{}_2$, htel$\mathbf{L}^{B}{}_3\mathbf{L}^{I}{}_3$, htel$\mathbf{L}^{B}{}_2\mathbf{L}^{I}{}_4$). Again, the formation of G-quadruplexes with a clear antiparallel topology was observed by CD spectroscopy (see **Figures S28, S29**). Likewise, comparison of the thermal stabilities showed the destabilizing effect of $\mathbf{L}^{B}$ (htel$\mathbf{L}^{B}{}_4\mathbf{L}^{I}{}_2$ T_m = 17°C, htel$\mathbf{L}^{B}{}_3\mathbf{L}^{I}{}_3$ T_m = 26°C, htel$\mathbf{L}^{B}{}_2\mathbf{L}^{I}{}_4$ T_m = 26°C), however, not in the linear fashion as observed for the series htel$\mathbf{L}^{B}{}_{4-n}\mathbf{L}^{I}{}_n$ (n = 0–4). For the examined set of six-ligand-containing sequences, however, direct T_m comparison is not appropriate due to the chosen modification pattern (see **Table 1**). When investigating the interaction with metal cations, for htel$\mathbf{L}^{B}{}_4\mathbf{L}^{I}{}_2$, a clear stabilization after addition of Cu^{II} (ΔT_m = + 6°C) was observed. Considering that for htel$\mathbf{L}^{B}{}_2\mathbf{L}^{I}{}_2$ almost no stabilization was observed (ΔT_m = + 1°C), we conclude that in htel$\mathbf{L}^{B}{}_4\mathbf{L}^{I}{}_2$ an involvement of one or two ligandosides $\mathbf{L}^{B}$ into metal coordination is very likely. When further replacing $\mathbf{L}^{B}$ with $\mathbf{L}^{I}$ as in htel$\mathbf{L}^{B}{}_3\mathbf{L}^{I}{}_3$ and htel$\mathbf{L}^{B}{}_2\mathbf{L}^{I}{}_4$, the Cu^{II}-mediated thermal stabilization successively increased from ΔT_m = + 9°C (htel$\mathbf{L}^{B}{}_3\mathbf{L}^{I}{}_3$) to ΔT_m = + 34°C (htel$\mathbf{L}^{B}{}_2\mathbf{L}^{I}{}_4$). This extremely high thermal stabilization

TABLE 1 | Sequences investigated in this study and respective denaturation temperatures T_m (and ΔT_m) in absence and presence of 1 equiv. of Cu^{II}, Ni^{II}, Zn^{II}, Co^{II} (assumed to be oxidized to Co^{III} under the experimental conditions).

Name	Sequence 5′ 3′	No metal	Co^{II}	Ni^{II}	Cu^{II}	Zn^{II}
$\mathbf{L}^{I}G_n$[a]	$\mathbf{L}^{I}\mathbf{G}_n$	36	63 (+27)	73 (+37)	76 (+40)	52 (+16)
$\mathbf{L}^{B}G_n$	$\mathbf{L}^{B}\mathbf{G}_n$	27	27 (0)	27 (0)	27 (0)	27 (0)
htel$\mathbf{L}^{I}{}_4$A[a]	AGG $\mathbf{L}^{I}$TT A$\mathbf{L}^{I}$G GTT AGG $\mathbf{L}^{I}$TT A$\mathbf{L}^{I}$G G	33	35 (+2)	45 (+12)	56 (+23)	36 (+3)
htel$\mathbf{L}^{B}{}_4$	AGG $\mathbf{L}^{B}$TT A$\mathbf{L}^{B}$G GTT AGG $\mathbf{L}^{B}$TT A$\mathbf{L}^{B}$G G	12	12 (0)	12 (0)	12 (0)	12 (0)
htel$\mathbf{L}^{I}{}_4$B	AGG $\mathbf{L}^{I}$TT T$\mathbf{L}^{I}$G GTT AGG $\mathbf{L}^{I}$TT T$\mathbf{L}^{I}$G G	40	40 (0)	46 (+6)	60 (+20)	40 (0)
htel$\mathbf{L}^{B}{}_3\mathbf{L}^{I}$	AGG $\mathbf{L}^{I}$TT A$\mathbf{L}^{B}$G GTT AGG $\mathbf{L}^{B}$TT A$\mathbf{L}^{B}$G G	17	17 (0)	17 (0)	17 (0)	17 (0)
htel$\mathbf{L}^{B}{}_2\mathbf{L}^{I}{}_2$	AGG $\mathbf{L}^{I}$TT A$\mathbf{L}^{B}$G GTT AGG $\mathbf{L}^{I}$TT A$\mathbf{L}^{B}$G G	23	23 (0)	23 (+0)	24 (+1)	23 (0)
htel$\mathbf{L}^{B}\mathbf{L}^{I}{}_3$	AGG $\mathbf{L}^{I}$TT A$\mathbf{L}^{I}$G GTT AGG $\mathbf{L}^{I}$TT A$\mathbf{L}^{B}$G G	28	28 (0)	28 (+0)	32 (+4)	28 (0)
htel$\mathbf{L}^{I}{}_6$[a]	AGG $\mathbf{L}^{I}$T$\mathbf{L}^{I}$ T$\mathbf{L}^{I}$G GTT AGG $\mathbf{L}^{I}$T$\mathbf{L}^{I}$ T$\mathbf{L}^{I}$G G	36	44 (+8)	59 (+23)	54 (+18)	44 (+8)
htel$\mathbf{L}^{B}{}_4\mathbf{L}^{I}{}_2$	AGG $\mathbf{L}^{B}$T$\mathbf{L}^{I}$ T$\mathbf{L}^{B}$G GTT AGG $\mathbf{L}^{B}$T$\mathbf{L}^{I}$ T$\mathbf{L}^{B}$G G	17	17 (0)	18 (+1)	23 (+6)	18 (+1)
htel$\mathbf{L}^{B}{}_3\mathbf{L}^{I}{}_3$	AGG $\mathbf{L}^{B}$T$\mathbf{L}^{I}$ T$\mathbf{L}^{I}$G GTT AGG $\mathbf{L}^{B}$T$\mathbf{L}^{B}$ T$\mathbf{L}^{I}$G G	26	25 (−1)	26 (+0)	35 (+9)	31 (+5)
htel$\mathbf{L}^{B}{}_2\mathbf{L}^{I}{}_4$	AGG $\mathbf{L}^{I}$T$\mathbf{L}^{B}$ T$\mathbf{L}^{I}$G GTT AGG $\mathbf{L}^{I}$T$\mathbf{L}^{B}$ T$\mathbf{L}^{I}$G G	26	27 (+1)	48 (+22)	60 (+34)	32 (+6)

Marked in bold font are the incorporated ligandosides $\boldsymbol{L^B}$ *and* $\boldsymbol{L^I}$*. Conditions: 4 μM (tetramolecular) or 1.88 μM (unimolecular) ssDNA, 100 mM NaCl (tetramolecular) or KCl (unimolecular), 10 mM lithium cacodylate buffer (LiCaCo) pH 7.2 and, if present, 1 equiv. transition metal cation (with respect to the folded G-quadruplex). [a] Punt and Clever (2019b).*

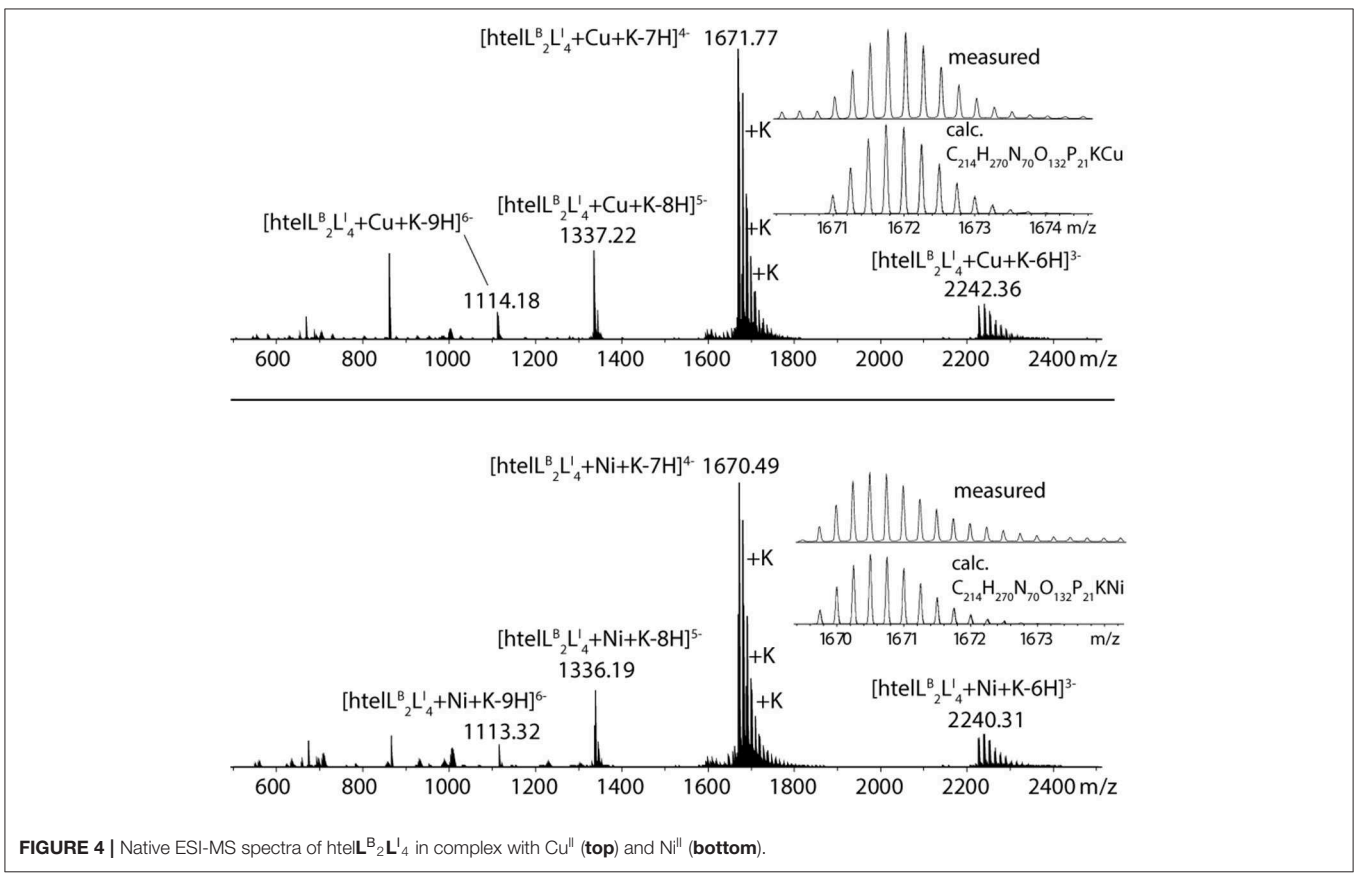

FIGURE 4 | Native ESI-MS spectra of htel$\mathbf{L}^{B}{}_2\mathbf{L}^{I}{}_4$ in complex with Cu^{II} (**top**) and Ni^{II} (**bottom**).

is unprecedented for unimolecular G-quadruplexes and much higher compared to the reported G-quadruplexes htel$\mathbf{L}^{I}{}_6$ ($\Delta T_m = +18°C$) and htel$\mathbf{L}^{I}{}_4$A ($\Delta T_m = +23°C$) (Punt and Clever, 2019b).

The formation of 1:1 complexes for htel$\mathbf{L}^{B}{}_2\mathbf{L}^{I}{}_4$ with Cu^{II} and Ni^{II} was further confirmed by native ESI mass spectrometry. To understand whether a G-quadruplex is folded or unfolded in the gas phase, the intrinsic property of G-quadruplexes is exploited that in their folded state they always bind $n-1$ potassium ions (where n = number of G-tetrads). For a folded G-quadruplex with two G-tetrads, a main signal corresponding to the adduct with one distinct potassium ion would be expected, followed by a statistical distribution of adducts with further unspecifically bound potassium cations. On the other hand, for an unfolded

G-quadruplex, the main signal would correspond to the mass of the DNA strand without potassium ions. The mass spectrum shows a main signal corresponding to [htel$\mathbf{L}^{B}{}_{2}\mathbf{L}^{I}{}_{4}$+Cu+K-7H]$^{4-}$ (**Figure 4**), thus strongly indicating a folded G-quadruplex coordinating to a Cu^{II} or Ni^{II} ion in the gas phase (D'Atri et al., 2015; Lecours et al., 2017).

Jahn-Teller-distorted Cu^{II} usually favors the coordination of four strongly associated ligands in a square planar geometry, with two additional ligands more loosely bound in axial positions (Halcrow, 2012). After proving a 1:1 complex for htel$\mathbf{L}^{B}{}_{2}\mathbf{L}^{I}{}_{4}$ and Cu^{II}, the question was if all six ligands are participating in metal coordination or if only $\mathbf{L}^{I}$ is involved. Therefore, a new sequence htel$\mathbf{L}^{I}{}_{4}$B was synthesized where $\mathbf{L}^{B}$ was replaced with thymidines. Addition of Cu^{II} led to a thermal stabilization of $\Delta T_m = +20°C$, much lower compared to htel$\mathbf{L}^{B}{}_{2}\mathbf{L}^{I}{}_{4}$ ($\Delta T_m = +34°C$). However, when looking at the absolute melting temperature T_m in presence of Cu^{II}, one notices that they are the same for both sequences (htel$\mathbf{L}^{B}{}_{2}\mathbf{L}^{I}{}_{4}$ $T_m = 60°C$, htel$\mathbf{L}^{I}{}_{4}$B $T_m = 60°C$). This could mean that Cu^{II} coordination by htel$\mathbf{L}^{B}{}_{2}\mathbf{L}^{I}{}_{4}$ simply compensates the destabilizing effect of $\mathbf{L}^{B}$ and no benzoate ligand was involved in Cu^{II} coordination. Further studies are required to shed light on this question.

Besides Cu^{II}, the addition of Zn^{II} and Ni^{II} to htel$\mathbf{L}^{B}{}_{2}\mathbf{L}^{I}{}_{4}$ and htel$\mathbf{L}^{B}{}_{3}\mathbf{L}^{I}{}_{3}$ led to thermal stabilizations. These results were highly intriguing for two reasons. Quadruplex htel$\mathbf{L}^{B}{}_{2}\mathbf{L}^{I}{}_{4}$ was significantly more stabilized with Ni^{II} ($\Delta T_m = +22°C$) compared to Zn^{II} ($\Delta T_m = +6°C$). However, in htel$\mathbf{L}^{B}{}_{3}\mathbf{L}^{I}{}_{3}$, the opposite effect was observed, showing a higher stabilization after Zn^{II} addition ($\Delta T_m = +5°C$), while for Ni^{II} no complexation was observed. This adds to the established variation of ligand number and position a third layer to our system to fine-tune metal affinities by the introduction of heteroleptic systems. As last question, we were interested whether Zn^{II} in htel$\mathbf{L}^{B}{}_{3}\mathbf{L}^{I}{}_{3}$ is coordinated by one or more benzoates. Interestingly, other sequences shown to complex Zn^{II} (htel$\mathbf{L}^{I}{}_{4}$A $\Delta T_m = +3°C$, htel$\mathbf{L}^{I}{}_{6}$ $\Delta T_m = +8°C$) always contain at least four counts of $\mathbf{L}^{I}$. Since in htel$\mathbf{L}^{B}{}_{3}\mathbf{L}^{I}{}_{3}$ only three $\mathbf{L}^{I}$ were available, we conclude that an involvement of $\mathbf{L}^{B}$ in coordination to the Zn^{II} cation is likely.

CONCLUSION

A new benzoate-based ligandoside $\mathbf{L}^{B}$ was established in tetramolecular and unimolecular G-quadruplex structures. Homoleptic G-quadruplex $(\mathbf{L}^{B}G_4)_4$ was found to form a clear parallel topology. Its thermal stability indicated a strongly destabilizing effect of $\mathbf{L}^{B}$ compared to $\mathbf{L}^{I}$ which was attributed to an accumulation of negative charges. Also, no interactions between a series of transition metal cations and $(\mathbf{L}^{B}G_4)_4$ were found. Similarly, for the unimolecular G-quadruplex htel$\mathbf{L}^{B}{}_{4}$, a destabilizing effect of $\mathbf{L}^{B}$ and no interactions with transition metal cations were observed. The successive replacement of $\mathbf{L}^{B}$ with $\mathbf{L}^{I}$ in htel$\mathbf{L}^{B}{}_{3}\mathbf{L}^{I}$, htel$\mathbf{L}^{B}{}_{2}\mathbf{L}^{I}{}_{2}$, htel$\mathbf{L}^{B}\mathbf{L}^{I}{}_{3}$, and htel$\mathbf{L}^{I}{}_{4}$ resulted in a linear increase of the thermal stability. In addition, for htel$\mathbf{L}^{B}\mathbf{L}^{I}{}_{3}$, a weak thermal stabilization after addition of 1 equiv. Cu^{II} indicated specific binding.

When moving to systems with six incorporated ligands, a tremendously high thermal stabilization was observed after addition of Cu^{II} to htel$\mathbf{L}^{B}{}_{2}\mathbf{L}^{I}{}_{4}$ ($\Delta T_m = +34°C$). In comparison, for htel$\mathbf{L}^{I}{}_{4}$B, addition of Cu^{II} resulted in a stabilization of only $\Delta T_m = +20°C$. However, the absolute melting temperatures T_m of htel$\mathbf{L}^{B}{}_{2}\mathbf{L}^{I}{}_{4}$ ($T_m = 60°C$) and htel$\mathbf{L}^{I}{}_{4}$B ($T_m = 60°C$) are the same, indicating that Cu^{II} complexation is rather compensating the destabilizing effect of $\mathbf{L}^{B}$. More interesting were the results for htel$\mathbf{L}^{B}{}_{2}\mathbf{L}^{I}{}_{4}$ and htel$\mathbf{L}^{B}{}_{3}\mathbf{L}^{I}{}_{3}$ after addition of Zn^{II} and Ni^{II}, respectively. Htel$\mathbf{L}^{B}{}_{2}\mathbf{L}^{I}{}_{4}$ was significantly more stabilized by Ni^{II} ($\Delta T_m = +22°C$) compared to Zn^{II} ($\Delta T_m = +6°C$). However, in htel$\mathbf{L}^{B}{}_{3}\mathbf{L}^{I}{}_{3}$, the opposite effect was observed, showing a higher stabilization after Zn^{II} addition ($\Delta T_m = +5°C$) while for Ni^{II} no complexation was found. This expands our toolbox to design tailored binding sites for various transition metal cations. Previously, we had shown to fine-tune coordination environments by varying position and number of ligands. Here, we expand this approach by combining two ligandosides, $\mathbf{L}^{B}$ and $\mathbf{L}^{I}$, which we regard as an important step for the design of metal-selective G-quadruplexes with application in diagnostics, selective catalysis, and DNA nanotechnology.

DATA AVAILABILITY STATEMENT

The datasets generated for this study can be found in the Cambridge Crystallographic Data Center under the CCDC identifier 1961648.

AUTHOR CONTRIBUTIONS

PP and LS conducted all syntheses and DNA experiments. SS contributed to the tetramolecular systems. LK and CS contributed the X-ray structure of compound 4. PP, LS, and GC designed the study, conceived the experiments, analyzed the data, and authored the manuscript.

FUNDING

Funded by the Deutsche Forschungsgemeinschaft (DFG, German Research Foundation) under Germany's Excellence Strategy—EXC 2033—Projektnummer 390677874. We thank Markus Hüffner for contributing the elemental analyses and also the European Research Council (ERC Consolidator grant 683083, RAMSES) for support.

ACKNOWLEDGMENTS

Prof. Herbert Waldmann from the MPI Dortmund is thankfully acknowledged for access to the MALDI-TOF spectrometer.

SUPPLEMENTARY MATERIAL

The Supplementary Material for this article can be found online at: https://www.frontiersin.org/articles/10.3389/fchem.2020.00026/full#supplementary-material

REFERENCES

Abdelhamid, M. A., Fábián, L., MacDonald, C. J., Cheesman, M. R., Gates, A. J., and Waller, Z. A. (2018). Redox-dependent control of i-Motif DNA structure using copper cations. *Nucleic Acids Res.* 46, 5886–5893. doi: 10.1093/nar/gky390

Ali, A., Bullen, G. A., Cross, B., Dafforn, T. R., Little, H. A., Manchester, J., et al. (2019). Light-controlled thrombin catalysis and clot formation using a photoswitchable G-quadruplex DNA aptamer. *Chem. Commun.* 55, 5627–5630. doi: 10.1039/C9CC01540J

Anderson, J. S., Rittle, J., and Peters, J. C. (2013). Catalytic conversion of nitrogen to ammonia by an iron model complex. *Nature* 501, 84–87. doi: 10.1038/nature12435

Baskin, M., and Maayan, G. (2016). A rationally designed metal-binding helical peptoid for selective recognition processes. *Chem. Sci.* 7, 2809–2820. doi: 10.1039/C5SC04358A

Baskin, M., Zhu, H., Qu, Z.-W., Chill, J. H., Grimme, S., and Maayan, G. (2018). Folding of unstructured peptoids and formation of hetero-bimetallic peptoid complexes upon side-chain-to-metal coordination. *Chem. Sci.* 10, 620–632. doi: 10.1039/C8SC03616K

Boersma, A. J., Coquière, D., Geerdink, D., Rosati, F., Feringa, B. L., and Roelfes, G. (2010a). Catalytic enantioselective syn hydration of enones in water using a DNA-based catalyst. *Nat. Chem.* 2, 991–995. doi: 10.1038/nchem.819

Boersma, A. J., Megens, R. P., Feringa, B. L., and Roelfes, G. (2010b). DNA -based asymmetric catalysis. *Chem. Soc. Rev.* 39, 2083–2092. doi: 10.1039/b811349c

Clever, G. H., Kaul, C., and Carell, T. (2007). DNA–metal base pairs. *Angew. Chem. Int. Ed.* 46, 6226–6236. doi: 10.1002/anie.200701185

Colquhoun, H. M., Stoddart, F. J., and Williams, D. J. (1986). Second-sphere coordination – a novel role for molecular receptors. *Angew. Chem. Int. Ed.* 25, 487–507. doi: 10.1002/anie.198604873

Coquière, D., Feringa, B. L., and Roelfes, G. (2007). DNA-based catalytic enantioselective michael reactions in water. *Angew. Chem. Int. Ed.* 46, 9308–9311. doi: 10.1002/anie.200703459

Cornish, A. J., Ginovska, B., Thelen, A., da Silva, J. C., Soares, T. A., Raugei, S., et al. (2016). Single-amino acid modifications reveal additional controls on the proton pathway of [FeFe]-hydrogenase. *Biochemistry* 55, 3165–3173. doi: 10.1021/acs.biochem.5b01044

D'Atri, V., Porrini, M., Rosu, F., and Gabelica, V. (2015). Linking molecular models with ion mobility experiments. Illustration with a rigid nucleic acid structure. *J. Mass. Spectrom.* 50, 711–726. doi: 10.1002/jms.3590

Degtyarenko, K. (2000). Bioinorganic motifs: towards functional classification of metalloproteins. *Bioinformatics* 16, 851–864. doi: 10.1093/bioinformatics/16.10.851

Dicke, B., Hoffmann, A., Stanek, J., Rampp, M., Grimm-Lebsanft, B., Biebl, F., et al. (2018). Transferring the entatic-state principle to copper photochemistry. *Nat. Chem.* 10, 355–362. doi: 10.1038/nchem.2916

Drienovská, I., Alonso-Cotchico, L., Vidossich, P., Lledós, A., Maréchal, J.-D., and Roelfes, G. (2017). Design of an enantioselective artificial metallo-hydratase enzyme containing an unnatural metal-binding amino acid. *Chem. Sci.* 8, 7228–7235. doi: 10.1039/C7SC03477F

Drienovská, I., Mayer, C., Dulson, C., and Roelfes, G. (2018). A designer enzyme for hydrazone and oxime formation featuring an unnatural catalytic aniline residue. *Nat. Chem.* 10, 946–952. doi: 10.1038/s41557-018-0082-z

Engelhard, D. M., Meyer, A., Berndhäuser, A., Schiemann, O., and Clever, G. H. (2018a). Di-copper(ii) DNA G-quadruplexes as EPR distance rulers. *Chem. Commun.* 54, 7455–7458. doi: 10.1039/C8CC04053B

Engelhard, D. M., Nowack, J., and Clever, G. H. (2017). Copper-induced topology switching and thrombin inhibition with telomeric DNA G-quadruplexes. *Angew. Chem. Int. Ed.* 56, 11640–11644. doi: 10.1002/anie.201705724

Engelhard, D. M., Pievo, R., and Clever, G. H. (2013). Reversible stabilization of transition-metal-binding DNA G-quadruplexes. *Angew. Chem. Int. Ed.* 52, 12843–12847. doi: 10.1002/anie.201307594

Engelhard, D. M., Stratmann, L. M., and Clever, G. H. (2018b). Structure–property relationships in CuII-binding tetramolecular G-quadruplex DNA. *Chem. Eur. J.* 24, 2117–2125. doi: 10.1002/chem.201703409

Ghosh, T., Ghosh, P., and Maayan, G. (2018). A copper-peptoid as a highly stable, efficient, and reusable homogeneous water oxidation electrocatalyst. *ACS Catal.* 8, 10631–10640. doi: 10.1021/acscatal.8b03661

Greenblatt, H. M., Feinberg, H., Tucker, P. A., and Shoham, G. (1998). Carboxypeptidase a: native, zinc-removed and mercury-replaced forms. *Acta Cryst.* D54, 289–305. doi: 10.1107/S0907444997010445

Halcrow, M. A. (2012). Jahn–Teller distortions in transition metal compounds, and their importance in functional molecular and inorganic materials. *Chem. Soc. Rev.* 42, 1784–1795. doi: 10.1039/C2CS35253B

Hänsel-Hertsch, R., Antonio, M., and Balasubramanian, S. (2017). DNA G-quadruplexes in the human genome: detection, functions and therapeutic potential. *Nat. Rev. Mol. Cell. Bio.* 18, 279–284. doi: 10.1038/nrm.2017.3

Holm, R. H., Kennepohl, P., and Solomon, E. I. (1996). Structural and functional aspects of metal sites in biology. *Chem. Rev.* 96, 2239–2314. doi: 10.1021/cr9500390

Jeschek, M., Reuter, R., Heinisch, T., Trindler, C., Klehr, J., Panke, S., et al. (2016). Directed evolution of artificial metalloenzymes for *in vivo* metathesis. *Nature* 537, 661–665. doi: 10.1038/nature19114

Kanady, J. S., Tsui, E. Y., Day, M. W., and Agapie, T. (2011). A synthetic model of the Mn3Ca subsite of the oxygen-evolving complex in photosystem II. *Science* 333, 733–736. doi: 10.1126/science.1206036

Katz, S. (1963). The reversible reaction of Hg (II) and double-stranded polynucleotides a step-function theory and its significance. *Biochim. Biophys. Acta* 68, 240–253. doi: 10.1016/0926-6550(63)90435-3

Key, H. M., Dydio, P., Clark, D. S., and Hartwig, J. F. (2016). Abiological catalysis by artificial haem proteins containing noble metals in place of iron. *Nature* 534, 534–537. doi: 10.1038/nature17968

Knight, A. S., Kulkarni, R. U., Zhou, E. Y., Franke, J. M., Miller, E. W., and Francis, M. B. (2017). A modular platform to develop peptoid-based selective fluorescent metal sensors. *Chem. Commun.* 53, 3477–3480. doi: 10.1039/C7CC00931C

Koehntop, K. D., Emerson, J. P., and Que, L. (2005). The 2-His-1-carboxylate facial triad: a versatile platform for dioxygen activation by mononuclear non-heme iron(II) enzymes. *J. Biol. Inorg. Chem.* 10, 87–93. doi: 10.1007/s00775-005-0624-x

Lecours, M. J., Marchand, A., Anwar, A., Guetta, C., Hopkins, S. W., and Gabelica, V. (2017). What stoichiometries determined by mass spectrometry reveal about the ligand binding mode to G-quadruplex nucleic acids. *Biochim. Biophys. Acta* 1861, 1353–1361. doi: 10.1016/j.bbagen.2017.01.010

Litman, Z. C., Wang, Y., Zhao, H., and Hartwig, J. F. (2018). Cooperative asymmetric reactions combining photocatalysis and enzymatic catalysis. *Nature* 560, 355–359. doi: 10.1038/s41586-018-0413-7

Lu, Y., Yeung, N., Sieracki, N., and Marshall, N. M. (2009). Design of functional metalloproteins. *Nature* 460, 855–862. doi: 10.1038/nature08304

Mandal, S., Hebenbrock, M., and Müller, J. (2016). A dinuclear mercury(II)-mediated base pair in DNA. *Angew. Chem. Int. Ed.* 55, 15520–15523. doi: 10.1002/anie.201608354

Mandal, S., and Müller, J. (2017). Metal-mediated DNA assembly with ligand-based nucleosides. *Curr. Opin. Chem. Biol.* 37, 71–79. doi: 10.1016/j.cbpa.2017.01.019

Mayer, C., Dulson, C., Reddem, E., Thunnissen, A. W., and Roelfes, G. (2019). Directed evolution of a designer enzyme featuring an unnatural catalytic amino acid. *Angew. Chem. Int. Ed.* 58, 2083–2087. doi: 10.1002/anie.201813499

Miyoshi, D., Karimata, H., Wang, Z.-M., Koumoto, K., and Sugimoto, N. (2007). Artificial G-wire switch with 2,2′-bipyridine units responsive to divalent metal ions. *J. Am. Chem. Soc.* 129, 5919–5925. doi: 10.1021/ja068707u

Neidle, S. (2017). Quadruplex nucleic acids as targets for anticancer therapeutics. *Nat. Rev. Chem.* 1:0041. doi: 10.1038/s41570-017-0041

Punt, P. M., and Clever, G. H. (2019a). Imidazole-modified G-quadruplex DNA as metal-triggered peroxidase. *Chem. Sci.* 10, 2513–2518. doi: 10.1039/C8SC05020A

Punt, P. M., and Clever, G. H. (2019b). Tailored transition-metal coordination environments in imidazole-modified DNA G-quadruplexes. *Chem. Eur. J.* 25, 13987–13993. doi: 10.1002/chem.201903445

Raven, J. A., Evans, M. C., and Korb, R. E. (1999). The role of trace metals in photosynthetic electron transport in O_2-evolving organisms. *Photosynth. Res.* 60, 111–150. doi: 10.1023/A:1006282714942

Rioz-Martínez, A., Oelerich, J., Ségaud, N., and Roelfes, G. (2016). DNA-accelerated catalysis of carbene-transfer reactions by a DNA/cationic iron porphyrin hybrid. *Angew. Chem. Int. Ed.* 55, 14136–14140. doi: 10.1002/anie.201608121

Roelfes, G., and Feringa, B. L. (2005). DNA-based asymmetric catalysis. *Angew. Chem. Int. Ed.* 44, 3230–3232. doi: 10.1002/anie.200500298

Rubino, J. T., and Franz, K. J. (2012). Coordination chemistry of copper proteins: how nature handles a toxic cargo for essential function. *J. Inorg. Biochem.* 107, 129–143. doi: 10.1016/j.jinorgbio.2011.11.024

Samuel, A. P., Co, D. T., Stern, C. L., and Wasielewski, M. R. (2010). Ultrafast photodriven intramolecular electron transfer from a zinc porphyrin to a readily reduced diiron hydrogenase model complex. *J. Am. Chem. Soc.* 132, 8813–8815. doi: 10.1021/ja100016v

Sandmann, N., Bachmann, J., Hepp, A., Doltsinis, N. L., and Müller, J. (2019). Copper(ii)-mediated base pairing involving the artificial nucleobase 3 H -imidazo[4,5- f]quinolin-5-ol. *Dalton Trans.* 48, 10505–10515. doi: 10.1039/C9DT02043H

Shook, R. L., and Borovik, A. (2010). Role of the secondary coordination sphere in metal-mediated dioxygen activation. *Inorg. Chem.* 49, 3646–3660. doi: 10.1021/ic901550k

Smith, N. M., Amrane, S., Rosu, F., Gabelica, V., and Mergny, J.-L. (2012). Mercury–thymine interaction with a chair type G-quadruplex architecture. *Chem. Commun.* 48, 11464–11466. doi: 10.1039/c2cc36481f

Tanaka, K., Clever, G. H., Takezawa, Y., Yamada, Y., Kaul, C., Shionoya, M., et al. (2006). Programmable self-assembly of metal ions inside artificial DNA duplexes. *Nat. Nanotechnol.* 1, 190–194. doi: 10.1038/nnano.2006.141

Tanaka, K., Yamada, Y., and Shionoya, M. (2002). Formation of silver(I)-mediated DNA duplex and triplex through an alternative base pair of pyridine nucleobases. *J. Am. Chem. Soc.* 124, 8802–8803. doi: 10.1021/ja020510o

Valdez, C. E., Smith, Q. A., Nechay, M. R., and Alexandrova, A. N. (2014). Mysteries of metals in metalloenzymes. *Acc. Chem. Res.* 47, 3110–3117. doi: 10.1021/ar500227u

Waldron, K. J., Rutherford, J. C., Ford, D., and Robinson, N. J. (2009). Metalloproteins and metal sensing. *Nature* 460, 823–830. doi: 10.1038/nature08300

Wang, J., Yue, L., Li, Z., Zhang, J., Tian, H., and Willner, I. (2019). Active generation of nanoholes in DNA origami scaffolds for programmed catalysis in nanocavities. *Nat. Commun.* 10:4963. doi: 10.1038/s41467-019-12933-9

Wu, S., Zhou, Y., Rebelein, J. G., Kuhn, M., Mallin, H., Zhao, J., et al. (2019). Breaking symmetry: engineering single-chain dimeric streptavidin as host for artificial metalloenzymes. *J. Am. Chem. Soc.* 141, 15869–15878. doi: 10.1021/jacs.9b06923

Xu, Y., Suzuki, Y., Lönnberg, T., and Komiyama, M. (2009). Human telomeric DNA sequence-specific cleaving by G-quadruplex formation. *J. Am. Chem. Soc.* 131, 2871–2874. doi: 10.1021/ja807313x

Zhang, L., Peritz, A., and Meggers, E. (2005). A simple glycol nucleic acid. *J. Am. Chem. Soc.* 127, 4174–4175. doi: 10.1021/ja042564z

Zhang, L., Peritz, A. E., Carroll, P. J., and Meggers, E. (2006). Synthesis of glycol nucleic acids. *Synthesis* 2006, 645–653. doi: 10.1055/s-2006-926313

Zhao, M., Wang, H.-B., Ji, L.-N., and Mao, Z.-W. (2013). Insights into metalloenzyme microenvironments: biomimetic metal complexes with a functional second coordination sphere. *Chem. Soc. Rev.* 42, 8360–8375. doi: 10.1039/c3cs60162e

Conflict of Interest: The authors declare that the research was conducted in the absence of any commercial or financial relationships that could be construed as a potential conflict of interest.

frontiers in Chemistry

ORIGINAL RESEARCH
published: 31 January 2020
doi: 10.3389/fchem.2020.00041

Deep Eutectic Solvents as Media for the Prebiotic DNA-Templated Synthesis of Peptides

*Samuel Núñez-Pertíñez and Thomas R. Wilks**

School of Chemistry, University of Birmingham, Birmingham, United Kingdom

Translation of genetic information into peptide products is one of the fundamental processes of biology. How this occurred prebiotically, in the absence of enzyme catalysts, is an intriguing question. Nucleic acid-templated synthesis (NATS) promotes reactions by bringing building blocks tethered to complementary DNA strands into close proximity and has been shown to enable peptide synthesis without enzymes—it could therefore serve as a model for prebiotic translation of information stored in nucleic acid sequences into functional peptides. The decomposition of highly reactive DNA adapters has so far limited the effectiveness of NATS, but these studies have been performed exclusively in aqueous solution. Deep eutectic solvents (DESs) have been proposed as a feasible solvent for prebiotic replication of nucleic acids, and here are studied as media for prebiotic translation using NATS as a model. DESs are shown to enhance the stability of DNA-conjugated activated esters, the precursors of peptides. However, this enhanced stability was coupled with decreased amine reactivity that hampered the formation of peptide bonds in DESs. These properties are exploited to demonstrate the storage of DNA-conjugated activated esters in a DES followed by transfer into aqueous buffer to activate the NATS of peptides "on demand." These findings, together with the reported functions of DESs in prebiotic processes, shed light on how DESs could have facilitated the non-enzymatic translation of genetic information into functional peptides on the early Earth.

Keywords: prebiotic, translation, deep eutectic solvent, templated synthesis, nucleic acids

OPEN ACCESS

Edited by:
Janarthanan Jayawickramarajah, Tulane University, United States

Reviewed by:
Sriram Kanvah, Indian Institute of Technology Gandhinagar, India
Harekrushna Sahoo, National Institute of Technology Rourkela, India

****Correspondence:***
Thomas R. Wilks
t.r.wilks@bham.ac.uk

Specialty section:
This article was submitted to Supramolecular Chemistry, a section of the journal Frontiers in Chemistry

Received: *08 November 2019*
Accepted: *14 January 2020*
Published: *31 January 2020*

Citation:
Núñez-Pertíñez S and Wilks TR (2020) Deep Eutectic Solvents as Media for the Prebiotic DNA-Templated Synthesis of Peptides. Front. Chem. 8:41. doi: 10.3389/fchem.2020.00041

INTRODUCTION

Living organisms preserve the information required to synthesize their molecular components in nucleic acid sequences (Crick, 1970). The replication of this genetic material, and its translation into active catalytic proteins is regulated and catalyzed by highly complex molecular machines. Perhaps the most impressive example is the biosynthesis of peptides and proteins by the ribosome (Steitz, 2008; Yonath, 2009). A key question is how these processes were performed prebiotically, in the absence of such complex machinery. Based on the fact that the core of the ribosome is made from RNA, it has been proposed that replication and translation were first performed by simple nucleic acids, giving rise to the "RNA world" (Crick, 1968; Orgel, 1968; Kruger et al., 1982; Guerrier-Takada et al., 1983; Gilbert, 1986) and "RNA/peptide world" hypotheses (Yarus, 2001; Turk et al., 2010). Several nucleic acid systems that display enzyme-free self-replication have been described (Ekland and Bartel, 1996; Johnston et al., 2001; Paul and Joyce, 2002; Li et al., 2017; Hänle and Richert, 2018; Liu et al., 2018; Mariani et al., 2018; Zhang et al., 2019), and there have been a handful of

mechanisms proposed for prebiotic translation (Zhang and Cech, 1997; Tamura and Schimmel, 2001, 2004). However, these studies have highlighted a number of obstacles to achieving efficient replication and translation in the absence of enzymes: (1) the hydrolysis of the highly reactive, activated monomers required for both processes is rapid in aqueous solution (Kanavarioti et al., 1989); (2) hydrolysed monomers can inhibit replication and induce errors in translation (Deck et al., 2011); (3) after replication, long strands will hybridize to form stable duplexes, blocking further replication by template inhibition (Szostak, 2012).

Most studies in this area have assumed that the solvent for these prebiotic processes was aqueous, but deep eutectic solvents (DESs) have recently emerged as an alternative (He et al., 2017). DESs are a family of solvents, closely related to ionic liquids, composed of a hydrogen bond donor and a salt that form a eutectic mixture at a specific molar ratio (Abbott et al., 2003). Most DESs have high viscosity, low vapor pressure and a very high concentration of ionic species (Zhang et al., 2012; Smith et al., 2014), and their basic components, such as glycerol or urea, are likely to have been present on the early Earth (Kaiser et al., 2015; Okamura et al., 2019). DESs composed of quaternary ammonium salts and hydrogen bond donors (e.g., reline, a mixture of urea and choline chloride) have been shown to be compatible with protein and nucleic acid biomolecules (Wagle et al., 2014; Xu et al., 2017; Pätzold et al., 2019). For example, it was demonstrated that DNA was stable and retained its structural integrity for at least 6 months when stored in a DES (Mondal et al., 2013), that tertiary structures such as A- and B-DNA duplexes, and G-quadruplexes, were maintained (Mamajanov et al., 2010; Lannan et al., 2012; Zhao et al., 2013; Gállego et al., 2015), and that enzymatic peptide synthesis could be performed efficiently (Maugeri et al., 2013). DESs have also been shown to be favorable media for nucleic acid replication. For example, DESs promote the formation of activated organophosphates from mineral phosphate, which is a necessary step in the formation of the activated monomers required for replication (Gull et al., 2014, 2017; Burcar et al., 2016). The high viscosities of DESs also enable more efficient non-enzymatic replication: the faster diffusion of monomers compared to long oligonucleotides in these solvents has been shown to help overcome the template inhibition problem (He et al., 2017). High viscosity also favors intramolecular folding over intermolecular interactions, enabling, for example, the recovery of ribozyme activity following a replication process (He et al., 2019).

Based on this previous work around replication, we asked whether DESs could also be suitable media for non-enzymatic translation and chose nucleic acid-templated synthesis (NATS) of a dipeptide as a simple model for this process. NATS promotes reactions by using hybridization to bring reactants tethered to complementary oligonucleotides into close proximity, and has been extensively used in the literature for the programmed production of oligopeptides (Li and Liu, 2004; O'Reilly et al., 2017). Importantly, this previous work has been limited by hydrolysis of the activated building blocks required (Meng et al., 2016). Here, we investigate the NATS of peptides in an archetypal DES, glycholine (a mixture of glycerol and choline chloride). We find that glycholine protects DNA-conjugated activated esters, the necessary precursors of oligopeptide products, from solvolysis. By comparing the NATS of peptides in DESs and aqueous buffered solution we also uncover the inhibitory effect of glycholine on amide bond formation. We exploit these properties to demonstrate the extended storage of otherwise unstable peptide building blocks in glycholine, followed by shuttling into aqueous solution to activate NATS "on demand." Combined with recent theories about the role of compartmentalisation in prebiotic self-replicating systems (Mann, 2012), these experiments hint at a possible role for DESs in enabling non-enzymatic construction of oligopeptides on the early Earth.

MATERIALS AND METHODS

Nuclear magnetic resonance (NMR): One-dimensional ^{1}H and ^{13}C NMR, and two-dimensional NMR spectra were recorded on a Bruker Advance 300 MHz, Bruker Advance III 400 MHz or a Bruker Advance III 500 MHz instrument at 25°C. Deuterated solvents chloroform-*d* (99.8 D atom%), methanol-d_4 (99.8 D atom%), dimethyl sulfoxide-d_6 (DMSO-d_6, 99.8 D atom%) acetone-d_6 (99.9 D atom%) were purchased from Sigma Aldrich. The residual non-deuterated solvent peak was used as a chemical shift (δ, ppm) internal standard. The data were processed using Mestrenova (Mestrelab research) v.12.0.2 and ADC/NMR software. *High resolution mass spectrometry (HRMS):* HRMS was performed on a Bruker Q-ToF Maxis Plus spectrometer or on a Waters Xevo GS2-XS qToF system. A relative error under 5 ppm was ensured. *Reversed-phase high performance liquid chromatography (RP-HPLC):* RP-HPLC was performed in a Varian 920LC system with a photodiode array UV detector (PDA), and a fluorescence detector. *Liquid chromatography-Mass spectrometry (LC-MS):* LC-MS was performed on an Agilent 1200 HPLC system coupled to a Bruker AmazonX high resolution ion trap, in negative ion mode. The desalted oligonucleotide samples were eluted though a XBridge oligonucleotide BEH C18 column (130 Å, 2.5 μm, 4.6 × 50 mm) using a 5 vol% MeOH, 10 mM ammonium acetate (buffer A) and a 70 vol% MeOH, 10 mM ammonium acetate (buffer B) solvent system. The data were processed using Compass Data Analysis (Bruker) v.4.1 software, and the MaxEnt integrated deconvolution algorithm. Alternatively, LC-MS was performed on a Waters ACQUITY UPLC system coupled to a Xevo GS2-XS qToF mass spectrometer in negative sensitivity mode with leucine-enkephalin $[M–H]^-$ 554.2620 Lockspray. The oligonucleotides were eluted through an AQUITY UPLC oligonucleotide BEH C18 column (130 Å, 1.7 μm, 2.1 × 50 mm) using a 50 mM triethylammonium acetate (TEAA, pH 7.0) solution in H_2O (buffer A) and a 50 mM TEAA solution in MeCN (buffer B) at 60°C and a 0.2 mL·min^{-1} flow. *Fluorescence spectroscopy:* Fluorescence spectral data were recorded on an Agilent Cary Eclipse fluorescence spectrophotometer equipped with a photomultiplier tube (PMT) detector. Quartz cuvettes from Starna scientific (Type 3/Q/10) with four polished sides were used for fluorescence. The emission

and excitation spectra were recorded using Cary Eclipse v.1.2.0.0 software. *Karl Fischer titration:* The water content in DESs was determined using an automated CA-200 (Mitsubishi chemicals) Karl Fischer coulometric titrator. Aqualine (Fisher) auxiliary reagent mixture and Aquamicron solution P (Aquamicron, 3.8–4.0 mg $H_2O{\cdot}mL^{-1}$) calibration standards were used. *pH measurements:* An Accumet AP110 pH meter kit (Fisher) equipped with a pH sensitive glass electrode was used to determine the pH in aqueous solution. Prior to sample analysis, the instrument was calibrated with pH 4, pH 7, and pH 10 standard solution buffers.

DNA Sequences and Modifications

Sequences were optimized, and the expected assemblies predicted with NUPACK (Zadeh et al., 2009). Modified DNA strands were purchased from Integrated DNA Technologies and further modified as described below. Sequence data and modification structures are given in **Table S1** and **Scheme S1**.

Synthesis of DESs

DESs were prepared by mixing appropriate amounts of hydrogen bond donor and choline chloride in a Schlenk round bottom flask under positive nitrogen pressure, heating to 100°C and stirring until a homogeneous mixture was obtained. DESs were dried at 80°C under vacuum prior to use (Abbott et al., 2004). The H_2O content of glycholine was determined by Karl Fischer titration. H_2O content was then adjusted to the desired value. For simplicity, we refer to the volume percentage content of H_2O in the DES using a subscript number e.g., glycholine containing 7 vol% H_2O is written as $Gly_{0.07}$.

Measurement of DES Solution pH

DES (1 mL) was diluted in H_2O (4 mL) and the pH was determined using a pH-sensitive glass electrode. The error was evaluated in two different series of samples, by performing triplicate measurements and determining the standard deviation.

^{1}H-NMR Spectroscopy Study of The Stability of Small Molecule Activated Esters

Solutions of **1** (5 mM) in different solvent mixtures were stirred at 24 °C. After 2, 4, 6 and 24 h the solutions were extracted with 0.7 mL of either acetone-d_6 (DES solutions) or chloroform-*d* (phosphate buffer solutions). The relative proportions of **1** and **3** were determined by ^{1}H-NMR spectroscopy (**Figure S1**).

RP-HPLC Stability Study of Activated Esters

Activated ester **1** (4.1 mg) was dissolved in DES (2 mL). Each solution was prepared 40 min after the previous one. The solutions were stirred over a period of 29 h. After stirring for 5, 24, and 29 h, a 100 μL aliquot of each sample was diluted in H_2O (900 μL) and the sample analyzed by RP-HPLC. Method: column Discovery C18 (Sigma Aldrich, 5 μm, 10 × 4.6 cm), flow 1 $mL{\cdot}min^{-1}$, temperature 40°C and injection volume 10 μL. Solvent A: H_2O, 0.05 vol% TFA. Solvent B: 70 vol% MeCN, 0.05 vol% TFA.

Thermal Stability of dsDNA in DESs

The thermal stability of dsDNA in DES solutions was determined using fluorophore and quencher labeled DNA strands (**S15** and **S16**). Solutions of 100 nM dsDNA were briefly centrifuged and placed in a qPCR instrument. Samples were heated and cooled at $1°C{\cdot}min^{-1}$. The melting temperature (T_m) was determined as the middle-point of the sigmoidal trace defined by the fluorescence emission intensity as a function of temperature.

Synthesis of NHS-Activated Fluorescein, S18 (Gao et al., 2002)

Fluorescein free carboxylic acid (**S17**, 3.322 g, 10 mmol) and *N*-hydroxysuccinimide (1.151 g, 10 mmol) were dissolved in dry DMF (19 mL) under positive nitrogen pressure in a dry Schlenk tube (**Scheme 1**). Then, *N,N′*-dicyclohexylcarbodiimide (DCC, 2.063 g, 10 mmol) was added and the resulting solution stirred at 60°C for 2 h under positive nitrogen pressure. *N,N′*-dicyclohexylurea (DCU) was removed by cooling down the reaction mixture to −20°C for 2 h and the white precipitate was filtered off. The solvent was removed under reduced pressure and the crude solid was purified by SiO_2 column chromatography using an EtOAc/acetone gradient. The desired fractions were combined to produce **S18** as a bright orange solid (2.002 g, 47%). The ^{1}H-NMR spectroscopic analysis was in good agreement with the reported characterization (Gao et al., 2002). **TLC** (EtOAc:MeOH 6:4) $R_f = 0.1$. **^{1}H-NMR** (300 MHz, DMSO-d_6) δ (ppm): 8.36 (1H, d $J = 7.7$ Hz, Ar-*H*), 7.96 (2H, m, Ar-*H*), 7.65 (1H, d $J = 7.5$ Hz, Ar-*H*), 6.79 (2H, d $J = 9.6$ Hz, Ar-*H*), 6.53 (4H,

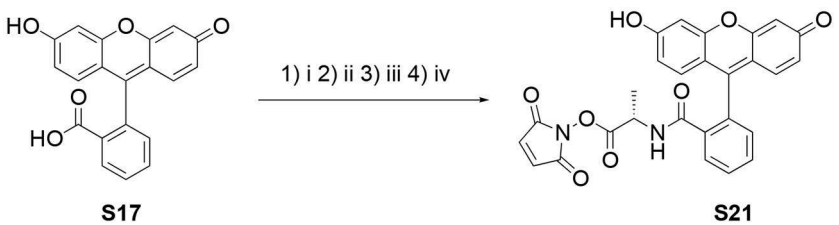

SCHEME 1 | Synthesis of the *N*-hydroxymaleimide ester **S21**. (i) SuOH, DCC, DMF, 60°C, 2 h; (ii) TsOH·H-Ala-OBn, Et_3N, DCM, r.t. 3 h; (iii) Pd/C (10 wt%), H_2, MeOH, r.t., 1.5 h; (iv) *N*-hydroxymaleimide, DCC, EtOAc:1,4-dioxane (2:1), r.t., o.n.

m, Ar-*H*), 2.73 (4H, s^{br}, (CH_2)$_2$ succinimide). **HRMS** (ESI–) *m/z* [M–H]$^-$ calcd. 428.0770 found 428.0763.

Synthesis of S19

S18 (1.000 g, 2.23 mmol) and TsOH·H-*L*-Ala-OBn (1.637 g) were dissolved in dry DMF (15 mL) under positive nitrogen pressure in a dry round bottom Schlenk flask. Then, Et_3N (1.1 mL, 8.16 mmol) was added drop wise over 10 min and the resulting solution was stirred at room temperature for 6 h. The solvent was removed under reduced pressure and the crude product was purified by SiO_2 column chromatography using a DCM/MeOH (100:0 to 75:15) gradient to produce **S19** as a bright orange solid (704 mg, 61%). **TLC** (EtOAc:MeOH 6:4) R_f = 0.6. **^{1}H-NMR** (400 MHz, methanol-d_4) δ (ppm): 7.76 (1H, m, Ar-*H*), 7.55 (1H, m, Ar-*H*), 7.41 (1H, m, Ar-*H*), 7.21 (2H, m, Ar-*H*), 7.11 (4H, m, Ar-*H*), 6.88 (1H, m, Ar-*H*), 6.56 (1H, m, Ar-*H*), 6.51 (1H, m, Ar-*H*), 6.45 (1H, m, Ar-*H*), 6.20 (1H, d J = 8.7 Hz, Ar-*H*), 5.97 (1H, dd J_1 = 8.7 Hz J_2 = 2.5 Hz, Ar-*H*), 4.80 (2H, m, OCH_2), 3.59 (1H, q J = 7.2 C*H*-CH_3), 1.02 (3H, d J = 7.2 Hz, CH-CH_3). **^{13}C-NMR** (100 MHz, methanol-d_4) δ (ppm): 171.75 (*C*=O), 168.79 (*C*=O), 160.29 (*C*=O), 160.13 (Ar*C*), 154.54 (Ar*C*), 154.36 (Ar*C*), 154.24 (Ar*C*), 136.95 (Ar*C*), 134.40 (Ar*C*-H), 132.13 (Ar*C*-H), 130.71 (Ar*C*-H), 130.60 (Ar*C*-H), 129.89 (Ar*C*-H), 129.53 (Ar*C*), 129.37 (Ar*C*-H), 129.35 (Ar*C*-H), 129.15 (Ar*C*), 129.09 (Ar*C*), 125.13 (Ar*C*-H), 123.55 (Ar*C*-H), 113.26 (Ar*C*-H), 112.95 (Ar*C*-H), 110.26 (Ar*C*), 109.24 (Ar*C*), 103.59 (Ar*C*-H), 103.08 (Ar*C*-H), 68.08 (OCH_2), 51.55 (N*C*H), 15.44 CH_3). **HRMS** (ESI–) *m/z* [M–H]$^-$ calcd. 492.1447 found 492.1457.

Synthesis of S20

Pd/charcoal (50 mg, 10 wt%) was placed in a dry round bottom Schlenk flask under positive nitrogen pressure. **S19** (500 mg, 1.01 mmol) was added and dissolved in degassed MeOH (50 mL). The nitrogen atmosphere was replaced with hydrogen by bubbling the solution for 3 min with a hydrogen balloon. The positive hydrogen pressure was maintained for 1.5 h with constant stirring at room temperature. The solid-supported catalyst was removed by filtration through celite. The solvent was removed under reduced pressure to produce **S20** as a bright yellow solid (375 mg, 92%). **TLC** (DCM:MeOH 9:1) R_f = 0.2. **^{1}H-NMR** (500 MHz, methanol-d_4) δ (ppm): 7.05 (1H, m, Ar-*H*), 6.61 (3H, m, Ar-*H*), 6.48 (2H, m, Ar-*H*), 6.41 (1H, dd J_1 = 8.7 Hz J_2 = 2.4 Hz, Ar-*H*), 3.67 (1H, q J = 7.2 Hz, C*H*CH_3), 1.20 (3H, d J = 7.2 Hz CHCH_3). **^{13}C-NMR** (160 MHz, methanol-d_4) δ (ppm): 173.6 (*C*=O), 169.1 (*C*=O), 160.6 (*C*=O), 160.4 (Ar*C*), 154.9 (Ar*C*), 154.6 (Ar*C*),154.4 (Ar*C*), 134.5 (Ar*C*), 132.5 (Ar*C*), 132.4 (Ar*C*-H), 130.9 (Ar*C*-H), 130.0 (Ar*C*-H), 113.4 (Ar*C*-H), 113.0 (Ar*C*-H), 110.6 (Ar*C*), 109.6 (Ar*C*), 103.7 (Ar*C*-H), 103.2 (Ar*C*-H), 51.7 (*C*H-CH_3), 15.7 (CH-*C*H_3). **HRMS** (ESI–) *m/z* [M–H]$^-$ calcd. 402.0983 found 402.0982.

Synthesis of S21

S20 (50 mg, 0.124 mmol), DCC (25 mg, 0.121 mmol) and *N*-hydroxymaleimide (14 mg, 0.124 mmol) were dissolved in EtOAc/1,4-dioxane (2:1, 2 mL) and stirred at room temperature overnight. Then, the solvent was lyophilised on a Schlenk line, the crude solid was dissolved in EtOAc (2.5 mL) and cooled down to 4°C for 1 h. The white precipitate of DCU was removed by centrifugation at 4°C and 21 kRCF for 15 min. The supernatant was dried to produce **S21** as a bright yellow powder (58 mg, 95%). The NMR spectra showed extra peaks which were attributed to atropoisomers and the presence of trace amounts of DCU. **^{1}H-NMR** (500 MHz, DMSO-d_6) δ (ppm): 9.99 (1H, s, O*H* or N*H*), 9.89 (1H, s, O*H* or N*H*), 7.83 (1H, m, Ar-*H*), 7.57 (2H, m, Ar-*H*), 7.17 (2H, s^{br}, maleimide Ar-*H*), 7.05 (1H, m, Ar-*H*), 6.61 (2H, m, Ar-*H*), 6.55 (1H, m, Ar-*H*), 6.49 (2H, m, Ar-*H*), 6.38 (1H, m, dd J_1 = 8.7 Hz J_2 = 2.4 Hz, Ar-*H*), 4.11 (1H, q J = 7.1 Hz, C*H*-CH_3), 1.26 (3H, d J = 7.1 Hz, CH-CH_3)0.1**^{3}C-NMR** (160 MHz, DMSO-d_6) δ (ppm): 167.28 (*C*=O), 165.96 (*C*=O), 164.38 (*C*=O), 158.71 (*C*=O), 157.36 (Ar*C*), 153.20 (Ar*C*), 152.13 (Ar*C*), 133.43 and 133.09 (maleimide *C*H=*C*H), 131.91 (Ar*C*-H), 130.07 (Ar*C*-H), 129.68 (Ar*C*), 129.45 (Ar*C*-H), 128.78 (Ar*C*-H), 123.85 (Ar*C*-H), 122.58 (Ar*C*-H), 112.37 (Ar*C*-H), 112.11 (Ar*C*-H), 108.47 (Ar*C*), 107.62 (Ar*C*), 102.41 (Ar*C*-H), 102.06 (Ar*C*-H), 48.16 (*C*H-CH_3), 15.05 (CH-*C*H_3). **HRMS** (ESI–) *m/z* [M–H]$^-$ calcd. 497.0985 found 497.0992.

Fluorescence Spectroscopy Study of the Stability of DNA-Conjugated Activated Esters

The tetramethylrhodamine (TAMRA)/disulfide-labeled DNA hairpin **S4** (1 μL, 1 mM in H_2O, 1 nmol) was thermally annealed with the complementary biotinylated strand **S5** (1.1 μL, 1.1 mM in H_2O, 1.1 nmol) in phosphate buffer solution (PBS, 10 μL, 0.1 M, pH 7.0). The disulfide group was reduced with tris(2-carboxyethyl)phosphine hydrochloride (TCEP, 0.5 μL, 0.5 M in H_2O) at 18°C for 1.25 h. Then, the resulting double stranded DNA (dsDNA) was conjugated to streptavidin-coated magnetic nanoparticles (Dynabeads, Thermofisher), and transferred into $Gly_{0.07}$ (200 μL). The maleimide ester **S21** (1 mg, 2.5 μmol) was added to the solution and allowed to react for 2 h. The nanoparticle-supported DNA-conjugated activated ester was transferred into clean $Gly_{0.07}$ and the hairpin was released by toehold-mediated strand exchange by addition of one equivalent of strand **S6** at 18°C for 2 h to produce an approximately 5 μM solution of **4**. Finally, the solution of **4** (5 μL) was diluted in the DES of interest (95 μL), the resulting solution briefly centrifuged, and the fluorescein (FAM) fluorescence recorded over 24 h in a Mx3005P qPCR instrument (Agilent). The spectral overlap between FAM fluorophore (**S21**) and TAMRA-labeled DNA (**S4**) was also determined (**Figure S4**).

DNA-Templated Synthesis of Peptide Bonds

Disulfide-labeled DNA **S7** (10 μL, 1 mM in H_2O, 10 nmol) was mixed with TCEP solution (2 μL, pH 4 corrected with 5 M NaOH, 1 μmol) in a microcentrifuge tube. The solution was shaken at 18°C for 1.25 h. Maleimide activated ester **S21** (108 μL, 37 mM in DMF, 4 μmol) was added and the combined solution shaken at 18°C for 1.0 h to produce the DNA-conjugated activated ester, **6**. The volume of the solution was reduced to approximately 50 μL by freeze-drying. The previous solution was diluted with $Gly_{0.07}$ (4,950 μL), and

amine-labeled DNA **7** (10 μL, 1 mM in H_2O, 10 nmol) added. The resulting mixture was vigorously shaken until the solution was homogeneous and then shaken at 18°C overnight. The DES solution was diluted with an excess of H_2O and the DNA strands transferred into H_2O for HPLC/LC-MS analysis by repeated centrifugal ultrafiltration using a 3 kDa molecular weight cut-off (MWCO) Amicon spin filter. When the DNA-templated reaction was performed in aqueous solution, the activated ester solution in DMF was diluted with PBS (4,950 μL, 0.1 M, pH 7.5) containing the complementary amine-labeled DNA **7**.

Amine-Labeled DNA Reactivity in DES/Triethylamine (Et_3N)

Amine-labeled DNA **10** (1 μL, 1 mM in H_2O, 1 nmol) was diluted in the appropriate solvent (100 μL). *N*-hydroxysuccinimide ester **11** (∼0.3 mg, 1 μmol) was added, and the mixture shaken overnight at 20°C. The product was transferred into H_2O by dilution of the samples and successive centrifugal ultrafiltration using a 3 kDa MWCO Amicon spin filter. The product was analyzed by HPLC and LC-MS.

Storage of Activated Esters in $Gly_{0.07}$

Disulfide-labeled DNA **S11** (3 μL, 1 mM in H_2O, 3 nmol) was mixed with TCEP solution (3 μL, pH 4 corrected with 5 M NaOH, 1.5 μmol) in a microcentrifuge tube. The solution was shaken at 18°C for 1.25 h. Maleimide activated ester **S21** (54 μL, 22 mM in DMF, 1.2 μmol) was added and the combined solution was shaken at 18°C for 1.0 h to produce the DNA-conjugated activated ester **13**. This sample was divided into 3 aliquots and used as follows. (1) *Storage in* $Gly_{0.07}$: the activated ester solution (20 μL) was diluted with $Gly_{0.07}$ (180 μL), and the resulting solution was shaken at 18°C for 2.0 h. The solution was diluted with PBS (1.3 mL, 0.1 M, pH 7.5) containing complementary amine-labeled DNA **15** (1 μL, 1 mM in H_2O, 1 nmol). The solution was shaken at 18°C for 5 h. Finally, the solution was diluted with 1 vol. of H_2O, the precipitate was centrifuged, and the DNA products were transferred into H_2O by successive steps of dilution of the supernatant with H_2O and concentration by centrifugal ultrafiltration on a 3 kDa MWCO Amicon spin filter. The product was analyzed by HPLC and LC-MS. (2) *Storage in PBS*: the activated ester solution (20 μL) was diluted with PBS (180 μL, 0.1 M, pH 7.0), and the resulting solution was shaken at 18°C for 2.0 h. Then, the sample was treated as in (1). (3) *Fast reaction in PBS:* the activated ester solution (20 μL) was diluted with PBS (1,480 μL, 0.1 M, pH 7.5) containing complementary amine-labeled DNA **15** (1 nmol). The solution was shaken at 18°C for 5.0 h. The products were transferred into H_2O for LC-MS analysis as described previously. (4) *Off-template control:* maleimide activated ester (**S21**) (18 μL, 22 mM in DMF, 400 nmol) was diluted in PBS (1,482 μL, 0.1 M, pH 7.5) containing amine-labeled DNA **15** (1 μL, 1 mM in H_2O, 1 nmol). The solution was shaken at 18°C for 5.0 h and the product was transferred into H_2O for LC-MS analysis as described above.

RESULTS AND DISCUSSION

The Stability of Activated Esters in DES and Aqueous Buffer

We used the *N*-hydroxysuccinimide ester of *L*-alanine (NHS-Ala) as a model activated peptide building block. This had similar solution stability to more prebiotically feasible activating groups while allowing us to use established techniques to prepare the required DNA-conjugated esters (He and Liu, 2011). A preliminary stability experiment was performed using a small-molecule NHS-Ala, **1**. We followed the hydrolysis of **1** in several glycholine/water mixtures and in aqueous PBS using proton nuclear magnetic resonance (^{1}H-NMR) spectroscopy (**Figure 1** and **Figure S1**). **1** was dissolved in the appropriate solvent mixture and then left for 24 h at 24°C. Samples were extracted with immiscible deuterated solvent at set timepoints, and the relative proportions of activated ester and degradation products (**2** and **3**) were determined based on their distinctive methyl ^{1}H-NMR signals. Both the proportion of water and the presence of basic additives were investigated for their effect on the rate of ester degradation.

As expected, rapid degradation of the ester in aqueous PBS was observed, with only 25% remaining after 24 h. In stark contrast, degradation in $Gly_{0.07}$ was very slow, with ∼90% of the activated ester intact after 24 h. Increasing the H_2O content to 50 vol% accelerated solvolysis substantially. We attempted to deliberately accelerate the degradation in glycholine by use of a basic additive, triethylamine (Et_3N). The presence of 2 mM Et_3N in $Gly_{0.07}$ had the same destabilizing effect as increasing the water content to 50 vol%, while 10 mM Et_3N led to a similar rate of degradation to that observed in PBS. The effect of basic additives was studied by diluting the DES in H_2O

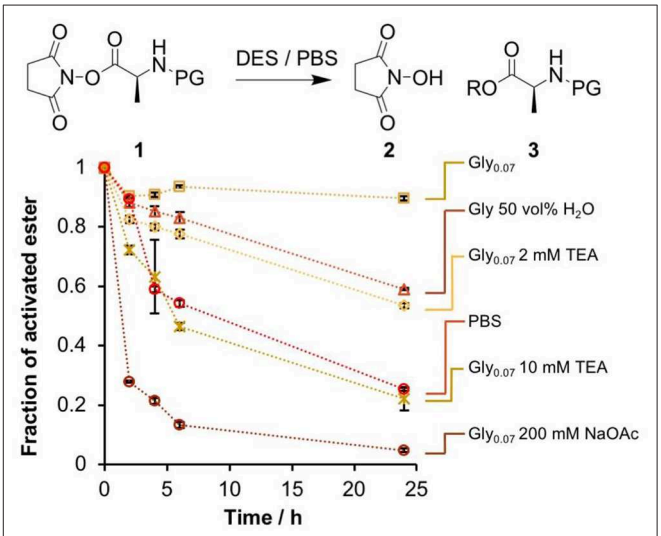

FIGURE 1 | Comparison of the stability of the NHS ester 1 in several glycholine and aqueous PBS solutions. The fraction of 1 remaining at set time points was determined by ^{1}H-NMR spectroscopy by extraction into an immiscible deuterated solvent. Error bars correspond to the standard deviation over multiple integration events.

and measuring the pH of the resulting solution. 2 mM Et_3N produced a pH of 7.5, while 10 mM Et_3N produced a pH of 9.9 (**Table S2**), it therefore seems likely that the observed differences in degradation rate arose as a result of the increased basicity of the solution.

The above ^{1}H-NMR analysis could have been biased by differences in the extraction efficiency of **1** and **3** into the deuterated solvent used, so a complementary study that did not rely on this assumption was performed using reversed-phase high performance liquid chromatography (RP-HPLC, **Figure S2**). The results were highly consistent with the ^{1}H-NMR study, so we concluded that glycholine was indeed effective at stabilizing activated esters, and moved on to DNA-based experiments.

The thermal stability of double-stranded DNA (dsDNA) in glycholine/H_2O was assessed by fluorescence quenching and revealed that the duplex remained stable down to at least 7 vol% H_2O: in $Gly_{0.07}$ the T_m of a 24 base pair dsDNA was 48°C (**Figure S3**). The addition of moderate volumes of H_2O to DES has been used to reduce its viscosity and melting point (Ma et al., 2018; Smith et al., 2019), and resulted in increased conversion in enzymatic reactions (Durand et al., 2013; Guajardo et al., 2017). Furthermore, it has been shown that the microstructure of the DES is at least partially preserved upon the addition H_2O, up to 50 wt% (Hammond et al., 2017; Gabriele et al., 2019). Given this precedent, as well as the good stability of activated esters demonstrated above, $Gly_{0.07}$ was used for experiments from this point onwards.

We were interested in assessing the stability of DNA-conjugated activated esters *in situ*, avoiding the possibility of degradation occurring during analysis. To this end, a fluorescence quenching experiment was designed (**Figure 2**). A FAM-labeled NHS-Ala (**S21**) was synthesized from **S17** through a multi-step procedure (**Scheme 1** and **Scheme S2**, intermediates **S18** to **S20**) and conjugated to a TAMRA-labeled DNA hairpin through thia-Michael addition. This design meant that in the ester form (**4**), FAM fluorescence would be quenched by the neighboring TAMRA group. Upon solvolysis of the ester to give **5**, the FAM-labeled amino acid would diffuse away, triggering a measurable increase in fluorescence. We measured the fluorescence excitation and emission spectra of FAM and TAMRA in glycholine to ensure good spectral overlap was maintained in this solvent (**Figure S4**).

The DNA hairpin was supported on streptavidin-coated magnetic nanoparticles and transferred to $Gly_{0.07}$ for activated ester synthesis, ensuring minimal hydrolysis of the activated ester. Excess reagents were removed by magnetic purification, the hairpins were released into solution by toehold-mediated strand displacement and the nanoparticles removed with a magnet. The hairpin solution was diluted into an excess of the solvent of interest, and the evolution of the fluorescence over a 24 h period was recorded (**Figure S5**).

All experiments showed the expected increase in fluorescence due to solvolysis of the activated ester (**Figure 2**). While a rigorous quantitative kinetic analysis of the data was not possible due to uncertainties in the minimum and maximum fluorescence values, the results showed exactly the same trend as the small molecule experiments, with slow hydrolysis observed in $Gly_{0.07}$. We therefore concluded that glycholine was also effective at stabilizing DNA-conjugated activated esters.

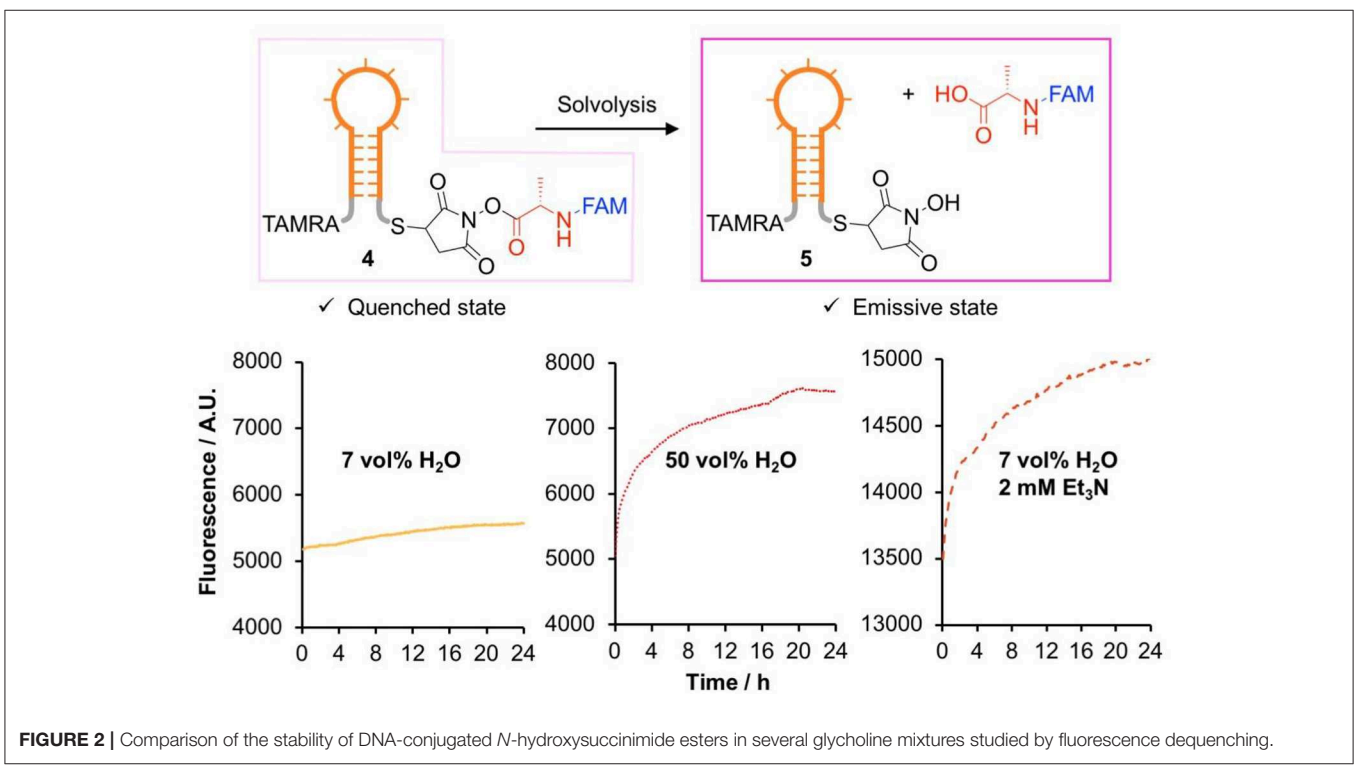

FIGURE 2 | Comparison of the stability of DNA-conjugated *N*-hydroxysuccinimide esters in several glycholine mixtures studied by fluorescence dequenching.

Nucleic Acid-Templated Synthesis of Peptide Bonds in DES

Having demonstrated the higher stability of the activated esters in glycholine, we moved to a single-step NATS reaction using NHS-Ala (**Figure 3A**). The DNA-conjugated activated ester **6** was prepared in 90 vol% DMF and then transferred into a DES solution containing the complementary acceptor strand **7**. The DMF content was reduced to 1 vol%, which did not substantially

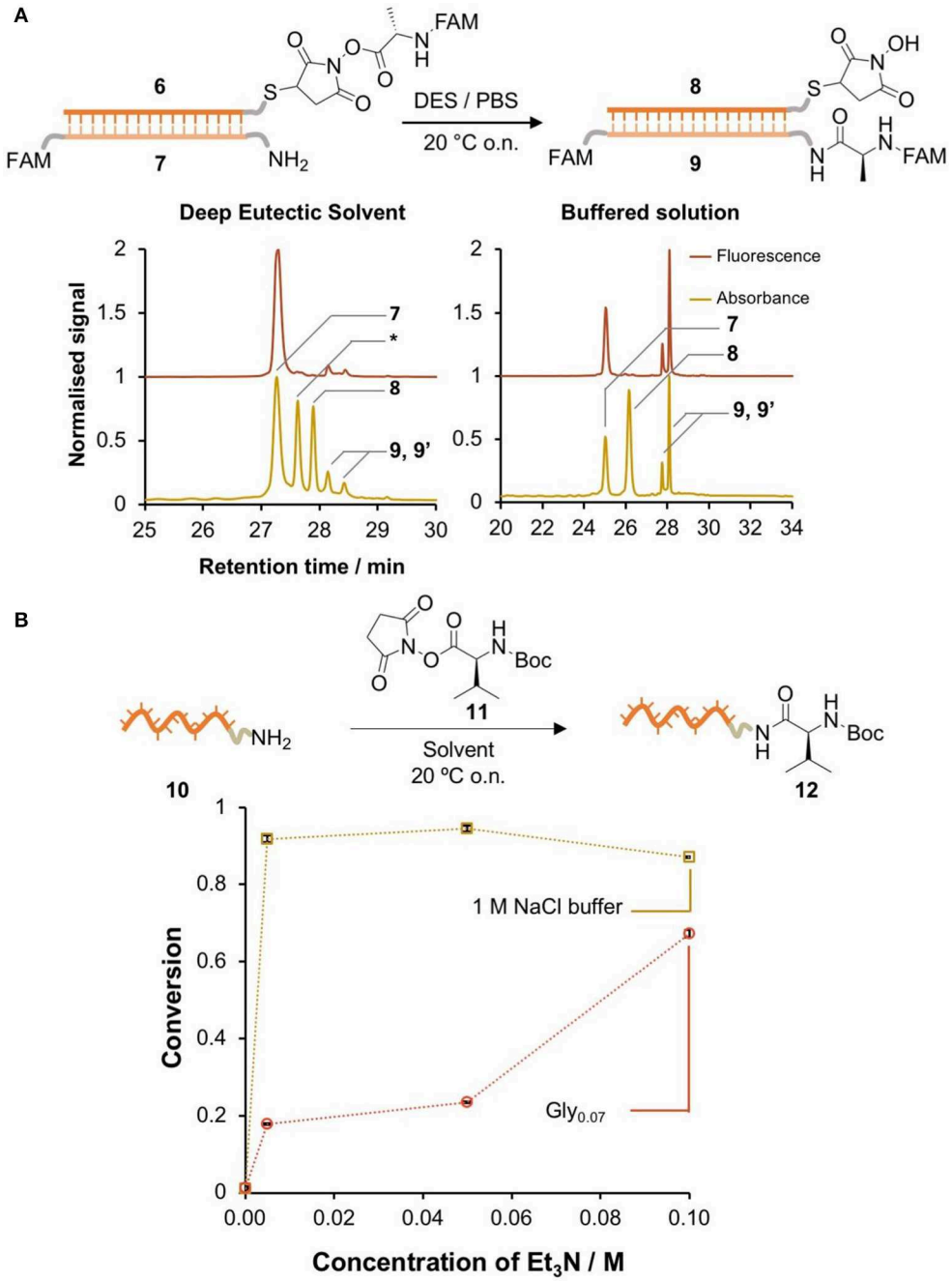

FIGURE 3 | DNA-templated formation of peptide bonds in DES. **(A)** Single-step DNA-templated synthesis of a peptide bond in glycholine and in PBS. The conversion was determined by HPLC integration of the signals corresponding to 7, 9, and 9' (isomers of the product). Peaks were identified by LC-MS (Bruker AmazonX): 7 $[M\text{-}H]^-$ *m/z* calcd. 9337.2 found 9336.0; *DNA-SH $[M\text{-}H]^-$ *m/z* calcd. 10615.2 found 10599.6; 8 $[M\text{-}H]^-$ *m/z* calcd. 10712.0 found 10712.4; 9 and 9' (isomers) $[M\text{-}H]^-$ *m/z* calcd. 9723.6 **(B)** comparison of the reactivity of an amine-labeled DNA (10) in the presence of an excess of activated ester (11) in $Gly_{0.07}$ / Et_3N and 1 M NaCl (aq)/Et_3N. The conversion was determined by HPLC integration of the signals corresponding to 10 and 12. Peaks were identified by LC-MS (Bruker AmazonX): 10 $[M\text{-}H]^-$ *m/z* calcd. 3897.7 found 3898.6; 11 $[M\text{-}H]^-$ *m/z* calcd. 4096.8 found 4097.7. Error bars correspond to the standard deviation over multiple integration events.

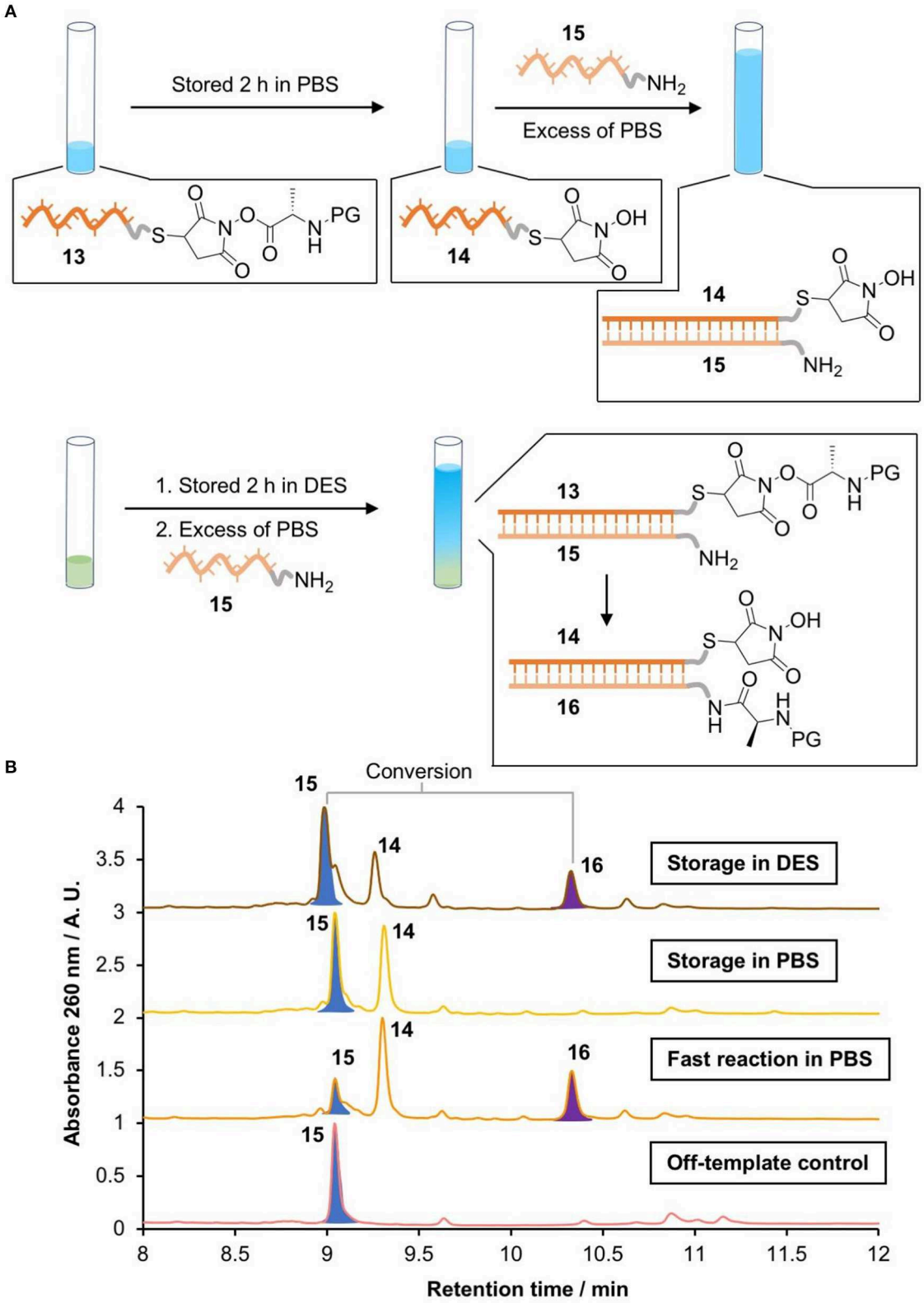

FIGURE 4 | Activating NATS "on demand." **(A)** Scheme of the storage of a DNA conjugated activated ester in PBS (0.1 M pH 7.0) or $Gly_{0.07}$, followed by DNA-templated peptide bond formation in PBS. **(B)** LC-MS chromatograms of the products (Waters Xevo-G2-XS). 15 $[M]^0$ *m/z* calcd. 10891.855 found 10891.522; 14 $[M]^0$ *m/z* calcd. 9558.632 found 9558.581. 16 $[M]^0$ *m/z* calcd. 11201.935 found 11201.489.

affect the duplex T_m. Alternatively, **6** was synthesized in $Gly_{0.07}$; this required longer reaction times (2 h) to reach the same yield attained in DMF, which we speculate was due to the higher viscosity of the DES. Controls mixing the acceptor strand with the small molecule reagents showed that no off-template reactions took place.

A control NATS reaction in PBS was also performed. While hydrolysis of the activated esters in aqueous solution was very fast, if the DNA conjugate **6** was isolated rapidly and transferred to a solution that contained the complementary amine-labeled DNA **7**, the amide product **9** was formed in 48% conversion. By contrast, the formation of **9** in DES was only detected in very low yield (**Figure 3A**). A series of attempts to improve the conversion through the use of additives were not successful in raising the yield of **9** above ∼5% (**Table S3**). We hypothesized that the low conversion in DES was due to a lack of reactivity of the amine moiety. To test this, amino-modified DNA **10** was reacted with a large excess of a small-molecule activated ester **11** in aqueous 1 M NaCl and glycholine solution that contained varying concentrations of Et_3N (**Figure 3B**). In aqueous solution, the conversion in the absence of base was very low, however the addition of a minimal amount of Et_3N resulted in nearly quantitative conversion. By contrast, in DES, very large amounts of Et_3N were required to achieve only moderate conversion (60%). It is interesting to note that NATS of peptide bonds has previously been reported in pH 7.5 buffered solution, similar to the pH of the glycholine/Et_3N solutions measured above, so pH cannot by itself explain the lack of amine reactivity in these solvent mixtures (He and Liu, 2010).

These results highlighted that glycholine by itself could not have promoted prebiotic peptide synthesis. Stabilization of the activated ester comes at the cost of reduced amine reactivity, and increasing the reactivity of the amine can only be achieved by use of additives that destabilize the ester. However, recent hypotheses have proposed an important role for compartmentalisation in prebiotic processes (Mann, 2012). One could imagine a prebiotic system in which activated species are generated and stored in pockets of DES, and then transferred into aqueous solution to facilitate the formation of peptide products. We designed a transfer experiment to investigate this possibility (**Figure 4A**).

The DNA-conjugated activated ester **13** was stored in PBS or glycholine for 2 h. The solution was then diluted with an excess of PBS containing the acceptor amino-DNA strand **15**. The templated synthesis of the peptide product **16** was then quantified via HPLC by comparing peak areas (**Figure 4B**). The identity of the product was confirmed by LC-MS. A positive control was performed by removing the storage step and adding the acceptor strand (**15**) immediately after the synthesis of the activated ester **13**. This resulted in 68% conversion to the peptide product. To check the importance of DNA templating, an off-template negative control was performed by adding the acceptor strand **15** to a solution of the small molecule activated ester **S21** at the same concentration as the DNA strand (670 nM). This showed no evidence of the formation of the peptide product **16**, as expected. When the DNA-templated peptide synthesis was attempted following storage of the activated ester in PBS for 2 h, no product was observed (**Figure 4B**). By contrast, DNA-templated synthesis following storage in glycholine resulted in 30% conversion to the peptide product.

DISCUSSION

Here, we demonstrate that glycholine-based DESs have a positive impact on the stability of DNA-conjugated activated esters when compared with buffered aqueous solutions. However, there is a marked reduction in the reactivity of amines, which prevents the NATS of peptides in these solvents. Our results highlight that it is very challenging to produce activated esters in aqueous media for subsequent templated reactions, as they quickly decompose; however, the synthesis of the activated ester in $Gly_{0.07}$ provides a solution to this problem. By applying a two-stage process in which the activated ester was stored in DES and then transferred into PBS solution to trigger templated synthesis we achieved a moderate yield of 30%. By comparison, no product was observed if the activated ester was stored in PBS.

It may be possible to circumvent the issue of amine deactivation we observe by the use of alternative DESs or other viscous solvents. For example, glycerol containing an appropriate concentration of NaCl has been shown to stabilize DNA duplexes (Bonner and Klibanov, 2000). Future work could investigate whether such solvent mixtures are more effective at promoting nucleic acid-templated peptide synthesis, and thus shine further light on whether increased activated ester stability is inevitably linked to decreased amine reactivity in these environments.

Finally, it is interesting to speculate how our results might be relevant to prebiotic translation. The high viscosity of DESs means that they mix only slowly with aqueous solutions, so this may have allowed a primitive form of compartmentalization in which the production and stabilization of activated species took place in a DES phase, followed by diffusion into the aqueous phase where templated chemistry could occur. Future experiments using simple DES/aqueous interfaces of this kind could provide fascinating insights into such prebiotic processes.

DATA AVAILABILITY STATEMENT

The datasets generated for this study are available on request to the corresponding author.

AUTHOR CONTRIBUTIONS

SN-P and TW designed the experiments, analyzed the data, and wrote and formatted the manuscript. SN-P carried out the experimental work.

FUNDING

This work was funded entirely by the European Research Council (grant ID 615142), which provided a studentship for SN-P and

a postdoctoral fellowship for TW. Open access publication fees were funded by the University of Birmingham.

ACKNOWLEDGMENTS

The authors thank Prof. Rachel O'Reilly for her invaluable support during the performance of this work and Prof. Andrew Turberfield, Dr. Jonathan Bath, and Dr. Robert Oppenheimer for advice on the design of the DNA constructs and helpful discussions.

SUPPLEMENTARY MATERIAL

The Supplementary Material for this article can be found online at: https://www.frontiersin.org/articles/10.3389/fchem.2020.00041/full#supplementary-material

REFERENCES

Abbott, A. P., Boothby, D., Capper, G., Davies, D. L., and Rasheed, R. K. (2004). Deep eutectic solvents formed between choline chloride and carboxylic acids: versatile alternatives to ionic liquids. *J. Am. Chem. Soc.* 126, 9142–9147. doi: 10.1021/ja048266j

Abbott, A. P., Capper, G., Davies, D. L., Rasheed, R. K., and Tambyrajah, V. (2003). Novel solvent properties of choline chloride/urea mixtures. *Chem. Commun.* 2003, 70–71. doi: 10.1039/b210714g

Bonner, G., and Klibanov, A. M. (2000). Structural stability of DNA in nonaqueous solvents. *Biotechnol. Bioeng.* 68, 339–344. doi: 10.1002/(SICI)1097-0290(20000505)68:33.0.CO;2-O

Burcar, B., Pasek, M., Gull, M., Cafferty, B. J., Velasco, F., Hud, N. V., et al. (2016). Darwin's warm little pond: a one-pot reaction for prebiotic phosphorylation and the mobilization of phosphate from minerals in a urea-based solvent. *Angew. Chem. Int. Ed.* 55, 13249–13253. doi: 10.1002/anie.201606239

Crick, F. (1968). The origin of the genetic code. *J. Mol. Biol.* 38, 367–379. doi: 10.1016/0022-2836(68)90392-6

Crick, F. (1970). Central dogma of molecular biology. *Nature* 227, 561–563. doi: 10.1038/227561a0

Deck, C., Jauker, M., and Richert, C. (2011). Efficient enzyme-free copying of all four nucleobases templated by immobilized RNA. *Nat. Chem.* 3, 603–608. doi: 10.1038/nchem.1086

Durand, E., Lecomte, J., Baréa, B., Dubreucq, E., Lortie, R., and Villeneuve, P. (2013). Evaluation of deep eutectic solvent-water binary mixtures for lipase-catalyzed lipophilization of phenolic acids. *Green Chem.* 15, 2275–2282. doi: 10.1039/c3gc40899j

Ekland, E. H., and Bartel, D. P. (1996). RNA-catalysed RNA polymerization using nucleoside triphosphates. *Nature* 382, 373–376. doi: 10.1038/382373a0

Gabriele, F., Chiarini, M., Germani, R., Tiecco, M., and Spreti, N. (2019). Effect of water addition on choline chloride/glycol deep eutectic solvents: characterization of their structural and physicochemical properties. *J. Mol. Liq.* 291:111301. doi: 10.1016/j.molliq.2019.111301

Gállego, I., Grover, M. A., and Hud, N. V. (2015). Folding and imaging of DNA nanostructures in anhydrous and hydrated deep-eutectic solvents. *Angew. Chem. Int. Ed.* 54, 6765–6769. doi: 10.1002/anie.201412354

Gao, J., Wang, P., and Giese, R. W. (2002). Xanthamide fluorescent dyes. *Anal. Chem.* 74, 6397–6401. doi: 10.1021/ac020368+

Gilbert, W. (1986). Origin of life: the RNA world. *Nature* 319:618. doi: 10.1038/319618a0

Guajardo, N., Domínguez de María, H. P., Ahumada, K., Schrebler, R. A., Ramírez-Tagle, R., Crespo, F. A., et al. (2017). Water as cosolvent: nonviscous deep eutectic solvents for efficient lipase-catalyzed esterifications. *Chem. Cat Chem.* 9, 1393–1396. doi: 10.1002/cctc.201601575

Guerrier-Takada, C., Gardiner, K., Marsh, T., Pace, N., and Altman, S. (1983). The RNA moiety of ribonuclease P is the catalytic subunit of the enzyme. *Cell* 35, 849–857. doi: 10.1016/0092-8674(83)90117-4

Gull, M., Cafferty, B. J., Hud, N. V., and Pasek, M. A. (2017). Silicate-promoted phosphorylation of glycerol in non-aqueous solvents: a prebiotically plausible route to organophosphates. *Life* 7:29. doi: 10.3390/life7030029

Gull, M., Zhou, M., Fernández, F. M., and Pasek, M. A. (2014). Prebiotic phosphate ester syntheses in a deep eutectic solvent. *J. Mol. Evol.* 78, 109–117. doi: 10.1007/s00239-013-9605-9

Hammond, O. S., Bowron, D. T., and Edler, K. J. (2017). Effect of water upon deep eutectic solvent nanostructure: an unusual transition from ionic mixture to aqueous solution. *Angew. Chem. Int. Ed.* 56, 9782–9785. doi: 10.1002/anie.201702486

Hänle, E., and Richert, C. (2018). Enzyme-free replication with two or four bases. *Angew. Chem. Int. Ed.* 57, 8911–8915. doi: 10.1002/anie.201803074

He, C., Gállego, I., Laughlin, B., Grover, M. A., and Hud, N. V. (2017). A viscous solvent enables information transfer from gene-length nucleic acids in a model prebiotic replication cycle. *Nat. Chem.* 9, 318–324. doi: 10.1038/nchem.2628

He, C., Lozoya-Colinas, A., Gállego, I., Grover, M. A., and Hud, N. V. (2019). Solvent viscosity facilitates replication and ribozyme catalysis from an RNA duplex in a model prebiotic process. *Nucleic Acids Res.* 47, 6569–6577. doi: 10.1093/nar/gkz496

He, Y., and Liu, D. R. (2010). Autonomous multistep organic synthesis in a single isothermal solution mediated by a DNA walker. *Nat. Nanotechnol.* 5, 778–782. doi: 10.1038/nnano.2010.190

He, Y., and Liu, D. R. (2011). A sequential strand-displacement strategy enables efficient six-step DNA-templated synthesis. *J. Am. Chem. Soc.* 133, 9972–9975. doi: 10.1021/ja201361t

Johnston, W. K., Unrau, P. J., Lawrence, M. S., Glasner, M. E., and Bartel, D. P. (2001). RNA-catalyzed RNA polymerization: accurate and general RNA-templated primer extension. *Science* 292, 1319–1325. doi: 10.1126/science.1060786

Kaiser, R. I., Maity, S., and Jones, B. M. (2015). Synthesis of prebiotic glycerol in interstellar ices. *Angew. Chem. Int. Ed.* 54, 195–200. doi: 10.1002/anie.201408729

Kanavarioti, A., Bernasconi, C. F., Doodokyan, D. L., and Alberas, D. J. (1989). Magnesium ion catalyzed phosphorus-nitrogen bond hydrolysis in imidazolide-activated nucleotides. relevance to template-directed synthesis of polynucleotides. *J. Am. Chem. Soc.* 111, 7247–7257. doi: 10.1021/ja00200a053

Kruger, K., Grabowski, P. J., Zaug, A. J., Sands, J., Gottschling, D. E., and Cech, T. R. (1982). Self-splicing RNA: autoexcision and autocyclization of the ribosomal RNA intervening sequence of tetrahymena. *Cell* 31, 147–157. doi: 10.1016/0092-8674(82)90414-7

Lannan, F. M., Mamajanov, I., and Hud, N. V. (2012). Human telomere sequence DNA in water-free and high-viscosity solvents: G-quadruplex folding governed by kramers rate theory. *J. Am. Chem. Soc.* 134, 15324–15330. doi: 10.1021/ja303499m

Li, L., Prywes, N., Tam, C. P., Oflaherty, D. K., Lelyveld, V. S., Izgu, E. C., et al. (2017). Enhanced nonenzymatic RNA copying with 2-aminoimidazole activated nucleotides. *J. Am. Chem. Soc.* 139, 1810–1813. doi: 10.1021/jacs.6b13148

Li, X., and Liu, D. R. (2004). DNA-templated organic synthesis: nature's strategy for controlling chemical reactivity applied to synthetic molecules. *Angew. Chem. Int. Ed.* 43, 4848–4870. doi: 10.1002/anie.200400656

Liu, Z., Mariani, A., Wu, L., Ritson, D., Folli, A., Murphy, D., et al. (2018). Tuning the reactivity of nitriles using Cu(ii) catalysis-potentially prebiotic activation of nucleotides. *Chem. Sci.* 9, 7053–7057. doi: 10.1039/C8SC02513D

Ma, C., Laaksonen, A., Liu, C., Lu, X., and Ji, X. (2018). The peculiar effect of water on ionic liquids and deep eutectic solvents. *Chem. Soc. Rev.* 47, 8685–8720. doi: 10.1039/C8CS00325D

Mamajanov, I., Engelhart, A. E., Bean, H. D., and Hud, N. V. (2010). DNA and RNA in anhydrous media: duplex, triplex, and G-quadruplex secondary structures in a deep eutectic solvent. *Angew. Chem. Int. Ed.* 49, 6310–6314. doi: 10.1002/anie.201001561

Mann, S. (2012). Systems of creation: the emergence of life from nonliving matter. *Acc. Chem. Res.* 45, 2131–2141. doi: 10.1021/ar200281t

Mariani, A., Russell, D. A., Javelle, T., and Sutherland, J. D. (2018). A light-releasable potentially prebiotic nucleotide activating agent. *J. Am. Chem. Soc.* 140, 8657–8661. doi: 10.1021/jacs.8b05189

Maugeri, Z., Leitner, W., and Domínguez De María, P. (2013). Chymotrypsin-catalyzed peptide synthesis in deep eutectic solvents. *Eur. J. Org. Chem.* 2013, 4223–4228. doi: 10.1002/ejoc.201300448

Meng, W., Muscat, R. A., McKee, M. L., Milnes, P. J., El-Sagheer, A. H., Bath, J., et al. (2016). An autonomous molecular assembler for programmable chemical synthesis. *Nat. Chem.* 8, 542–548. doi: 10.1038/nchem.2495

Mondal, D., Sharma, M., Mukesh, C., Gupta, V., and Prasad, K. (2013). Improved solubility of DNA in recyclable and reusable bio-based deep eutectic solvents with long-term structural and chemical stability. *Chem. Commun.* 49, 9606–9608. doi: 10.1039/c3cc45849k

Okamura, H., Crisp, A., Hübner, S., Becker, S., Rovo, P., and Carell, T. (2019). Proto-urea-RNA (Wöhler RNA) containing unusually stable urea nucleosides. *Angew. Chem. Int. Ed.* 58, 18691–18696. doi: 10.1002/anie.201911746

O'Reilly, R. K., Turberfield, A. J., and Wilks, T. R. (2017). The evolution of DNA-templated synthesis as a tool for materials discovery. *Acc. Chem. Res.* 50, 2496–2509. doi: 10.1021/acs.accounts.7b00280

Orgel, L. E. (1968). Evolution of the genetic apparatus. *J. Mol. Biol.* 38, 381–393. doi: 10.1016/0022-2836(68)90393-8

Pätzold, M., Siebenhaller, S., Kara, S., Liese, A., Syldatk, C., and Holtmann, D. (2019). Deep eutectic solvents as efficient solvents in biocatalysis. *Trends Biotechnol.* 37, 943–959. doi: 10.1016/j.tibtech.2019.03.007

Paul, N., and Joyce, G. F. (2002). A self-replicating ligase ribozyme. *Proc. Natl. Acad. Sci. U.S.A.* 99, 12733–12740. doi: 10.1073/pnas.202471099

Smith, E. L., Abbott, A. P., and Ryder, K. S. (2014). Deep eutectic solvents (DESs) and their applications. *Chem. Rev.* 114, 11060–11082. doi: 10.1021/cr300162p

Smith, P. J., Arroyo, C. B., Lopez Hernandez, F., and Goeltz, J. C. (2019). Ternary deep eutectic solvent behavior of water and urea choline chloride mixtures. *J. Phys. Chem. B* 123, 5302–5306. doi: 10.1021/acs.jpcb.8b12322

Steitz, T. A. (2008). A structural understanding of the dynamic ribosome machine. *Nat. Rev. Mol. Cell Biol.* 9, 242–253. doi: 10.1038/nrm2352

Szostak, J. W. (2012). The eightfold path to non-enzymatic RNA replication. *J. Syst. Chem.* 3:2. doi: 10.1186/1759-2208-3-2

Tamura, K., and Schimmel, P. (2001). Oligonucleotide-directed peptide synthesis in a ribosome- and ribozyme-free system. *Proc. Natl. Acad. Sci. U.S.A.* 98, 1393–1397. doi: 10.1073/pnas.98.4.1393

Tamura, K., and Schimmel, P. (2004). Chiral-selective aminoacylation of an RNA minihelix. *Science* 305:1253. doi: 10.1126/science.1099141

Turk, R. M., Chumachenko, N. V., and Yarus, M. (2010). Multiple translational products from a five-nucleotide ribozyme. *Proc. Natl. Acad. Sci. U.S.A.* 107, 4585–4589. doi: 10.1073/pnas.0912895107

Wagle, D. V., Zhao, H., and Baker, G. A. (2014). Deep eutectic solvents: sustainable media for nanoscale and functional materials. *Acc. Chem. Res.* 47, 2299–2308. doi: 10.1021/ar5000488

Xu, P., Zheng, G.-W., Zong, M.-H., Li, N., and Lou, W.-Y. (2017). Recent progress on deep eutectic solvents in biocatalysis. *Bioresour. Bioprocess.* 4, 34–52. doi: 10.1186/s40643-017-0165-5

Yarus, M. (2001). On translation by RNAs alone. *Cold Spring Harb. Symp. Quant. Biol.* 66, 207–216. doi: 10.1101/sqb.2001.66.207

Yonath, A. (2009). Large facilities and the evolving ribosome, the cellular machine for genetic-code translation. *J. R. Soc. Interface* 6, S575–S585. doi: 10.1098/rsif.2009.0167.focus

Zadeh, J. N., Steenberg, C. D., Bois, J. S., Wolfe, B. R., Pierce, M. B., Khan, A. R., et al. (2009). NUPACK: analysis and design of nucleic acid systems. *J. Comput. Chem.* 32, 170–173. doi: 10.1002/jcc.21596

Zhang, B., and Cech, T. R. (1997). Peptide bond formation by *in vitro* selected ribozymes. *Nature* 390, 96–100. doi: 10.1038/36375

Zhang, Q., De Oliveira Vigier, K., Royer, S., and Jérôme, F. (2012). Deep eutectic solvents: syntheses, properties and applications. *Chem. Soc. Rev.* 41, 7108–7146. doi: 10.1039/c2cs35178a

Zhang, W., Pal, A., Ricardo, A., and Szostak, J. W. (2019). Template-directed nonenzymatic primer extension using 2-methylimidazole-activated morpholino derivatives of guanosine and cytidine. *J. Am. Chem. Soc.* 141, 12159–12166. doi: 10.1021/jacs.9b06453

Zhao, C., Ren, J., and Qu, X. (2013). G-quadruplexes form ultrastable parallel structures in deep eutectic solvent. *Langmuir* 29, 1183–1191. doi: 10.1021/la3043186

Conflict of Interest: The authors declare that the research was conducted in the absence of any commercial or financial relationships that could be construed as a potential conflict of interest.

frontiers in Chemistry

ORIGINAL RESEARCH
published: 31 January 2020
doi: 10.3389/fchem.2020.00040

Tricky Topology: Persistence of Folded Human Telomeric i-Motif DNA at Ambient Temperature and Neutral pH

Mahmoud A. S. Abdelhamid[1,2]* *and Zoë A. E. Waller*[1,2]*

[1] School of Pharmacy, University of East Anglia, Norwich Research Park, Norwich, United Kingdom, [2] Centre for Molecular and Structural Biochemistry, University of East Anglia, Norwich Research Park, Norwich, United Kingdom

i-Motifs are four-stranded DNA structures formed from sequences rich in cytosine, held together by hemi-protonated cytosine-cytosine base pairs. These structures have been utilized extensively as pH-switches in DNA-based nanotechnology. Recently there has been an increasing interest in i-motif structures in biology, fuelled by examples of when these can form under neutral conditions. Herein we describe a cautionary tale regarding handling of i-motif samples. Using CD and UV spectroscopy we show that it is important to be consistent in annealing i-motif DNA samples as at neutral pH, i-motif unfolding kinetics is dependent on the time allowed for annealing and equilibration. We describe how the quadruplex structure formed by the human telomeric i-motif sequence can be shown to form and persist in the same conditions of neutral pH and ambient temperature in which, once at thermodynamic equilibrium, it exists predominantly as a random coil. This study has implications not only for work with i-motif DNA structures, but also in the uses and applications of these in nanotechnological devices.

Keywords: i-motif, cytosine, quadruplex, DNA, topology, kinetics

OPEN ACCESS

Edited by:
James Tucker, University of Birmingham, United Kingdom

Reviewed by:
Tangxin Xiao, Changzhou University, China
Sriram Kanvah, Indian Institute of Technology Gandhinagar, India

***Correspondence:**
Mahmoud A. S. Abdelhamid
m.abdelhamid@uea.ac.uk
Zoë A. E. Waller
z.waller@uea.ac.uk

Specialty section:
This article was submitted to Supramolecular Chemistry, a section of the journal Frontiers in Chemistry

Received: *05 November 2019*
Accepted: *14 January 2020*
Published: *31 January 2020*

Citation:
Abdelhamid MAS and Waller ZAE (2020) Tricky Topology: Persistence of Folded Human Telomeric i-Motif DNA at Ambient Temperature and Neutral pH. Front. Chem. 8:40. doi: 10.3389/fchem.2020.00040

INTRODUCTION

The i-motif is a quadruplex DNA structure formed from cytosine-rich sequences and has wide-ranging uses in nanotechnology as well as having potential to impact biological processes (Gehring et al., 1993; Alberti et al., 2006; Abou Assi et al., 2018). While sequences have been identified which form i-motif at pH > 7 (Brazier et al., 2012; Wright et al., 2017a; Dzatko et al., 2018), the dependence of i-motif formation on acidic pH is much better understood (Day et al., 2014; Dembska, 2016). This is owing to the structure's cytosine core, consisting of intercalated cytosine-cytosine^{+} base pairs, where the N3 of one of the pair of cytosines is protonated. Other factors such as molecular crowding (Cui et al., 2013; Tateishi-Karimata et al., 2013; Saxena et al., 2017), low temperature (Zhou et al., 2010; Nguyen et al., 2017), silver (I) (Day et al., 2013) and copper (I) (Abdelhamid et al., 2018) cations and negative superhelicity (Sun and Hurley, 2009) have been shown to be favorable for formation of i-motif.

Much work has been done to understand the behavior of i-motif structures in different environments including studying the effect of varying the cytosine tract and loop lengths (Arora et al., 2009; Gurung et al., 2015), using epigenetically modified cytosine analogs (Bhavsar-Jog et al., 2014; Xu et al., 2015), and modification of the DNA backbone (Assi et al., 2016), amongst other modifications (Tsvetkov et al., 2018; Školáková et al., 2019). Owing to the importance of pH in

the control of folding, pH has been examined extensively to understand its effect on the i-motif to learn about its stability at different pH values and its effect on the thermodynamic and kinetic properties of the structure. On the other hand, the effect of temperature on the structure has been studied much less comprehensively. Unusual temperature-dependent effects have been observed previously for the i-motif in the context of exploring its response to changes in pH. This includes the hysteresis that is commonly observed between thermal melting and annealing curves for the structure (Mergny and Lacroix, 2003; Wright et al., 2017a), as well as isothermal hysteresis in pH transitions (Rogers et al., 2018). Kinetic partitioning has also been observed, where the i-motif will initially fold rapidly into one conformation in response to a decrease in pH and then, over time, unfold and refold to a slower forming, but more stable conformation (Lieblein et al., 2012). This led to the description of the i-motif structure existing in an equilibrium of slowly interconverting conformers at a given pH and temperature (Lieblein et al., 2013). As a result of this dynamic nature, the effect of temperature is an important variable that should be given due consideration.

The sequence from the human telomeric region 3′-$(AATCCC)_n$-5′, and variants with slight modifications, have been used frequently by researchers as a model system for learning about i-motif structure (Phan and Mergny, 2002; Chen et al., 2012; Jonchhe et al., 2018). The i-motif from the human telomeric region has previously been shown to be able to form at pH 7.0 at low temperature (Zhou et al., 2010). To the best of our knowledge, this is the only study to directly examine the effect of low temperature on the i-motif at neutral or slightly alkaline pH values. In their experiments, Zhou et al. showed that dilution of HT (a sequence based on the cytosine-rich human telomeric region) into pH 7.0 buffer pre-incubated at 4°C, led to intramolecular i-motif formation within 700 s. Herein, we describe another peculiar temperature-dependent phenomenon observed during the course of working with the human telomeric i-motif at pH values >7. We found that at pH 7.11 the sequence from the human telomere (5′-$(CCC\text{-}TAA)_4$-3′, hTeloC) will still form i-motif when cooled to 4°C, albeit more slowly than what was observed by Zhou et al. Most interestingly however, was the observation that extended incubation times at low temperature resulted in a significant change in the unfolding kinetics of the structure, resulting in much slower unfolding at 20°C. This has implications on how samples should be handled before, during and between experiments, to have consistent and comparable observations and prevent unintended convolution of results. Crucially though, as the i-motif is used extensively in nanotechnological applications, this presents another way for researchers to achieve more precise control of the dynamic equilibrium of this exquisite structure.

MATERIALS AND METHODS

Oligonucleotide Synthesis and Sample Preparation

The hTeloC oligonucleotide 5′-$[(TAA\text{-}CCC)_4]$-3′ was supplied by Eurogentec (Belgium), synthesized on a 200 nmol scale and purified by reverse phase HPLC. hTeloC was dissolved at approximately 1 mM in ultrapure water (18.2 MΩ·cm) and quantified using a nanodrop. DNA Samples for experiments were thermally annealed at 10 μM in 10 mM sodium cacodylate buffer at pH 7.11 in a thermal heating block by holding at 95°C for 5 min followed by slow cooling to room temperature overnight.

Circular Dichroism (CD) and Ultraviolet (UV) Spectroscopy

CD and UV spectra were recorded on a Jasco J-810 spectropolarimeter equipped with a Peltier thermostatted single cell holder, a PTC-423S temperature controller and a MCB-100 mini circulation bath set to 4.0°C. Each sample volume was 100 μL and was measured using a 1 mm path length quartz cuvette. The equilibrations at 4°C for 3 and 6 h were performed *in situ* in the spectrometer; the temperature of the sample holder was set to 4°C and acquisition of spectra began when the sample holder's internal temperature probe reached the target temperature. For the longer equilibration times samples were stored at 4°C in a refrigerator for the indicated time. Following the 4°C equilibrations the temperature of the sample holder was set to 20°C and acquisition of spectra began when the sample holder's internal temperature probe reached the desired temperature. Spectra were acquired using the Jasco Spectra Manager application's Interval Scan Measurement program with the parameters set to measure from 320 to 200 nm, with a scanning speed of 200 nm/min, response time of 1 s, 0.5 nm data pitch and 2 nm bandwidth. A time interval between 2 and 5 min was used depending on the experiment. Melting experiments were performed using the Temperature/Wavelength Scan program using the same measurement parameters as above while heating the sample at a rate of 1°C/min from 5 to 95°C and measuring at 5°C intervals. In the case of the melting experiments as time was not a variable each data point was able to be acquired via an accumulation of four scans.

Sample Temperature Monitoring

A HANNA instruments type K thermocouple was used to directly measure the temperature of 100 μL samples in the 1 mm quartz cuvettes when inside the cell holder of the spectropolarimeter to determine the delay between the temperature reported by the sample holder's probe and the temperature of the sample itself. For the cooling from 20 to 4°C this was found to be within 3 min and for the transition from 4 to 20°C this was found to be <1 min.

RESULTS AND DISCUSSION

The sequence hTeloC has a transitional pH of 6.11 at room temperature in 10 mM sodium cacodylate buffer with 100 mM sodium chloride (Wright et al., 2017b). This is the pH at which the population is evenly split between the folded and unfolded states. A lower pH would result in the sequence being predominantly folded into the i-motif and the inverse true at higher pH. Cytosine-cytosine base pair stability is optimum when the pH is equal to the pK_a of the cytosine, however cytosines can still pick up free H^+ from solution, even at neutral pH but these cytosine-cytosine base pairs are less stable than they would be at a lower pH (Mergny et al., 1995). The stimulus for this

study was the observation that a sample of hTeloC, which had been annealed at 10 μM in 10 mM sodium cacodylate buffer at pH 7.0, appeared to be folding into i-motif over time. Samples had been prepared as described commonly in the literature: the oligonucleotide was diluted to the desired concentration (10 μM) in buffer (10 mM sodium cacodylate) and held in a heating block at 95°C for 5 min and then allowed to cool to room temperature slowly overnight. This is done to maintain the uniformity of the population and allow the adoption of the equilibrium structure under those conditions. Finally, measurements were being collected at room temperature (∼20°C).

Originally measurements at room temperature and pH 7.0 were used so that the hTeloC sequence would predominantly be unfolded (**Figure 1A**). However, it became apparent that, over time, this sample appeared to be folded, as evidenced by the characteristic CD spectrum of folded i-motif, similar to that observed at pH 5 (**Figure 1B**). The only change that was taking place over time was a difference in the temperature: samples were stored in a refrigerator (4°C) between measurements, but enough time was allowed for them to return to room temperature before measurement. Previous work on the human telomeric i-motif had shown that it was possible to fold at neutral and slightly alkaline pH at low temperature, but as the temperature was raised to room temperature, the structure unfolds to a random coil. The melting temperature for the structure at pH 7.0 was 13°C, and above this temperature the structure was previously shown to return to an unfolded state (Zhou et al., 2010). Therefore, it was initially presumed that temporary cold storage would have little effect on measurements taken at room temperature, providing the sample was adequately equilibrated at room temperature.

To better understand what was happening, new samples were prepared in the same way, in this case at pH 7.11, to go above the pH used in the experiments described by Zhou et al. The possibility that under these conditions the i-motif had very slow folding kinetics at room temperature (∼20°C) and was forming at pH 7.0 over the course of several days was considered. However, this was determined not to be the case as samples kept at room temperature did not exhibit this folding form over time (**Supplementary Figure 1**). On the other hand, samples stored at 4°C were found to fold into i-motif over time, shown by the presence of a characteristic i-motif spectrum in the CD (**Supplementary Figures 2A,C**). To determine the folding kinetics of i-motif formation, samples were monitored as a function of both the CD ellipticity at 288 nm and the UV absorbance at 295 nm vs. time. The folding of the structure results in characteristic hyperchromicity at these wavelengths, both of which are used regularly to study the i-motif. Under the experimental conditions used here the folding kinetics are considerably slower than those observed by Zhou et al. Their work did not explicitly state the concentration of DNA used, only that concentrated aliquots were diluted into buffer pre-incubated at low temperature. In our hands, we were able to, as much as possible without the exact details, replicate their experiments and observed more comparable folding kinetics (**Supplementary Figure 3**). However, we found using annealed DNA, at a lower concentration, resulted in very different folding kinetics.

It was decided that for this work, a thermal melt and slow anneal should be performed first to reduce variability and ensure that what was being observed was not an artifact of the dilution or sudden change in temperature. A sample was equilibrated at 4°C for 3 h in the spectropolarimeter and its CD and UV signals measured over time; an analogous sample was treated in the same manner, except the equilibration period was extended to 6 h. It can be seen from **Supplementary Figure 2** that both samples folded into i-motif over time, identified using CD signals which are characteristic for i-motif: a large positive signal at ∼288 nm and a negative signal at ∼255 nm. Further samples were stored at 4°C in a refrigerator for up to a week (168 h) and comparison of the CD spectra of the hTeloC samples held at low temperature from 3 to 168 h did not show any noticeable difference; at all of these times the samples of hTeloC at neutral pH folded into i-motif in response to equilibration at low temperature (**Supplementary Figure 4**). The adoption of i-motif structure under neutral conditions was further confirmed by the hyperchromicity observed over time in both the ellipticity at 288 nm and the absorbance at 295 nm, monitored for the samples equilibrated *in situ*. Under the experimental conditions used

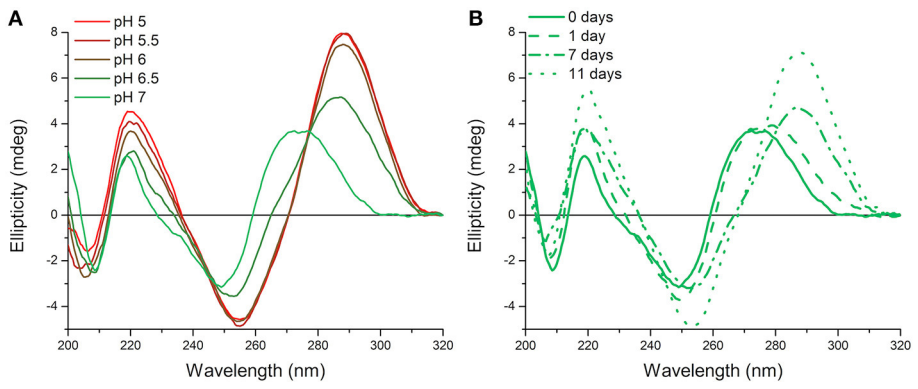

FIGURE 1 | CD spectra of 10 μM hTeloC in 10 mM sodium cacodylate buffer at room temperature. **(A)** Spectra of samples at different pH values measured without storage at low temperature. **(B)** Spectra of samples at pH 7.0 measured after storage at 4°C for the indicated time.

here, when compared to the conditions used by Zhou et al. there was a marked decrease in the rate of i-motif folding; with the slow folding process reaching a steady-state equilibrium close to the 3 h mark (**Supplementary Figure 5**) as opposed to the rapid 700 s observed when concentrated DNA is added to pre-cooled buffer. This dramatic difference in the kinetics of the folding process under these different experimental conditions has implications for the handling of i-motif samples during experimentation and for i-motif-based nanotechnological applications. While this difference was interesting it did not explain the observation from our previous experiments (**Figure 1B**) where the hTeloC sequence at pH 7 appeared to be folded into i-motif at room temperature. This was hypothesized to possibly be caused by a change in the thermodynamics or kinetics of the system as a result of storage at low temperature. Consequently, samples were once again held at 4°C for different periods of time, equilibrated at 20°C for 30 min, and then melted in the spectropolarimeter. It was found that extended storage at low temperature did not alter the melting temperature of the samples kept at 4°C for increasing lengths of time, with the melting temperatures of all samples being ∼28°C (**Supplementary Figure 6**). This is the first instance of the i-motif formed by the human telomeric sequence existing at such high pH (>7) and at ambient temperature; the cause of this however was not yet understood.

To test whether the kinetics of this system were affected by extended time at low temperature after equilibration at 4°C, the temperature was changed to 20°C. The CD spectra were measured, this time to monitor the unfolding process, and over time all the samples unfolded as expected (**Supplementary Figure 7**). Even from these CD spectra, a clear difference is visible in the rate at which the structure unfolds. A more rapid disappearance of the signature i-motif spectra was observed in the samples kept at 4°C for shorter periods of time. Using the ellipticity data at 288 nm and the absorbance at 295 nm and plotting those against time this difference was able to be quantified (**Figure 2**). It transpired that an increase in equilibration time at 4°C had a dramatic and unexpected effect on the kinetics of the unfolding process. Samples equilibrated at 4°C for 3, 6, 24, and 72 h displayed strikingly different unfolding kinetics; extended time equilibrating at low temperature led to a decrease in the rate of i-motif unfolding at 20°C (**Figure 2**). These data could be fitted to determine the half-life of the folded structure after different equilibration times (**Table 1**). From these results it can be seen clearly that extended storage at low temperature leads to a change in the unfolding kinetics where the i-motif unfolds more slowly.

In trying to determine the underlying mechanisms that could explain these results it was considered that they were likely caused by some form of structural reconfiguration of the hTeloC i-motif. From the literature it is known that the i-motif is a dynamic structure and it was proposed that in this scenario hTeloC could be adopting a more thermodynamically stable form by (a) changing from an intramolecular i-motif to an intermolecular form or (b) changing between the 3′E and 5′E conformations. The fact that the melting temperature was unaffected by length of time spent at 4°C indicates that the former explanation is unlikely. The melting temperature of an intermolecular i-motif structure is concentration dependent (Mergny et al., 1995) and although all of the samples used in this work had a DNA concentration of 10 μM, a slow, low-temperature induced, formation of i-motif would result in there being different concentrations of the intermolecular structure at the different time points; and consequently a difference in the melting temperatures, which we do not observe.

TABLE 1 | Half-life values calculated from fitting ellipticity at 288 nm (CD) and normalized absorbance at 295 nm (UV) to one-phase exponential decay functions of 10 μM hTeloC in 10 mM sodium cacodylate buffer pH 7.11 at 20°C after equilibration at 4°C for 3, 6, 24, and 72 h.

Time at 4°C (h)	CD	UV
	Half-life (min)	
3	16.4 ± 1.7	8.0 ± 0.6
6	37.2 ± 3.3	49.4 ± 3.4
24	74.8 ± 3.8	53.3 ± 1.4
72	82.8 ± 4.1	68.8 ± 2

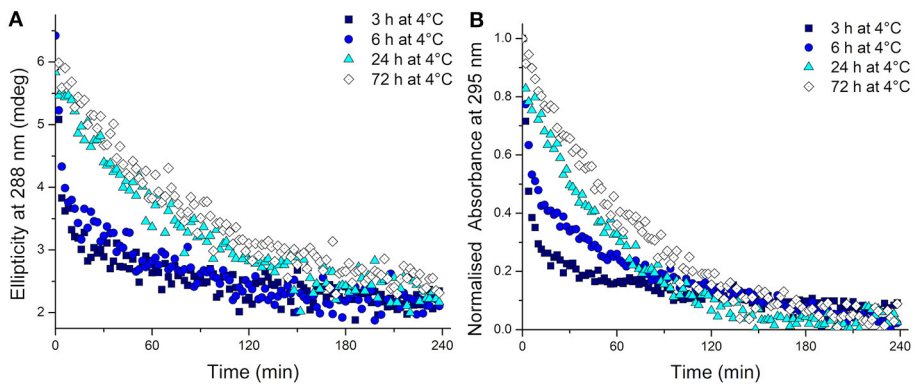

FIGURE 2 | (A) Ellipticity at 288 nm and **(B)** normalized absorbance at 295 nm of 10 μM hTeloC in 10 mM sodium cacodylate buffer pH 7.11 measured every 2 min after storage at 4°C for the indicated time.

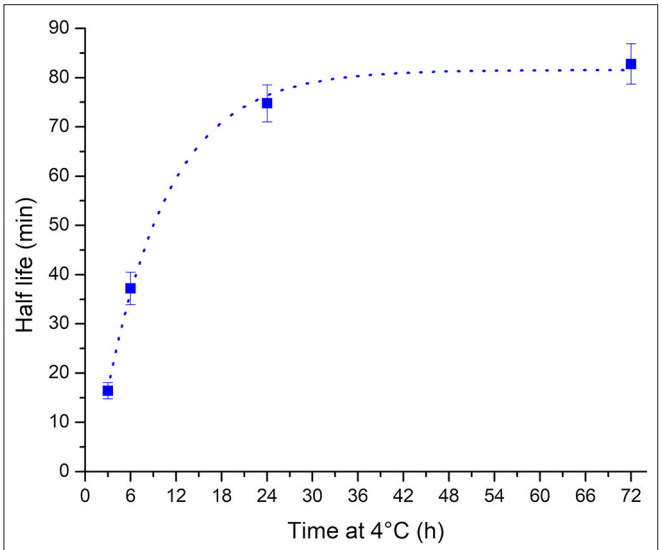

FIGURE 3 | Plot of half-life vs. storage time at 4°C showing that the half-life increases with increasing length of time at low temperature. The relationship is well fitted to a one phase exponential growth function (dotted line).

Furthermore, the latter explanation mirrors exactly what was described by Lieblein et al. when studying the folding of their variant of the human telomeric i-motif sequence 5′-[(CCC-TAA)$_3$CCC]-3′ (which differs from the hTeloC sequence used here only by the absence of three flanking bases). Their study found that in response to a drop in pH from 9 to 6 their sequence formed the less stable 3′E conformation more rapidly than the more stable 5′E conformation (Lieblein et al., 2012). Therefore, it seems from the data we have gathered that an analogous conformational change occurs at low temperature with hTeloC at slightly alkaline pH: it more rapidly forms a kinetically favored, but less stable, conformation and this converts slowly to a more thermodynamically stable conformation over time.

The observed change in the unfolding kinetics explains the initial unintended observation of folded i-motif at pH 7 at room temperature after storage of samples in the refrigerator between measurements. While the samples were taken out of the refrigerator so that they could return to room temperature prior to measurement, the only consideration cannot simply be the sample's temperature but the extension in the unfolding half-life must also be considered. The calculated half-life values vs. the length of time spent at 4°C are well fitted (R^2 = 0.997) to a one-phase exponential growth function (**Figure 3**). Using this method the half-life of the i-motif at a given temperature after cold storage for different lengths of time can be calculated. The cautionary tale of this surprisingly slow change in the kinetics of the i-motif's unfolding has led to the discovery of a phenomenon that adds a further avenue in the design of i-motif based nanotechnologies. For example, slow unfolding kinetics could be utilized in the release of a drug over a period of hours using these conditions. In addition to having systems which have their response tuned to the myriad combinations of changes in pH, cations or temperature; this introduces the ability to control the rate of unfolding of i-motif sensors and systems on the order of minutes or hours as opposed to the rapid transitions seen in response to changes in pH or temperature and without having to change its environment. This finding also lends credence to the i-motif playing a role in the control of biological processes. This sequence from the human telomeric region has not been known previously to be able to exist in the folded i-motif state above neutral pH and at room temperature. Knowing now the dramatic changes possible in the thermodynamic and kinetic stability of the structure it is not unreasonable to imagine how physiological conditions of molecular crowding, superhelical stress, interactions with proteins, or many others, could give rise to stable i-motifs *in vivo*.

We have found that the i-motif forming sequence from the human telomeric region not only folds into i-motif above neutral pH at low temperature. Moreover, this quadruplex structure can persist in the same conditions of neutral pH and ambient temperature in which, once at thermodynamic equilibrium, it exists predominantly as a random coil. The i-motif unfolding kinetics were found to be dependent on the time allowed for annealing and equilibration, and crucially the temperature at which samples are maintained. This research demonstrates the importance of consistency when annealing and storing i-motif samples, and highlights the dynamic nature of the quadruplex. Our findings have implications not only for work with i-motif DNA structures, but also in the uses and applications of i-motifs in nanotechnological devices.

DATA AVAILABILITY STATEMENT

The raw data supporting the conclusions of this article will be made available by the authors, without undue reservation, to any qualified researcher.

AUTHOR CONTRIBUTIONS

MA and ZW conceived and designed the experiments and wrote the paper. MA performed the experiments and analyzed the results. Both authors verified the data, contributed to the manuscript, and approved the final version.

FUNDING

This work was supported by the Biotechnology and Biological Sciences Research Council [BB/L02229X/1].

SUPPLEMENTARY MATERIAL

The Supplementary Material for this article can be found online at: https://www.frontiersin.org/articles/10.3389/fchem.2020.00040/full#supplementary-material

REFERENCES

Abdelhamid, M. A. S., Fábián, L., MacDonald, C. J., Cheesman, M. R., Gates, A. J., and Waller, Z. A. E. (2018). Redox-dependent control of i-Motif DNA structure using copper cations. *Nucleic Acids Res.* 46, 5886–5893. doi: 10.1093/nar/gky390

Abou Assi, H., Garavís, M., González, C., and Damha, M. J. (2018). i-Motif DNA: structural features and significance to cell biology. *Nucleic Acids Res.* 46, 8038–8056. doi: 10.1093/nar/gky735

Alberti, P., Bourdoncle, A., Saccà, B., Lacroix, L., and Mergny, J.-L. (2006). DNA nanomachines and nanostructures involving quadruplexes. *Org. Biomol. Chem.* 4:3383. doi: 10.1039/b605739j

Arora, A., Nair, D. R., and Maiti, S. (2009). Effect of flanking bases on quadruplex stability and Watson-Crick duplex competition. *FEBS J.* 276, 3628–3640. doi: 10.1111/j.1742-4658.2009.07082.x

Assi, H. A., Harkness, R. W., Martin-Pintado, N., Wilds, C. J., Campos-Olivas, R., Mittermaier, A. K., et al. (2016). Stabilization of i-motif structures by 2′-β-fluorination of DNA. *Nucleic Acids Res.* 44, 4998–5009. doi: 10.1093/nar/gkw402

Bhavsar-Jog, Y. P., Van Dornshuld, E., Brooks, T. A., Tschumper, G. S., and Wadkins, R. M. (2014). Epigenetic modification, dehydration, and molecular crowding effects on the thermodynamics of i-Motif structure formation from C-Rich DNA. *Biochemistry* 53, 1586–1594. doi: 10.1021/bi401523b

Brazier, J. A., Shah, A., and Brown, G. D. (2012). I-Motif formation in gene promoters: unusually stable formation in sequences complementary to known G-quadruplexes. *Chem. Commun.* 48:10739. doi: 10.1039/c2cc30863k

Chen, Y., Qu, K., Zhao, C., Wu, L., Ren, J., Wang, J., et al. (2012). Insights into the biomedical effects of carboxylated single-wall carbon nanotubes on telomerase and telomeres. *Nat. Commun.* 3:1074. doi: 10.1038/ncomms2091

Cui, J., Waltman, P., Le, V. H., and Lewis, E. A. (2013). The effect of molecular crowding on the stability of human c-MYC promoter sequence I-motif at neutral pH. *Molecules* 18, 12751–12767. doi: 10.3390/molecules181012751

Day, H. A., Huguin, C., and Waller, Z. A. E. (2013). Silver cations fold i-motif at neutral pH. *Chem. Commun.* 49:7696. doi: 10.1039/c3cc43495h

Day, H. A., Pavlou, P., and Waller, Z. A. E. (2014). i-Motif DNA: structure, stability and targeting with ligands. *Bioorg. Med. Chem.* 22, 4407–4418. doi: 10.1016/j.bmc.2014.05.047

Dembska, A. (2016). The analytical and biomedical potential of cytosine-rich oligonucleotides: a review. *Anal. Chim. Acta* 930, 1–12. doi: 10.1016/j.aca.2016.05.007

Dzatko, S., Krafcikova, M., Hänsel-Hertsch, R., Fessl, T., Fiala, R., Loja, T., et al. (2018). Evaluation of the stability of DNA i-Motifs in the nuclei of living mammalian cells. *Angew. Chemie Int. Ed.* 57, 2165–2169. doi: 10.1002/anie.201712284

Gehring, K., Leroy, J.-L., and Guéron, M. (1993). A tetrameric DNA structure with protonated cytosine-cytosine base pairs. *Nature* 363, 561–565. doi: 10.1038/363561a0

Gurung, S. P., Schwarz, C., Hall, J. P., Cardin, C. J., and Brazier, J. A. (2015). The importance of loop length on the stability of i-motif structures. *Chem. Commun.* 51, 5630–5632. doi: 10.1039/C4CC07279K

Jonchhe, S., Shrestha, P., Ascencio, K., and Mao, H. (2018). A new concentration jump strategy reveals the lifetime of i-Motif at physiological pH without force. *Anal. Chem.* 90, 3205–3210. doi: 10.1021/acs.analchem.7b04661

Lieblein, A. L., Buck, J., Schlepckow, K., Fürtig, B., and Schwalbe, H. (2012). Time-resolved NMR spectroscopic studies of DNA i-Motif folding reveal kinetic partitioning. *Angew. Chemie Int. Ed.* 51, 250–253. doi: 10.1002/anie.201104938

Lieblein, A. L., Fürtig, B., and Schwalbe, H. (2013). Optimizing the kinetics and thermodynamics of DNA i-Motif folding. *ChemBioChem* 14, 1226–1230. doi: 10.1002/cbic.201300284

Mergny, J.-L., and Lacroix, L. (2003). Analysis of thermal melting curves. *Oligonucleotides* 13, 515–537. doi: 10.1089/154545703322860825

Mergny, J.-L., Lacroix, L., Han, X., Leroy, J.-L., and Helene, C. (1995). Intramolecular folding of pyrimidine oligodeoxynucleotides into an i-DNA Motif. *J. Am. Chem. Soc.* 117, 8887–8898. doi: 10.1021/ja00140a001

Nguyen, T., Fraire, C., and Sheardy, R. D. (2017). Linking pH, temperature, and K + concentration for DNA i-Motif formation. *J. Phys. Chem. B* 121, 7872–7877. doi: 10.1021/acs.jpcb.7b06317

Phan, A. T., and Mergny, J.-L. (2002). Human telomeric DNA: G-quadruplex, i-motif and Watson-Crick double helix. *Nucleic Acids Res.* 30, 4618–4625. doi: 10.1093/nar/gkf597

Rogers, R. A., Fleming, A. M., and Burrows, C. J. (2018). Unusual isothermal hysteresis in DNA i-Motif pH transitions: a Study of the RAD17 Promoter Sequence. *Biophys. J.* 114, 1804–1815. doi: 10.1016/j.bpj.2018.03.012

Saxena, S., Joshi, S., Shankaraswamy, J., Tyagi, S., and Kukreti, S. (2017). Magnesium and molecular crowding of the cosolutes stabilize the i-motif structure at physiological pH. *Biopolymers* 107:e23018. doi: 10.1002/bip.23018

Školáková, P., Renčiuk, D., Palacký, J., Krafčík, D., Dvoráková, Z., and Kejnovská, I., et al. (2019). Systematic investigation of sequence requirements for DNA i-motif formation. *Nucleic Acids Res.* 47, 2177–2189. doi: 10.1093/nar/gkz046

Sun, D., and Hurley, L. H. (2009). The importance of negative superhelicity in inducing the formation of G-quadruplex and i-Motif structures in the c-Myc promoter: implications for drug targeting and control of gene expression. *J. Med. Chem.* 52, 2863–2874. doi: 10.1021/jm900055s

Tateishi-Karimata, H., Nakano, S. I., and Sugimoto, N. (2013). Quantitative analyses of nucleic acid stability under the molecular crowding condition induced by cosolutes. *Curr. Protoc. Nucleic Acid Chem.* 53, 1–17. doi: 10.1002/0471142700.nc0719s53

Tsvetkov, V. B., Zatsepin, T. S., Belyaev, E. S., Kostyukevich, Y. I., Shpakovski, G. V., Podgorsky, V. V., et al. (2018). i-Clamp phenoxazine for the fine tuning of DNA i-motif stability. *Nucleic Acids Res.* 46, 2751–2764. doi: 10.1093/nar/gky121

Wright, E. P., Huppert, J. L., and Waller, Z. A. E. (2017a). Identification of multiple genomic DNA sequences which form i-motif structures at neutral pH. *Nucleic Acids Res.* 45, 2951–2959. doi: 10.1093/nar/gkx090

Wright, E. P., Lamparska, K., Smith, S. S., and Waller, Z. A. E. (2017b). Substitution of cytosine with guanylurea decreases the stability of i-Motif DNA. *Biochemistry* 56, 4879–4883. doi: 10.1021/acs.biochem.7b00628

Xu, B., Devi, G., and Shao, F. (2015). Regulation of telomeric i-motif stability by 5-methylcytosine and 5-hydroxymethylcytosine modification. *Org. Biomol. Chem.* 13, 5646–5651. doi: 10.1039/C4OB02646B

Zhou, J., Wei, C., Jia, G., Wang, X., Feng, Z., and Li, C. (2010). Formation of i-motif structure at neutral and slightly alkaline pH. *Mol. BioSyst.* 6, 580–586. doi: 10.1039/B919600E

Conflict of Interest: The authors declare that the research was conducted in the absence of any commercial or financial relationships that could be construed as a potential conflict of interest.

frontiers in Chemistry

ORIGINAL RESEARCH
published: 12 February 2020
doi: 10.3389/fchem.2020.00060

Surface Dependent Dual Recognition of a G-quadruplex DNA With Neomycin-Intercalator Conjugates

Nihar Ranjan[1,2], *Katrine F. Andreasen*[1], *Yashaswina Arora*[2], *Liang Xue*[1] and *Dev P. Arya*[1]*

[1] Laboratory for Medicinal Chemistry, Department of Chemistry, Clemson University, Clemson, SC, United States,
[2] Department of Medicinal Chemistry, National Institute of Pharmaceutical Education and Research, Raebareli, India

G-quadruplexes have been characterized as structures of vital importance in the cellular functioning of several life forms. They have subsequently been established to serve as a therapeutic target of several diseases including cancer, HIV, tuberculosis and malaria. In this paper, we report the binding of aminosugar-intercalator conjugates with a well-studied anti-parallel G-quadruplex derived from *Oxytricha Nova* G-quadruplex DNA. Of the four neomycin-intercalator conjugates studied with varying surface areas, BQQ-neomycin conjugate displayed the best binding to this DNA G-quadruplex structure with an association constant of $K_a = (1.01 \pm 0.03) \times 10^7$ M^{-1} which is nearly 100-fold higher than the binding of neomycin to this quadruplex. The binding of BQQ-neomycin displays a binding stoichiometry of 1:1 indicating the presence of a single and unique binding site for this G-quadruplex. In contrast, the BQQ-neomycin displays very weak binding to the bacterial A-site rRNA sequence showing that BQQ-does not enhance the neomycin binding to its natural target, the bacterial rRNA A-site. The BQQ-neomycin conjugate is prone to aggregation even at low micromolar concentrations (4 μM) leading to some ambiguities in the analysis of thermal denaturation profiles. Circular dichroism experiments showed that binding of BQQ-neomycin conjugate causes some structural changes in the quadruplex while still maintaining the overall anti-parallel structure. Finally, the molecular docking experiments suggest that molecular surface plays an important role in the recognition of a second site on the G-quadruplex. Overall, these results show that molecules with more than one binding moieties can be made to specifically recognize G-quadruplexes with high affinities. The dual binding molecules comprise of quadruplex groove binding and intercalator units, and the molecular surface of the intercalator plays an important part in enhancing binding interaction to the G-quadruplex structure.

Keywords: G-quadruplex, *Oxytricha Nova*, neomycin, DNA, FID

OPEN ACCESS

Edited by:
Janarthanan Jayawickramarajah, Tulane University, United States

Reviewed by:
Miguel Angel Aleman Garcia, Eindhoven University of Technology, Netherlands
Narayanan Selvapalam, Kalasalingam University, India

***Correspondence:**
Dev P. Arya
dparya@clemson.edu

Specialty section:
This article was submitted to Supramolecular Chemistry, a section of the journal Frontiers in Chemistry

Received: *16 November 2019*
Accepted: *20 January 2020*
Published: *12 February 2020*

Citation:
Ranjan N, Andreasen KF, Arora Y, Xue L and Arya DP (2020) Surface Dependent Dual Recognition of a G-quadruplex DNA With Neomycin-Intercalator Conjugates. Front. Chem. 8:60. doi: 10.3389/fchem.2020.00060

INTRODUCTION

G-quadruplex structures are highly polymorphic DNA structures that can exist in dynamic equilibrium with other possible orientations of the same structure (Seenisamy et al., 2004). G-quadruplexes have been found at the telomeric ends and they have also been shown to form in several segments of the genomic DNA as well (Huppert and Balasubramanian, 2007). In several cases, the formation of G-quadruplex is only transient to propagate cellular functions and often they work in tandem with proteins (Wen and Gray, 2002; Hegyi, 2015). Because of the ability of

G-quadruplex to serve as a central structure to control cell integrity and its role in transcriptional control, they have been regarded as a target for developing new therapeutics, especially for cancer (Neidle, 2010). However, several other life forms such as bacteria, fungus and viruses have been shown to possess regions capable of forming G-quadruplex and they have been suggested to play prominent roles in their life progression (Thakur et al., 2014; Artusi et al., 2015; Perrone et al., 2017). Due to these advances in the field, G-quadruplexes have moved far away from being a cancer-centric target to a structure which has relevance in the design of new antibacterial, antifungal and antiviral agents.

Formation of G-quadruplex requires stacked G-tetrads which are formed by the planar assembly of four guanines using eight Hoogsteen hydrogen bonds thus making these structures highly thermally stable (Burge et al., 2006). Each quadruplex discovered till date has unique distinguishing features. The uniqueness primarily lies in their distinct folding patterns. The differences in the folding patterns are inherent to changes in the loop connectivity and stabilizing metal cations resulting in large differences in the groove structures (Hazel et al., 2004; Bhattacharyya et al., 2016). Therefore, unlike the defined groove features of A-form and B-form DNA structures, quadruplex grooves show large variations in groove widths, depths, inter-phosphate distances between the DNA strands and base orientations which are ultimately related to the size of the stabilizing metal cations, as well as, the length, base composition and directionality of the loops. The differences in the groove widths and shapes offer new vistas for their recognition where dual recognition strategies can be employed given to the proven predilection of G-tetrads for chemical moieties containing planar fused polycyclic aromatic rings with extended π-systems (Monchaud and Teulade-Fichou, 2008).

Using different recognition strategies, we have tailored the synthesis of dual and triple binding ligands to achieve molecular recognition of a variety of nucleic acid forms including duplexes, triplexes, quadruplexes and single-stranded nucleic acids and nucleic acid models of functionally relevant regions of DNA and RNA structures (Xue et al., 2002, 2011; Charles et al., 2007; Xi et al., 2009; Willis and Arya, 2010; Kumar and Arya, 2011; Ranjan and Arya, 2013, 2016; Ranjan et al., 2013a,b; Watkins et al., 2013, 2017; Kellish et al., 2014; Jiang et al., 2015; Nahar et al., 2015; Kumar et al., 2016; Degtyareva et al., 2017; Story et al., 2019). We have previously reported that neomycin (**Figure 1**), which is an antibiotic belonging to the aminoglycoside class, can recognize DNA G-quadruplex structures with moderate (Ranjan et al., 2010) to high affinities (Ka $\sim$ 10^5-10^8 M^{-1}) and its binding can be modulated by converting it into a dual binding ligand (Xue et al., 2011; Ranjan et al., 2013a). Conjugating neomycin with G-quadruplex binding moieties can lead to up to 1,000-fold enhancement in the binding affinity to target G-quadruplexes than the individual moieties (Ranjan et al., 2013a). Taking cues from these results, we wished to explore the effect of fused aromatic surfaces in the DNA G-quadruplex recognition. Accordingly, four neomycin-intercalator conjugates (**Figure 1**) that differed in the ring size and composition of the intercalator were taken to study the effect of the stacking surfaces in the G-quadruplex recognition. For the G-quadruplex, we chose the telomeric G-quadruplex derived from *Oxytricha Nova* which is a well-resolved (Schultze et al., 1994), structurally well-understood and well-defined DNA quadruplex structure that adopts anti-parallel orientation (Smith and Feigon, 1992). Moreover, given our prior understating of neomycin binding to the G-quadruplex DNA structure (Ranjan et al., 2010), we chose this sequence to understand the π-surface area and composition effects in the dual recognition of G-quadruplexes.

In the presence of sodium salt, *Oxytricha Nova* telomeric DNA adopts an antiparallel G-quadruplex structure with four grooves of widths ∼6–18 Å (Schultze et al., 1994). The four grooves, formed in this quadruplex are potential binding sites of aminoglycosides. In this report, we sought to understand the effect of ring size and composition on G-quadruplex dual recognition in which neomycin was presumed to play the anchor role. To see the relevance of these conjugates in nucleic acid selectivity, we have compared the binding of the best binder with a duplex DNA and the bacterial rRNA A-site which is the natural and high affinity target of aminoglycosides (Arya, 2007).

MATERIALS AND METHODS

Nucleic Acid Samples

The DNA oligonucleotides samples used in this study were purchased from IDT (Coraville, IA). The RNA oligonucleotides were purchased from Dharmacon Research. All nucleic acid samples were used without further purification. The concentrations of both DNA and RNA sample solutions were determined by measuring UV absorbance at 85°C to ensure that the nucleic acids did not possess any secondary structure. The DNA quadruplex structure was formed by heating the stock nucleotide solution in a buffer solution containing sodium ions (Na^+, 100 mM), to 95°C for 15 min and then slowly cooling the samples back to room temperature in a non-controlled manner. The DNA quadruplex samples were then left to incubate at 4°C for 2 days before they were used for further experiments. The DNA duplex sample was formed by heating it to 95°C for 5 min in a buffer containing 10 mM sodium cacodylate, 0.5 mM EDTA and 100 mM NaCl at pH 7.0. The sample was brought to room temperature by allowing it to self-cool and then incubating it at 4°C overnight before it was used for experiments. The bacterial rRNA A-site oligonucleotide sample was heated to 95°C for 5 min in a buffer containing 10 mM sodium cacodylate, 0.5 mM EDTA, and 100 mM NaCl at pH 7.0 and then it was quickly snap-cooled on ice. It was then stored at 4°C overnight before it was used for further experiments.

Chemicals

Aminoglycosides used in the study were purchased from MP Biomedicals (Solon, OH). All chemicals were used without further purification. The neomycin conjugates used in this study were prepared in-house (Xue et al., 2010).

UV-vis Spectroscopy

The thermal denaturation experiments were obtained on a Cary 100 UV-vis spectrophotometer containing a multi-cell (12

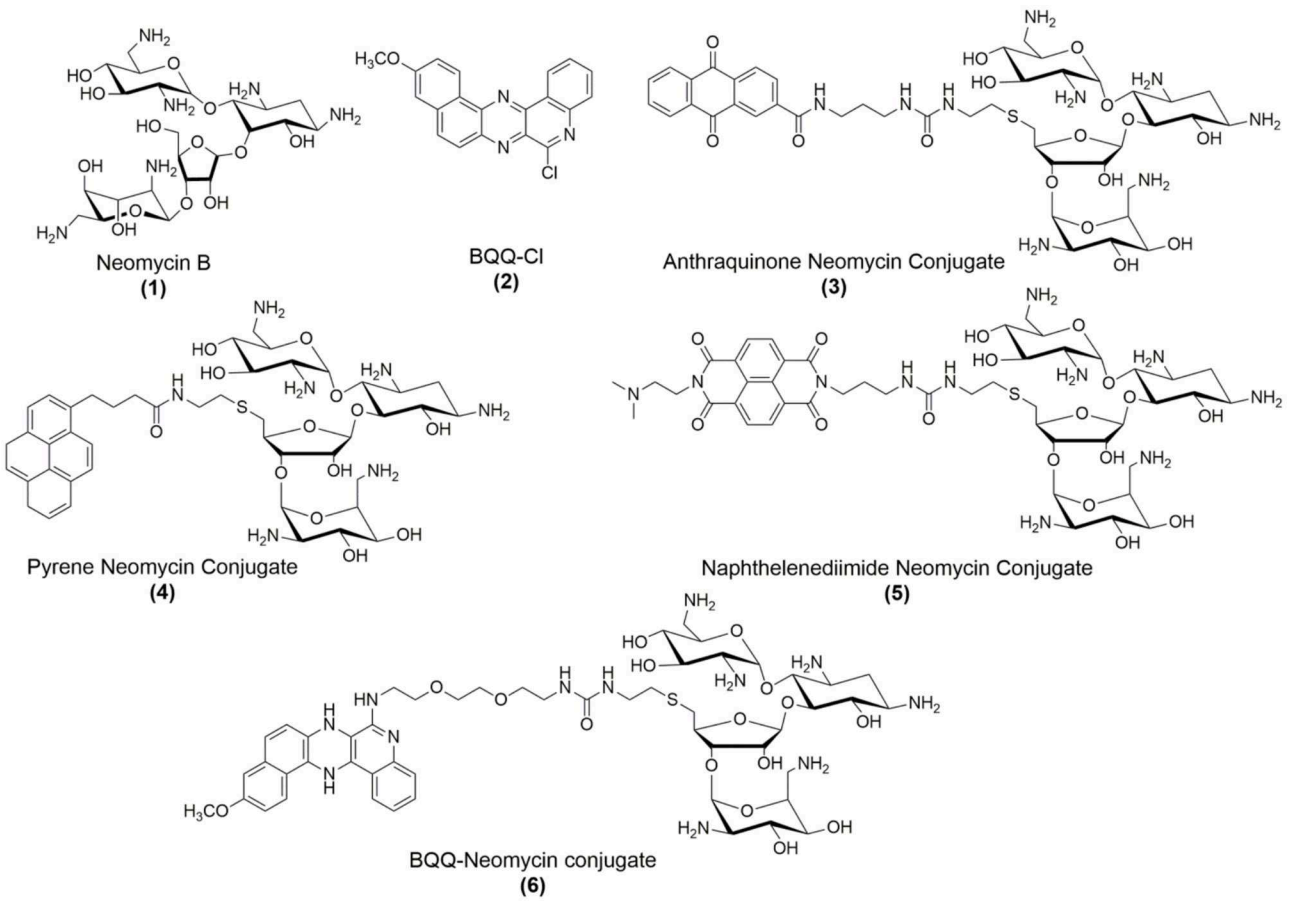

FIGURE 1 | Chemical structures of compounds used in this study.

cell) holder equipped with pettier thermal controller. For all experiments, Quartz cells with 1 cm path length were used. The spectrophotometer stability was checked prior to each melting point experiment. The DNA melting was monitored at 260, 235, and 295 nm wavelengths and the samples were denatured between 20 and 98°C at the heating rate of 0.2°C/min. Data points were recorded every 1.0°C. The resulting temperature-absorbance plots were plotted using Kaleidagraph 3.5 software. The melting temperatures were determined as described by Mergny (Mergny and Lacroix, 2003).

Circular Dichroism Experiments

The circular dichroism (CD) experiments were performed using a JASCO J-810 spectropolarimeter containing a four cell multi-cell holder and equipped with thermo-electrically controlled Chiller. Each CD spectrum was recorded as an average of three scans at 20°C. For CD titration experiments, a concentrated solution of the ligand was serially added to the DNA quadruplex sample and allowed to equilibrate for 5 min before a scan was taken. The resulting scan was plotted for CD signal changes with respect to wavelength or with respect to the number of equivalents taken to get the stoichiometry details.

Fluorescence Intercalator Displacement (FID) Studies

The fluorescence intercalator displacement experiments reported in this study were performed on a Photon Technology International instrument (Lawrenceville, NJ) equipped with a temperature controller. All experiments reported in this study were performed at 20°C. The experiments were performed in a 3 mL quartz cell having a path length of 10 mm. The concentration of nucleic acid solutions used in this study was 0.25 μM/quadruplex or duplex or strand (for bacterial rRNA A-site studies). For each FID experiment the nucleic acid sample was mixed with Thiazole orange (TO) with a concentration of 0.50 μM. All experiments reported in this study were performed in 10 mM sodium cacodylate, 0.5 mM EDTA and 100 mM NaCl at buffer pH 7.0. The ligands were then serially added to the DNA/TO solution until the TO fluorescence was completely quenched. Each ligand addition was followed by a 4 min equilibration time before the fluorescence spectrum was recorded. The TO excitation was at 501 nm and the emission was then recorded from 510 to 650 nm. In all the experiments, the excitation and emission slit widths were 1.5 mm. For determination of binding constant, Scatchard analysis was done using

the procedure described previously by Boger et al. (2001) in which—

$$(\Delta F_X/\Delta F_{Sat}).(1/X) = \text{Fraction of DNA} - \text{ligand Complex} \quad (1)$$

$$[1 - (\Delta F_X/\Delta F_{Sat}).(1/X)] = \text{Fraction of free ligand} \quad (2)$$

$$[DNA]_T.[X - (\Delta F_X/\Delta F_{Sat})] = [\text{Free ligand}] \quad (3)$$

Where,

X = Molar equivalent of ligand to quadruplex DNA
ΔF_X = Change in fluorescence
ΔF_{Sat} = Change in fluorescence when the quadruplex DNA is fully saturated with ligand
$[DNA]_T$ = Total DNA concentration.

Aggregation Studies

The aggregation behavior of BQQ-neomycin conjugate was checked using the Cary 100 UV-vis spectrophotometer. Both thermal melting and concentration-dependent absorbance studies were done to check the aggregation behavior. In thermal melting studies, the BQQ-neomycin conjugate was heated in 10 mM sodium cacodylate, 0.5 mM EDTA and 100 mM NaCl at buffer pH 7.0 at 2.5 and 5.0 μM concentration between 30 and 98°C and resulting absorbance vs. temperature graph was plotted. For concentration-dependent absorbance studies, different concentrations (0.2–36 μM) of the BQQ-neomycin conjugate were scanned between 200 and 600 nm and the resulting absorbance vs. concentration graph was plotted. The experiments were done in buffer 10 mM sodium cacodylate, 0.5 mM EDTA and 100 mM NaCl at buffer pH 7.0 at 23°C.

Molecular Docking Studies

All docking experiments were performed as blind dockings where the blind docking refers to the use of a grid box which is large enough to cover all possible ligand-receptor interactions. AutoDock Vina, which has several advantages over its preceding version AutoDock 4.2, was used to perform docking experiments. The G-quadruplex receptor structure was obtained from Protein Data Bank (PDB ID: 156D) which was used for docking experiments without any further modification in the structure. The ligand structures were created using ChemDraw 14 and then brought to their energetically minimized structures using the Vega ZZ program (Pedretti et al., 2004) utilizing a conjugate gradient method with SP4 force field. Autodock tools version 1.5.6 was used to convert the ligand and receptor molecules to the proper file formats for docking. The docking experiments were performed using an exhaustiveness value 50. All other parameters were used as defaults. All rotatable bonds within the ligand were allowed to rotate freely, and the receptor was considered rigid. The final rendering of the docked structures was done using PyMol (www.pymol.org).

RESULTS AND DISCUSSION

Fluorescence Intercalator Displacement Experiments

Fluorescence intercalator displacement assay (FID) was developed in Boger's laboratory (Boger and Tse, 2001; Boger et al., 2001; Tse and Boger, 2004) allowing for the screening of a variety of structurally and chemically diverse set of ligands. Unlike some other ligand screening methods which mandate the presence of a fluorophore in the ligand to be screened, this assay can be used to screen both fluorescent as well as non-fluorescent molecules binding to the nucleic acids. The utility of this assay has been demonstrated by many laboratories which have used both canonical and non-canonical nucleic acid structures of biological interest (Monchaud et al., 2006; Kumar and Arya, 2011; Kumar et al., 2011, 2015; Kellish et al., 2014). More importantly several applications of this assay have been shown to be useful in discovering G-quadruplex binding ligands (Monchaud et al., 2006).

In essence, this assay exploits the fluorescence enhancement of nucleic acid binding dyes that show non-specific binding and moderate affinities to their cognate structures. The intercalating dyes such as ethidium bromide or Thiazole orange are traditional intercalators used in this assay but recently the use of dyes such as Thioflavin T (ThT) is gaining momentum due to its special liking for certain G-quadruplex structures (Mohanty et al., 2012; Verma et al., 2019). In a typical experiment, the nucleic acid of interest is mixed with the intercalating dye in an appropriate ratio. The ratio of nucleic acid to the intercalator to be used in this assay is determined usually by running a fluorescence titration experiment in which the nucleic acid of interest is titrated against the intercalator ligand and the resulting fluorescence changes are used to construct a plot giving the stoichiometry of the intercalator-nucleic acid interaction. The FID assay is thus developed in which the ligand library to be screened is titrated into a solution containing the nucleic acid and the intercalator at a fixed ratio.

In our FID experiments, we used Thiazole orange (TO) which is much more responsive to fluorescence emission in comparison to the other popularly used intercalator: ethidium bromide (Boger et al., 2001). Thiazole orange binds to the *Oxytricha Nova* G-quadruplex DNA with a stoichiometry of 2:1 and for that reason, we took the same ratio of receptor to intercalator in our FID experiments. Addition of different ligands to the G-quadruplex-intercalator complex caused successive decrease in the fluorescence signal till the fluorescence signal reached the level of Thiazole orange fluorescence emission in the absence of the G-quadruplex DNA.

A representative example is shown in **Figure 2A** in which BQQ-neomycin conjugate (compound 6) was successively added to *Oxytricha Nova*-TO complex. As increasing amounts of compound **6** were added, the fluorescence emission intensity of TO continued to decrease suggesting displacement of bound Thiazole orange. The addition of ligand was continued till no more changes in the intensity of the TO emission signal was observed suggesting complete displacement of the bound TO. Such TO displacement titrations can also be used to determine the binding stoichiometry by plotting the percent fluorescent change with respect to number of the equivalents of the ligand added. As shown in **Figure 2B**, the displacement assay revealed that BQQ-neomycin conjugate (compound **6**) binds to the *Oxytricha Nova* G-quadruplex in 1:1 ratio. The

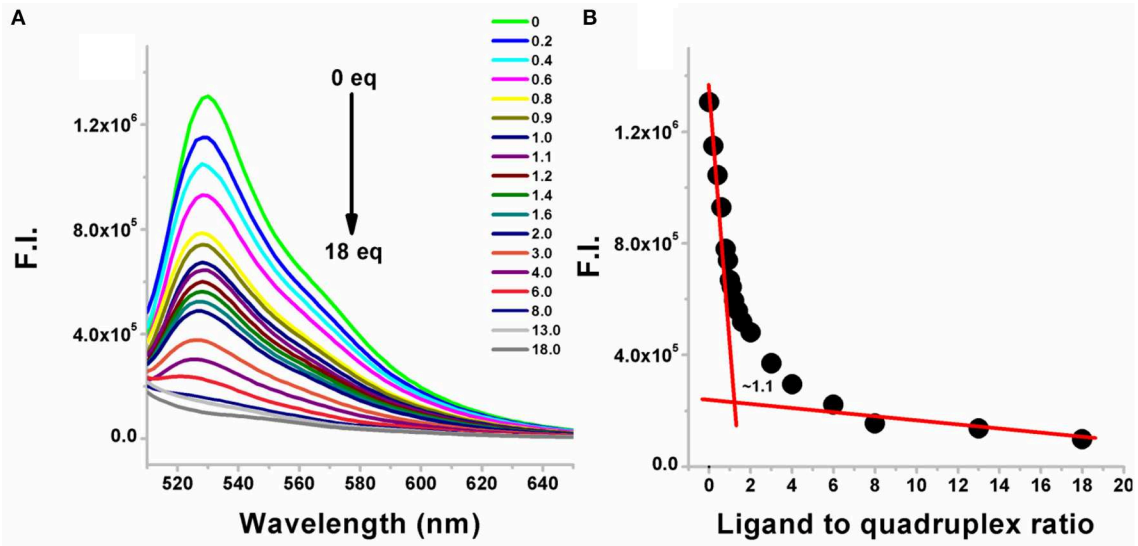

FIGURE 2 | (A) Fluorescence emission changes in the G-quadruplex-thiazole orange complex upon addition of neomycin-BQQ conjugate (compound **6**). The number of equivalents of compound **6** added from 0 to 18 equivalents is shown for each point. **(B)** The binding stoichiometry plot showing the binding stoichiometry of compound **6** with the *Oxytricha Nova* quadruplex. The experiments were performed in buffer 10 mM sodium cacodylate, 0.5 mM EDTA, 100 mM NaCl at pH 7.0 (T = 20°C). Thiazole orange was excited at 501 nm and the emission spectrum was recorded between 510 and 650 nm.

resulting displacement pattern was then plotted to obtain DC_{50} values where DC_{50} refers to the ligand concentration required to displace half of the bound intercalator from the G-quadruplex in these assays.

As shown in **Table 1**, **Figure S1**, DC_{50} values were calculated for different neomycin conjugates (**Figure 1**) along with the control ligands. Among the intercalators studied, BQQ-neomycin conjugate (compound **6**) showed the least amount of ligand (422-fold lesser than neomycin) required to displace 50% intercalator followed by anthraquinone-neomycin conjugate (253-fold lesser than neomycin). The other neomycin-intercalator conjugates studied, pyrene-neomycin (compound **4**) and naphthalenediimide-neomycin (compound **5**), also showed superior DC_{50}values than neomycin (16 and 10-folds lower, respectively). As a control, we performed the DC_{50} determination of a control duplex sequence d(AGGGGTTTTCCCCT) (**Table 1**, **Figure S2**). The DC_{50} values obtained for this experiment showed that the preference for quadruplex for BQQ-neomycin conjugate (compound **6**) was at least 3.5-fold higher while the same for pyrene-neomycin (compound **4**) was 2-fold higher than the duplex DNA. The other neomycin intercalators conjugates showed DC_{50} values lower for duplexes. These results clearly established that neomycin-anthraquinone and neomycin-BQQ conjugates preferentially bind to *Oxytricha Nova* G-quadruplex in comparison to a duplex DNA sequence whereas for neomycin pyrene and neomycin naphthalenediimide conjugates preference for the DNA duplex was more. Therefore, we turned our attention to the best quadruplex binder of the compounds studied, the neomycin-BQQ conjugate (compound **6**) for further detailed studies.

TABLE 1 | A table listing the DC_{50} values for different neomycin intercalator conjugates (compounds 1–6) with *Oxytricha Nova* G-quadruplex DNA and a DNA duplex sequence.

Ligand	d(GGGGTTTTGGGG) DC_{50} (μM)	d(AGGGGTTTTCCCCT) DC_{50} (μM)
Neomycin	76.02	53.44
BQQ-Cl	>250	–
Neomycin- Pyrene	4.73	2.61
Neomycin-Anthraquinone	0.30	0.75
Neomycin-BQQ	0.18	0.64
Neomycin-Naphthalenediimide	7.89	0.83

Determination of Association Constant of BQQ-Neomycin Conjugate

Since neomycin-BQQ conjugate binds to *Oxytricha Nova* G-quadruplex DNA sequence in a 1:1 ratio (**Figure 2B**), we performed a Scatchard analysis of the BQQ-neomycin FID titration data as described by Boger et al. (2001) and Yeung et al. (2003). The analysis (**Figure 3**) revealed that BQQ-neomycin conjugate (compound **6**) binds to the *Oxytricha Nova* G-quadruplex sequence with an affinity of $K_a = (1.01 \pm 0.03) \times 10^7\ M^{-1}$. We have previously shown that under same conditions the association constant (K_a) of neomycin for *Oxytricha Nova* sequence was $(1.03 \pm 0.50) \times 10^5\ M^{-1}$ (Ranjan et al., 2010). This result shows that conjugation of neomycin to BQQ leads to 98-fold higher affinity for the quadruplex. However, the affinity of BQQ-neomycin was found to be temperature-dependent as

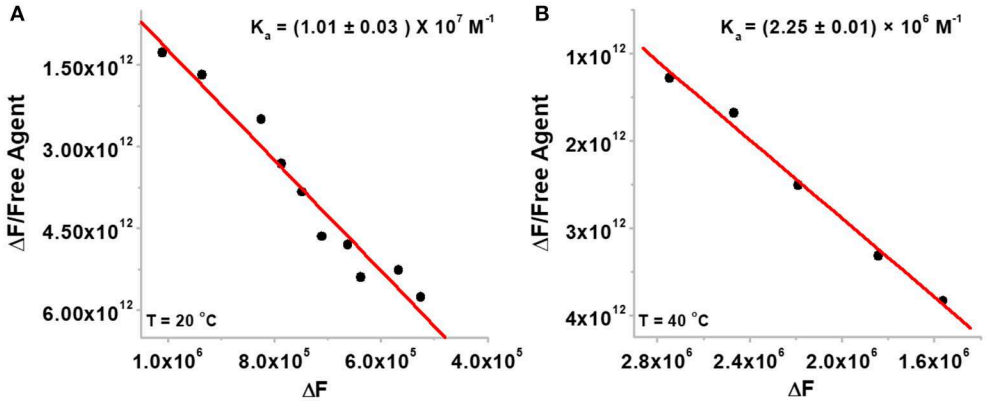

FIGURE 3 | The Scatchard plots of BQQ-neomycin binding to *Oxytricha Nova* G-quadruplex DNA at **(A)** 20°C and **(B)** 40°C. The experiments were performed in buffer 10 mM sodium cacodylate, 0.5 mM EDTA, 100 mM NaCl at pH 7.0.

increasing the study temperature to 40°C led to nearly a 4-fold decrease in the affinity of the conjugate with a $K_a = (2.25 \pm 0.01) \times 10^6\ M^{-1}$.

Comparative Binding With the Bacterial A-Site RNA

Since the bacterial rRNA A-site is the natural target of aminoglycosides, we investigated how the conjugation of neomycin affects the binding of neomycin to the bacterial rRNA A-site and how does the overall binding of BQQ-neomycin compare to all of its possible binding targets. As shown in **Figure 4A**, the addition of BQQ-neomycin conjugate to the bacterial rRNA-TO complex led to a continuous decrease in the fluorescence emission of TO. The FID titration was stopped when further addition of BQQ- neomycin led to negligible changes in the emission signal of TO. Further analysis of the binding event showed that like the *Oxytricha Nova* G-quadruplex DNA, it binds with the rRNA A-site sequence with 1:1 binding stoichiometry (**Figure 4B**). Scatchard analysis (**Figure 4C**) revealed that BQQ-neomycin binds with the rRNA A-site with an affinity of $K_a = (9.10 \pm 0.23) \times 10^6\ M^{-1}$ which is lower than the binding of the same with the *Oxytricha Nova* G-quadruplex sequence. Further analysis of the results showed that the DC_{50} value for this FID experiment was (276.0 ± 8.2) nM while the same for neomycin was (135.4 ± 9.4) nM. These results showed that conjugation of BQQ to neomycin makes it a poor bacterial rRNA A-site binder by nearly 2-fold change in the affinity.

CD Experiments Show Evidence of Complexation of *Oxytricha nova* Quadruplex With the BQQ-Neomycin Conjugate

Circular dichroism experiments have been extensively used for the study of G-quadruplexes (Randazzo et al., 2012; Vorlíčková et al., 2012). The different types of G-quadruplexes show unique CD signature peaks in which parallel quadruplexes show absorption maximum at 260 nm and the minimum at 240 nm, while the antiparallel quadruplexes show an absorption maxima at 295 nm and the minimum is observed at 260 nm (Balagurumoorthy and Brahmachari, 1994). We performed CD titrations to find out (a) the ligand-induced changes in the CD signal to observe any conformational change accompanying the ligand binding, and (b) to find out the binding site size for the ligand to quadruplex. The CD titration of the *Oxytricha nova* quadruplex was initially performed with the BQQ-neomycin conjugate (**Figure 5A**). In the absence of ligand, the maximum of the CD signal was observed at ∼295 nm while the minimum was at ∼260 nm which was consistent with the antiparallel structure of this G-quadruplex as reported previously (Balagurumoorthy et al., 1992).

When BQQ-neomycin was added to the *Oxytricha Nova* quadruplex, significant changes in the CD signal were observed (**Figure 5A**). With the addition of small aliquots of the ligand, the positive CD signal at 295 nm continuously diminished. At high ligand to quadruplex ratios (more than three equivalents of ligand to the DNA), DNA precipitation was observed. Concurrently, the CD signal at 260 nm became much more negative upon addition of incremental amounts of ligand. From this titration, it is sufficiently evident that the mode of interaction of BQQ-neomycin conjugate is very different from neomycin which produces no change in the CD signal of the quadruplex even at much higher ligand concentrations than what has been used in this experiment. This reaction also confirms complexation of BQQ-neomycin to the *Oxytricha nova* G-quadruplex DNA. Analysis of the CD signal changes with respect to the ligand ratios added yielded the binding stoichiometry plot which showed 1:1 binding of the BQQ-neomycin conjugate with the *Oxytricha nova* G-quadruplex (**Figure 5B**). The binding of BQQ-Cl did not lead to any observable change in the CD signal (**Figure 5C**), which suggests that in the case of BQQ-neomycin titration, both neomycin and the BQQ moieties bind synergistically with the G-quadruplex. A series of compounds which are structurally similar to BQQ have shown quadruplex binding properties (Hounsou et al., 2007). These compounds have been proposed to have π-stacking interactions with the guanine bases. Another example

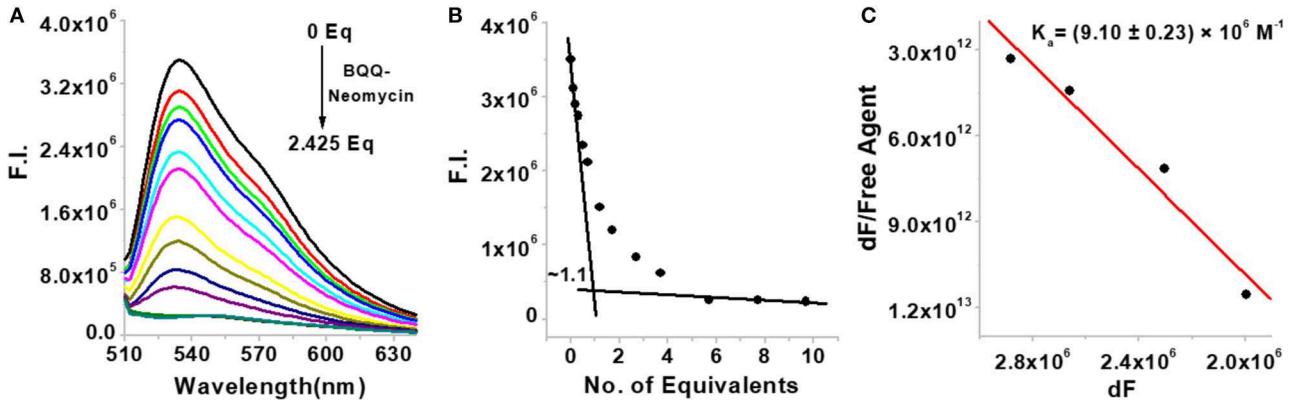

FIGURE 4 | (A) FID titration of bacterial rRNA A-site with BQQ-neomycin conjugate **(B)** binding stoichiometry plot of BQQ-neomycin conjugate's interaction with the rRNA A-site. **(C)** Scatchard analysis of binding interaction. The concentration of rRNA A-site was 0.25 μM and the experiments were performed in buffer 10 mM sodium cacodylate, 0.5 mM EDTA, 100 mM NaCl at pH 7.0 at 20°C.

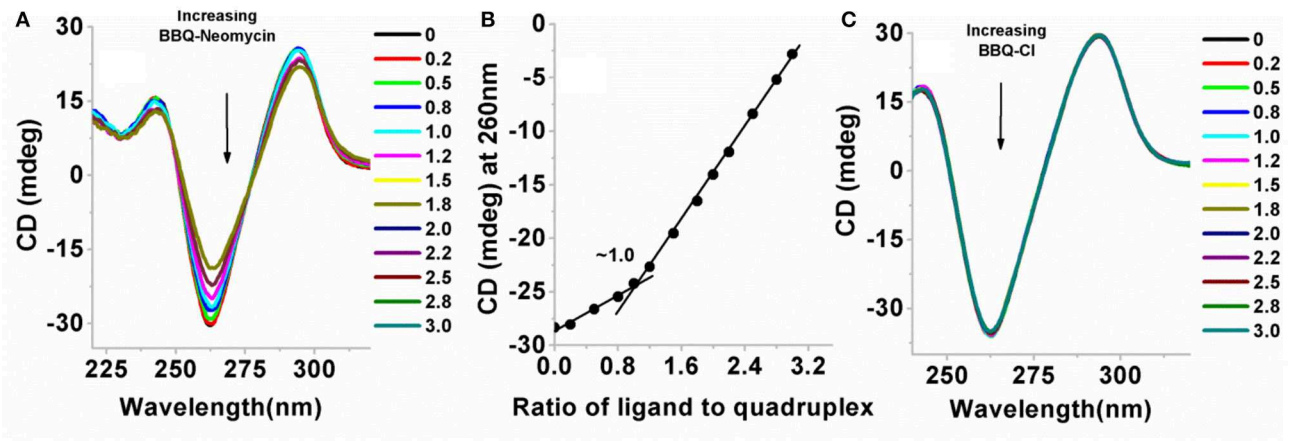

FIGURE 5 | (A) CD titration plot of BQQ-neomycin with the *Oxytricha Nova* G-quadruplex DNA. The ratios of BQQ-neomycin to the quadruplex are indicated in the legend. **(B)** CD detected binding stoichiometry plot of BQQ-neomycin interacting with the *Oxytricha Nova* G-quadruplex DNA. **(C)** Control titration experiment of BQQ-Cl with the *Oxytricha Nova* G-quadruplex DNA. The DNA concentration used in the experiments was 10 μM/strand and both the experiments were performed in buffer 10 mM sodium cacodylate, 0.5 mM EDTA, 100 mM NaCl at pH 7.0 at 20°C. Small aliquots of ligand were serially added [as indicated on plots **(A,C)**] to the DNA solution. During the titration, the DNA solution was stirred with the added ligand for 5 min followed by another 5 min of equilibration time. The CD signal represents an average of three scans.

where neomycin has been conjugated to such planar aromatic compounds has also been reported (Kaiser et al., 2006). It has been proposed that the planar aromatic part in this molecule also involves π- stacking interactions with the G-tetrad and neomycin has a role in establishing this conjugate as a G-quadruplex specific ligand (Kaiser et al., 2006). Altogether, the results obtained with CD experiments are in agreement with the previously reported findings.

UV Thermal Melting Experiments

UV monitored thermal denaturation experiments of nucleic acids are routinely used to study ligand-biomolecule interactions. The thermal melting experiments were performed to find any ligand-induced thermal stabilization by doing experiments both in the absence and presence of ligands. We monitored the changes in absorbance with respect to temperature at both 260 and 295 nm wavelengths. While in most quadruplexes the changes in absorbance are more prominent at 295 nm as compared to 260 nm (Mergny et al., 1998), we got satisfactory thermal melting profiles at 260 nm as shown in **Figure 6**. The *Oxytricha nova* quadruplex melted at 56.9°C in the absence of any ligand (**Figure 6A**). In the presence of pyrene-neomycin, anthraquinone neomycin, naphthalenediimide-neomycin (**Figure 6B**) or BQQ-Cl and neomycin alone, appreciable thermal stabilization was not observed (**Table 2**). However, in the presence of BQQ-neomycin, we saw signs of thermal stabilization of the G-quadruplex DNA as a biphasic thermal denaturation curve was obtained (**Figure 6A**). The first transition was observed at 59.8°C which is nearly three degree Celsius stabilization of the G-quadruplex. However, soon after the

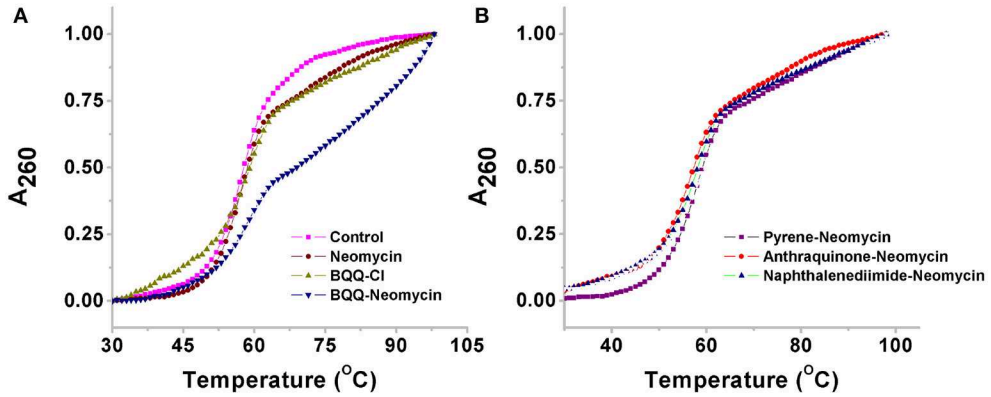

FIGURE 6 | Thermal denaturation profiles of **(A)** *Oxytricha Nova* G-quadruplex DNA in the absence and presence of BQQ-neomycin conjugate and its constituent ligand neomycin and BQQ-Cl. **(B)** *Oxytricha Nova* G-quadruplex DNA in the presence of pyrene-neomycin, anthraquinone neomycin and naphthalenediimide-neomycin conjugates. The experiments were performed at 10 μM/Strand (5 μM in quadruplex) DNA concentration and the ligands were added at 1:1 quadruplex to ligand ratio. The heating was done at a rate of 0.2°C per minute. All experiments were in buffer 10 mM sodium cacodylate, 0.5 mM EDTA, 100 mM NaCl at pH 7.0 and the absorbance data was normalized for comparison.

TABLE 2 | UV detected thermal denaturation temperatures of *Oxytricha Nova* G-quadruplex DNA in the presence of various ligands.

Ligand	Melting temperatures	
	T_m	ΔT_m (in °C)
None	56.9	–
Neomycin	56.9	0.0
BQQ-Cl	56.9	0.0
Pyrene-neomycin	58.8	1.9
Anthraquninone-neomycin	57.4	0.5
Naphthalenediimide-neomycin	57.5	0.6
BQQ-neomycin	59.8, 82.0	2.9*

**Melting transition was masked by the ligand self-dissociation events.*

end of the first transition, a second transition begins which is much broader and with a middle point at 82.0°C. Such biphasic thermal denaturation profiles are usually observed when more than one nucleic acid species are involved in the melting process or different sets of complex events are taking place during the ligand-biomolecule interaction. Initially, we thought of higher temperature transition to be the result of thermal stabilization of the quadruplex by this ligand. However, such transition was completely missing when we carried out the CD melting experiment which showed only one transition belonging to the melting of the quadruplex (data not shown). Since molecules having polycyclic aromatic rings with extended π-conjugation are prone to self-stacking in polar media, we decided to perform further experiments to trace the origins of the second transition and study the aggregation behavior of BQQ-neomycin conjugate itself as discussed in the next section.

Aggregation Studies of BQQ-Neomycin Conjugate

As shown in **Figure 7A**, the thermal melting of BQQ-neomycin conjugate was studied in the absence of DNA. In the absence of any DNA, the transitions that are observed are purely the resultant of temperature-dependent hyperchroism shown by the ligand itself. When the BQQ-neomycin conjugate was melted at a concentration of 2.5 μM, a slow rise in the absorbance of BQQ-neomycin conjugate was observed up to 70°C which abruptly rose afterwards. The overall melting profile appears similar to the one usually obtained in the presence of DNA. We performed another thermal denaturation experiment of BQQ-neomycin conjugate at 5.0 μM concentration. The denaturation profile in this experiment showed a much clearer melting transition with a T_m of 82.6°C. These experiments showed that BQQ-neomycin itself can show DNA like melting transitions and, therefore, caution must be taken in the interpretation of thermal denaturation of DNA-ligand complexes as ligands capable of self-stacking may mask, complicate or give misleading thermal melting temperatures. Such transitions can be attributed to the destacking of the ligand at higher temperatures as shown previously with Hoechst 33258 binding with the DNA (Kaushik and Kukreti, 2003).

We, then, sought to understand the concentration dependence of aggregation of BQQ-neomycin conjugate. As shown in **Figure 7B**, the absorbance spectra of BQQ-neomycin was recorded from low (0.2 μM) to moderate (36.0 μM) micromolar concentrations. The absorbance peak at 414 nm was then used to plot absorbance vs. concentration plot (**Figure 7C**) which clearly shows that the loss in the linearity of the graph is easily discernible. The deviation in the linearity was detected early at 4.0 μM concentration which became more prominent at concentrations 5.0 μM and above clearly mirroring the results obtained with the thermal denaturation experiments. Overall, these results suggest that BQQ-neomycin conjugate is prone to aggregation in buffer solutions as used in these experiments.

Molecular Docking Studies

To gain further insights into the molecular interactions taking place during quadruplex recognition, we performed

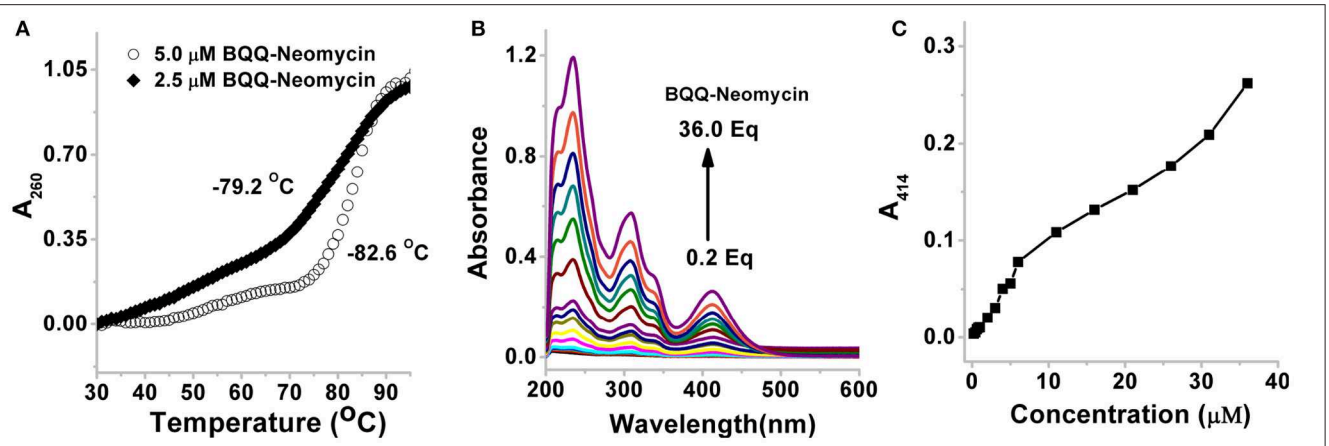

FIGURE 7 | (A) Thermal denaturation profile of BQQ-neomycin conjugate at 2.0 and 5.0 μM concentrations in buffer 10 mM sodium cacodylate, 0.5 mM EDTA, 100 mM NaCl at pH 7.0. No DNA was added in these experiments. **(B)** UV-vis absorption spectra of BQQ-neomycin conjugate at increasing concentrations (0.2–36.0 μM). **(C)** Absorbance vs. concentration plot of BQQ-neomycin. All experiments were performed in buffer 10 mM sodium cacodylate, 0.5 mM EDTA, 100 mM NaCl at pH 7.0. The absorbance spectra was recorded at room temperature (23°C).

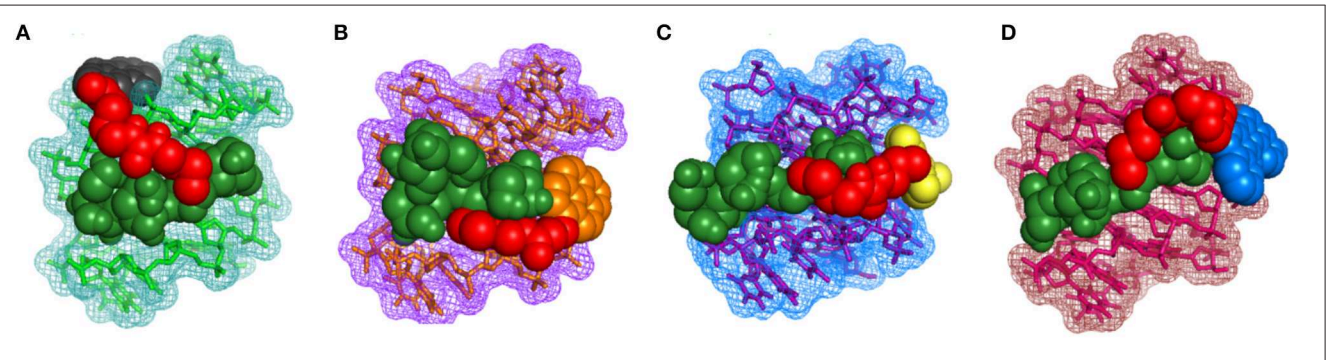

FIGURE 8 | Lowest energy docked structures of various neomycin-intercalator conjugates with the *Oxytricha Nova* structure **(A)** Anthraquinone-neomycin **(B)** Pyrene-neomycin **(C)** Naphthalenediimide-neomycin **(D)** BQQ-neomycin. In each figure neomycin, linker and the Intercalator moieties have been shown in different colors.

docking studies with all four neomycin-intercalator conjugates (compounds **3–6**). AutoDock Vina was chosen to perform docking experiments because of (a) its ability to improve the average accuracy of binding mode predictions (b) its ability to take advantage of multiple core processors which significantly shortens the running time (c) its more efficient search of potential energy surfaces and (d) its high accuracy with ligands possessing more than 20 rotatable bonds. The structure used in the docking studies was retrieved from the protein data bank (PDB ID: 156 D) which is a refined NMR solution structure of the telomeric sequence d(GGGGTTTTGGGG) (Schultze et al., 1994). This G-quadruplex has been shown to adopt an antiparallel structure with the thymine loops occupying the opposite ends in the presence of sodium salt. The G-quadruplex formed from this telomeric structure gives rise to four distinct quadruplex grooves of which two are of medium groove widths (∼12 Angstrom), one wide (∼17 Angstrom) and one narrow (∼6 Angstrom). We have previously shown that neomycin binds in the wide groove of this quadruplex as evidenced from solution NMR and molecular docking studies. The lowest energy docked structures for all four conjugates show that neomycin is positioned in the wide groove with linker extending the intercalating moieties more toward the thymine loop regions possibly to avoid steric clashes in the groove and also because of more vacant space available around thymine loops (**Figure 8**). BQQ-neomycin, naphthalenediimide neomycin and pyrene neomycin displayed nearly similar mode of binding in which the neomycin and the linker cover majority of the wide groove while the intercalator part of the molecule protrudes away toward the thymine. Despite this semblance in recognition, neomycin adopts different poses in all these structures to reorganize its rings in order to maximize the binding interactions. The predominant binding interaction involves hydrogen bonds, stacking and van der Waals interactions in all these interactions. The anthraquinone-neomycin conjugate displayed a strikingly different result in which the anthraquinone moiety moves out of the wide groove and then reaches out directly to the originating 5′-guanine base on one of the strands and makes stacking interactions

with the guanine base. Although, similar behavior would be expected from all other intercalator moieties used in this study, the difference could likely be the outcome of the ring size of the intercalator units used. Of the four intercalator moieties used in these studies, anthraquinone is the smallest of all with three fused rings whereas pyrene and naphthalenediimide have four rings each. BQQ has the largest intercalator part with five rings fused together. Because of these differences, the smallest anthraquinone moiety finds enough space to stack with the guanine while the other intercalator units face steric clashes to make such stacking contacts. Rather, their interactions are assisted through greater van der walls interaction in addition to the hydrogen bonding contacts made by the neomycin and linker units. To check if the variations in the linker composition had any effect on the binding poses displayed by these conjugates, we also ran additional set of docking experiments using the same linker as used in the case of Neomycin-BQQ conjugate. These docking experiments showed almost identical binding poses (**Supporting Information**, **Figure S3**) as obtained previously showing that linker composition didn't have any profound effect on the binding of the conjugates presented here. In summary, the intercalator moiety's total surface areas, nature of atoms present on them (hydrogen bonding donor or acceptor) and the ring size appear to be the prime determinants of these interactions where a smaller interacting may likely interact directly through the π-stacking interactions with the guanine bases.

Interaction of BQQ-Neomycin With Other Nucleic Acids

In this section, we present the results of our previously reported BQQ-neomycin conjugate which varied slightly in the linker composition than the BQQ-neomycin presented in this article. Previously, a Neomycin-BQQ conjugate, which contained an oxygen free thiourea bearing linker, was studied for its binding to a variety of nucleic acids including an antiparallel human telomeric G-quadruplex DNA. Neomycin and BQQ are the two binding moieties which are known for their liking for triplex nucleic acid structures (Arya et al., 2001, 2003). BQQ-neomycin conjugate was found to be one of the best triplex binding agents known as yet (Arya et al., 2003). The results obtained using competition dialysis have shown that BQQ-neomycin's preference was highest for an RNA triplex followed by a DNA triplex in a quadruplex free assay. In case of a DNA triplex, the binding constant of BQQ-neomycin was $K_a = 2.7 \times 10^8$ M^{-1} (Xue et al., 2010). For the human telomeric quadruplex, the fluorescent intercalator displacement assay showed that BQQ-neomycin conjugate's liking was behind the anthraquinone-neomycin, pyrene neomycin and napthalenediimide-neomycin (Ranjan et al., 2013a). The binding constant obtained with the best binder anthraquinone-neomycin (Ranjan et al., 2013a) was $K_a = 1.25 \times 10^7$ M^{-1}, a value which was very close the value of the same obtained with BQQ-neomycin used in this study ($K_a = 1.01 \times 10^7$ M^{-1}). This result shows that quadruplex topoplogy plays an important role in its binding to different ligands. Overall the results demonstrate that nucleic acid systems providing large surface areas for interactions, such as quadruplexes and triplexes are preferred nucleic acids for BQQ-neomycin conjugates where its binding affinity is in the range of $K_a \sim 10^7$-10^8 M^{-1}.

CONCLUSIONS

The ability of ligands to recognize G-quadruplex DNA structures has been shown to impede with the functions of telomerase. The core aspect of this inhibition lies in the differential recognition of different quadruplex surfaces with chemically diverse set of ligands. We have previously reported with the human telomeric G-quadruplex DNA that a combination of stacking and groove binding moieties can lead up to 1,000-fold binding affinity enhancement in the G-quadruplex recognition process. We have extended these studies by probing a well-resolved G-quadruplex DNA structure derived from the *Oxytricha Nova* telomeric DNA. From our studies, the following conclusions can be drawn:

(1) *BQQ-neomycin is the best Oxytricha Nova G-quadruplex binder of all neomycin-intercalators studied in this work*. The DC_{50} values obtained from FID titrations show that BQQ-neomycin is best in displacing the fluorescent probe bound to the G-quadruplex. The other neomycin-intercalator conjugates are at least 10 times better in displacing half of the fluorescent probe bound to these quadruplexes than neomycin. Hence conjugation of intercalators to neomycin improves their G-quadruplex binding. (2) *BQQ-neomycin binds Oxytricha Nova G-quadruplex DNA with 1:1 binding stoichiometry*. Both fluorescence and CD spectroscopy detected experiments confirm that BQQ-neomycin binds with the G-quadruplex in a 1:1 ligand to quadruplex ratio. The 1:1 binding stoichiometry is indicative of a single unique site for BQQ-neomycin complexation (3) *BQQ-neomycin binds with nearly 100-fold higher binding affinity than neomycin*. Scatchard analysis of the FID titration showed an association constant $K_a = (1.01 \pm 0.03) \times 10^7$ M^{-1} which is 100-fold higher than neomycin. This result shows that conjugation of two DNA binding moieties can lead to higher affinity G-quadruplex ligands. Comparison with the rRNA A-site binding showed that the BQQ-neomycin's affinity is lower than that of the quadruplex (4) *The binding mode of BQQ-neomycin is strikingly different than neomycin or BQQ-Cl alone*. The CD experiments showed that binding of either neomycin or BQQ-Cl brings negligible change in the CD signal. However, when BQQ-neomycin was complexed with the G-quadruplex, a large increase in CD signal was noticed indicating significant binding. However, no induced CD change was observed in the absorption region of BQQ, which suggests that the BQQ interaction does not involve stacking with the guanine bases. The remarkable 1:1 ligand to quadruplex binding shows a simultaneous binding of the two moieties at independent binding sites. (5) *BQQ-neomycin conjugate is prone to aggregation*. Thermal melting and UV-vis absorption studies clearly showed that BQQ-neomycin is prone to aggregate at concentrations 4 μM or above. Therefore, caution must be taken while interpreting thermal melting results and designing experiments that require higher ligand concentrations. (6) The

total surface area of the intercalator unit may have implications in stacking with guanine bases. The intercalator unit with three fused aromatic rings was found to have stacking interactions with the guanine bases while larger ring sizes prefer to interact predominantly through van der Walls interactions. Altogether, these results show that using our existing knowledge of ligands that are known to bind to quadruplex DNAs, a more potent ligand can be developed by combining the two separate ligands in a single molecule. As shown in this manuscript, the two binding moieties, neomycin and BQQ, have moderate binding, but when combined as one molecule, they result in a ligand with a much higher affinity and more importantly-selectivity in binding.

DATA AVAILABILITY STATEMENT

All datasets generated for this study are included in the article/**Supplementary Material**.

AUTHOR CONTRIBUTIONS

DA planned the experiments, supervised the data collection and analysis, and edited the manuscript. LX synthesized the conjugates. KA and NR performed the biophysical experiments. YA performed the docking studies. NR wrote the manuscript.

ACKNOWLEDGMENTS

The authors thank National Institutes of Health (Grant GM097917 and AI126874 to DA) and DST-SERB, Ministry of Science and Technology, Govt. of India, Core Research Grant (CRG/2018/001860 to NR) for funding.

SUPPLEMENTARY MATERIAL

The Supplementary Material for this article can be found online at: https://www.frontiersin.org/articles/10.3389/fchem.2020.00060/full#supplementary-material

REFERENCES

Artusi, S., Nadai, M., Perrone, R., Biasolo, M. A., Palu, G., Flamand, L., et al. (2015). The herpes simplex virus-1 genome contains multiple clusters of repeated G-quadruplex: implications for the antiviral activity of a G-quadruplex ligand. *Antiviral Res*. 118, 123–131. doi: 10.1016/j.antiviral.2015.03.016

Arya, D. P. (2007). *Aminoglycoside Antibiotics: From Chemical Biology to Drug Discovery*. Hoboken, NJ: John Wiley & Sons. doi: 10.1002/9780470149676

Arya, D. P., Coffee, R. L., Willis, B., and Abramovitch, A. I. (2001). Aminoglycoside– nucleic acid interactions: remarkable stabilization of DNA and RNA triple helices by neomycin. *J. Am. Chem. Soc.* 123, 5385–5395. doi: 10.1021/ja003052x

Arya, D. P., Xue, L., and Tennant, P. (2003). Combining the best in triplex recognition: synthesis and nucleic acid binding of a BQQ– neomycin conjugate. *J. Am. Chem. Soc.* 125, 8070–8071. doi: 10.1021/ja034241t

Balagurumoorthy, P., and Brahmachari, S. K. (1994). Structure and stability of human telomeric sequence. *J. Biol. Chem*. 269, 21858–22169.

Balagurumoorthy, P., Brahmachari, S. K., Mohanty, D., Bansal, M., and Sasisekharan, V. (1992). Hairpin and parallel quartet structures for telomeric sequences. *Nucleic Acids Res*. 20, 4061–4067. doi: 10.1093/nar/20.15.4061

Bhattacharyya, D., Mirihana Arachchilage, G., and Basu, S. (2016). Metal cations in G-quadruplex folding and stability. *Front. Chem*. 4:38. doi: 10.3389/fchem.2016.00038

Boger, D. L., Fink, B. E., Brunette, S. R., Tse, W. C., and Hendrick, M. P. (2001). A simple, high-resolution method for establishing DNA binding affinity and sequence selectivity. *J. Am. Chem. Soc.* 123, 5878–5891. doi: 10.1021/ja010041a

Boger, D. L., and Tse, W. C. (2001). Thiazole orange as the fluorescent intercalator in a high resolution FID assay for determining DNA binding affinity and sequence selectivity of small molecules. *Bioorg. Med. Chem*. 9, 2511–2518. doi: 10.1016/S0968-0896(01)00243-7

Burge, S., Parkinson, G. N., Hazel, P., Todd, A. K., and Neidle, S. (2006). Quadruplex DNA: sequence, topology and structure. *Nucleic Acids Res*. 34, 5402–5415. doi: 10.1093/nar/gkl655

Charles, I., Xi, H. J., and Arya, D. P. (2007). Sequence-specific targeting of RNA with an oligonucleotide-neomycin conjugate. *Bioconjugate Chem*. 18, 160–169. doi: 10.1021/bc060249r

Degtyareva, N. N., Gong, C., Story, S., Levinson, N. S., Oyelere, A. K., Green, K. D., et al. (2017). Antimicrobial activity, AME resistance, and A-site binding studies of Anthraquinone–Neomycin conjugates. *ACS Infect. Dis*. 3, 206–215. doi: 10.1021/acsinfecdis.6b00176

Hazel, P., Huppert, J., Balasubramanian, S., and Neidle, S. (2004). Loop-length-dependent folding of G-quadruplexes. *J. Am. Chem. Soc*. 126, 16405–16415. doi: 10.1021/ja045154j

Hegyi, H. (2015). Enhancer-promoter interaction facilitated by transiently forming G-quadruplexes. *Sci. Rep*. 5:9165. doi: 10.1038/srep09165

Hounsou, C., Guittat, L., Monchaud, D., Jourdan, M., Saettel, N., Mergny, J. L., et al. (2007). G-quadruplex recognition by quinacridines: a SAR, NMR, and biological study. *ChemMedChem* 2, 655–666. doi: 10.1002/cmdc.200600286

Huppert, J. L., and Balasubramanian, S. (2007). G-quadruplexes in promoters throughout the human genome. *Nucleic Acids Res*. 35, 406–413. doi: 10.1093/nar/gkl1057

Jiang, L., Watkins, D., Jin, Y., Gong, C., King, A., Washington, A. Z., et al. (2015). Rapid synthesis, RNA binding, and antibacterial screening of a peptidic-aminosugar (PA) library. *ACS Chem. Biol*. 10, 1278–1289. doi: 10.1021/cb5010367

Kaiser, M., Sainlos, M., Lehn, J. M., Bombard, S., and Teulade-Fichou, M. P. (2006). Aminoglycoside-quinacridine conjugates: towards recognition of the P6.1 element of telomerase RNA. *Chembiochem* 7, 321–329. doi: 10.1002/cbic.200500354

Kaushik, M., and Kukreti, S. (2003). Temperature induced hyperchromism exhibited by Hoechst 33258: evidence of drug aggregation from UV-melting method. *Spectrochim. Acta A Mol. Biomol. Spectrosc*. 59, 3123–3129. doi: 10.1016/S1386-1425(03)00115-X

Kellish, P. C., Kumar, S., Mack, T. S., Spano, M. N., Hennig, M., and Arya, D. P. (2014). Multivalent amino sugars to recognize different TAR RNA conformations. *Medchemcomm* 5, 1235–1246. doi: 10.1039/C4MD00165F

Kumar, S., and Arya, D. P. (2011). Recognition of HIV TAR RNA by triazole linked neomycin dimers. *Bioorg. Med. Chem. Lett*. 21, 4788–4792. doi: 10.1016/j.bmcl.2011.06.058

Kumar, S., Ranjan, N., Kellish, P., Gong, C., Watkins, D., and Arya, D. P. (2016). Multivalency in the recognition and antagonism of a HIV TAR RNA–TAT assembly using an aminoglycoside benzimidazole scaffold. *Organ. Biomol. Chem*. 14, 2052–2056. doi: 10.1039/C5OB02016F

Kumar, S., Spano, M. N., and Arya, D. P. (2015). Influence of linker length in shape recognition of B* DNA by dimeric aminoglycosides. *Bioorg. Med. Chem*. 23, 3105–3109. doi: 10.1016/j.bmc.2015.04.082

Kumar, S., Xue, L., and Arya, D. P. (2011). Neomycin– neomycin dimer: an all-carbohydrate scaffold with high affinity for AT-rich DNA duplexes. *J. Am. Chem. Soc*. 133, 7361–7375. doi: 10.1021/ja108118v

Mergny, J., and Lacroix, L. (2003). Analysis of thermal melting curves. *Oligonucleotides* 13, 515–537. doi: 10.1089/154545703322860825

Mergny, J. L., Phan, A. T., and Lacroix, L. (1998). Following G-quartet formation by UV-spectroscopy. *FEBS Lett*. 435, 74–78. doi: 10.1016/S0014-5793(98)01043-6

Mohanty, J., Barooah, N., Dhamodharan, V., Harikrishna, S., Pradeepkumar, P., and Bhasikuttan, A. C. (2012). Thioflavin T as an efficient inducer and selective fluorescent sensor for the human telomeric G-quadruplex DNA. *J. Am. Chem. Soc*. 135, 367–376. doi: 10.1021/ja309588h

Monchaud, D., Allain, C., and Teulade-Fichou, M. (2006). Development of a fluorescent intercalator displacement assay (G4-FID) for establishing quadruplex-DNA affinity and selectivity of putative ligands. *Bioorg. Med. Chem. Lett*. 16, 4842–4845. doi: 10.1016/j.bmcl.2006.06.067

Monchaud, D., and Teulade-Fichou, M. (2008). A hitchhiker's guide to G-quadruplex ligands. *Organ. Biomol. Chem*. 6, 627–636. doi: 10.1039/B714772B

Nahar, S., Ranjan, N., Ray, A., Arya, D. P., and Maiti, S. (2015). Potent inhibition of miR-27a by neomycin–bisbenzimidazole conjugates. *Chem. Sci*. 6, 5837–5846. doi: 10.1039/C5SC01969A

Neidle, S. (2010). Human telomeric G-quadruplex: the current status of telomeric G-quadruplexes as therapeutic targets in human cancer. *FEBS J*. 277, 1118–1125. doi: 10.1111/j.1742-4658.2009.07463.x

Pedretti, A., Villa, L., and Vistoli, G. (2004). VEGA- an open platform to develop chemo-bio-informatics applications, using plug-in architecture and script programming. *J. Comput. Aided Mol. Des*. 18, 167–173. doi: 10.1023/B:JCAM.0000035186.90683.f2

Perrone, R., Lavezzo, E., Riello, E., Manganelli, R., Palù, G., Toppo, S., et al. (2017). Mapping and characterization of G-quadruplexes in *Mycobacterium tuberculosis* gene promoter regions. *Sci. Rep*. 7:5743. doi: 10.1038/s41598-017-05867-z

Randazzo, A., Spada, G. P., and da Silva, M. W. (2012). "Circular dichroism of quadruplex structures," in *Quadruplex Nucleic Acids (Topics in Current Chemistry)*, Vol. 330, eds J. B. Chaires and D. Graves (Springer), 67–86. doi: 10.1007/128_2012_331

Ranjan, N., Andreasen, K. F., Kumar, S., Hyde-Volpe, D., and Arya, D. P. (2010). Aminoglycoside binding to oxytricha nova telomeric DNA. *Biochemistry* 49, 9891–9903. doi: 10.1021/bi101517e

Ranjan, N., and Arya, D. P. (2013). Targeting C-myc G-quadruplex: dual recognition by aminosugar-bisbenzimidazoles with varying linker lengths. *Molecules* 18, 14228–14240. doi: 10.3390/molecules181114228

Ranjan, N., and Arya, D. P. (2016). Linker dependent intercalation of bisbenzimidazole-aminosugars in an RNA duplex; selectivity in RNA vs. DNA binding. *Bioorg. Med. Chem. Lett*. 26, 5989–5994. doi: 10.1016/j.bmcl.2016.10.076

Ranjan, N., Davis, E., Xue, L., and Arya, D. P. (2013a). Dual recognition of the human telomeric G-quadruplex by a neomycin–anthraquinone conjugate. *Chem. Commun*. 49, 5796–5798. doi: 10.1039/c3cc42721h

Ranjan, N., Kumar, S., Watkins, D., Wang, D., Appella, D. H., and Arya, D. P. (2013b). Recognition of HIV-TAR RNA unsing neomycin-benzimidazole conjugates. *Bioorg. Med. Chem. Lett*. 20, 5689–5693. doi: 10.1016/j.bmcl.2013.08.014

Schultze, P., Smith, F. W., and Feigon, J. (1994). Refined solution structure of the dimeric quadruplex formed from the oxytricha telomeric oligonucleotide d(GGGGTTTTGGGG). *Structure* 2, 221–233. doi: 10.1016/S0969-2126(00)00023-X

Seenisamy, J., Rezler, E. M., Powell, T. J., Tye, D., Gokhale, V., Joshi, C. S., et al. (2004). The dynamic character of the G-quadruplex element in the c-MYC promoter and modification by TMPyP4. *J. Am. Chem. Soc*. 126, 8702–8709. doi: 10.1021/ja040022b

Smith, F. W., and Feigon, J. (1992). Quadruplex structure of oxytricha telomeric DNA oligonucleotides. *Nature* 356, 164–168. doi: 10.1038/356164a0

Story, S., Skriba, M. J., Maiti, K., Ranjan, N., Degtyareva, N. N., Green, K. D., et al. (2019). Synthesis, antimicrobial activity, attenuation of aminoglycoside resistance in MRSA, and ribosomal A-site binding of pyrene-neomycin conjugates. *Eur. J. Med. Chem*. 163, 381–393. doi: 10.1016/j.ejmech.2018.11.022

Thakur, R. S., Desingu, A., Basavaraju, S., Subramanya, S., Rao, D. N., and Nagaraju, G. (2014). *Mycobacterium tuberculosis* DinG is a structure-specific helicase that unwinds G4 DNA: implications for targeting G4 DNA as a novel therapeutic approach. *J. Biol. Chem*. 289, 25112–25136. doi: 10.1074/jbc.M114.563569

Tse, W. C., and Boger, D. L. (2004). Sequence-selective DNA recognition: natural products and nature's lessons. *Chem. Biol*. 11, 1607–1617. doi: 10.1016/j.chembiol.2003.08.012

Verma, S., Ghuge, S. A., Ravichandiran, V., and Ranjan, N. (2019). Spectroscopic studies of thioflavin-T binding to c-myc G-quadruplex DNA. *Spectrochim. Acta A* 212, 388–395. doi: 10.1016/j.saa.2018.12.044

Vorlíčková, M., Kejnovská, I., Sagi, J., Renčiuk, D., Bednárová, K., Motlová, J., et al. (2012). Circular dichroism and guanine quadruplexes. *Methods* 57, 64–75. doi: 10.1016/j.ymeth.2012.03.011

Watkins, D., Gong, C., Kellish, P., and Arya, D. P. (2017). Probing A-form DNA: a fluorescent aminosugar probe and dual recognition by anthraquinone-neomycin conjugates. *Bioorg. Med. Chem*. 25, 1309–1319. doi: 10.1016/j.bmc.2016.11.003

Watkins, D., Ranjan, N., Kumar, S., Gong, C., and Arya, D. P. (2013). An assay for human telomeric G-quadruplex DNA binding drugs. *Bioorg. Med. Chem. Lett*. 23, 6695–6699. doi: 10.1016/j.bmcl.2013.10.030

Wen, J., and Gray, D. M. (2002). The ff gene 5 single-stranded DNA-binding protein binds to the transiently folded form of an intramolecular G-quadruplex. *Biochemistry* 41, 11438–11448. doi: 10.1021/bi020276e

Willis, B., and Arya, D. P. (2010). Triple recognition of B-DNA by a neomycin-hoechst 33258-pyrene conjugate. *Biochemistry* 49, 452–469. doi: 10.1021/bi9016796

Xi, H., Gray, D., Kumar, S., and Arya, D. P. (2009). Molecular recognition of single-stranded RNA: neomycin binding to poly (A). *FEBS Lett*. 583, 2269–2275. doi: 10.1016/j.febslet.2009.06.007

Xue, L., Charles, I., and Arya, D. P. (2002). Pyrene-neomycin conjugate: dual recognition of a DNA triple helix. *Chem. Commun*. 1, 70–71. doi: 10.1039/b108171c

Xue, L., Ranjan, N., and Arya, D. P. (2011). Synthesis and spectroscopic studies of the aminoglycoside (neomycin)– perylene conjugate binding to human telomeric DNA. *Biochemistry* 50, 2838–2849. doi: 10.1021/bi1017304

Xue, L., Xi, H., Kumar, S., Gray, D., Davis, E., Hamilton, P., et al. (2010). Probing the recognition surface of a DNA triplex: binding studies with Intercalator–Neomycin conjugates. *Biochemistry* 49, 5540–5552. doi: 10.1021/bi100071j

Yeung, B. K. S., Tse, W. C., and Boger, D. L. (2003). Determination of binding affinities of triplex forming oligonucleotides using a fluorescent intercalator displacement (FID) assay. *Bioorg. Med. Chem. Lett*. 13, 3801–3804. doi: 10.1016/j.bmcl.2003.07.005

Conflict of Interest: The authors declare that the research was conducted in the absence of any commercial or financial relationships that could be construed as a potential conflict of interest.

frontiers in Chemistry

ORIGINAL RESEARCH
published: 26 February 2020
doi: 10.3389/fchem.2020.00113

A Porphyrin-DNA Chiroptical Molecular Ruler With Base Pair Resolution

Jonathan R. Burns[1]*, *James W. Wood*[2] *and Eugen Stulz*[2]*

[1] Department of Chemistry, University College London, London, United Kingdom, [2] School of Chemistry & Institute for Life Sciences, University of Southampton, Southampton, United Kingdom

DNA-based molecular rulers enable scientists to determine important parameters across biology, from the measurement of protein binding interactions, to the study of membrane dynamics in cells. However, existing rulers can suffer from poor nanometre resolution due to the flexible nature of linkers used to tether to the DNA framework. We aimed to overcome this problem using zinc and free-base porphyrin chromophores attached via short and rigid acetylene linkers. This connectivity enables the distance and angle between the porphyrins to be fine-tuned along the DNA scaffold. The porphyrins undergo favorable energy transfer and chiral exciton coupling interactions to act as highly sensitive molecular ruler probes. To validate the system, we monitored the detection of small changes in DNA structure upon intercalation of ethidium bromide. CD spectroscopy showed the porphyrins undergo highly sensitive changes in excitation coupling to facilitate base pair resolution of the novel system.

Keywords: DNA, porphyrin, FRET, CD spectroscopy, ethidium bromide intercalation, exciton coupling

OPEN ACCESS

Edited by:
Janarthanan Jayawickramarajah, Tulane University, United States

Reviewed by:
Cristiano Zonta, University of Padova, Italy
Guzman Gil-Ramirez, University of Lincoln, United Kingdom

***Correspondence:**
Jonathan R. Burns
jonathan.burns@ucl.ac.uk
Eugen Stulz
est@soton.ac.uk

Specialty section:
This article was submitted to Supramolecular Chemistry, a section of the journal Frontiers in Chemistry

Received: *21 November 2019*
Accepted: *06 February 2020*
Published: *26 February 2020*

Citation:
Burns JR, Wood JW and Stulz E (2020) A Porphyrin-DNA Chiroptical Molecular Ruler With Base Pair Resolution. Front. Chem. 8:113. doi: 10.3389/fchem.2020.00113

INTRODUCTION

Förster resonance energy transfer (FRET) is routinely used in the determination of conformational changes or intermolecular interactions in biomolecules, where it gives insight into function and activity. However, most FRET systems have chromophores attached through long and flexible linkers which can limit their sensitivity (Wang et al., 2003; Sabanayagam et al., 2005; Preus and Wilhelmsson, 2012). Since the interaction of chromophores, in view of energy transfer, is highly dependent on their alignment, and FRET has an inverse sixth order distance (R) dependency, this does not allow for a precise distance measurement with sub-nanometre resolution due to fluctuations in position of the FRET pair (Wang et al., 2003), which can be overcome to some extent using time resolved FRET (trFRET) (Klostermeier and Millar, 2001). In addition, when the FRET pair distance is comparable to the linker length, contact quenching can occur. Yet the detection of small structural changes in DNA is highly desirable as it can give information on the DNA topology, e.g., upon binding of proteins (Andrabi et al., 2014), in intercalator–DNA interactions (Biebricher et al., 2015), or in base pair mismatches (Rossetti et al., 2015). To this end, tailor made DNA multi-chromophore systems are now well-established (Malinovskii et al., 2010; Teo and Kool, 2012). Specific systems include, for example, Cy3 and Cy5 dyes which are typically attached through short alkynyl linkers to the nucleobase and can provide useful FRET analysis at short distances, though this was not used for analysis of conformational changes (Hall et al., 2012). Analogously, fluorescent base analogs which were incorporated within the base stacking region of the DNA and thus are inherently held rigidly in place, resulted in a high control of the orientation factor (κ)

and hence very distinct FRET changes as the number of bases separating the base analogs were varied (Borjesson et al., 2009). The combination of Cy5/Cy3, however, is suitable to detect global structural changes in hairpin ribozymes (Bates et al., 2005), and in bivalent peptide complexes (Eberhard et al., 2011), even when having flexible linkers. Gating of the Cy5 dye with a green laser enabled FRET values at much shorter distances to be obtained than in conventional systems (Bates et al., 2005). Stilbene chromophores, which were attached to both ends of a DNA hairpin, showed exciton-coupled circular dichroism (EC-CD) which varied strongly along a helical turn and could serve as a molecular ruler; however, the CD signatures are very complex and not straight-forward to interpret (Lewis et al., 2005). The use of pyrenes has shown strong fluorescence enhancement when attached to DNA with short linkers and can serve as a structure-sensitive probe for DNA (Mayer-Enthart and Wagenknecht, 2006). Ultrafast Energy Transfer in pyrene dimers yielded information on structural dynamics of DNA, but the system is complicated by the presence of two electronic coupling pathways, involving the base pair of the DNA (Trifonov et al., 2005).

On a single molecule level, total internal reflection fluorescence (TIRF) microscopy, combined with single molecule FRET (TIRF-smFRET) enables single base pair resolution with 100 ms temporal resolution, though this requires sophisticated equipment setup (Holden et al., 2010). DNA origami tiles were used as an elegant breadboard for measuring distances using single molecule FRET systems (Steinhauer et al., 2009; Stein et al., 2011), but at much larger distances than single base pair resolution. Gold nanoparticles (AuNPs) have also been investigated and held at specific distances using dsDNA spacers; the plasmon coupling of 80 nm AuNPs was shown to allow distance measurements between 1 and 80 nm with a time resolution <50 ms and with absolute distance errors ranging from <1 nm to around 20 nm (Reinhard et al., 2005). Plasmon rulers could certainly be an alternative to FRET for *in vitro* single-molecule experiments (Sonnichsen et al., 2005), in particular because sub-nanometre resolution can be achieved (Liu et al., 2006). Methods other than FRET or plasmon resonance in using DNA as a molecular ruler that have been used include pulsed electron paramagnetic resonance (PELDOR) spectroscopy (Schiemann et al., 2004), X-ray scattering (Mathew-Fenn et al., 2008), and EPR spectroscopy (Nguyen et al., 2014).

Despite the advances made in determining the impact of sequence and external factors on the structure of DNA, including in a time dependent manner, a system with a simple optical readout that gives unambiguous information on local changes down to the single base pair level is still missing. We have studied the characteristics of porphyrin modified DNA extensively (Fendt et al., 2007). Notably a mixed free-base and zinc porphyrin zipper-array allowed for reversible formation of photonic wires (Nguyen et al., 2009). In particular CD spectroscopy has proven to be an invaluable tool in analyzing interactions in porphyrin-DNA due to the strong exciton coupling between the porphyrins, which shows strong dependence on the type of linker between porphyrin and DNA used, as well as on the underlying sequence of the DNA (Brewer et al., 2011; Singleton et al., 2016). Thus this system seemed perfectly well-suited to investigate its ability to monitor the local changes in DNA structure.

EXPERIMENTAL

The synthesis of the porphyrin-dU building block and its incorporation into DNA were performed as described previously (Fendt et al., 2007). Phosphoramidite chemistry and solid support DNA synthesis followed standard protocols for the natural nucleotides. For the incorporation of the porphyrin-dU, the phosphoramidite was dissolved in MeCN-DCM 10:1, and an extended coupling time of 5 min was used. The DNA strands were purified and analyzed using RP-HPLC. Post-synthetic metalation of the porphyrin strand was done in an aqueous solution using $Zn(OAc)_2$ as published earlier (Brewer et al., 2011).

UV-Vis spectroscopy was conducted using a Varian Cary 300 Bio spectrometer with quartz cells of 1 cm path length; scans were carried out at 25°C covering 200–800 nm. Fluorescence spectroscopy was conducted using a Varian Cary Eclipse spectrometer with quartz cells of 1 cm path length; scans were carried out at 25°C with excitation wavelength at $\lambda = 425$ nm. CD spectra were recorded at beamline B23 (Module B) at Diamond Light Source, equipped with an Olis DSM20 Monochromator and a photo multiplier tube detector. CD titration with ethidium bromide (EtBr) was performed using a 1.5 mM stock solution to give a total volume 500 μL (4 μM DNA), and a concentration of EtBr equal to 40, 80, 200, 400, and 800 μM. Concentrations and buffers are given in the figure legends. The theoretical predictions of FRET were performed as described previously, using a custom build MATLAB based program FRETmatrix described elsewhere (Preus et al., 2013). The geometry of the porphyrin-DNA duplexes was modeled using Schrödinger's software MacroModel (Mohamadi et al., 1990).

The data for the titration were analyzed using a non-linear fit of the Scatchard's plot of r/C_f vs. r using the following equation for n binding sites (Vardevanyan et al., 2003; Minasyan et al., 2006):

$$r/C_f = K(1 - nr)\left[\frac{1 - nr}{1 - (n-1)\,r}\right]^{n-1} \quad (1)$$

where $r = C_b/C_p$, $C_b = [\text{EtBr}]_{\text{bound}}$, $C_b = C_0 - C_f$, $C_0 = [\text{EtBr}]_{\text{total}}$, $C_f = [\text{EtBr}]_{\text{unbound}}$, $C_p = [\text{phosphate groups}]$.

For **Y1**, the $\Delta\theta$ at 415 nm was used, and for **Y2** the $\Delta\theta$ at 420 nm was used. The values of $|\theta_{max} - \theta_{min}|$ were fitted to obtain the theoretical value of maximum change (highest possible intercalation. From this, the fraction of bound EtBr was calculated, assuming that the intercalation on a global scale leads to a linear response of $\Delta\theta$.

RESULTS AND DISCUSSION

Synthesis and Stability of the FRET System

In this study, we used an electronically coupled system based on zinc porphyrin as donor (**Zn-P**) and free-base porphyrin as acceptor (**2H-P**) which has previously shown efficient energy transfer within a DNA supramolecular assembly

(Bouamaied et al., 2007; Nguyen et al., 2009; Brewer et al., 2011). We built an array of DNA duplexes to study the energy transfer properties for this two-porphyrin system (see **Figure 1**, **Z1** to **Z7**, and ESI for sequences). The position of the Zn-P was fixed throughout, whilst the 2H-P was varied. The corresponding base pair separation between the porphyrins change both the distance and dipole-dipole alignment between them. The porphyrin-nucleoside building block was synthesized according to previously published procedures and used for solid phase synthesis of the porphyrin-DNA (Bouamaied et al., 2007; Brewer et al., 2011). The thermal UV-denaturing analysis shows a T_m of ∼47°C for all porphyrin containing duplexes, with ΔT_m = ∼-3°C compared to the native DNA, which is in the expected range. Both porphyrins display the characteristic absorption and emission spectra when measured either as single strand or as duplex with the unmodified complementary strands (**Figure 2**). The ground state absorbances in the mixed porphyrin duplexes **Z1** to **Z7** are largely unperturbed and can be described as a superposition of the absorbance of DNA duplexes which contain either **Zn-P** (**Z8**) or **2H-P** (**Z9**).

Determining FRET Efficiency

The quantum yield and Förster distance of the **Zn-P**–**2H-P** pair were measured previously to be $\Phi = 0.12$ and $R_0 = 28.4$ Å, respectively (Burns et al., 2012). The distances and angles of the chromophores in the DNA duplexes used here were obtained from energy minimized structures, using the effective transition moment along the 5, 15-axis through the acetylene linker as determined by Berova et al. (Anderson, 1994; Matile et al., 1996; Huang et al., 2000). The calculated E_{FRET} values [see electronic supporting information [ESI] for details] (Preus et al., 2013) show deviation from the idealized model ($\kappa^2 = 2/3$) (**Figure 3A**); for the calculation of the E_{FRET} efficiencies, κ^2 was taken into

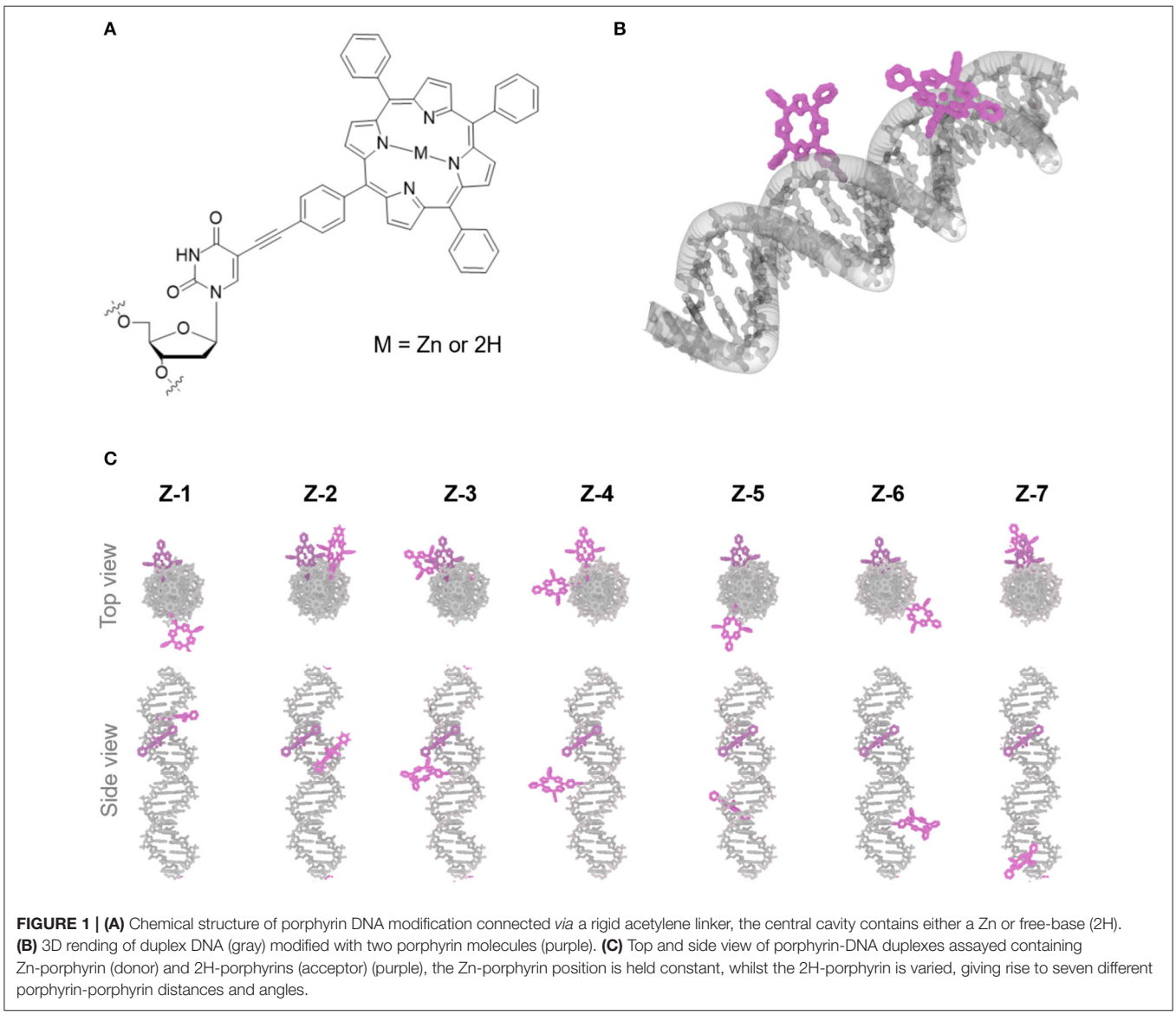

FIGURE 1 | (A) Chemical structure of porphyrin DNA modification connected *via* a rigid acetylene linker, the central cavity contains either a Zn or free-base (2H). **(B)** 3D rending of duplex DNA (gray) modified with two porphyrin molecules (purple). **(C)** Top and side view of porphyrin-DNA duplexes assayed containing Zn-porphyrin (donor) and 2H-porphyrins (acceptor) (purple), the Zn-porphyrin position is held constant, whilst the 2H-porphyrin is varied, giving rise to seven different porphyrin-porphyrin distances and angles.

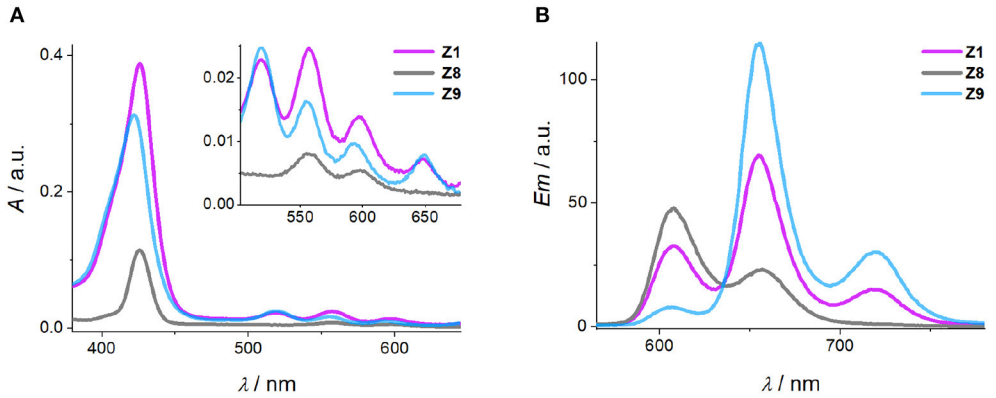

FIGURE 2 | Representative absorbance **(A)** and emission **(B)** spectra of the Zn and 2H-porphyrin FRET pair (**Z1**), Zn-porphyrin (**Z8**) and 2H-porphyrin (**Z9**). [DNA] = 2 μM, 100 mM NaCl, 100 mM Na_2HPO_4 buffer pH 7.0.

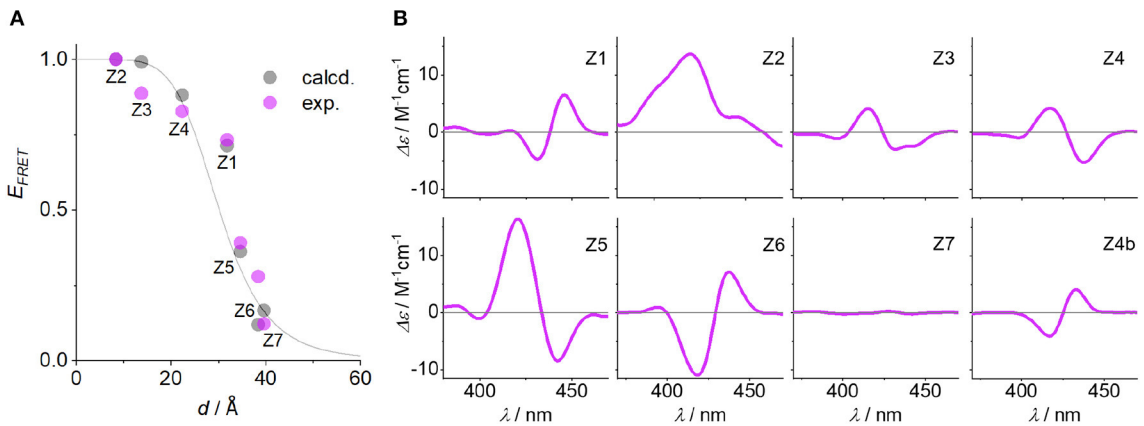

FIGURE 3 | (A) E_{FRET} as function of **Zn**-**P** distance (*d*), comparing calculated (Preus et al., 2013) and measured FRET efficiencies (the gray line represents idealized behavior with $\kappa^2 = 2/3$). **(B)** CD spectra of the **Zn**-**P** duplexes (porphyrin region), including the CD spectrum of **Z4b** where the angle of the porphyrin dipole moment has opposite sign to **Z4**. Conditions as in **Figure 2**.

account and calculated for each pair as described previously. The experimentally determined E_{FRET} values from the donor emission peak at 605 nm show a steady decrease in FRET efficiency with increasing donor-acceptor distance. As expected, **Z2** gives the highest E_{FRET} value due to the smallest porphyrin-porphyrin spacing. Conversely, **Z3** and **Z4** exhibit higher E_{FRET} values than **Z1**, even though they have the same base separation, or are separated by one extra base pair, respectively. These differences arise from the attachment points on the complementary strands which positions the porphyrins in **Z1** on opposite sides of the duplex, whereas in **Z2** and **Z3** the porphyrins are located in the same hemisphere of the duplex (see **Figure 1** for DNA models).

The influence of the angle between the chromophores is clearly visible in the CD spectra. The excitonic coupling between the porphyrins display both positive and negative Cotton effects as a function of angle between the dipole moments (**Figure 3B**), which is defined as the projection angle of the dipole moments and is either (+) or (−) (viewing down the helical axis of the DNA). Generally, a positive Cotton effect at longer wavelengths and negative one at shorter wavelengths determines a positive exciton couplet and arises from a positive angle (positive exciton chirality) (Berova et al., 2009). This theory has successfully been used to determine the chirality in systems having identical chromophores, but not with mixed chromophore systems. Here, the angles match perfectly well with the CD chirality (**Table 1**), but only when assuming both porphyrins as equal. Thus, the porphyrins are close to being degenerate: the small ground state differences from zinc to free-base porphyrin are not discriminated by the exciton chirality method, and the system reports two identical chromophores. This is in contrast to the direct energy transfer as seen in FRET. To demonstrate this, we have synthesized the duplex **Z4b** where the relative position of the two porphyrins is inverted with respect to **Z4**, meaning that in **Z4b** the zinc porphyrin is now downstream of the free-base porphyrin. While the base pair separation and through-space distance of the porphyrins is maintained, the repositioning of the porphyrins results in an inverted exciton chirality, and the

CD spectra are near mirror images of each other (**Figure 3B**; the E_{FRET} values were not determined for this system).

Detecting Ethidium Bromide Intercalation at Single Base Pair Level

We developed an intercalation assay to test the sensitivity of the porphyrin system. Given that the energy transfer method to measure distance changes is still ambiguous due to relatively small expected effects (e.g., see difference from **Z1** to **Z4**), the CD spectra seem to respond much more sensitively to the relative arrangement of the porphyrins. We therefore tested the response of the porphyrin arrays to the intercalation of ethidium bromide (EtBr). EtBr is a well-known intercalator by stacking inside the DNA duplex (sliding in-between base pairs) and is commonly used as a nucleic acid stain in gel electrophoresis to visualize the DNA bands. The binding of EtBr to DNA has been studied extensively, with reported global binding constants (K_D) in the range of 3.4×10^3 M^{-1} to 1.3×10^6 M^{-1}, depending mainly on salt concentration (Krugh et al., 1975; Scaria and Shafer, 1991; Vardevanyan et al., 2003; Alonso et al., 2006; Minasyan et al., 2006; Hayashi and Harada, 2007; Nafisi et al., 2007; Karacan and Okay, 2013). Also, the binding mode indicates that EtBr intercalates at approximately every two to three base pairs with n ~2.5 (Scaria and Shafer, 1991), though n-values ranging from 1.6 (Hayashi and Harada, 2007) up to 9 (Vardevanyan et al., 2003; Minasyan et al.,

TABLE 1 | Structural parameters, FRET efficiencies and CD data of the donor-acceptor systems.

DNA duplex	Base pair separation	Porphyrin distance [Å] and dipole angle [deg]	E_{FRET}, calcd. and exp. values	κ^2 value	Exciton couplet A^a_{CD} and exciton chirality[b]
Z1	2	30.2/+158	0.71/0.73	2.704	+11.3/(+)
Z2	0	11.0/+22	1/1	1.001	+16.2/(+)
Z3	2	13.7/−60	0.99/0.89	0.759	−7.1/(–)
Z4	3	22.0/−92	0.88/0.83	0.963	−9.5/(–)
Z4b	3	21.6/+90	n.d.[c]	n.d.[c]	+8.2/(+)
Z5	5	34.7/−167	0.36/0.39	1.012	−24.8/(–)
Z6	7	39.8/+121	0.12/0.28	0.448	+18.0/(+)
Z7	11	41.1/+23	0.17/0.12	0.806	+0.4/(+)

[a]The difference between the CD extrema at longer wavelengths and at shorter wavelengths (in Δε) determines the amplitude A_{CD} of the exciton couplet (Berova et al., 2009). [b]The exciton chirality corresponds to the sign of the dipole angle. [c]not determined.

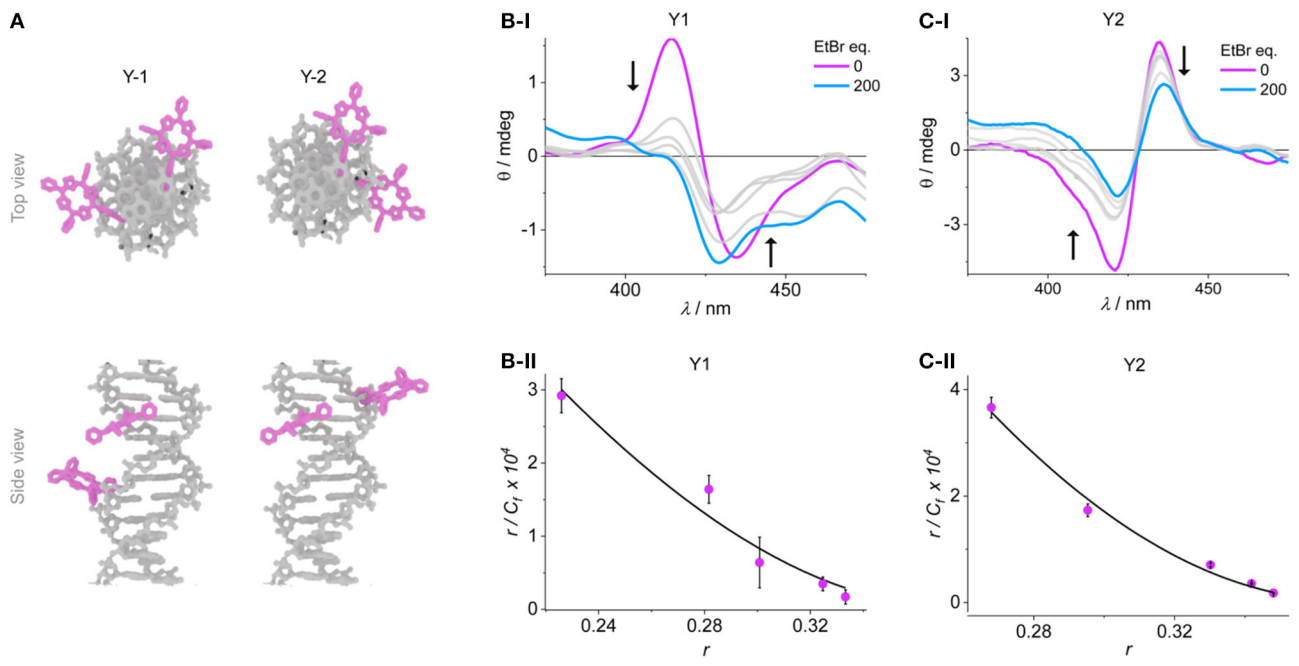

FIGURE 4 | (A) Representation of the duplexes **Y1** and **Y2**. Example CD spectra of the titration experiments of **(B-i) Y1** and **(C-i) Y2**, the arrows indicate the peak shift upon addition of EtBr. Scatchard plots are shown in **(B-ii)** and **(C-ii)**, respectively, together with the fitted curves according to Equation (1).

2006) have been reported. In addition, EtBr can show multiple binding interactions, including intercalation, semi-intercalation and electrostatic binding (Vardevanyan et al., 2003; Minasyan et al., 2006). We set out to test if our system would be suitable to directly detect the binding of an intercalator on both a large range and single base pair system.

We synthesized two additional porphyrin-DNA strands **Y1** and **Y2** (**Figure 4**), with two porphyrins being either at five base pairs apart, or on adjacent base pairs, respectively. This DNA system is shorter and simpler, providing only A-T base pairs in-between the porphyrin sites, and flanking G-C base pairs to maintain duplex stability. Since the metallation state does not influence the exciton coupling, both reporter porphyrins were used as 2H-porphyrins which also simplifies the synthesis by avoiding the post-synthetic metalation step. To probe the system, we titrated **Y1** with EtBr and observed a corresponding change in the exciton coupling of the porphyrins (**Figure 4A** and ESI). The large reduction in signal intensity can be attributed to a change in helicity of the DNA upon EtBr intercalation, and with it a change in chromophore distance and angle. The use of an excess of EtBr (>500 equivalents) did not indicate any significant changes in CD signal after addition of 200 equivalents, and up to that point the EtBr did not itself produce a significant signal in the porphyrin region that would interfere with the analysis. The binding constants were calculated from a non-linear fitting of the Scatchard plot of r/C_f vs. r (see Experimental section); the apparent global binding constant in our case is $K_D = 1.43 \pm 0.2 \times 10^5$ M^{-1}, with $n = 2.6$ binding sites. This tends toward the upper limit of binding constants reported. The analysis is based under the assumption that any outside binding, e.g., electrostatic interactions with the phosphate groups or groove binding, does not give rise to a change in porphyrin coupling as it would not lead to large structural changes. Also, we have not found any indication that EtBr would interact strongly with the porphyrins and lead to a change in CD signature (see ESI). Therefore, we can assume that this apparent K_D represents a value for the intercalation under our experimental conditions. The number of binding sites also compares well to reported values.

More interesting is the response of the system when the porphyrins are at adjacent base pairs as in **Y2**. The order of the porphyrins was switched to give opposite exciton chirality which distinguishes it clearly from the system **Y1**. The intercalation can again be monitored from a large reduction in the exciton coupling of the porphyrins. Here, it is assumed that any EtBr that would bind at random parts of the DNA (internally or externally) will not be detected, and only the single binding site occupation is observed. The data points were again fitted according to Equation (1) and yielded a K_D of $3.54 \pm 0.4 \times 10^5$ M^{-1}, with $n = 2.6$. The K_D is higher than the global binding constant, but the weaker binding is a reflection of the competing sites outside of the porphyrin region which would lead to a lower effective molarity of the available EtBr. This is also shown by the same n-value for both systems. This result shows that the intercalation of a molecule can clearly be detected on the single base pair level using the strong exciton coupling of porphyrins, which is very sensitive down to the nanometer scale.

CONCLUSIONS

Based on our previously established porphyrin-DNA system, we have demonstrated that varying the position of two porphyrins along a DNA helix can be used to create a molecular ruler, that responds well to changes in distance and structure. Using a well-established FRET pair based on zinc metalled and free-base porphyrins, the FRET efficiency can be correlated to the position of the porphyrins. However, the helicity can lead to ambiguity when FRET is used to determine the distance of the chromophores. This is mainly attributed to the helical structure and arrangement. Circular Dichroism, on the other hand, has revealed that the exciton coupling is independent on the metallation state, most likely because the absorbances of the two porphyrins (Zn, 2H) are very close. This is visible from the exciton couplet which follows the helical geometry of the porphyrin system, not the donor-acceptor energy order. Furthermore, the CD response is shown to be highly dependent on the relative orientation and distance of the porphyrins. This can be explored to monitor structural changes such as those that are induced by intercalation. While the system certainly needs to be evaluated in greater detail, the obtained binding constants for EtBr as a model system compare well with literature data. In this respect, changes can be detected down to the single base–pair level, which gives nanometer resolution in DNA analysis.

DATA AVAILABILITY STATEMENT

The datasets analyzed for this study can be found in the University of Southampton Institutional Research Repository, ePrints Soton: https://doi.org/10.5258/SOTON/D1227.

AUTHOR CONTRIBUTIONS

JB designed the ruler system. JB and JW synthesized the porphyrin-DNA strands and performed the experiments. JB, JW, and ES analyzed the data. ES supervised the project. ES and JB wrote the manuscript.

FUNDING

Financial support by ATDbio (Southampton) for JB is greatly acknowledged (EPSRC CASE award). The CD spectra were recorded at beamline B23, Diamond Light Source, Didcot, UK and supported through proposal No. SM11105.

SUPPLEMENTARY MATERIAL

The Supplementary Material for this article can be found online at: https://www.frontiersin.org/articles/10.3389/fchem.2020.00113/full#supplementary-material

REFERENCES

Alonso, A., Almendral, M. J., Curto, Y., Criado, J. J., Rodriguez, E., and Manzano, J. L. (2006). Determination of the DNA-binding characteristics of ethidium bromide, proflavine, and cisplatin by flow injection analysis: Usefulness in studies on antitumor drugs. *Anal. Biochem.* 355, 157–164. doi: 10.1016/j.ab.2006.06.004

Anderson, H. L. (1994). Conjugated porphyrin ladders. *Inorgan. Chem.* 33, 972–981. doi: 10.1021/ic00083a022

Andrabi, M., Mizuguchi, K., and Ahmad, S. (2014). Conformational changes in DNA-binding proteins: Relationships with precomplex features and contributions to specificity and stability. *Proteins Struct. Funct. Bioinform.* 82, 841–857. doi: 10.1002/prot.24462

Bates, M., Blosser, T. R., and Zhuang, X. W. (2005). Short-range spectroscopic ruler based on a single-molecule optical switch. *Phys. Rev. Lett.* 94:4. doi: 10.1103/PhysRevLett.94.108101

Berova, N., Pescitelli, G., Petrovic, A. G., and Proni, G. (2009). Probing molecular chirality by CD-sensitive dimeric metalloporphyrin hosts. *Chem. Commun.* 45, 5958–5980. doi: 10.1039/b909582a

Biebricher, A. S., Heller, I., Roijmans, R. F. H., Hoekstra, T. P., Peterman, E. J. G., and Wuite, G. J. L. (2015). The impact of DNA intercalators on DNA and DNA-processing enzymes elucidated through force-dependent binding kinetics. *Nat. Commun.* 6:12. doi: 10.1038/ncomms8304

Borjesson, K., Preus, S., El-Sagheer, A. H., Brown, T., Albinsson, B., and Wilhelmsson, L. M. (2009). Nucleic acid base analog FRET-pair facilitating detailed structural measurements in nucleic acid containing systems. *Journal of the American Chemical Society* 131, 4288–4293. doi: 10.1021/ja806944w

Bouamaied, I., Fendt, L. A., Häussinger, D., Wiesner, M., Thöni, S., Amiot, N., et al. (2007). Porphyrin-DNA: A supramolecular scaffold for functional molecules on the nanometre scale. *Nucleosides Nucleotides & Nucleic Acids* 26, 1533–1538. doi: 10.1080/15257770701544468

Brewer, A., Siligardi, G., Neylon, C., and Stulz, E. (2011). Introducing structural flexibility into porphyrin-DNA zipper arrays. *Organ. Biomol. Chem.* 9, 777–782. doi: 10.1039/C0OB00535E

Burns, J. R., Preus, S., Singleton, D. G., and Stulz, E. (2012). A DNA based five-state switch with programmed reversibility. *Chem. Commun.* 48, 11088–11090. doi: 10.1039/c2cc35799b

Eberhard, H., Diezmann, F., and Seitz, O. (2011). DNA as a molecular ruler: interrogation of a tandem SH2 domain with self-assembled, bivalent DNA-peptide complexes. *Angew. Chemie Int. Ed.* 50, 4146–4150. doi: 10.1002/anie.201007593

Fendt, L. A., Bouamaied, I., Thöni, S., Amiot, N., and Stulz, E. (2007). DNA as supramolecular scaffold for porphyrin arrays on the nanometer scale. *J. Am. Chem. Soc.* 129, 15319–15329. doi: 10.1021/ja075711c

Hall, L. M., Gerowska, M., and Brown, T. (2012). A highly fluorescent DNA toolkit: synthesis and properties of oligonucleotides containing new Cy3, Cy5 and Cy3B monomers. *Nucleic Acids Res.* 40:10. doi: 10.1093/nar/gks303

Hayashi, M., and Harada, Y. (2007). Direct observation of the reversible unwinding of a single DNA molecule caused by the intercalation of ethidium bromide. *Nucleic Acids Res.* 35:7. doi: 10.1093/nar/gkm529

Holden, S. J., Uphoff, S., Hohlbein, J., Yadin, D., Le Reste, L., Britton, O. J., et al. (2010). Defining the limits of single-molecule FRET resolution in TIRF microscopy. *Biophys. J.* 99, 3102–3111. doi: 10.1016/j.bpj.2010.09.005

Huang, X. F., Nakanishi, K., and Berova, N. (2000). Porphyrins and metalloporphyrins: versatile circular dichroic reporter groups for structural studies. *Chirality* 12, 237–255. doi: 10.1002/(SICI)1520-636X(2000)12:4<237::AID-CHIR10>3.0.CO;2-6

Karacan, P., and Okay, O. (2013). Ethidium bromide binding to DNA cryogels. *Reactive Funct. Polym.* 73, 442–450. doi: 10.1016/j.reactfunctpolym.2012.11.014

Klostermeier, D., and Millar, D. P. (2001). Time-resolved fluorescence resonance energy transfer: a versatile tool for the analysis of nucleic acids. *Biopolymers* 61, 159–179. doi: 10.1002/bip.10146

Krugh, T. R., Wittlin, F. N., and Cramer, S. P. (1975). Ethidium bromide-dinucleotide complexes - evidence for intercalation and sequence preferences in binding to double-stranded nucleic-acids. *Biopolymers* 14, 197–210. doi: 10.1002/bip.1975.360140114

Lewis, F. D., Zhang, L. G., Liu, X. Y., Zuo, X. B., Tiede, D. M., Long, H., et al. (2005). DNA as helical ruler: exciton-coupled circular dichroism in DNA conjugates. *J. Am. Chem. Soc.* 127, 14445–14453. doi: 10.1021/ja0539387

Liu, G. L., Yin, Y. D., Kunchakarra, S., Mukherjee, B., Gerion, D., Jett, S. D., et al. (2006). A nanoplasmonic molecular ruler for measuring nuclease activity and DNA footprinting. *Nat. Nanotechnol.* 1, 47–52. doi: 10.1038/nnano.2006.51

Malinovskii, V. L., Wenger, D., and Häner, R. (2010). Nucleic acid-guided assembly of aromatic chromophores. *Chem. Soc. Rev.* 39, 410–422. doi: 10.1039/B910030J

Mathew-Fenn, R. S., Das, R., Silverman, J. A., Walker, P. A., and Harbury, P. A. B. (2008). A molecular ruler for measuring quantitative distance distributions. *PLoS ONE* 3:e3229. doi: 10.1371/journal.pone.0003229

Matile, S., Berova, N., Nakanishi, K., Fleischhauer, J., and Woody, R. W. (1996). Structural studies by exciton coupled circular dichroism over a large distance: Porphyrin derivatives of steroids, dimeric steroids, and brevetoxin B. *J. Am. Chem. Soc.* 118, 5198–5206. doi: 10.1021/ja960126p

Mayer-Enthart, E., and Wagenknecht, H.-A. (2006). Structure-sensitive and self-assembled helical pyrene array based on DNA architecture. *Angew. Chem. Int. Ed.* 45, 3372–3375. doi: 10.1002/anie.200504210

Minasyan, S. H., Tavadyan, L. A., Antonyan, A. P., Davtyan, H. G., Parsadanyan, M. A., and Vardevanyan, P. O. (2006). Differential pulse voltammetric studies of ethidium bromide binding to DNA. *Bioelectrochemistry* 68, 48–55. doi: 10.1016/j.bioelechem.2005.03.006

Mohamadi, F., Richards, N. G. J., Guida, W. C., Liskamp, R., Lipton, M., Caufield, C., et al. (1990). Macromodel - an integrated software system for modeling organic and bioorganic molecules using molecular mechanics. *J. Comput. Chem.* 11, 440–467. doi: 10.1002/jcc.540110405

Nafisi, S., Saboury, A. A., Keramat, N., Neault, J. F., and Tajmir-Riahi, H. A. (2007). Stability and structural features of DNA intercalation with ethidium bromide, acridine orange and methylene blue. *J. Mol. Struct.* 827, 35–43. doi: 10.1016/j.molstruc.2006.05.004

Nguyen, T., Brewer, A., and Stulz, E. (2009). Duplex stabilization and energy transfer in zipper porphyrin-DNA. *Angew. Chemie Int. Ed.* 48, 1974–1977. doi: 10.1002/anie.200805657

Nguyen, T., Hakansson, P., Edge, R., Collison, D., Goodman, B. A., Burns, J. R., et al. (2014). EPR based distance measurement in Cu-porphyrin-DNA. *New J. Chem.* 38, 5254–5259. doi: 10.1039/C4NJ00673A

Preus, S., Kilsa, K., Miannay, F. A., Albinsson, B., and Wilhelmsson, L. M. (2013). FRETmatrix: a general methodology for the simulation and analysis of FRET in nucleic acids. *Nucleic Acids Res.* 41:e18. doi: 10.1093/nar/gks856

Preus, S., and Wilhelmsson, L. M. (2012). Advances in quantitative FRET-based methods for studying nucleic acids. *Chembiochem* 13, 1990–2001. doi: 10.1002/cbic.201200400

Reinhard, B. M., Siu, M., Agarwal, H., Alivisatos, A. P., and Liphardt, J. (2005). Calibration of dynamic molecular rulers based on plasmon coupling between gold nanoparticles. *Nano Lett.* 5, 2246–2252. doi: 10.1021/nl051592s

Rossetti, G., Dans, P. D., Gomez-Pinto, I., Ivani, I., Gonzalez, C., and Orozco, M. (2015). The structural impact of DNA mismatches. *Nucleic Acids Res.* 43, 4309–4321. doi: 10.1093/nar/gkv254

Sabanayagam, C. R., Eid, J. S., and Meller, A. (2005). Using fluorescence resonance energy transfer to measure distances along individual DNA molecules: Corrections due to nonideal transfer. *J. Chem. Phys.* 122:061103. doi: 10.1063/1.1854120

Scaria, P. V., and Shafer, R. H. (1991). Binding of ethidium-bromide to a dna triple helix - evidence for intercalation. *J. Biol. Chem.* 266, 5417–5423.

Schiemann, O., Piton, N., Mu, Y., Stock, G., Engels, J. W., and Prisner, T. F. (2004). A PELDOR-based nanometer distance ruler for oligonucleotides. *J. Am. Chem. Soc.* 126, 5722–5729. doi: 10.1021/ja0393877

Singleton, D. G., Hussain, R., Siligardi, G., Kumar, P., Hrdlicka, P. J., Berova, N., et al. (2016). Increased duplex stabilization in porphyrin-LNA zipper arrays with structure dependent exciton coupling. *Org. Biomol. Chem.* 14, 149–157. doi: 10.1039/C5OB01681A

Sonnichsen, C., Reinhard, B. M., Liphardt, J., and Alivisatos, A. P. (2005). A molecular ruler based on plasmon coupling of single gold and silver nanoparticles. *Nat. Biotechnol.* 23, 741–745. doi: 10.1038/nbt1100

Stein, I. H., Schuller, V., Bohm, P., Tinnefeld, P., and Liedl, T. (2011). Single-molecule FRET ruler based on rigid DNA origami blocks. *Chemphyschem* 12, 689–695. doi: 10.1002/cphc.201000781

Steinhauer, C., Jungmann, R., Sobey, T. L., Simmel, F. C., and Tinnefeld, P. (2009). DNA origami as a nanoscopic ruler for super-resolution microscopy. *Angew. Chemie Int. Ed.* 48, 8870–8873. doi: 10.1002/anie.200903308

Teo, Y. N., and Kool, E. T. (2012). DNA-multichromophore systems. *Chem. Rev.* 112, 4221–4245. doi: 10.1021/cr100351g

Trifonov, A., Raytchev, M., Buchvarov, I., Rist, M., Barbaric, J., Wagenknecht, H. A., et al. (2005). Ultrafast energy transfer and structural dynamics in DNA. *J. Phys. Chem. B* 109, 19490–19495. doi: 10.1021/jp052108c

Vardevanyan, P. O., Antonyan, A. P., Parsadanyan, M. A., Davtyan, H. G., and Karapetyan, A. T. (2003). The binding of ethidium bromide with DNA: interaction with single- and double-stranded structures. *Exp. Mol. Med.* 35, 527–533. doi: 10.1038/emm.2003.68

Wang, L., Gaigalas, A. K., Blasic, J., Holden, M. J., Gallagher, D. T., and Pires, R. (2003). Fluorescence resonance energy transfer between donor-acceptor pair on two oligonucleotides hybridized adjacently to DNA template. *Biopolymers* 72, 401–412. doi: 10.1002/bip.10482

Conflict of Interest: The authors declare that the research was conducted in the absence of any commercial or financial relationships that could be construed as a potential conflict of interest.

frontiers in Chemistry

REVIEW
published: 28 February 2020
doi: 10.3389/fchem.2020.00112

Probing of Nucleic Acid Structures, Dynamics, and Interactions With Environment-Sensitive Fluorescent Labels

Benoît Y. Michel[1], *Dmytro Dziuba*[1,2], *Rachid Benhida*[1,3], *Alexander P. Demchenko*[4,5] *and Alain Burger*[1]*

[1] Université Côte d'Azur, CNRS, Institut de Chimie de Nice, UMR 7272 – Parc Valrose, Nice, France, [2] Laboratoire de Bioimagerie et Pathologies, UMR 7021 CNRS, Faculté de Pharmacie, Université de Strasbourg, Illkirch, France, [3] Mohamed VI Polytechnic University, UM6P, Ben Guerir, Morocco, [4] Laboratory of Nanobiotechnologies, Palladin Institute of Biochemistry, Kyiv, Ukraine, [5] Institute of Physical, Technical and Computer Science, Yuriy Fedkovych National University, Chernivtsi, Ukraine

Fluorescence labeling and probing are fundamental techniques for nucleic acid analysis and quantification. However, new fluorescent probes and approaches are urgently needed in order to accurately determine structural and conformational dynamics of DNA and RNA at the level of single nucleobases/base pairs, and to probe the interactions between nucleic acids with proteins. This review describes the means by which to achieve these goals using nucleobase replacement or modification with advanced fluorescent dyes that respond by the changing of their fluorescence parameters to their local environment (altered polarity, hydration, flipping dynamics, and formation/breaking of hydrogen bonds).

Keywords: fluorescence sensing, emissive nucleobase, nucleoside analog, probing nucleic acids, probing interactions

OPEN ACCESS

Edited by:
James Tucker,
University of Birmingham,
United Kingdom

Reviewed by:
Adam Charles Sedgwick,
University of Texas at Austin,
United States
Xin Li,
Zhejiang University, China

***Correspondence:**
Alain Burger
alain.burger@univ-cotedazur.fr

Specialty section:
This article was submitted to Supramolecular Chemistry, a section of the journal Frontiers in Chemistry

Received: *09 November 2019*
Accepted: *06 February 2020*
Published: *28 February 2020*

Citation:
Michel BY, Dziuba D, Benhida R, Demchenko AP and Burger A (2020) Probing of Nucleic Acid Structures, Dynamics, and Interactions With Environment-Sensitive Fluorescent Labels. Front. Chem. 8:112. doi: 10.3389/fchem.2020.00112

INTRODUCTION

Rapid progress in genomics, transcriptomics, and epigenomics are driving a strong demand for reliable fluorescence-based tools for studying the structural and conformational polymorphisms of nucleic acids (NAs), their variability and internal dynamics, their interactions with proteins, metabolites, NA-targeting drugs, water molecules, and ions at sub-molecular and atomic levels (Wilhelmsson and Tor, 2016). Such tools should allow direct molecular recognition between tested NAs and probes that produces an easily recordable and interpretable output signal. They must be viable in different heterogeneous media, including living cells and tissues. Further complicating this task, ideally this technology ought to exclude double labeling of probing NA sequence(s): the requirement for energy transfer, electron transfer quenching or excimer formation between incorporated dyes. The informative signal should be generated by a single fluorescent nucleoside site-selectively incorporated into the probing NA strand and reporting any interactions by varying one of the fluorescence parameters: fluorescence intensity, fluorescence lifetime, optical anisotropy, fluorescence color (emission wavelength) or appearance of new bands in fluorescence emissions (Herdewijn, 2008). Ultra-high sensitivity is insufficient; the fluorescence reporting signal needs to be informative and perceptible to the weak intermolecular interactions that can be expressed as the effects of polarity and H-bonding at the sites of probe location (Demchenko, 2015). In this review, we show that such important developments have already become a reality and we analyze existing and prospective pathways leading to this ambitious goal.

Traditional fluorescence techniques, as well as more recently introduced approaches such as two-photon excitation and single molecular detection, can be useful and efficient here. Since the very weak fluorescence of natural NA bases prevents most applications, the key issue is the design of fluorescence reporters that can be incorporated into a system of interest with minimal perturbation of its structure and dynamics. Hundreds of fluorescent probes are commercially available and are used routinely and more are developed every year. Progress in this area will ultimately depend on the ability of chemists to rationally design fluorophores with parameters that are optimal for the detection methods and, at the same time, possess recognition units for a broader range of applications.

This review focuses on cutting-edge achievements and novel applications for single emissive nucleosides in the study of NA structures, dynamics and interactions. After summarizing both the major problems that can be overcome with this approach and the methodologies for incorporating fluorescent base analogs, we will critically analyze the applicability, achievements and prospects for each of the fluorescence detection methods.

RESOLVING PROBLEMS WITH SMART BASE SUBSTITUENTS

DNA is the hereditary material in all cellular organisms on Earth. In humans, about 1.5% of DNA encodes for proteins. The remaining 98.5% is non-coding DNA, which is essential for cell functions: non-coding DNA includes the regulatory elements of the protein-coding genes, such as promoters and enhancers, where numerous transcription factors bind to transcriptionally regulate the expression of corresponding genes. Furthermore, a large portion (up to 75%) of the non-coding DNA is transcribed into non-coding RNAs (Djebali et al., 2013). The classical examples are transfer RNAs (tRNAs) and ribosomal RNAs (rRNAs), the central components of the cellular protein biosynthesis machinery. In addition, micro-RNAs (miRNAs) and long non-coding RNAs (lncRNAs) are involved into post-transcriptional regulation of gene expression, shaping and maintaining of the chromatin landscape, and other key biological processes.

The functions of NAs correlate with their dynamics and structures. Although most DNA exists as double-stranded DNA, the single-stranded forms are important intermediates in the processes of DNA replication, transcription, repair, and recombination (Técher et al., 2017). The linear NA chains can also create a variety of tridimensional motifs, which define structural polymorphisms (Kaushik et al., 2016; Strobel et al., 2018). Beyond the well-known B-DNA and A-RNA forms, NA can fold into a Z duplex, triplex, quadruplex, or i-motif, and form bulges, loops, holiday junctions, and pseudoknots, etc. These non-canonical motifs are believed to have an important influence on major cellular processes. For instance, guanine-rich sequences found at the end of chromosomes can fold into G-quadruplexes, which are thought to protect chromosome integrity. RNA exhibits a superior degree of structural complexity and diversity. Many non-coding RNAs contain multiple structural motifs that can interact to build more diverse three-dimensional structures, such as those of tRNAs and ribozymes. NAs are anionic polyelectrolyte macromolecules that must adapt to the crowded cellular environment. Their structures and functions depend on their interplay with the surrounding water and ions, on chemical modifications (e.g., to DNA and RNA bases), pH, temperature and interactions with other NAs (e.g., non-coding RNAs) and/or proteins (e.g., histones and DNA polymerase). NA/NA and NA/protein interactions are central to cellular life and regulation, including replication, repair, recombination, base modifications, transcription, viral infections, and protein synthesis to name a few. For instance, the dynamic interactions between DNA and chromatin proteins and chemical modifications to specific nucleobases (e.g., methylation and demethylation) can dramatically affect gene expression. Above the genetic code, there is a supra code called the epigenetic code, which is involved in cell differentiation, regulation of gene expression, development, and suppression of transposable elements (Bird, 2007; Berger et al., 2009). As one of the major epigenetic modifications, DNA methylation is a multifunctional marker that plays a direct role in the regulation of gene expression and an indirect structural role for the adjacent chromatin, as well as in the expression of miRNAs encoded in the genome (Berney and McGouran, 2018). From its side, miRNA is part of an active RNA-induced silencing complex (RISC) containing multiple associated proteins. It is base paired with complementary mRNA sequences, which leads to mRNA silencing. Other proteins are known to destabilize base-pairing in duplexes and to withdraw a nucleobase from an intra-helical position into a binding pocket. This process corresponds to the so-called base flipping that is common for DNA-repair enzymes and DNA methyltransferases. To understand the functions of NAs, it is therefore important to study the molecular mechanisms, dynamics, conformational changes and interactions of NAs with their cellular partners. However, accessing this information is challenging due to dynamic nature of NAs, the instability of their many structures, and the transitory nature of the associated intermediates.

This overview highlights that methods are urgently needed to survey conformational heterogeneity and dynamics of NAs and for the detection and quantification of NAs and protein/NA interactions. Access to this information is of primary importance for both basic and biomedical research. This may result in new methods for molecular diagnostics, new therapeutic approaches and valuable data for medicinal chemists for the design of drug candidates. To achieve this goal, highly sensitive tools and methods are needed. This is coupled with a move away from traditional radioisotopic methods for NA detection, with a concomitant increase in the use of fluorescence-based technics for identifying NA species. These techniques have become the leading approaches to study complex systems and to visualize living cells due their increased sensitivity, down to single molecule resolution, and strong spatio-temporal detection. They also have numerous applications in high-throughput screening and molecular diagnostics. In this context, fluorescence methods based on single fluorescent nucleosides site-selectively incorporated into NAs have found applications for NA visualization within cells, genotyping, detection of single-nucleotide polymorphisms (SNP), studies of structures, thermodynamics, dynamics of NAs and their interactions with

proteins, and small molecules targeting NAs. How do these techniques work, where are we now and what are the prospects for this booming research area?

INCORPORATION OF FLUORESCENT NUCLEOSIDE ANALOGS (FNAs): METHODOLOGY

Exogenous fluorophores must be introduced into NA structures to perform these analyses (Nakatani and Tor, 2016). These labels need to exhibit high absorption coefficients and quantum yields, and have to be selectively excited in a domain where NAs and proteins are transparent. Fluorophores can be introduced in two distinct ways to make NAs fluoresce: either non-covalent or covalent labeling. Non-covalent labeling uses organic dyes of low molecular weight that bind to NA minor grooves or intercalate helices to increase fluorescence, such as the Hoechst and ethidium bromide dyes, respectively. The vast majority of stains are not sequence specific and many are based on non-covalent attachment to NAs, which are sensitive to conformational changes but do not exhibit specific base recognition (Tatikolov, 2012; Ma et al., 2013). Non-covalently attached fluorophores are mainly used for the visualization of NA in experimental biology procedures (Kapuscinski, 1995; Narayanaswamy et al., 2015). They can also be used to monitor folding and interactions of NAs with their targets but are not able to provide site-specific data and present many other limitations.

In contrast, covalent labeling can be achieved with high specificity and therefore has a broader range of applications (Davies et al., 2000). The chemical structure of NAs allows for multiple ways of attaching exogenous fluorophores: numerous and diverse examples of this type of labeling have previously been described. The label can be attached to certain position of the NA via a linker or may substitute one nucleobase within the NA (**Figure 1**). Fluorophores covalently attached to the backbone at one end or within the NA but outside the actual base stack are referred to as external modifications. Substituting a nucleobase inside the base stack is referred to as an internal modification (Wilhelmsson, 2010). External labeling with classical fluorophores, such as rhodamine, cyanine, and fluorescein dyes, linked to the nucleoside via a flexible spacer arm is very common (**Figures 1A,B**). These dyes are bright and are mainly used for fluorescent detection, for example in DNA sequencing as binary probes when combined with a second partner for Förster Resonance Energy Transfer (FRET). This type of oligodeoxyribonucleotide (ODN) labeling is also used for real time PCR detection, single-nucleotide mutation screening, studying NA conformational changes and NA interactions with target proteins. As an alternative to the FRET-interacting chromophore pairs, the formation or distortion of J-aggregates, H-aggregates, excimers, or exciplexes can be employed to generate changes in fluorescence (Okamoto, 2011; Wilson et al., 2018; and for reviews, see Didenko, 2001; Martí et al., 2007; Varghese and Wagenknecht, 2009; Kolpashchikov, 2010; Guo et al., 2012; Teo and Kool, 2012; Ma et al., 2013).

Despite widespread success, the bi- and multi-fluorophore approaches have several intrinsic disadvantages. Production of DNA or RNA probes bearing two and more different fluorophores leads to synthesis and purification issues that increase the cost by orders of magnitude. For instance, insufficient labeling can produce false results due to the absence of one of the components of the resonance energy transfer pair, which has been the major source of mistakes in FRET-based sensing (Lakowicz, 2006). These issues also apply to other ODN-based probes featuring interactions between two fluorophores. Binary probes display further limitations in structural and functional studies of NAs, for example, they are unable to sense interactions between NAs and their targets if these interactions do not induce sufficient changes in the distance separating the two probes. Further, fluorophores are often bulky and can perturb the system under study. The same comments apply when the binary probe is a NA and a protein.

Fluorescent probes based on emissive nucleoside analogs that are sensitive to the environment bypass double labeling and deserve special attention as powerful tools in bioanalysis, especially given the increasing development of this technology. These DNA-based structures are covalently labeled with a single type of fluorophore and it is possible to attach the probe, not only to a specific NA sequence, but also to position it in the structure in non-perturbing manner. Moreover, it is possible to probe both major and minor grooves in NA double helices. In these efforts, we have observed rapid progress toward technologies designed to address more specific interactions. From the structural point of view, this technology can be divided into categories. The fluorophore can replace one of the natural nucleobases, acting as a nucleobase mimic (**Figure 1D**). Alternatively, a chromophore (usually a fluorophore) can be grafted with a short linker to one of the nucleobases (**Figure 1C**) or attached directly to the sugar-phosphate. These fluorescent chemical entities, which are incorporated into the DNA, are usually referred as *fluorescent nucleoside analogs* (FNAs) (Sinkeldam et al., 2010). Depending on their chemical composition, fluorescent nucleobase mimics can be divided into isomorphic, expanded or extended base analogs that maintain or not Wtason-Crick base-pairing, or aromatic fluorophores that lack the H-bonding interactions between complementary bases (Sinkeldam et al., 2010). Due to their well-defined position, FNAs allow site-selective monitoring of conformational or constitutional changes of NAs and are therefore potent signal transducers. FNAs are a group of chemically diverse compounds that often (but not always) share partial deoxyribose moieties with natural nucleosides. A few hundred different FNAs have been described to date. This review is not intended to be a comprehensive catalog of all existing literature reports on FNAs: previous reviews are available on the topic (Asseline, 2006; Wilson and Kool, 2006; Dodd and Hudson, 2009; Srivatsan and Sawant, 2011) and the following comprehensive reviews are especially recommended (Sinkeldam et al., 2010; Wilhelmsson, 2010; Xu et al., 2017; Saito and Hudson, 2018).

The use of FNAs requires the site-selective location of the label within NA. Such a labeling has been well-described and is a methodologically mature area in bioorganic chemistry. Labeling can be accomplished according to different strategies. FNAs can be introduced using either solid-phase phosphoramidite chemical synthesis (Hogrefe et al., 2013) or enzymatic

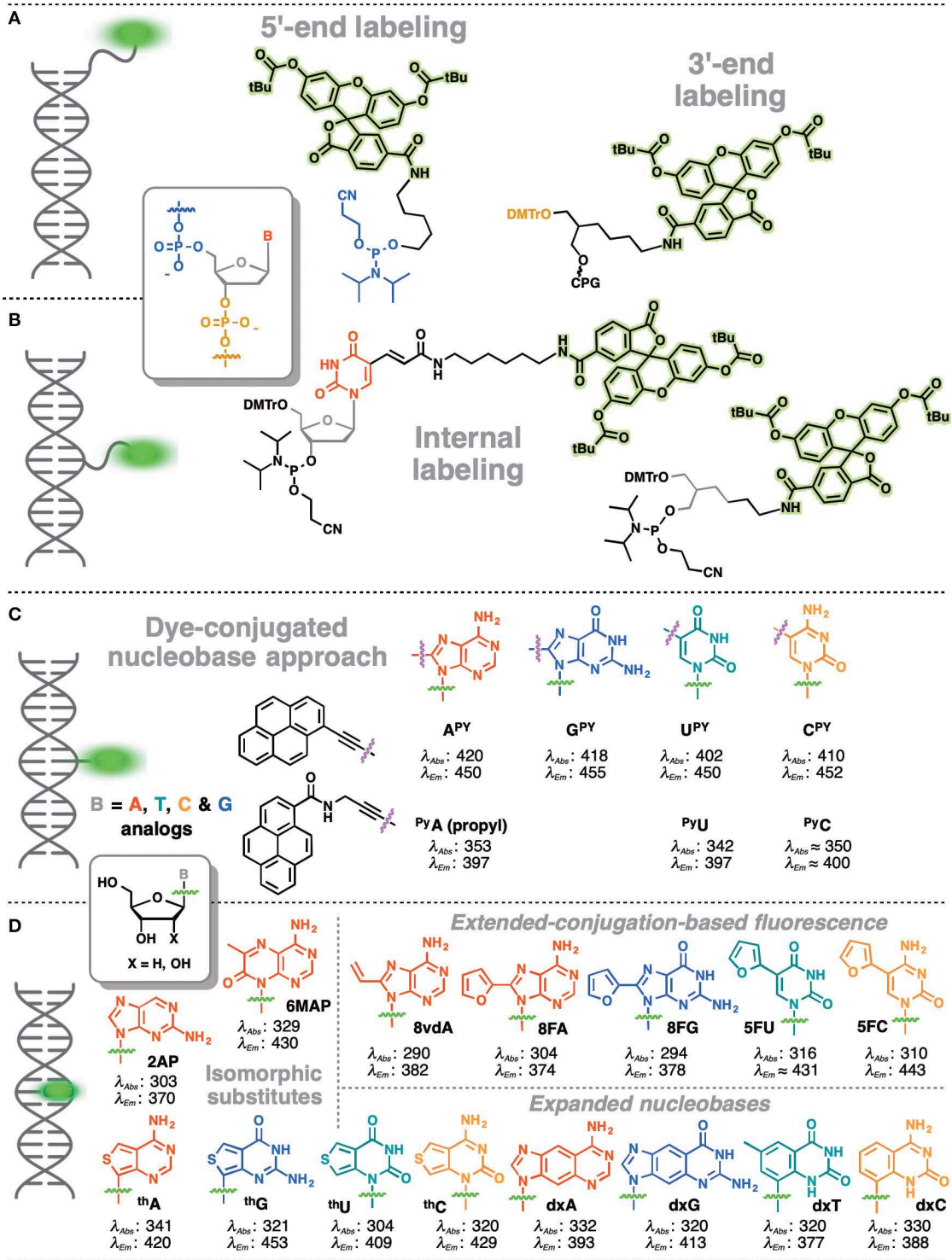

FIGURE 1 | Main strategies for covalent fluorescence labeling of NAs: via a flexible tether either at the 3′/5′-end **(A)**, or at an internal position **(B)** illustrated here by amidite building blocks bearing a fluorescein (Teo and Kool, 2012; Lavis and Raines, 2014); **(C)** through a short and rather rigid linker for extra-helical probing depicted by pyrene, an aromatic polycyclic dye connected to the pyrimidine C5 and purine C8 positions (Rist et al., 2003; Okamoto et al., 2004, 2005a; Saito et al., 2004; Hwang et al., 2005; Seo et al., 2005; Seo and Kim, 2006; Østergaard and Hrdlicka, 2011) and as a nucleobase surrogate for intra-helical probing **(D)** exemplified by selected isomorphic base mimics (Hawkins, 2001; McCoy et al., 2014; Park et al., 2014; Jones and Neely, 2015) and nucleobases made emissive by ring expansion (Gao et al., 2004; Liu et al., 2004; Krueger et al., 2007; Srivatsan et al., 2008a,b; Shin et al., 2011) or extension of conjugation (Gaied, 2005; Greco and Tor, 2005, 2007; Srivatsan and Tor, 2007a,b; Sinkeldam et al., 2008; Greco et al., 2009). Excitation and emission wavelengths were given in nm.

(polymerase) incorporation (Hocek, 2019). FNAs can be formulated as building blocks for the construction of NAs or can be introduced post-synthetically using bioorthogonal chemistry (post-synthetic labeling; Xu et al., 2017).

OPERATION WITH PARAMETERS OF FLUORESCENCE EMISSION

Fluorescence is the emission of light that can occur when a molecule absorbs a light quantum to become excited to the singlet state and then releases its energy and relaxes back to the ground state. Its essential features are the delay in time between light absorption and emission resulting in fluorescence decays in the picosecond (ps) to nanosecond (ns) time range and also the decrease in energy of emitted quanta (the Stokes shift). The time delay allows one to observe different processes occurring on this very short time scale, such as translational or rotational diffusion or resonance energy transfer. The Stokes shift enables not only the separation of the fluorescence signal from that of light scattering in detection devices but can also be the source of valuable information on the intermolecular interactions decreasing the excited-state energy.

The output signal is always the number of emitted light quanta that can be integrated and presented as fluorescence intensity. When the intensity is recorded as a function of time, its decay can be characterized by the fluorescence lifetime and gives rise to lifetime-based sensing. Excitation with linearly polarized light also results in polarized emission (optical anisotropy). Any rotational motion or transfer of energy to another fluorophore decreases the polarization. When the light intensity is recorded with spectral resolution, the resulting fluorescence emission spectra carry the information on the fluorophore interactions and reactivity in the excited state (that may lead to the generation of new bands), which, in turn, opens a new channel of information in sensing.

Thus, fluorescence offers a very limited number of parameters for quantitative detection of changes in a given system in terms of their structure, dynamics, and interactions (**Figure 2**). These include fluorescence intensity at a certain wavelength, fluorescence lifetime, fluorescence anisotropy, position of the emission maxima and, in special cases, the ratio of intensities at two selected wavelengths (Demchenko, 2010). All these parameters can be used in the creation of NA-based probes (Su et al., 2012). In the following sections, we discuss the use of FNAs as the fluorescent reporters that change these parameters in different contexts involving NAs. For each of them, we focus on structural requirements and sensing mechanisms that influence the fluorescence response. The outlined principles can be useful for the rational design of innovative NA-based fluorescent molecular probes.

The choice of detection method should be dictated by the aim of the research project or by the new technology to be developed. For instance, the double-helical conformation can be detected in a simple way, by increasing the intensity of intercalating dyes. Regarding intermolecular interactions and the conformational changes that accompany them, the appropriate choice of sensing method should be selected from those listed above, with an optimal design of the fluorophore and its proper incorporation into the desired sites. Thus, a hybridization assay should generate a strongly distinguishable signal upon binding or non-binding of the target DNA sequence. Ideally, this signal would be an OFF-ON switch in fluorescence intensity. For more complicated issues, such as the atomic-scale variations in structure (hydration), more sophisticated tools are required.

FNAs FOR INTENSITY-BASED SENSING

Fluorescence intensity is by far the most widely used parameter of fluorescence emission. It is a relative numerical representation of the number of emitted photons recorded by the detector. Since this parameter depends on fluorophore concentration and many instrumental factors (such as light source brightness, detector sensitivity and illuminated volume), its quantitative determination requires a reference. Within a single experiment series, all parameters related to the instrumental settings are typically kept constant and thus, all changes in fluorescence emission can be attributed to the changes in quantum yield (Φ). The latter is the absolute measure of fluorescence ability at given conditions that can be defined as the ratio of emitted quanta to the whole number of absorbed quanta. Accordingly, since it depends on the relative ratio of efficiencies of emissive and non-emissive excited state depopulation pathways, Φ can vary in broad ranges and is affected by numerous factors, such as the presence of molecular segments with rotational mobility, the formation or breaking of hydrogen bonds and the presence of internal or external quenchers. Hence, fluorescence intensity could change dramatically. Only in the ideal case of complete absence of non-radiative processes, Φ value will reach 100 % and the intensity will become maximal. Usually, with NA base substitutes, Φ is revealed to be much lower. In this respect, if complete quenching ($\Phi \approx 0$) is achieved, this may determine the broad dynamic range of an assay based on "OFF-ON" switching. The fluorescence intensity changes are usually measured at a single wavelength (usually the band maximum), which is the simplest and most convenient method to get information from a fluorescence reporter.

Many known FNAs have been shown to change their emission intensity in response to different molecular events such as stacking with the flanking nucleobases, forming hydrogen bonds with a complementary nucleobase, etc. Deep knowledge and understanding of the nature of different quenching and lightening mechanisms are beneficial for the rational design of new fluorescent probes.

FNAs Quenching Upon Stacking

Purines and pyrimidines are known to quench fluorescence of many organic fluorophores. A classic example is the quenching of tryptophan fluorescence by nucleobases within DNA–protein complexes, which is the basis of the first method used to observe DNA–protein interactions by fluorescence spectroscopy (Lakowicz, 2006). In view of this, it is not surprising that the fluorescence of many FNAs are quenched upon their incorporation into DNA. This effect has been widely used in

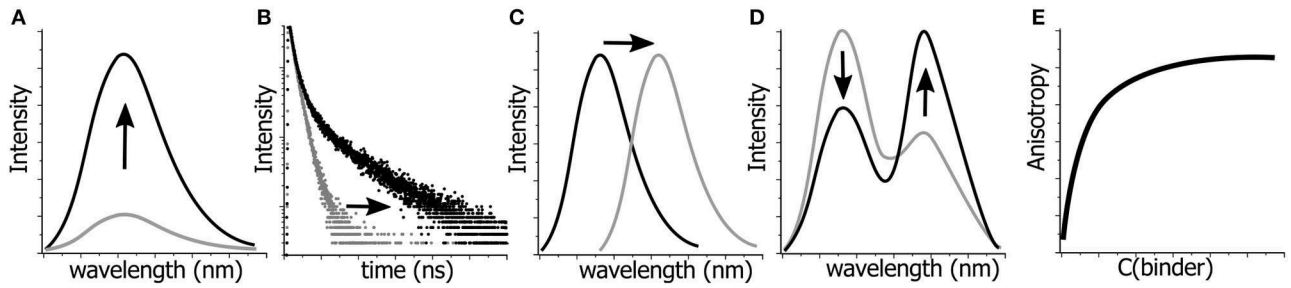

FIGURE 2 | Possibilities for monitoring the changes in molecular structures, dynamics and interactions by fluorescence spectroscopy. Variations in: **(A)** fluorescence intensity, **(B)** fluorescence lifetimes, **(C)** position of the emission maximum, i.e., emission color, **(D)** ratio of intensities at two wavelengths, and **(E)** fluorescence anisotropy can be detected and quantified.

the construction of conformation-sensitive fluorescent probes. FNAs that are quenched upon incorporation into DNA or RNA segments are a family of structurally diverse compounds. Selected examples will be discussed below. Of all FNAs, quenching of 2-aminopurine (**2AP**) has been the most widely studied because it has been the most popular probe for decades (**Figure 1D**). **2AP** can form stable hydrogen-bonded base pairs with T and C, thus, it can be used as an A and G mimic (Sowers et al., 1986; Law et al., 1996; Millar, 1996; Reha-Krantz et al., 2011). Incorporation of **2AP** introduces minimal, although notable perturbations to the dynamic and thermodynamic stability of double-stranded DNA (Dallmann et al., 2010). The absorption of **2AP** overlaps the red edge of the NA absorption band and its emission shows a relatively large Stokes shift (**Figure 1D**). In a free form, **2AP** is brightly fluorescent in water ($\Phi = 0.68$). Meanwhile, upon incorporation into ODNs, the fluorescence of **2AP** is severely quenched, reaching up to a 200-fold reduction (Ward et al., 1969).

2AP is quenched by all four natural bases with G being the most efficient quencher (Somsen et al., 2005). Similarly, FNAs can be quenched by all four canonical DNA nucleobases or selectively by a few of them. The degree of quenching typically depends on the DNA conformation and the sequence context. Many fluorophores are quenched by Photoinduced Electron Transfer (PET) mechanisms. Upon PET quenching, FNAs can be either reduced or oxidized to form a charge-transfer (CT) complex with one of the surrounding nucleobases and further undergoing radiationless relaxation to the ground state. The PET efficiency is given by the Rehm–Weller equation (Rehm and Weller, 1970; Farid et al., 2011), and the possibility of PET quenching can be estimated by a comparison of the redox potentials of the natural nucleobases with that of the corresponding FNA (Seidel et al., 1996; Psciuk et al., 2012). Among the different canonical nucleobases, guanine, with the lowest oxidation potential, is known to be the most efficient electron donor in PET resulting in strong quenching of many organic dyes upon contact with the G base (Seidel et al., 1996; Torimura et al., 2001). Other mechanisms have been proposed to explain FNA quenching, such as the formation of dark non-emissive states via mixing and delocalizing of molecular orbitals of the fluorophore among neighboring nucleobases, as it has been proposed for **2AP** and 8-vinyladenosine (**8vdA**, **Figure 1D**; Gaied, 2005). In general, the quenching mechanisms are complex and may involve multiple non-radiative relaxation pathways. The relative contribution of these quenching mechanisms in DNA is not fully understood, even for **2AP**. Despite these gray zones, many FNAs of this group are effectively used in fluorescence sensing.

FNAs that are strongly quenched upon incorporation into ss- and ds-NAs can be used for the development of fluorogenic probes. Within this approach, the "OFF" state is represented by a DNA construct incorporating the emissive nucleoside analog quenched by the neighboring bases. Transition of the fluorescence signal results in the "ON" state, which is observed upon binding of the target (NA, protein or small molecule). A representative set of examples of such probes is given below.

Probing the Single-Nucleotide Polymorphism

SNPs, also known as single-base mutations, are the most prevalent genetic variations (White and Cantsilieris, 2017). Oligonucleotides incorporating stacking-sensitive nucleosides have been studied for direct probing of single-nucleotide polymorphisms (SNPs), and pyrrolo-cytosines (**pC,** C mimic) are representative for this approach. Typically, the fluorophore is positioned in the probe strand at the position opposite to the SNP site. Hybridization to a perfectly matched target causes the fluorophore to stack between the surrounding nucleobases. A light-down response (OFF) is observed in this case (**Figure 3A**). However, in the case of mismatch, a perfectly stacked conformation cannot be achieved and a light-up response (ON) is observed (Hudson and Ghorbani-Choghamarani, 2007). Numerous SNP-detecting probes showing such mismatch detection responses have been described (Okamoto et al., 2005a; Dodd and Hudson, 2009), including the aromatic anthracene probe (Duprey et al., 2011). Notably, anthracene is sensitive enough to report single point variants (Zhao Z.-Y. et al., 2012; Duprey et al., 2018) as well as to discriminate cytosine from 5-methylcytosine and even the challenging 5-hydroxymethylcytosine (C vs. 5 mC and 5 hmC; Duprey et al., 2011, 2016). The quencher-free molecular beacon developed by Kim et al. proposes the reverse strategy to distinguish a fully complementary strand from a mismatched target (Hwang et al., 2004; Ryu et al., 2007). For this purpose, a deoxyuridine

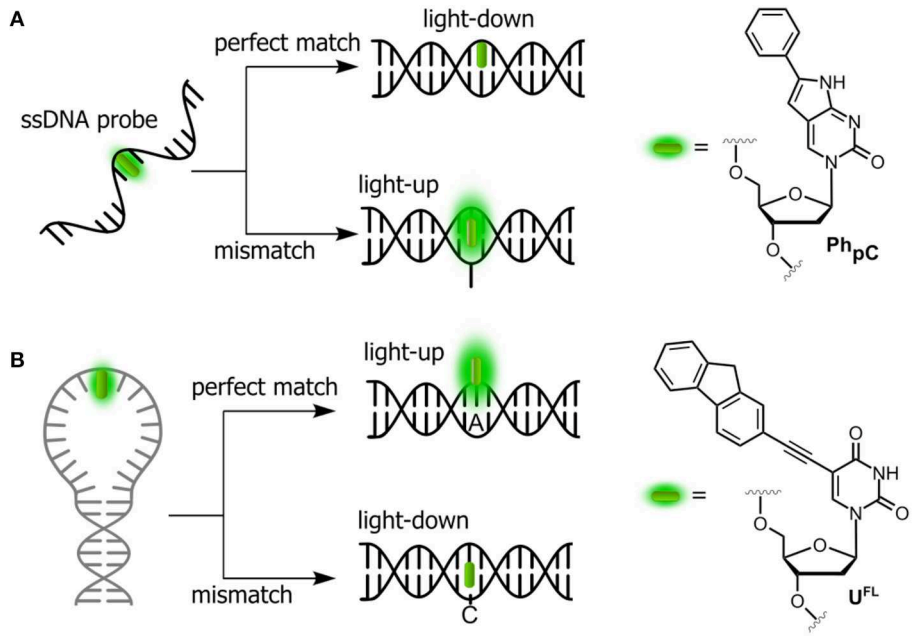

FIGURE 3 | Single-dye hybridization probes for the detection of SNPs. **(A)** Pyrrolocytosine nucleobase allowing mismatch discrimination by a fluorescent turn-on response; and **(B)** quencher-free molecular beacon approach revealing match cases by a light-up signal.

derivative connected to fluorene at position 5 ($\mathbf{U}^{FL}$, **Figure 3B**) was used as fluorescent probe and incorporated into the loop region of a hairpin. The beacon signal exhibited a 2-fold increase and a 6-fold decrease upon hybridization with fully complementary and single-base mismatched ODNs, respectively.

Detection of Protein-NA Interactions

Assays based on FNAs can be used for real-time sensitive detection of protein–DNA interactions including monitoring the activity of different enzymes (Dai and Kool, 2011). A number of enzymes are known to break down the integrity of NAs via hydrolysis of the phosphate diester links. For instance, nucleases are responsible for the degradation of undesirable DNA and RNA fragments. A viral integrase cleaves short oligonucleotide fragments from the 3′-end of double-stranded DNA to prepare for the integration of the DNA into the genome of host cell. The activity of enzymes can be monitored by DNA and RNA-based probes incorporating emissive nucleoside analogs. Representative examples are shown in **Figure 4**.

The intact form of the probe incorporates one of the nucleosides sensitive to stacking interactions. The enzyme hydrolyzes the NA strand, thus uncaging the fluorophore. Kool et al. developed a set of nuclease probes basing on the pyrene nucleoside (**Y**, **Figure 4A**). They exploited the fact that pyrene can be quenched by a neighboring thymine, but not quenched by a flanking adenine. By constructing different combinations of pyrene, T and A on a DNA scaffold, they obtained a set of fluorogenic chemosensors for distinct classes of nucleases (Jung et al., 2013). Oligonucleotides 5′-AYT, 5′-YT$(A)_8$ and YTTY were designed to be the probes for 3′-exonucleases, 5′-exonucleases and endonucleases, respectively. The oligonucleotides were tested using RNase T, $RecJ_f$ and nuclease S1 as representatives of different classes of nucleases. All nucleotides exhibited a significant light-up response, ranging from 40- to 250-fold, upon interaction with their targets (**Figure 4A**). The rise of fluorescence is caused by the cleavage of Y-T pairs. Remarkably, all nuclease probes were found to be highly selective for the assigned targets, allowing selective detection of nucleases. This assay was applied to measure the nuclease activities in biological liquids (Jung et al., 2013). Hudson et al. described an RNase assay (**Figure 4B**) based on 6-phenylpyrrolocytidine (^{Ph}**pC**, **Figure 3A**). The modified riboside was incorporated into RNA–DNA hybrids in which its emission was quenched. The cleavage of the RNA strand was observed in real time as the fluorescence intensity increased (**Figure 4B**). The method was reported to be superior to molecular beacon-based detection in terms of cost and sensitivity (Wahba et al., 2010).

Understanding, at the molecular level, the dynamics and functions of enzymes in interactions with their DNA targets is of primary importance in biology and medicine. Enzymes that catalyze reactions at specific sites in DNA, primarily face the substantial problems of finding the specific site and then forming specific interactions to obtain the catalytically productive enzyme-substrate complex (Stivers et al., 1999). FNAs become the instruments of choice for real-time monitoring of fluctuations and distortions to normal DNA structure that occur in many cases, over a short timescale (**Figure 5**).

Allan and Reich reported one of the first **2AP**-based assays for monitoring the single-base flipping caused by interaction with the enzyme under steady-state conditions. To do so, one

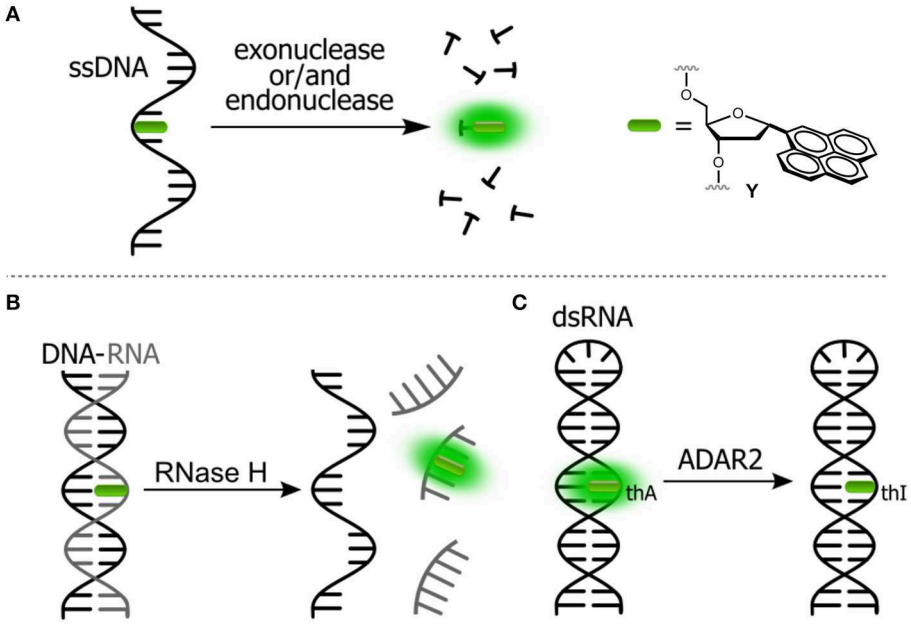

FIGURE 4 | Fluorogenic probes for sensing interactions with enzymes based on NAs labeled with a single FNA: **(A)** ssDNA probe for endo- and exonucleases; **(B)** ds-RNA/DNA probe for RNase H; and **(C)** hairpin RNA probe for adenosine deaminase.

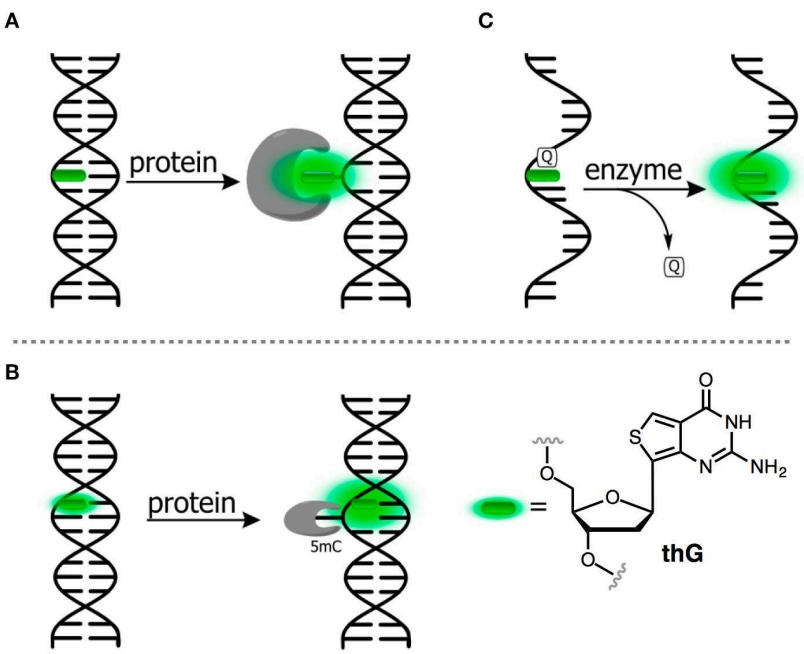

FIGURE 5 | FNAs as a base mimic and stacking-sensitive reporter **(A,B)** for sensing single-base flipping; **(C)** for sensing DNA damage and repair. Q, quencher being either U or 1-methyladenine.

of the adenines within the recognition site of EcoRI DNA methyltransferase was replaced by a **2AP** residue (**Figure 5A**). A 14-fold increase in fluorescence intensity with a 10-nm blue shift was observed upon interaction with the protein, indicating flipping of **2AP** into the hydrophobic binding site (Allan and Reich, 1996). A more detailed picture of enzymatic mechanisms can be attained when the reaction is investigated using stopped-flow techniques and under pre-steady state conditions (Fedorova et al., 2010). Tor et al. have introduced derivatives of thieno nucleobases with the aim to obtain mimics as close as possible

to the structure of all four of the natural bases (**Figure 1D**). Among these was thienoguanine (**thG**, **Figure 5B**), which, when incorporated into DNA, can faithfully substitute a G residue while remaining emissive, in contrast to **2AP** (Shin et al., 2011; Sholokh et al., 2015a, 2016). **thG** was incorporated in hemi-methylated DNA and was used to report the flipping of a neighboring methylcytosine into the binding pocket of ubiquitin-like containing PHD and RING finger domains 1 (UHRF1), a key protein involved in the replication and maintenance of the DNA methylation pattern (Kilin et al., 2017). Notably, **2AP** failed to monitor such base flipping. The adenosine analog (**thA**, **Figure 1**) was introduced in RNA strands and employed to analyze Adenosine Deaminase Acting on RNAs 2 (ADAR2, **Figure 4C**). This enzyme catalyzes deamination of adenosine into inosine with selectivity for RNA duplexes containing A. Inosine can substitute guanosine, often leading to codon changes in mRNA. The fluorescent **thA** was processed by ADAR2 as the natural nucleobase to give the corresponding analog of the inosine product. The product showed a reduced quantum yield, therefore enabling the monitoring of the reaction progress and facilitating mechanistic studies of RNA editing (Mizrahi et al., 2015).

Unraveling the Mechanisms of DNA Reactions With Chemicals, Photodamage, and Repair

DNA nucleobases can accumulate chemical damage upon exposure to exogenous or endogenous factors. The most important exogenous factors are genotoxic chemicals and UV-irradiation. Endogenous factors include reactive oxygen species (ROS) and other reactive chemicals, among others (De Bont and van Larebeke, 2004). Furthermore, the intrinsic DNA instability leads to the spontaneous formation of lesions under near-physiological conditions. Examples of DNA lesions include the formation of thymine photodimers, hydrolytic depurination leading to the abasic site lesions, oxidation of guanine to give 8-oxoguanine, hydrolytic deamination of cytosine and 5-methylcytosine leading to C→ U, 5mC→ T mutations and alkylation of G, to name a few (Schärer, 2003; Gillet and Schärer, 2006). Assays that are capable of detecting and quantifying DNA damage are important for the study of diseases caused by DNA damage, such as cancers. FNAs quenched within the DNA structure are perfect tools for site-selective detection of DNA damage and repair due to their high sensitivity to the local electronic structure of neighboring nucleobases.

Kool et al. reported a fluorescence assay for uracil-DNA glycosylase (UDG), an enzyme that participates in DNA repair by removing uracil from DNA (Ono et al., 2012). A fluorogenic NA substrate was constructed by placing the pyrene **Y** as a nucleobase substitute between two uracil residues within the NA-based probe such that the pyrene emission is strongly quenched by the flanking pyrimidine residues (**Figure 5C**). The activity of UDG afforded a cleavage of the uracil from the DNA strand. This cleavage was observed by the increased pyrene fluorescence. In another example, the ability of the positively charged 1-methyladenine to quench a pyrene nucleobase was used to design probes to monitor DNA repair (**Figure 5C**). The intracellular activity of the demethylation enzyme, ALKBH3, which is involved in tumor genesis, was measured using this probe (Beharry et al., 2016; Xu et al., 2017).

FNAs in Signaling Aptamers

The design of NAs with specific target binding properties (aptamers) has greatly broadened the application of NA fluorescent probes to the detection of a large variety of analytes, including small molecules, proteins, ions, and even whole cells (Juskowiak, 2010; Gustmann et al., 2018). The recognition properties of aptamers and the sensing properties of emissive nucleoside analogs were fused at the beginning of the 2000s to form a new strategy in the design of fluorescent biosensors (Jhaveri S. D. et al., 2000; Jhaveri S. et al., 2000). FNAs that are quenched by stacking interactions with nucleobases are especially useful in this respect. They can be used in a single-dye format, which simplifies the production of such aptamers. Due to their strong sensitivity to the conformation of NA strand, even minor conformational changes occurring upon binding can be detected. Katilius et al. explored the capability of FNAs to generate binding-specific fluorescence response (Katilius et al., 2006), and found that binding to the target can induce an increase in the fluorescence signal of up to 30-fold in the case of a thrombin aptamer incorporating the pteridine, **6MAP** (**Figure 1**). The approach was suggested to be of general use for the development of signaling aptamers targeting other proteins. Li et al. described an aptamer-based fluorescent probe featuring competitive hybridization with a **pC**-containing strand. The intact form of the probe was constituted by a double-stranded NA containing a sensing aptamer strand and a **pC**-containing signaling strand, where **pC** fluorescence was strictly quenched. The binding to the target released the signaling strand, providing a light-up fluorescence response (Li et al., 2010).

FNAs With Segmental Mobility

The group of fluorophores known as fluorescent molecular rotors, are composed of two or more aromatic rings connected by a few flexible chemical bond, exhibit low quantum yields in solutions at room temperature because of the free internal rotation that serves as a radiationless relaxation channel. In a rigid environment, increased quantum yields are observed due to the restricted intramolecular rotation. Several FNAs are known to exhibit low fluorescence in the "OFF" state due to internal rotation and show an increase in the fluorescence intensity after packing or increased viscosity leading to an "ON" state (**Figure 6**). They have been used for the detection of abasic sites in DNA, for the construction of hybridization probes and for the sensing of both protein–DNA interactions and local viscosity.

Tor et al. described a series of emissive pyrimidine analogs containing a furan ring linked to their position 5 (**Figure 6A**). Hybridization of a single-stranded DNA incorporating a furan-modified deoxyuridine (**5FU**) increased fluorescence upon hybridization to a complementary DNA strand containing an abasic site complementary to the fluorophore (Greco and Tor, 2005). Hybridization to the fully complementary strand (with no abasic site) resulted in a decrease of fluorescence. These results were rationalized using a molecular rotor model (Sinkeldam et al., 2011). Rotation around the single bond between

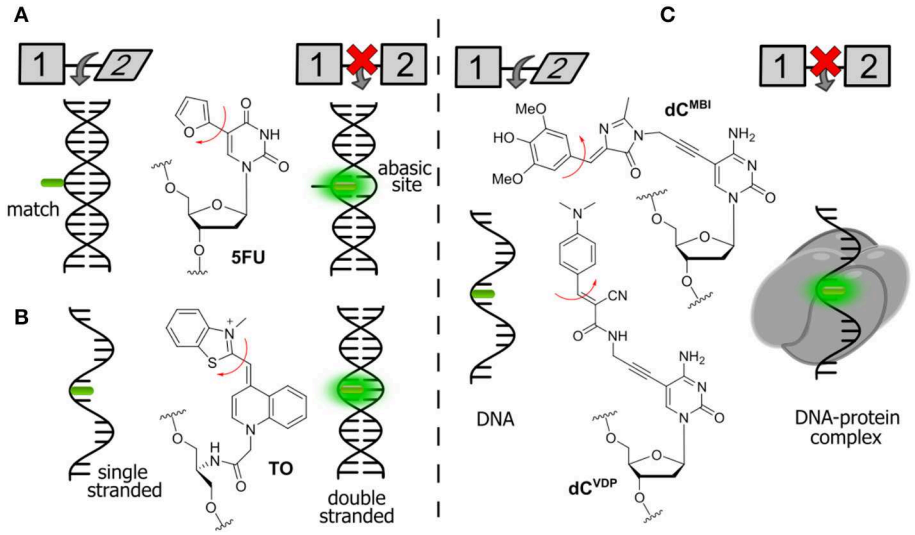

FIGURE 6 | Selected examples of FNAs featuring segmental mobility and their applications in sensing. **(A)** Furan-decorated uridine used as an abasic site sensor; **(B)** peptide-type FNA becoming emissive by forced intercalation; and **(C)** bearing flexible dyes, cytidine FNAs affording fluorescence enhancement upon protein interactions.

uracil and furan was proposed as the principal radiationless relaxation pathway. When the nucleoside faces an abasic site, it becomes sandwiched between the two neighboring Watson-Crick base pairs, which restricts its conformational freedom and therefore increases the fluorescence. When the nucleoside faces an adenosine on the fully complementary strand, the furan becomes exposed to the major groove, where its rotation is no longer restricted.

The Seitz group reported the construction of forced intercalation probes (FIT probes), which were originally designed as single-stranded PNA (Peptide Nucleic Acid) strands containing one cyanine dye (such as thiazole orange, **TO**) as a nucleobase surrogate (**Figure 6B**). FIT probes were smartly utilized as light-up fluorescent hybridization probes for sensitive detection of DNA and RNA (Köhler et al., 2005). In a single-stranded form, the probes incorporating **TO** exhibit low fluorescence. The formation of the probe–target duplex results in a well-ordered structure, where the fluorophore is forced to intercalate between flat aromatic nucleobases. The FIT probes were found to be useful for the detection of DNA in quantitative Polymerase Chain Reaction (qPCR) and for wash-free detection of RNA in cells and tissues (Socher and Seitz, 2008; Kummer et al., 2011; Hövelmann et al., 2012, 2013).

A similar approach can be used for the detection of protein–DNA interactions. Binding of proteins is known to increase the quantum yield of cyanine dyes attached to DNA due to an increase in local viscosity. This phenomenon is known as protein-induced fluorescence enhancement (PIFE; Hwang and Myong, 2014). It was further utilized by the Hocek group with a series of new FNAs suitable for the detection of protein–DNA interactions. In the first example, a GFP-like fluorophore (**dC**^{MBI}) was incorporated into DNA (**Figure 6C**). Fluorescence titration experiments showed that the fluorescence of DNA conjugates increased more than 2-fold upon addition of the single-strand binding protein from *E. coli* (SSB) and transcription factor p53 (Riedl et al., 2012a). In the second study, an improved fluorogenic dCTP analog (**dC**^{VDP}) was reported, in which the GFP-like fluorophore was substituted by cyanoacetamide-based fluorescent molecular rotors (**Figure 6C**). Single-stranded DNA labeled with this fluorophore exhibited around 4-fold fluorescence enhancement upon binding to SSB (Dziuba et al., 2015).

Merits and Limitations of Intensity-Based Sensing

As we have described above, the options for fluorophores that satisfy the requirements of intensity sensing are rather broad. The advantages of this method include the overall simplicity of fluorescence measurements and the adaptability of the instrumentation for developing integrated detection devices and micro-arrays. Due to high sensitivity, and since all the emitted light quanta can be collected over the spectrum with any polarization or time delay, this method is very popular. However, intensity-based sensing has intrinsic drawbacks. Fluorescence intensity is always represented in arbitrary units and the results are not precisely reproducible if measured on different instruments. Furthermore, it is strongly dependent on the concentration of the fluorescent molecular probe in the test system, which is often not exactly known. This raises the problem *of calibrating the sensor element*, which may be not so simple. In addition, the effects of light absorption, light scattering, photobleaching and/or time-dependent degradation of the sensor affinity can be difficult if not impossible to compensate or to calibrate. These difficulties have therefore stimulated intense efforts from researchers in proposing new dyes, detection, and imaging methods intended to correct or exclude these

limiting factors. In contrast, sensing methods based on lifetime, anisotropy, and ratiometric emission have strong potential because they give analytical signals that are independent from instrumental settings and probe concentrations (Gryczynski et al., 2003; Demchenko, 2005b, 2014).

FNAs FOR LIFETIME-BASED SENSING

After the initial electronic excitation of molecules, fluorescence develops in the sub-nanosecond to nanosecond time range. The decay function of the fluorescent light emitted by these molecules is essentially concentration-independent and, therefore, no reference is needed. For independent and structurally identical fluorescent molecules, the decay time of excited states typically follow a single exponential function of time, like the decay of radioactive compounds. However, in the case of fluorophore interactions, dynamics, and various reactions, the emission rates can become heterogeneous. As a consequence, the complex multiexponential fluorescence decay profiles of fluorophores incorporated into DNA are frequently observed. NAs can adopt multiple conformations simultaneously and can exhibit a specific combination of different lifetime components corresponding to different subpopulations. Therefore, the lifetime can become the source of valuable information. Resolving the ultrafast decay profiles of **2AP**-labeled DNA and RNA provides information about the site-specific dynamics and heterogeneity of the existing conformations of NAs including those with abasic sites and mismatched base pairs, as well as triplexes (Nordlund et al., 1989; Guest et al., 1991; Edward et al., 2001; Ramreddy et al., 2007, 2009; Xia, 2008; Zhao and Xia, 2009).

2AP has been widely used in lifetime-based NA research. It exhibits mono-exponential decay in water, whereas, upon incorporation into DNA, the decay is resolved as a sum of four exponential components with typical lifetimes ranging from 10 ps to 10 ns (Neely, 2005). These lifetime components are thought to reflect different degrees of stacking and conformations. The shortest lifetime component is the most significant and is typically a strongly quenched **2AP**-stacked conformation. The other species represent small populations of partially stacked and unstacked **2AP**. The longest lifetime component was assigned to unstacked **2AP**, which is highly emissive, with a conformation, in which **2AP** protruded from the contact with the natural nucleobases. These minor species are readily detected because their fluorescence is much higher than that of stacked base pairs. In addition to distinguishing different conformations, time-resolved fluorescence can also be used to analyze the variation of their relative populations. Thus, **2AP** can serve to probe site-specific transitions of DNA conformations. For instance, the measurements of fluorescence lifetimes and steady-state experiments of **2AP** were used to register the transitions in a DNA duplex at temperatures significantly below the transition temperature for melting (T_m; Xu et al., 1994). A dynamic pre-melting transition involving increased exposure of **2AP** to water was observed at temperatures more than 10°C below T_m.

2AP was also employed as a lifetime probe for studying the kinetics and thermodynamics of conformational changes of DNA or RNA upon binding to proteins (Nguyen et al., 2011). In particular, a time-resolved technique was used to monitor flipping of **2AP** within complexes of double-stranded DNA with the DNA methyltransferases M.HhaI and M.TaqI. In the double helix, the short-lifetime component of the stacked **2AP** was determined to be the major contribution in the decay profile. Upon binding to the enzyme, the disappearance of the short-lifetime component, together with an increase of the long lifetime component was used as an indication of flipping of the fluorescent adenine mimic into the protein-binding site. The interpretation of time-resolved fluorescence decays was supported by X-ray crystal structure analysis (Neely, 2005; Lenz et al., 2007). However, **2AP** is excited with short-wavelength UV light (300 nm) and exhibits very low brightness in DNA, which is incompatible with live-cell imaging. Recently, a BODIPY moiety connected to dC absorbing and emitting light in the blue-green region of the visible spectrum was developed as a molecular rotor (**Figure 7**). When introduced to DNA, the probe responded upon binding to transcription factor p53 by increasing of fluorescence intensity and lifetime (from 0.8 to 2.1 ns). The latter properties were exploited to visualize the local viscosity using fluorescence-lifetime imaging microscopy in living cells (Dziuba et al., 2016a).

FNAs FOR ANISOTROPY-BASED SENSING

Anisotropy describes the extent of polarized emissions. It can be created by using polarized light that excites only those fluorophores with definite directions. The preferentially excited fluorophores are those that have their absorption transition moments align with the electric field vector of the incident polarized light. After excitation, the emission can become polarized if the fluorophores are immobile on a time scale of fluorescence decay (*high anisotropy*). Rotational diffusion may randomly change the orientation of the fluorophore transition moment, producing emitted light in all space directions and causing depolarization (*low anisotropy*). However, if the size of the rotating unit or the local viscosity increases during the operating experiment, then the rotation will decrease resulting in increase of fluorescence anisotropy (or polarization). The fluorescence lifetime τ_F is an important parameter that defines the time window for rotation. A larger τ_F will allow more time to rotate and anisotropy will decrease. Thus, both rates of rotation and fluorescence emission determine the response in anisotropy (**Figure 8A**). Methods based on anisotropy are very useful for studying interactions and bindings of smaller molecules bearing a fluorophore to larger molecules since these interactions should result in reduced mobilities of the probes and increased anisotropies. The ratio of the polarized components recorded at two orthogonal polarizations to the total intensity defines anisotropy. As a consequence, it is independent from the absolute fluorescence intensity and fluorophore concentration, giving a direct response to intermolecular interactions. However, one must be careful to exclude the contribution of light scattering that can strongly influence the results. The anisotropy-based technique is also less sensitive than other techniques since the intensity of the excitation beam is reduced due to the

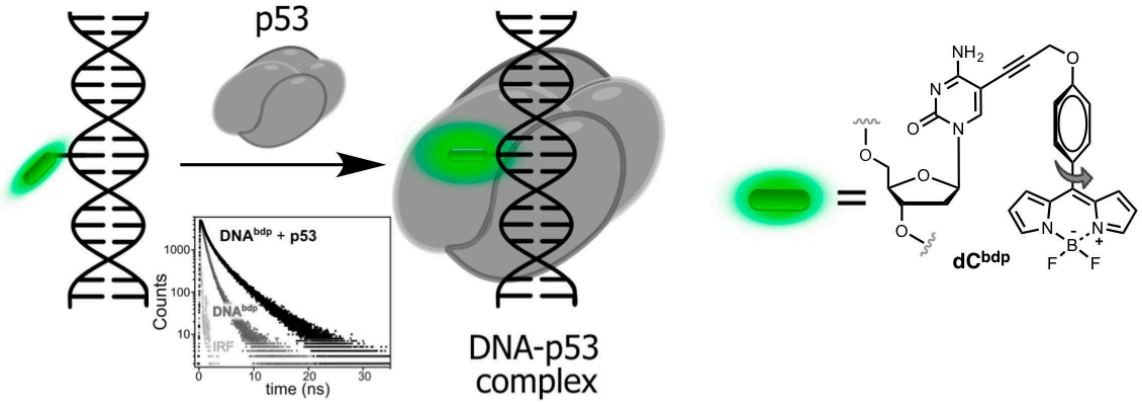

FIGURE 7 | Sequence-specific binding of the transcription factor p53 to DNA sensed via lifetime experiments. Fluorescence decays of labeled DNA before (light gray) and after (dark gray) binding to p53.

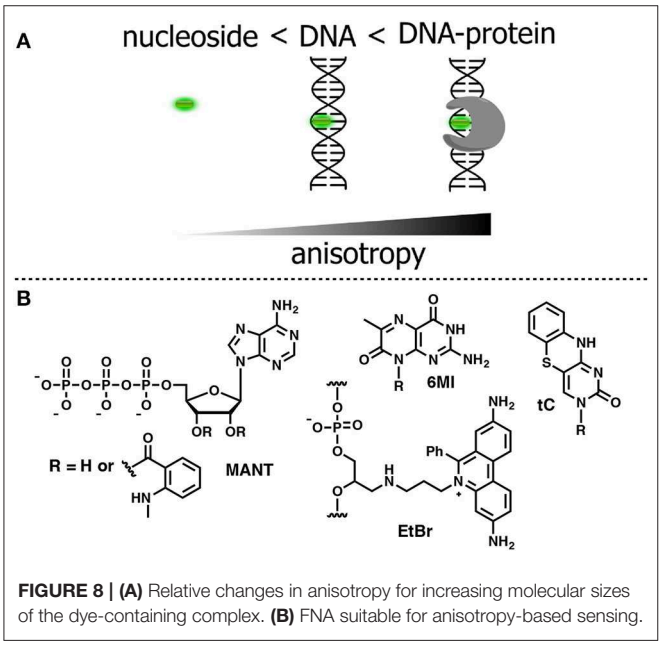

FIGURE 8 | (A) Relative changes in anisotropy for increasing molecular sizes of the dye-containing complex. **(B)** FNA suitable for anisotropy-based sensing.

use of polarization filters; therefore, higher concentrations of the fluorescent probe are often required to obtain a sufficient signal. Fluorescence anisotropy is widely used for the study of nucleoside–protein and protein–DNA interactions. For the latter, short NA fragments labeled with FNAs are preferred as they exhibit low anisotropy, whereas their binding to a target with larger molecular weight, such as a protein, gives rise to enhanced anisotropy.

To be used in an anisotropy-based assay, a fluorophore must exhibit a robust fluorescence emission with minor sensitivity to the environment. The *N*-Methylanthraniloyl fluorophore (**MANT**) is especially useful in this respect. It is a compact, blue-emitting fluorescent molecule, which can be attached to position 2′ or 3′ of ribose via an ester bond. A series of nucleoside substrates for anisotropy-based studies of nucleotide–protein interactions was developed based on the **MANT** fluorophore. Mocz et al. used 2′- and 3′-**MANT**-labeled ATP (**Figure 8B**) to study ATP–dynein binding. The fluorescent nucleotides exhibited a modest ≈ 2.2-fold enhancement in fluorescent emission. Meanwhile, the observed anisotropy of the nucleoside–protein complex was as high as 0.38, which is close to the theoretical limit for the absence of rotational mobility. The anisotropy titration data was used to determine the association constants of the complex (Mocz et al., 1998). The binding of **MANT**-modified GTP and GDP with erythrocyte transglutaminase was also monitored by anisotropy (Murthy and Lorand, 2000).

The first experiments employing fluorescence anisotropy for studying of protein–DNA or aptamer–target interactions were performed using DNA molecules labeled with a fluorescent dye, such as fluorescein (**Figure 1A**), tethered to the 5′ end of the polynucleotide (Ozers et al., 1997; Fang et al., 2001; Li et al., 2007; Zou et al., 2012). The strategy based on 5′-terminal labeling has an intrinsic drawback. Although slower rotational motions of the protein–DNA complex give rise to the measured anisotropy, the fluorophore remains flexible due to the non-rigid nature of the linker attaching it to the sugar-phosphate backbone. The residual local motions of the fluorophore reduce the observed anisotropy and decrease sensitivity of the detection (Hawkins, 2008). Indeed, only about 15% of the linker-attached fluorescein undergoes rotation coupled to global motion of the DNA (Hawkins, 2008). In this respect, a fluorophore with rotational motions that are restricted by incorporation into DNA has a distinct advantage (Shi and Herschlag, 2009).

Accordingly, a FNA must meet several criteria to be suitable for anisotropy-based assays. The fluorophore must be a flat organic molecule in order to minimize its own rotational motions by stacking with natural nucleobases. Furthermore, it must exhibit bright emission insensitive to environmental changes. In an ideal case, the fluorescence quantum yield and lifetime should not change upon binding of the sensor to the target. Bahr et al. investigated the influence of different dye-labeling topologies on the sensitivity of anisotropy-based assays. A DNA-containing the dye tethered to the 5′-end was compared to intercalating dye upon binding to the DNA methyltransferase

M.TaqI. The ethidium bromide (EtBr) fluorophore was chosen as the base surrogate (**Figure 8B**; Bahr et al., 2007). The fluorophore was covalently attached to an acyclic deoxyribose moiety and incorporated into DNA via solid-phase phosphoramidite synthesis. Ethidium bromide is known to be an excellent intercalator, exhibiting bright fluorescence when stacked between base pairs in DNA. In addition, its fluorescent emission shows only minor variations in response to the surrounding nucleobase context (Huber et al., 2004). The intensity of fluorescence also remained stable upon binding to the DNA methyltransferases, indicating the absence of non-specific dye–protein interactions. The changes of emission anisotropy were measured upon binding of DNAs to the methyltransferase with the different reporter groups. Using the conjugate-containing fluorophore as a base surrogate gave the best result in terms of increased fluorescence anisotropy. An approximately 2.5-fold increase of anisotropy was observed, which was not observed in non-specific interactions of the protein with fluorophore. Such a strong increase in anisotropy reflects the rotational dynamic of entire protein–DNA complex with minimal contribution of local fluorophore motions (Bahr et al., 2007). These data indicate that an appropriate FNA offers significant advantages over fluorophores attached in other ways.

The bright emissive nucleoside analogs **tC** (**Figure 8B**) incorporating the nucleobase surrogate 1,3-diaza-2-oxophenothiazine was developed as a cytidine analog (Lin et al., 1995; Wilhelmsson et al., 2001). The tricyclic nucleobase **tC** exhibits interesting properties for anisotropy-based sensing. Base pairing with G, **tC** has a well-defined position and geometry within the DNA double helix, and exhibits bright fluorescence with negligible sensitivity to the surrounding bases (Sandin, 2005). Furthermore, this FNA demonstrates a base-flipping rate that does not interfere with the signal measured in fluorescence anisotropy. The anisotropy of **tC** was used by Wilhemsson et al. to study the incorporation of the analog into DNA by DNA polymerase and to determine in competitive binding essays, the dissociation constant of natural or unnatural nucleotides (Sandin et al., 2009). Pteridine nucleobases can also be employed as fluorescent reporters in anisotropy sensing (Hawkins, 2008). For instance, the **6MI** label (**Figure 8B**) was effective in anisotropy binding measurements with the *Escherichia coli* protein integration host factor at DNA concentrations of 1 nM and fluorescence intensity measurements at 50 pM DNA (Moreno et al., 2012).

FNAs FOR EMISSION-SHIFT-BASED SENSING

A group of fluorophores is known to red-shift their emission spectra when placed in a medium of increased polarity. This effect is referred to *solvatofluorochromism* and is caused by enhanced dipole–dipole interactions between the excited fluorophore and the surrounding molecules that decrease the excited-state energy (Klymchenko and Mély, 2013). Environment-sensitive fluorophores exhibiting solvatofluorochromic properties are important tools for biophysics and molecular sensing (Klymchenko, 2017). Steady-state and time-resolved fluorescent spectra of these dyes yield information about specific and non-specific interactions with the surrounding molecules, the rates of their dielectric relaxations, etc. Given that they are designed as analogs of amino acids and lipids, such dyes are widely used for probing proteins and lipid membranes (Demchenko et al., 2009; Loving et al., 2010; Krueger and Imperiali, 2013). The general principles governing the performance of these dyes are well-understood. They must contain functional groups attached to aromatic rings that can become strong electron donors and acceptors in the excited state. Being appended to the opposite sides of the π-electronic structure, they generate a strong dipole moment that, by interacting with local molecular environment, results in modulation of the energy of the electronic transition and spectral shift. This shift to longer wavelengths (red shift) is stronger the higher the polarity of the environment. Such a shift can also be modulated by intermolecular H-bonding of one of these groups in a polar environment.

Many efforts have been made to develop FNAs possessing solvent-dependent shifts. The difficulty is the requirement to incorporate the fluorophore into the NA structure, without changing the topology or interactions. Several approaches for the construction of solvatofluorochromic nucleosides have been described (**Figure 9**). For the first approach, the dye was grafted to deoxyribose, typically via C-glycoside bond, to be further intercalated between nucleobases within the DNA (Okamoto et al., 2006; Weinberger et al., 2013). The second approach requires a fluorescent dye to be linked to the natural nucleobases, typically at position 5 of pyrimidines and positions 7 and 8 of purines (**Figure 9B**; Kimura et al., 2005, 2006; Tainaka et al., 2007; Riedl et al., 2012b). The third approach features minor conjugated decoration of the expanded nucleobase with additional chemical functionalities endowing with solvatofluorochromic properties (Greco and Tor, 2005; Shin et al., 2011; Noé et al., 2012; Sinkeldam et al., 2012). The latter seems to have a distinct advantage, since minimal perturbations are introduced to the structure of DNA.

Nile Red and 4-aminophthalimide (**API**) are among the dyes that exhibit the strongest solvent-dependent shifts of fluorescence spectra (**Figure 9A**). However, being incorporated into DNA as base substitutes, these dyes showed only a moderate sensitivity to different structural contexts. For instance, upon transition from a single to a double-stranded DNA form, **API** showed only a small 10 nm blue shift of its emission maximum, and the **Nile Red**-based nucleoside did not demonstrate any fluorescence band shift (Weinberger et al., 2013). Only a moderate blue shift was observed upon interaction of DNA labeled with these dyes with β-cyclodextrin (Okamoto et al., 2006). This occurs because the dyes were incorporated in such a way that their π-electronic system interacts mainly with neighboring bases and these interactions do not change substantially upon structural transformations of the DNA.

Probes from the second group contain a fluorophore attached to the nucleobase via a linker, which allows them to be exposed to the major or minor groove of DNA. A series of PRODAN-nucleoside conjugates was developed, where the fluorophore was attached via a short linker to the *N*-4 and *N*-2 exocyclic

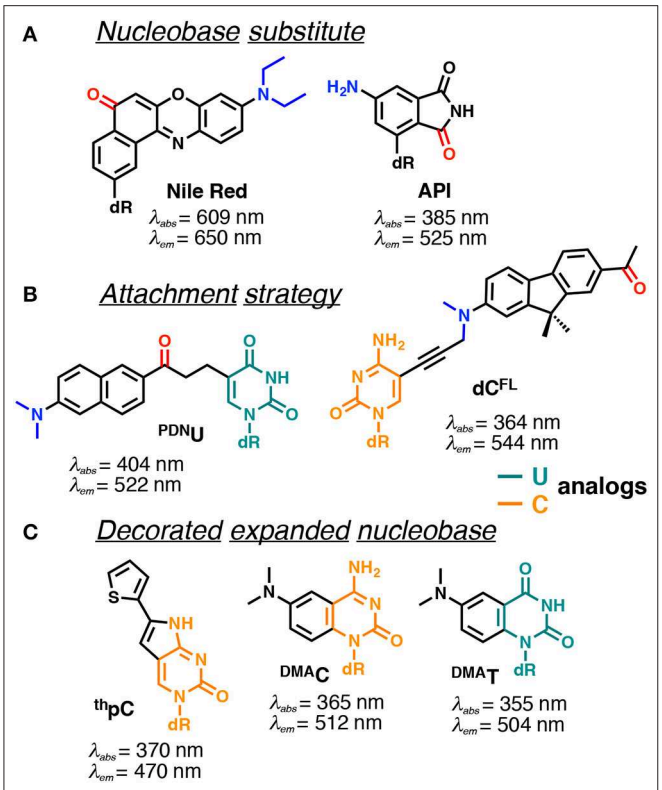

FIGURE 9 | Selected examples of solvatofluorochromic FNAs demonstrating intramolecular charge transfer (ICT): **(A)** employed as nucleobase surrogates; **(B)** covalently and flexibly attached to a pyrimidine; and **(C)** mimicking nucleobases by an appropriate expansion. dR indicates 2'-deoxyribosyl; donor and acceptor groups are depicted in blue and red, respectively (Barawkar and Ganesh, 1995; Okamoto et al., 2006; Tainaka et al., 2007; Noé et al., 2012; Riedl et al., 2012b; Weinberger et al., 2013; Mata and Luedtke, 2015; Mata et al., 2016). Excitation and emission wavelengths were given in nm.

amino group of cytosine and guanine, respectively (Kimura et al., 2005, 2006) or to the C-5 of pyrimidines (^{PDN}**U**, **Figure 9B**) and the C-8 of purines (Tainaka et al., 2007). In contrast to the probes following the first approach, the fluorophore exposed to the major or minor grooves of DNA was more exposed for direct interactions with water and therefore showed significant spectral shifts depending on the NA polymorph in question. Indeed, the label was able to distinguish the polarity of the microenvironment in the minor and major grooves of B-DNA, A-DNA/RNA hybrids and Z-DNA (Kimura et al., 2005, 2006). Okamoto and co-workers extended this approach to the synthesis of the four nucleobases set (U, C, A, G) for single-nucleotide polymorphism genotyping. All the investigated probes showed a substantial increase in fluorescence intensity upon hybridization to a perfectly matched sequence, together with increase in the Stokes shift (Tainaka et al., 2007).

Hocek et al. used a dC analog incorporating a push–pull fluorene fluorophore (**dC**^{FL}) to sense the protein–DNA interactions as a color change that was distinguishable to the naked eye (**Figure 9B**). The triphosphate of **dC**^{FL} was prepared and incorporated into the DNA using two DNA polymerases. Labeled DNA showed significant changes in the emission wavelength upon interaction with the human transcription factor p53. A substantial blue shift of the emission maximum from 581 to 567 nm was observed upon binding to p53, indicating sufficient screening of the fluorophore from the polar aqueous medium (Dziuba et al., 2016b).

Probes from the third group contain a natural nucleobase core rendered to be solvatofluorochromic by additional chemical functionalities. An example is **5FU**, which was designed for the detection of DNA abasic sites (**Figures 1D**, **6A**). The wavelength of its emission band shifts from 395 nm in diethylether to 431 nm in water (Greco and Tor, 2005). Solvent-dependent emission sensitivity was also observed for a structurally related compound containing thiophene, namely for 6-aza-uridines (Sinkeldam et al., 2012), based on thieno-fused pyrrolo cytosines (th**pC**, **Figure 9C**; Noé et al., 2012) and a thieno[3,4-d]-pyrimidine scaffold (Shin et al., 2011). However, being incorporated into polynucleotides, these compounds show only minor shifts in their emission bands, and are more useful for the construction of intensity-based probes. Such behavior is typical for dyes quenched by water, which masks the spectral shift (Demchenko, 2005a). Luedtke et al. designed and synthesized a push–pull FNA composed of dimethylaniline fused to deoxycytidine (^{DMA}**C**, **Figure 9C**). ^{DMA}**C** is a mimic of the natural nucleobase, which, upon pH decrease and base (*N3*) protonation, exhibits remarkable red-shifted absorption and emission maxima. These properties were exploited to study the dynamics of folding and unfolding of i-motif and DNA duplexes of telomeric repeat sequences under real-time conditions (**Figure 10**; Mata and Luedtke, 2015).

FNAs FOR DUAL-BAND RATIOMETRIC SENSING

The sensitivity of fluorescence probes to report intermolecular interactions can be greatly increased if the sensing signal is based on the change between two spectrally resolved forms. This is because the wavelength-ratiometric signal will be recorded as a ratio of intensities, not at the slopes of spectral bands but at the band maxima, thus providing a comparison of fluorescence intensities at a higher level and achieving higher wavelength precision (**Figure 11A** vs. **Figure 11B**; Demchenko, 2010, 2014). In order to achieve this, the researcher must select a fluorophore that can exist in two ground- or excited-state forms. Moreover, the switching between these forms should occur in the desired range of changes of the intermolecular interactions in question. This approach is fundamentally different from that based on FRET-based switching, which requires the presence of two dyes (donor and acceptor) at a specific distance (**Figure 11C**; Demchenko, 2014). Such an approach avoids the difficulties arising from double labeling within the same molecular system but it is more challenging, since these properties are very specific and only "smart," specially designed dyes possess them.

Switching between ground-state forms of such smart fluorophores allows one to extract the effects from fluorescence

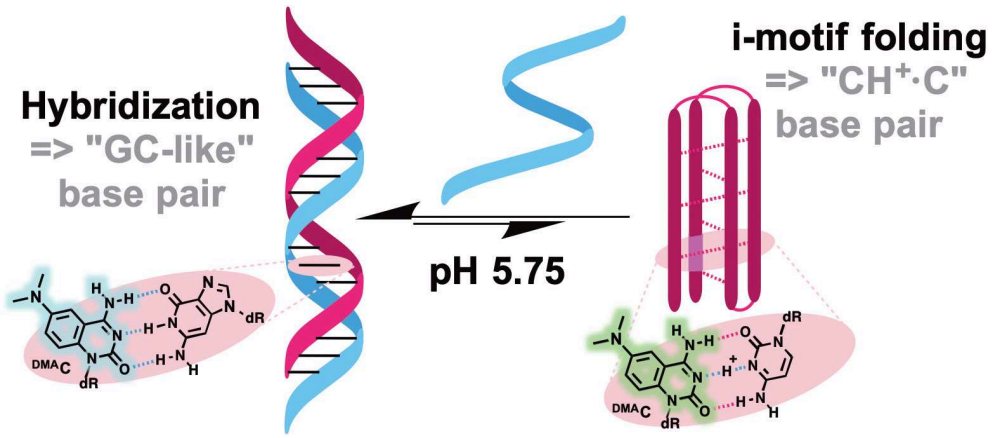

FIGURE 10 | pH-induced i-motif folding monitored by color change of ^{DMA}**C** fluorescence.

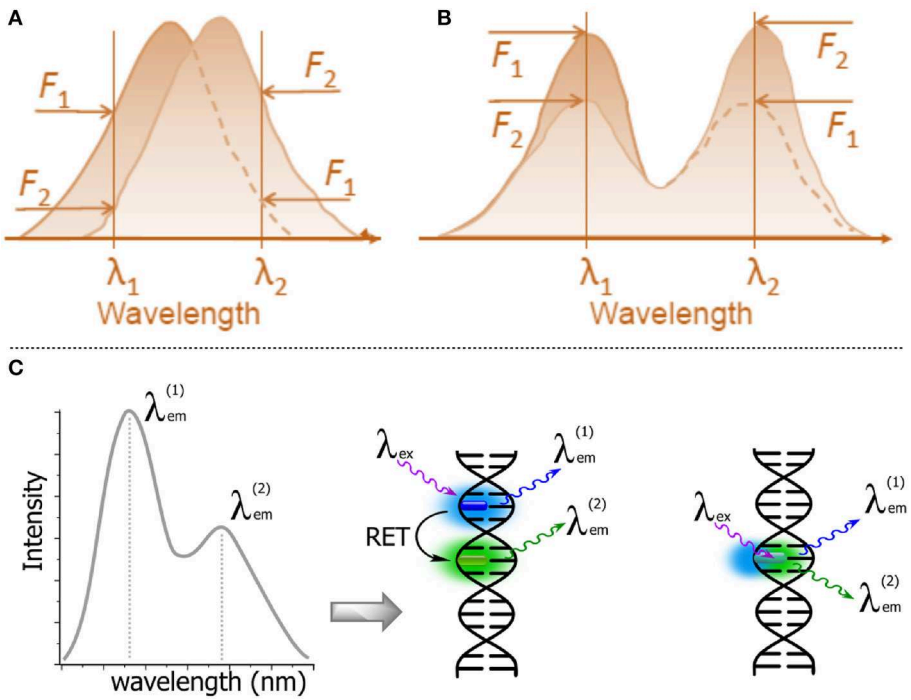

FIGURE 11 | Schematic representations of λ-ratiometric sensing recorded at two fixed wavelengths for a single fluorescent probe. **(A)** The spectral shift defines the sensing response (e.g., Nile Red). **(B)** The decrease of intensity of one band λ_1 and the concomitant increase of intensity at a different band λ_2 define the sensing response. Calculating the change in the intensity ratio $F(\lambda_1)/F(\lambda_2)$ enables quantitative measurements (Demchenko, 2013). **(C)** Dual emission: two-dyes (e.g., exhibiting resonance energy transfer, RET) vs. a one-dye approach based on the generation of a new band for the recording of a ratiometric signal.

excitation spectra, and the first λ-ratiometric fluorescent probes for calcium ions were based on this principle (Grynkiewicz et al., 1985). In order to produce interplay between intensities in fluorescence emission spectra, the dye has to be present in two excited-state forms with finely tunable switching between them. An additional requirement is the presence of such two forms of comparable fluorescence intensities. All this makes for a very limited selection of dyes with the appropriate responses.

One of the excited-state reactions that can be explored is the intramolecular charge transfer (ICT) that has to be stabilized by isomerization (twisting). Such twisted intramolecular charge transfer (TICT) can drastically modulate the emission spectra depending on the environment, since it is only under conditions of high polarity that the charge-transfer form can be stabilized (**Figure 12A**). Since the two isomers that appear in the excited state emit light quanta of different energies, they show two well-resolved emission bands. The very large Stokes shift of the

long wavelength band due to the emission of the generated excited-state isomer is characteristic for this type of dual probe (Cao et al., 2014; Oesch and Luedtke, 2015).

The other reaction that generates two bands in emission spectra is the excited-state intramolecular proton transfer (ESIPT), which proceeds between proton donor and acceptor groups, closely located in the dye structure (and commonly connected by intramolecular H-bonding, **Figure 12C**). This reaction is subject to perturbation by the change of polarity in the environment and to the formation of additional intermolecular H-bonds (Han and Zhao, 2010; Tomin et al., 2015).

Fluorophores demonstrating TICT and ESIPT can be introduced as smart NA base analogs that are able to respond to different changes in the properties of their local environment (**Figures 12B,D**). They have significant potential in the practical sense because the intensity ratio of the two emission bands is highly sensitive to the environment and since single labeling is sufficient for λ-ratiometric detection (*self-calibrated sensing*; Demchenko, 2005b,c).

Single-Fluorophore Ratiometric Probes Based on TICT

In the TICT system, the donor and the acceptor moieties are joined by a chemical bond (σ or π) and the shift of π-electron density is accompanied by a twist about this bond in the excited state (**Figure 12A**; Rettig, 1986; Bhattacharyya and Chowdhury, 1993; de Silva et al., 1997; Wu et al., 2011). The prototype and historical example of a TICT fluorophore is 4-dimethylaminobenzonitrile (Lippert, 1955). This planar compound has a well-conjugated push–pull electron system. After light absorption, the initially, locally excited form (LE) has similarly planar geometry and intramolecular relaxation results in twisting, generating the isomer form. In the TICT excited state, the dimethylamino unit becomes orthogonal to the rest of the π-system. Twisting through 90° can achieve full charge separation resulting in an amino cation and a benzonitrile anion and a dipole moment of the TICT rotamer becoming larger that of the LE form. Therefore, an increase in solvent polarity favors the TICT form that, interacting with polar environment, demonstrates a red-shifted emission. Since the TICT form is generated from the rotation between the donor and acceptor segments of the same molecule, restriction to the twisting motion, due to the environment or by increasing the viscosity of the medium, will favor the LE state. On the other hand, temperature increases will favor the TICT state. Whereas, the LE state is emissive, the emission from TICT state is poor in general, which may create a problem for λ-ratiometric analysis.

Okamoto et al. reported the first example of DNA labeled with a dual-emissive TICT probe (Okamoto et al., 2005b). This TICT-based probe was a pyrene derivative electronically coupled to a dimethylamino donor and an amide acceptor (**Figure 12B**). This probe was tethered to deoxuridine for incorporation into DNA and hybridization with DNA and RNA. While the nucleoside conjugate **PyrU** showed a single-band emission at 540 nm, ss- and ds-ODNs showed dual emission with the appearance of a new band centered at 440 nm. The quantum yield increased together with the dual emission. The fluorescence bands at a shorter wavelength (440 nm) and at a longer wavelength (540 nm) were assigned to the emission of the LE and TICT states, respectively. The TICT emission was largely dominating in ss-ODN, while in ds-DNA, a 1:1 ratio was observed. Therefore, the fluorescent twisted **PyrU** is sensitive to hybridization, as indicated by a change of its color. It was proposed that the equilibrium between the LE and TICT states, and thus the intensity ratio of these two bands, was due to the restricted twisting motion in the ODN environment, which was more pronounced in the duplex. In this case, the steric hindrance and a narrow free space in the duplex acted as a barrier to the internal rotation of the fluorophore instead of a viscous solvent. Recent publications have underlined the effort to find new nucleoside analogs with TICT properties and to extend this new approach for DNA labeling and sensing (Mata and Luedtke, 2013; Suzuki et al., 2014; Schweigert et al., 2017).

Single-Fluorophore Ratiometric Probes Based on ESIPT

The ESIPT reaction is observed only in those aromatic compounds having proton donor and acceptor groups in close proximity and connected by an intramolecular hydrogen bond. Common proton donors and acceptors are hydroxyl or amino groups and carbonyl oxygen or imino nitrogen, respectively. After photon absorption, the electronic charges are redistributed making the proton donor more acidic and the acceptor more basic, thus favoring the intramolecular proton transfer in the excited state (Zhao J. et al., 2012; Demchenko et al., 2013; Sedgwick et al., 2018).

3-Hydroxychromones (**3HCs**) are typical representatives of ESIPT dyes and are one of the most useful probe families for practical applications. **3HCs** are heterocyclic compounds bearing hydroxyl and carbonyl groups involved in a 5-member H-bonding ring system. Due to ESIPT, **3HC** fluorophores exhibit two excited states, which generate two well-resolved emission bands (**Figure 12C**; Demchenko, 2006). The short-wavelength band is due to the emission from the normal (N*) excited form, whereas the long-wavelength band is produced by the tautomer form (T*). In the excited normal state (N*), the oxygen carbonyl is more basic, making this group sensitive to the donating ability of hydrogen bond of protic solvents and hydration. As a consequence, increased acidity of the solvent or of the hydration rate favors H-bonding to the carbonyl oxygen resulting in decreased relative intensity of the T* due to a slower ESIPT reaction. Another consequence of the electronic charge distribution for the N* state is related to the dipole moment, which is larger than that for the N* and T* forms. The magnitude of the N* dipole moment can be finely tuned by appropriate chemical modifications, while the dipole moment of the T* state is much less affected. For instance, the electron-rich aryl groups at position 2 (e.g., 4-dimethylaminophenyl) dramatically increase the magnitude of the dipole moment of the N* state due to internal charge transfer (ICT), rendering 3HCs sensitive to polarity change in aprotic solvents. In polar solvents, strong and favorable dipole–dipole interactions between solvent molecules and the dye stabilize the N* state much more than the T* state, resulting in increased emission of the N* state. The N*/T* ratio is therefore a robust analytical signal that directly reports on the properties of the microenvironment of **3HC** fluorophore.

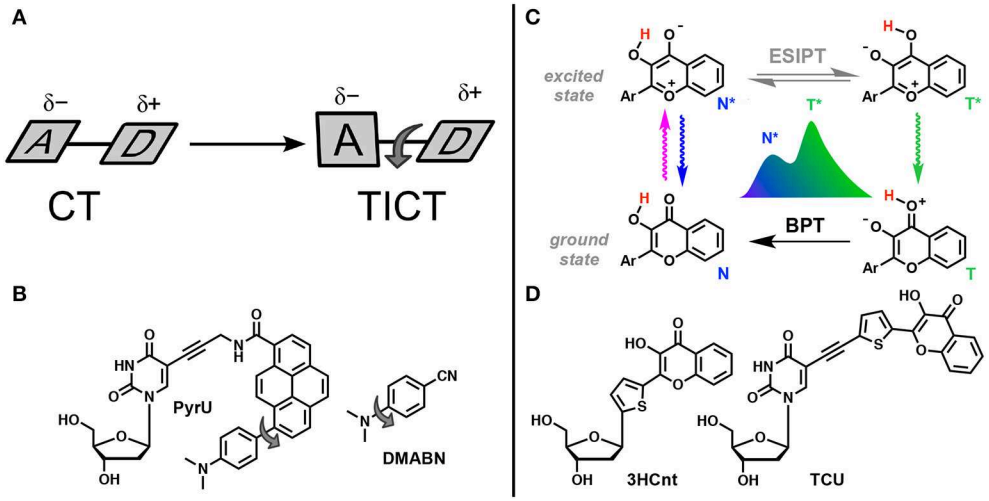

FIGURE 12 | TICT vs. ESIPT. **(A)** Schematic representation of geometrical arrangements of normal charge transfer (CT) and twisted intramolecular charge transfer (TICT) excited states (Rettig, 1986). **(B)** FNA containing fluorophore undergoing TICT reported by Okamoto et al. (2005b). **(C)** Tautomeric equilibrium explaining the dual-band emission of 3-hydroxychromones. ESIPT, excited-state intramolecular proton transfer; BPT, back proton transfer; N* and T* states for normal and tautomer excited forms, respectively. **(D)** Dual-emissive nucleoside analogs based on 3-hydroxychromones (Dziuba et al., 2012; Barthes et al., 2015).

These features have been used extensively for the construction of environment-sensitive fluorescent dyes to probe proteins and lipid membranes (Klymchenko and Kreder, 2014; Zamotaiev et al., 2014; Sholokh et al., 2015b).

3HCs bearing a thienyl or furyl ring at position 2 are known to be extremely sensitive to hydration. The emission switches from the dominating N* band in water to T* emission in aprotic media. **2-Thienyl-3HC** was therefore selected for DNA labeling. It was formulated as a deoxyribose derivative (**3HCnt**, **Figure 12D**) and incorporated into DNA via the standard phosphoramidite method. The dye showed a dominant tautomer (T*) emission in the single-stranded form. A further increase of the T* band emission was typically observed upon hybridization to a complementary strand (Dziuba et al., 2012). Minimal DNA perturbation by the dye incorporation and its intercalation mode were supported by CD, Tm and NMR investigations (Zargarian et al., 2017). Importantly, the emission of single-stranded DNA was highly sensitive to the formation of the complex with the HIV-1 nucleocapsid protein (NC). A strong increase of the N* emission was observed, indicating that the **3HC** nucleoside can be a good sensor for protein–DNA interactions (Dziuba et al., 2012). The **3HC** label was employed to study the conversion of the (–)DNA copy of the HIV-1 primer binding site (–)PBS stem-loop into the (+/–)PBS duplex in the absence and presence of the NC chaperone protein. In contrast to **2AP**, the **3HC** probe provided the first complete mechanistic description of this critical process in HIV-1 replication (Sholokh et al., 2018). In a comparison study with commercially available FNAs, the fluorescent label was exploited to investigate the mechanism of the DNA repair enzyme, endonuclease VIII, in interactions with damaged DNA. The results of this study showed that this label exhibits higher sensitivity and yields more information about the conformational changes of DNA binding and processing. Using **3HC**-based molecular probes, the kinetic mechanism of action of endonuclease VIII was specified (Kuznetsova et al., 2014). The FNA was also successfully employed to record the stepwise binding of the ubiquitin-like domains 1 containing PHD and RING finger (UHRF1) followed by the flipping of a 5-methylcytosine (5 mC, **Figure 5B**). The increased lifetime of UHRF1 bound to DNA containing 5 mC supports the idea that UHRF1 is the key partner for the recruitment of DNA methyltransferase 1 to the correct site for faithful replication of the DNA methylation pattern (Kilin et al., 2017).

The internal **3HC** base surrogate proved to be extremely sensitive to proximal disturbances, although its sensitivity to hydration changes was not optimal. Probes sensitive to hydration are desirable for sensor development because the interactions between proteins and other ligands, as well as structural changes, affect the proximal distribution of water molecules around the NA (Barthes et al., 2016). The possibility to connect the 3HC dye to uracil and adenine nucleobases for external labeling of NA (for example, in the major grooves of DNA duplexes) has been also explored (Dziuba et al., 2014; Barthes et al., 2016; Le et al., 2019). The new conjugated nucleobase–**3HC** fluorophores demonstrated strong sensitivity to hydration (Barthes et al., 2015; Le et al., 2019). DNA strands incorporating the emissive deoxyuridine analog were synthesized and studied (Barthes et al., 2016; Gavvala et al., 2016), and the resulting probe exhibited two-color emission and provided high sensitivity allowing discrimination between matched and mismatched DNA duplexes, and B-DNA/DNA and A-DNA/RNA forms (Barthes et al., 2016). The change between these different forms was easily identified by a color change due to the variation of N*/T*, which was attributed to the change of hydration in the proximity of the fluorescent base reporting group. Compared to the wavelength shift of the dimethylaminonaphtalene (dan) fluorophore, which displayed only a 5% variation in the λ-shift of the emission

maximum (Kimura et al., 2005), the dual-emissive uracil probe demonstrated about 11-fold enhanced sensitivity to detect the B to A transition with a 55% variation of its N*/T* ratio.

CONCLUSIONS AND PERSPECTIVES

FNAs have become indispensable tools in biophysics and analytical chemistry. Despite significant progress and the large number of FNAs reported to date, new efforts continue and further developments in this field are expected (Manna et al., 2018; Sabale et al., 2018). As the reader may have noticed, the intensity-based probes are over-represented in the literature, whereas less attention has been paid to FNAs that exploit other reporting principles. We expect further progress in the development of FNAs that use the prospective reporting modes, described above.

Rapid progress is expected in the application of molecular probes based on FNAs in complex biological media, such as living cells. Given their minimal perturbation of DNA or RNA structures, fluorescent hybridization probes can enable visualization of these molecules, providing information on their location and transportation, but they can also reveal dynamics and interactions with cellular components. Ideally, fluorescence response should be increased to a level that does not require any target amplification, purification or removal of unreacted probes. Strong similarity to natural nucleosides and the minimal perturbance from their interactions with complementary bases allow for high specificity. Moreover, the possibility to assess polarity- and H-bond-sensitive responses in these smartly designed probes yields deeper understanding of NA structure, dynamics and interactions at the sub-molecular level. Because of their native-like linkage to DNA or RNA, these probes are very closely associated with neighboring bases, rendering them exquisitely sensitive to the subtle changes that occur in the atomic-level structure surrounding them. Therefore, changes in base stacking or base pairing in the vicinity of these probes are reflected by distinct changes in fluorescence response. Thus, new concepts and probes demonstrating advanced properties have a promising future.

The majority of known nucleoside analogs are excited by UV and blue light, and are therefore prone to photodamage and interference from autofluorescence, which might have to be overcome in future molecular design strategies. For this reason, new nucleosides that are excitable at longer wavelengths are highly desirable. Alternatively, the situation can be improved by the development of two-photon excitable FNAs. Two-photon absorption (2PA) is a physical process where the chromophore is excited by the simultaneous absorption of two low-energy photons, which match the energy of a single photon of higher energy that corresponds to normal excitation. Fluorophores with high 2PA cross-sections are of great importance for fluorescence microscopy and intracellular studies, because the two-photon excitation decreases the background signal caused by autofluorescence and reduces the sample photodamage. The existing FNAs possess quite low 2PA cross-sections. For instance, the measured values of **2AP**, pteridines and **tC** are in the range between 0.2 and 3.5 GM units (Stanley et al., 2005; Lane and Magennis, 2012). Consequently, FNAs with higher 2PA are expected to appear in the future, which will open new possibilities in two-photon microscopy. Likewise, this will enable single-molecule detection to become more efficient within the living cells.

FNAs will not only be used as passive fluorescence emitters, but will also perform additional functions. Several literature reports have shown that fluorescently labeled NAs can be used as a dual probe for fluorescence detection combined with electron microscopy (Holzhauser et al., 2013) or NMR spectroscopy (Sabale et al., 2018). In the first study, the fluorophore used induced photochemical polymerization of 3,3′-diaminobenzidine, enabling electron microscopy detection. In the second example, the dual probe combines a fluorescent molecular rotor and a ^{19}F label allowing detection and resolution of the topologies of G quadruplexes in cells. Another attractive possibility is the use of FNAs as light-controlled molecular triggers. Site-selective incorporation of photochemically reactive nucleoside makes it possible to change the conformation and chemical structure of NAs by light; for example, light-controlled hybridization (Ogasawara and Maeda, 2008) or controlled formation of inter-strand cross-links (Haque et al., 2014). Finally, the integration of FNAs into functional NAs could be a powerful strategy for the creation of light-guided catalytic systems. An example is the **6MI**-modified DNAzyme that can harness violet light to repair DNA damages (Barlev and Sen, 2013). New examples of FNAs that are used in the rational design of light-controlled molecular systems are expected to appear in the future.

AUTHOR CONTRIBUTIONS

DD and BM produced figures. DD, BM, and AB wrote the sections Operation With Parameters of Fluorescence Emission, FNAs for Intensity-Based Sensing, FNAs for Lifetime-Based Sensing, FNAs for Anisotropy-Based Sensing, FNAs for Emission-Shift-Based Sensing, and FNAs for Dual-Band Ratiometric Sensing. RB wrote the section Incorporation of Fluorescent Nucleoside Analogs (FNAs): Methodology. AD, DD, BM, and AB wrote the sections Introduction, Resolving Problems With Smart Base Substituents, Incorporation of Fluorescent Nucleoside Analogs (FNAs): Methodology, and Conclusions and Perspectives.

FUNDING

This research was financially supported by the Agence Nationale de la Recherche (ANR-12- BS08-0003-02) and the Région PACA (DNAfix-2014-02862).

ACKNOWLEDGMENTS

We thank the Agence Nationale de la Recherche (UCAJEDI project: ANR-15-IDEX-01) for the Ph.D. grant to DD.

REFERENCES

Allan, B. W., and Reich, N. O. (1996). Targeted base stacking disruption by the EcoRI DNA methyltransferase. *Biochemistry* 35, 14757–14762. doi: 10.1021/bi9615708

Asseline, U. (2006). Development and applications of fluorescent oligonucleotides. *Curr. Org. Chem.* 10, 491–518. doi: 10.2174/138527206776055349

Bahr, M., Valis, L., Wagenknecht, H.-A., and Weinhold, E. (2007). DNA labelling topologies for monitoring DNA-protein complex formation by fluorescence anisotropy. *Nucleos. Nucleot. Nucl.* 26, 1581–1584. doi: 10.1080/15257770701547347

Barawkar, D. A., and Ganesh, K. N. (1995). Fluorescent d(CGCGAATTCGCG): characterization of major groove polarity and study of minor groove interactions through a major groove semantophore conjugate. *Nucl. Acids Res.* 23, 159–164. doi: 10.1093/nar/23.1.159

Barlev, A., and Sen, D. (2013). Catalytic DNAs that harness violet light to repair thymine dimers in a DNA substrate. *J. Am. Chem. Soc.* 135, 2596–2603. doi: 10.1021/ja309638j

Barthes, N. P. F., Gavvala, K., Dziuba, D., Bonhomme, D., Karpenko, I. A., Dabert-Gay, A. S., et al. (2016). Dual emissive analogue of deoxyuridine as a sensitive hydration-reporting probe for discriminating mismatched from matched DNA and DNA/DNA from DNA/RNA duplexes. *J. Mater. Chem. C* 4, 3010–3017. doi: 10.1039/C5TC03427B

Barthes, N. P. F., Karpenko, I. A., Dziuba, D., Spadafora, M., Auffret, J., Demchenko, A. P., et al. (2015). Development of environmentally sensitive fluorescent and dual emissive deoxyuridine analogues. *RSC Adv.* 5, 33536–33545. doi: 10.1039/C5RA02709H

Beharry, A. A., Lacoste, S., O'Connor, T. R., and Kool, E. T. (2016). Fluorescence monitoring of the oxidative repair of DNA alkylation damage by ALKBH3, a prostate cancer marker. *J. Am. Chem. Soc.* 138, 3647–3650. doi: 10.1021/jacs.6b00986

Berger, S. L., Kouzarides, T., Shiekhattar, R., and Shilatifard, A. (2009). An operational definition of epigenetics. *Genes Dev.* 23, 781–783. doi: 10.1101/gad.1787609

Berney, M., and McGouran, J. F. (2018). Methods for detection of cytosine and thymine modifications in DNA. *Nat. Rev. Chem.* 2, 332–348. doi: 10.1038/s41570-018-0044-4

Bhattacharyya, K., and Chowdhury, M. (1993). Environmental and magnetic field effects on exciplex and twisted charge transfer emission. *Chem. Rev.* 93, 507–535. doi: 10.1021/cr00017a022

Bird, A. (2007). Perceptions of epigenetics. *Nature* 447, 396–398. doi: 10.1038/nature05913

Cao, C., Liu, X., Qiao, Q., Zhao, M., Yin, W., Mao, D., et al. (2014). A twisted-intramolecular-charge-transfer (TICT) based ratiometric fluorescent thermometer with a mega-Stokes shift and a positive temperature coefficient. *Chem. Commun.* 50, 15811–15814. doi: 10.1039/C4CC08010F

Dai, N., and Kool, E. T. (2011). Fluorescent DNA-based enzyme sensors. *Chem. Soc. Rev.* 40, 5756–5770. doi: 10.1039/c0cs00162g

Dallmann, A., Dehmel, L., Peters, T., Mügge, C., Griesinger, C., Tuma, J., et al. (2010). 2-Aminopurine incorporation perturbs the dynamics and structure of DNA. *Angew. Chem. Int. Ed.* 49, 5989–5992. doi: 10.1002/anie.201001312

Davies, M. J., Shah, A., and Bruce, I. J. (2000). Synthesis of fluorescently labelled oligonucleotides and nucleic acids. *Chem. Soc. Rev.* 29, 97–107. doi: 10.1039/a905230e

De Bont, R., and van Larebeke, N. (2004). Endogenous DNA damage in humans: a review of quantitative data. *Mutagenesis* 19, 169–185. doi: 10.1093/mutage/geh025

de Silva, A. P., Gunaratne, H. Q. N., Gunnlaugsson, T., Huxley, A. J. M., McCoy, C. P., Rademacher, J. T., et al. (1997). Signaling recognition events with fluorescent sensors and switches. *Chem. Rev.* 97, 1515–1566. doi: 10.1021/cr960386p

Demchenko, A. P. (2005a). Optimization of fluorescence response in the design of molecular biosensors. *Anal. Biochem.* 343, 1–22. doi: 10.1016/j.ab.2004.11.041

Demchenko, A. P. (2005b). The future of fluorescence sensor arrays. *Trends Biotechnol.* 23, 456–460. doi: 10.1016/j.tibtech.2005.06.003

Demchenko, A. P. (2005c). The problem of self-calibration of fluorescence signal in microscale sensor systems. *Lab Chip* 5, 1210–1214. doi: 10.1039/b507447a

Demchenko, A. P. (2006). Visualization and sensing of intermolecular interactions with two-color fluorescent probes. *FEBS Lett.* 580, 2951–2957. doi: 10.1016/j.febslet.2006.03.091

Demchenko, A. P. (2010). The concept of λ-ratiometry in fluorescence sensing and imaging. *J. Fluoresc.* 20, 1099–1128. doi: 10.1007/s10895-010-0644-y

Demchenko, A. P. (2013). Nanoparticles and nanocomposites for fluorescence sensing and imaging. *Methods Appl. Fluoresc.* 1:022001. doi: 10.1088/2050-6120/1/2/022001

Demchenko, A. P. (2014). Practical aspects of wavelength ratiometry in the studies of intermolecular interactions. *J. Mol. Struct.* 1077, 51–67. doi: 10.1016/j.molstruc.2013.11.045

Demchenko, A. P. (2015). *Introduction to Fluorescence Sensing, 2nd Edn*. Heidelberg: Springer.

Demchenko, A. P., Mély, Y., Duportail, G., and Klymchenko, A. S. (2009). Monitoring biophysical properties of lipid membranes by environment-sensitive fluorescent probes. *Biophys. J.* 96, 3461–3470. doi: 10.1016/j.bpj.2009.02.012

Demchenko, A. P., Tang, K.-C., and Chou, P.-T. (2013). Excited-state proton coupled charge transfer modulated by molecular structure and media polarization. *Chem. Soc. Rev.* 42, 1379–1408. doi: 10.1039/C2CS35195A

Didenko, V. V. (2001). DNA probes using fluorescence resonance energy transfer (FRET): designs and applications. *Biotechniques* 31, 1106–1116. doi: 10.2144/01315rv02

Djebali, S., Davis, C. A., Merkel, A., Dobin, A., Lassmann, T., Mortazavi, A., et al. (2013). Landscape of transcription in human cells. *Nature* 488, 101–108. doi: 10.1038/nature11233

Dodd, D. W., and Hudson, R. (2009). Intrinsically fluorescent base-discriminating nucleoside analogs. *Mini Rev. Org. Chem.* 6, 378–391. doi: 10.2174/157019309789371659

Duprey, J.-L. H. A., Bassani, D. M., Hyde, E. I., Jonusauskas, G., Ludwig, C., Rodger, A., et al. (2018). Rationalisation of a mechanism for sensing single point variants in target DNA using anthracene-tagged base discriminating probes. *Org. Biomol. Chem.* 16, 6576–6585. doi: 10.1039/C8OB01710G

Duprey, J.-L. H. A., Bullen, G. A., Zhao, Z.-Y., Bassani, D. M., Peacock, A. F. A., Wilkie, J., et al. (2016). Single site discrimination of cytosine, 5-Methylcytosine, and 5-Hydroxymethylcytosine in target DNA using anthracene-Tagged fluorescent probes. *ACS Chem. Biol.* 11, 717–721. doi: 10.1021/acschembio.5b00796

Duprey, J.-L. H. A., Zhao, Z.-Y., Bassani, D. M., Manchester, J., Vyle, J. S., and Tucker, J. H. R. (2011). Detection of DNA base variation and cytosine methylation at a single nucleotide site using a highly sensitive fluorescent probe. *Chem. Commun.* 47:6629. doi: 10.1039/c1cc11205h

Dziuba, D., Jurkiewicz, P., Cebecauer, M., Hof, M., and Hocek, M. (2016a). A rotational BODIPY nucleotide: an environment-sensitive fluorescence-lifetime probe for DNA interactions and applications in live-cell microscopy. *Angew. Chem. Int. Ed.* 55, 174–178. doi: 10.1002/anie.201507922

Dziuba, D., Karpenko, I. A., Barthes, N. P. F., Michel, B. Y., Klymchenko, A. S., Benhida, R., et al. (2014). Rational design of a solvatochromic fluorescent uracil analogue with a dual-band ratiometric response based on 3-hydroxychromone. *Chem. Eur. J.* 20, 1998–2009. doi: 10.1002/chem.201303399

Dziuba, D., Pohl, R., and Hocek, M. (2015). Polymerase synthesis of DNA labelled with benzylidene cyanoacetamide-based fluorescent molecular rotors: fluorescent light-up probes for DNA-binding proteins. *Chem. Commun.* 51, 4880–4882. doi: 10.1039/C5CC00530B

Dziuba, D., Pospisil, P., Matyasovsky, J., Brynda, J., Nachtigallova, D., Rulíšek, L., et al. (2016b). Solvatochromic fluorene-linked nucleoside and DNA as color-changing fluorescent probes for sensing interactions. *Chem. Sci.* 7, 5775–5785. doi: 10.1039/C6SC02548J

Dziuba, D., Postupalenko, V. Y., Spadafora, M., Klymchenko, A. S., Guérineau, V., Mély, Y., et al. (2012). A universal nucleoside with strong two-band switchable fluorescence and sensitivity to the environment for investigating DNA interactions. *J. Am. Chem. Soc.* 134, 10209–10213. doi: 10.1021/ja3030388

Edward, L., Rachofsky, Eleanore, S.eibert, James, T., Stivers, Roman Osman, A., and J. B., Alexander Ross (2001). Conformation and dynamics of abasic sites in DNA investigated by time-resolved fluorescence of 2-Aminopurine†. *Biochemistry* 40, 957–967. doi: 10.1021/bi001665g

Fang, X., Cao, Z., Beck, T., and Tan, W. (2001). Molecular aptamer for real-time oncoprotein platelet-derived growth factor monitoring by fluorescence anisotropy. *Anal. Chem.* 73, 5752–5757. doi: 10.1021/ac010703e

Farid, S., Dinnocenzo, J. P., Merkel, P. B., Young, R. H., Shukla, D., and Guirado, G. (2011). Reexamination of the Rehm-Weller data set reveals electron transfer quenching that follows a Sandros-Boltzmann dependence on free energy. *J. Am. Chem. Soc.* 133, 11580–11587. doi: 10.1021/ja2024367

Fedorova, O. S., Kuznetsov, N. A., Koval, V. V., and Knorre, D. G. (2010). Conformational dynamics and pre-steady-state kinetics of DNA glycosylases. *Biochemistry* 75, 1225–1239. doi: 10.1134/S0006297910100044

Gaied, N. B. (2005). 8-vinyl-deoxyadenosine, an alternative fluorescent nucleoside analog to 2'-deoxyribosyl-2-Aminopurine with improved properties. *Nucl. Acids Res.* 33, 1031–1039. doi: 10.1093/nar/gki253

Gao, J., Liu, H., and Kool, E. T. (2004). Expanded-size bases in naturally sized DNA: evaluation of steric effects in Watson-Crick pairing. *J. Am. Chem. Soc.* 126, 11826–11831. doi: 10.1021/ja048499a

Gavvala, K., Barthes, N. P. F., Bonhomme, D., Dabert-Gay, A. S., Debayle, D., Michel, B. Y., et al. (2016). A turn-on dual emissive nucleobase sensitive to mismatches and duplex conformational changes. *RSC Adv.* 6, 87142–87146. doi: 10.1039/C6RA19061H

Gillet, L. C. J., and Schärer, O. D. (2006). Molecular mechanisms of mammalian global genome nucleotide excision repair. *Chem. Rev.* 106, 253–276. doi: 10.1021/cr040483f

Greco, N. J., Sinkeldam, R. W., and Tor, Y. (2009). An emissive c analog distinguishes between G, 8-oxoG, and T. *Org. Lett.* 11, 1115–1118. doi: 10.1021/ol802656n

Greco, N. J., and Tor, Y. (2005). Simple fluorescent pyrimidine analogues detect the presence of DNA abasic sites. *J. Am. Chem. Soc.* 127, 10784–10785. doi: 10.1021/ja052000a

Greco, N. J., and Tor, Y. (2007). Furan decorated nucleoside analogues as fluorescent probes: synthesis, photophysical evaluation and site-specific incorporation. *Tetrahedron* 63, 3515–3527. doi: 10.1016/j.tet.2007.01.073

Gryczynski, Z., Gryczynski, I., and Lakowicz, J. R. (2003). Fluorescence-sensing methods. *Meth. Enzymol.* 360, 44–75. doi: 10.1016/S0076-6879(03)60106-0

Grynkiewicz, G., Poenie, M., and Tsien, R. Y. (1985). A new generation of Ca2+ indicators with greatly improved fluorescence properties. *J. Biol. Chem.* 260, 3440–3450.

Guest, C. R., Hochstrasser, R. A., Sowers, L. C., and Millar, D. P. (1991). Dynamics of mismatched base pairs in DNA. *Biochemistry* 30, 3271–3279. doi: 10.1021/bi00227a015

Guo, J., Ju, J., and Turro, N. J. (2012). Fluorescent hybridization probes for nucleic acid detection. *Anal. Bioanal. Chem.* 402, 3115–3125. doi: 10.1007/s00216-011-5526-x

Gustmann, H., Segler, A.-L. J., Gophane, D. B., Reuss, A. J., Grünewald, C., Braun, M., et al. (2018). Structure guided fluorescence labeling reveals a two-step binding mechanism of neomycin to its RNA aptamer. *Nucl. Acids Res.* 47, 15–28. doi: 10.1093/nar/gky1110

Han, K.-L., and Zhao, G.-J. (Eds.). (2010). *Hydrogen Bonding and Transfer in the Excited State,* Vol. 2. Chichester: John Wiley & Sons Inc.

Haque, M. M., Sun, H., Liu, S., Wang, Y., and Peng, X. (2014). Photoswitchable formation of a DNA interstrand cross-link by a coumarin-modified nucleotide. *Angew. Chem. Int. Ed.* 53, 7001–7005. doi: 10.1002/anie.201310609

Hawkins, M. E. (2001). Fluorescent pteridine nucleoside analogs: a window on DNA interactions. *CBB* 34, 257–281. doi: 10.1385/CBB:34:2:257

Hawkins, M. E. (2008). "Fluorescent pteridine probes for nucleic acid analysis," in *Methods in Enzymology, Fluorescence Spectroscopy,* eds L. Brand and M. L. Johnson (Oxford: Academic Press), 201–231.

Herdewijn, P. (Ed.). (2008). "Modified nucleosides," in *Biochemistry, Biotechnology and Medicine,* ed P. Herdewijn (Weinheim: Wiley-VCH), 658.

Hocek, M. (2019). Enzymatic synthesis of base-functionalized nucleic acids for sensing, cross-linking, and modulation of protein–DNA binding and transcription. *Acc. Chem. Res.* 52, 1730–1737. doi: 10.1021/acs.accounts.9b00195

Hogrefe, R. I., Midthune, B., and Lebedev, A. (2013). Current challenges in nucleic acid synthesis. *Isr. J. Chem.* 53, 326–349. doi: 10.1002/ijch.201300032

Holzhauser, C., Kracher, S., Rubner, M. M., Schmucker, W., Wagenknecht, H.-A., and Witzgall, R. (2013). Photochemically active fluorophore-DNA/RNA conjugates for cellular imaging of nucleic acids by readout in electron microscopy. *Chemistry Open* 2, 136–140. doi: 10.1002/open.201300017

Hövelmann, F., Bethge, L., and Seitz, O. (2012). Single labeled DNA FIT probes for avoiding false-positive signaling in the detection of DNA/RNA in qPCR or cell media. *ChemBioChem* 13, 2072–2081. doi: 10.1002/cbic.201200397

Hövelmann, F., Gaspar, I., Ephrussi, A., and Seitz, O. (2013). Brightness enhanced DNA FIT-Probes for wash-free RNA imaging in tissue. *J. Am. Chem. Soc.* 135, 19025–19032. doi: 10.1021/ja410674h

Huber, R., Amann, N., and Wagenknecht, H.-A. (2004). Synthesis of DNA with phenanthridinium as an artificial DNA base. *J. Org. Chem.* 69, 744–751. doi: 10.1021/jo0355404

Hudson, R., and Ghorbani-Choghamarani, A. (2007). Selective fluorometric detection of guanosine-containing sequences by 6-Phenylpyrrolocytidine in DNA. *Synlett* 2007, 0870–0873. doi: 10.1055/s-2007-973869

Hwang, G. T., Seo, Y. J., and Kim, B. H. (2004). A highly discriminating quencher-free molecular beacon for probing DNA. *J. Am. Chem. Soc.* 126, 6528–6529. doi: 10.1021/ja049795q

Hwang, G. T., Seo, Y. J., and Kim, B. H. (2005). Pyrene-labeled deoxyuridine and deoxyadenosine: fluorescent discriminating phenomena in their oligonucleotides. *Tetrahedron Lett.* 46, 1475–1477. doi: 10.1016/j.tetlet.2005.01.015

Hwang, H., and Myong, S. (2014). Protein induced fluorescence enhancement (PIFE) for probing protein–nucleic acid interactions. *Chem. Soc. Rev.* 43, 1221–1229. doi: 10.1039/C3CS60201J

Jhaveri, S., Rajendran, M., and Ellington, A. D. (2000). *In vitro* selection of signaling aptamers. *Nat. Biotechnol.* 18, 1293–1297. doi: 10.1038/82414

Jhaveri, S. D., Kirby, R., Conrad, R., Maglott, E. J., Bowser, M., Kennedy, R. T., et al. (2000). Designed signaling aptamers that transduce molecular recognition to changes in fluorescence intensity. *J. Am. Chem. Soc.* 122, 2469–2473. doi: 10.1021/ja992393b

Jones, A. C., and Neely, R. K. (2015). 2-Aminopurine as a fluorescent probe of DNA conformation and the DNA–enzyme interface. *Q. Rev. Biophys.* 48, 244–279. doi: 10.1017/S0033583514000158

Jung, J. W., Edwards, S. K., and Kool, E. T. (2013). Selective fluorogenic chemosensors for distinct classes of nucleases. *Chembiochem* 14, 440–444. doi: 10.1002/cbic.201300001

Juskowiak, B. (2010). Nucleic acid-based fluorescent probes and their analytical potential. *Anal. Bioanal. Chem.* 399, 3157–3176. doi: 10.1007/s00216-010-4304-5

Kapuscinski, J. (1995). DAPI: a DNA-specific fluorescent probe. *Biotech. Histochem.* 70, 220–233. doi: 10.3109/10520299509108199

Katilius, E., Katiliene, Z., and Woodbury, N. W. (2006). Signaling aptamers created using fluorescent nucleotide analogues. *Anal. Chem.* 78, 6484–6489. doi: 10.1021/ac060859k

Kaushik, M., Kaushik, S., Roy, K., Singh, A., Mahendru, S., Kumar, M., et al. (2016). A bouquet of DNA structures: emerging diversity. *Biochem. Biophys. Rep.* 5, 388–395. doi: 10.1016/j.bbrep.2016.01.013

Kilin, V., Gavvala, K., Barthes, N. P. F., Michel, B. Y., Shin, D., Boudier, C., et al. (2017). Dynamics of methylated cytosine flipping by UHRF1. *J. Am. Chem. Soc.* 139, 2520–2528. doi: 10.1021/jacs.7b00154

Kimura, T., Kawai, K., and Majima, T. (2005). Monitoring of microenvironmental changes in the major and minor grooves of DNA by dan-modified oligonucleotides. *Org. Lett.* 7, 5829–5832. doi: 10.1021/ol052473m

Kimura, T., Kawai, K., and Majima, T. (2006). Probing the microenvironments in the grooves of Z-DNA using dan-modified oligonucleotides. *Chem. Commun.* 1542–1544. doi: 10.1039/b600026f

Klymchenko, A. S. (2017). Solvatochromic and fluorogenic dyes as environment-sensitive probes: design and biological applications. *Acc. Chem. Res.* 50, 366–375. doi: 10.1021/acs.accounts.6b00517

Klymchenko, A. S., and Kreder, R. (2014). Fluorescent probes for lipid rafts: from model membranes to living cells. *Chem. Biol.* 21, 97–113. doi: 10.1016/j.chembiol.2013.11.009

Klymchenko, A. S., and Mély, Y. (2013). "Fluorescent environment-sensitive dyes as reporters of biomolecular interactions," in *Progress in Molecular Biology and*

Translational Science, Vol. 113, ed M. C. Morris (Burlington, MA: Academic Press), 35–58.

Köhler, O., Jarikote, D. V., Singh, I., Parmar, V. S., Weinhold, E., and Seitz, O. (2005). Forced intercalation as a tool in gene diagnostics and in studying DNA–protein interactions. *Pure Appl. Chem.* 77, 327–338. doi: 10.1351/pac200577010327

Kolpashchikov, D. M. (2010). Binary probes for nucleic acid analysis. *Chem. Rev.* 110, 4709–4723. doi: 10.1021/cr900323b

Krueger, A. T., and Imperiali, B. (2013). Fluorescent amino acids: modular building blocks for the assembly of new tools for chemical biology. *Chembiochem* 14, 788–799. doi: 10.1002/cbic.201300079

Krueger, A. T., Lu, H., Lee, A. H. F., and Kool, E. T. (2007). Synthesis and properties of size-expanded DNAs: toward designed, functional genetic systems. *Acc. Chem. Res.* 40, 141–150. doi: 10.1021/ar068200o

Kummer, S., Knoll, A., Socher, E., Bethge, L., Herrmann, A., and Seitz, O. (2011). Fluorescence imaging of influenza H1N1 mRNA in living infected cells using single-chromophore FIT-PNA. *Angew. Chem. Int. Ed.* 50, 1931–1934. doi: 10.1002/anie.201005902

Kuznetsova, A. A., Kuznetsov, N. A., Vorobjev, Y. N., Barthes, N. P. F., Michel, B. Y., Burger, A., et al. (2014). New environment-sensitive multichannel DNA fluorescent label for investigation of the protein-DNA interactions. *PLoS ONE* 9:e100007. doi: 10.1371/journal.pone.0100007

Lakowicz, J. R. (2006). *Principles of Fluorescence Spectroscopy*, 3rd Edn. New York, NY: Springer.

Lane, R. S. K., and Magennis, S. W. (2012). Two-photon excitation of the fluorescent nucleobase analogues 2-AP and tC. *RSC Adv.* 2, 11397–11398. doi: 10.1039/c2ra21881j

Lavis, L. D., and Raines, R. T. (2014). Bright building blocks for chemical biology. *ACS Chem. Biol.* 9, 855–866. doi: 10.1021/cb500078u

Law, S. M., Eritja, R., Goodman, M. F., and Breslauer, K. J. (1996). Spectroscopic and calorimetric characterizations of DNA duplexes containing 2-Aminopurine†. *Biochemistry* 35, 12329–12337. doi: 10.1021/bi9614545

Le, H.-N., Zilio, C., Barnoin, G., Barthes, N. P. F., Guigonis, J.-M., Martinet, N., et al. (2019). Rational design, synthesis, and photophysics of dual-emissive deoxyadenosine analogs. *Dyes Pigm.* 170:107553. doi: 10.1016/j.dyepig.2019.107553

Lenz, T., Bonnist, E. Y. M., Pljevaljcić, G., Neely, R. K., Dryden, D. T. F., and Scheidig, A. J., et al. (2007). 2-Aminopurine flipped into the active site of the adenine-specific DNA methyltransferase M.TaqI: crystal structures and time-resolved fluorescence. *J. Am. Chem. Soc.* 129, 6240–6248. doi: 10.1021/ja069366n

Li, T., Fu, R., and Park, H. G. (2010). Pyrrolo-dC based fluorescent aptasensors for the molecular recognition of targets. *Chem. Commun.* 46, 3271–3273. doi: 10.1039/b923462d

Li, W., Wang, K., Tan, W., Ma, C., and Yang, X. (2007). Aptamer-based analysis of angiogenin by fluorescence anisotropy. *Analyst* 132, 107–113. doi: 10.1039/B614138B

Lin, K.-Y., Jones, R. J., and Matteucci, M. (1995). Tricyclic 2'-Deoxycytidine Analogs: syntheses and incorporation into oligodeoxynucleotides which have enhanced binding to complementary RNA. *J. Am. Chem. Soc.* 117, 3873–3874. doi: 10.1021/ja00118a026

Lippert, E. (1955). Dipolmoment und elektronenstruktur von angeregten molekülen. *Z. Nat. Forsch. A* 10, 541–545. doi: 10.1515/zna-1955-0707

Liu, H., Gao, J., Maynard, L., Saito, Y. D., and Kool, E. T. (2004). Toward a new genetic system with expanded dimensions: size-expanded analogues of deoxyadenosine and thymidine. *J. Am. Chem. Soc.* 126, 1102–1109. doi: 10.1021/ja038384r

Loving, G. S., Sainlos, M., and Imperiali, B. (2010). Monitoring protein interactions and dynamics with solvatochromic fluorophores. *Trends Biotechnol.* 28, 73–83. doi: 10.1016/j.tibtech.2009.11.002

Ma, D.-L., He, H.-Z., Leung, K.-H., Zhong, H.-J., Chan, D. S.-H., and Leung, C.-H. (2013). Label-free luminescent oligonucleotide-based probes. *Chem. Soc. Rev.* 42, 3427–3440. doi: 10.1039/c2cs35472a

Manna, S., Sarkar, D., and Srivatsan, S. G. (2018). A dual-app nucleoside probe provides structural insights into the human telomeric overhang in live cells. *J. Am. Chem. Soc.* 140, 12622–12633. doi: 10.1021/jacs.8b08436

Martí, A. A., Jockusch, S., Stevens, N., Ju, J., and Turro, N. J. (2007). Fluorescent hybridization probes for sensitive and selective DNA and RNA detection. *Acc. Chem. Res.* 40, 402–409. doi: 10.1021/ar600013q

Mata, G., and Luedtke, N. W. (2013). Synthesis and solvatochromic fluorescence of biaryl pyrimidine nucleosides. *Org. Lett.* 15, 2462–2465. doi: 10.1021/ol400930s

Mata, G., and Luedtke, N. W. (2015). fluorescent probe for proton-coupled dna folding revealing slow exchange of i-motif and duplex structures. *J. Am. Chem. Soc.* 137, 699–707. doi: 10.1021/ja508741u

Mata, G., Schmidt, O. P., and Luedtke, N. W. (2016). A fluorescent surrogate of thymidine in duplex DNA. *Chem. Commun.* 52, 4718–4721. doi: 10.1039/C5CC09552B

McCoy, L. S., Shin, D., and Tor, Y. (2014). Isomorphic emissive gtp surrogate facilitates initiation and elongation of *in vitro* transcription reactions. *J. Am. Chem. Soc.* 136, 15176–15184. doi: 10.1021/ja5039227

Millar, D. P. (1996). Fluorescence studies of DNA and RNA structure and dynamics. *Curr. Opin. Struct. Biol.* 6, 322–326. doi: 10.1016/S0959-440X(96)80050-9

Mizrahi, R. A., Shin, D., Sinkeldam, R. W., Phelps, K. J., Fin, A., Tantillo, D. J., et al. (2015). A Fluorescent adenosine analogue as a substrate for an A-to-I RNA editing enzyme. *Angew. Chem. Int. Ed.* 127, 8837–8840. doi: 10.1002/ange.201502070

Mocz, G., Helms, M. K., Jameson, D. M., and Gibbons, I. R. (1998). Probing the nucleotide binding sites of axonemal dynein with the fluorescent nucleotide analogue 2′(3′)-O-(-N-Methylanthraniloyl)-adenosine 5′-Triphosphate†. *Biochemistry* 37, 9862–9869. doi: 10.1021/bi9730184

Moreno, A., Knee, J., and Mukerji, I. (2012). Applying 6-methylisoxanthopterin-enhanced fluorescence to examine protein–DNA interactions in the picomolar range. *Biochemistry* 51, 6847–6859. doi: 10.1021/bi300466d

Murthy, S. N., and Lorand, L. (2000). Nucleotide binding by the erythrocyte transglutaminase/Gh protein, probed with fluorescent analogs of GTP and GDP. *Proc. Natl. Acad. Sci. U.S.A.* 97, 7744–7747. doi: 10.1073/pnas.140210197

Nakatani, K., and Tor, Y. (eds.). (2016). "Modified nucleic acids," in *Nucleic Acids and Molecular Biology*, eds K. Nakatani and Y. Tor (Cham: Springer International Publishing AG), 276.

Narayanaswamy, N., Das, S., Samanta, P. K., Banu, K., Sharma, G. P., Mondal, N., et al. (2015). Sequence-specific recognition of DNA minor groove by an NIR-fluorescence switch-on probe and its potential applications. *Nucl. Acids Res.* 43, 8651–8663. doi: 10.1093/nar/gkv875

Neely, R. K. (2005). Time-resolved fluorescence of 2-Aminopurine as a probe of base flipping in M.HhaI-DNA complexes. *Nucl. Acids Res.* 33, 6953–6960. doi: 10.1093/nar/gki995

Nguyen, H.-N., Zhao, L., Gray, C. W., Gray, D. M., and Xia, T. (2011). Ultrafast fluorescence decay profiles reveal differential unstacking of 2-Aminopurine from neighboring bases in single-stranded DNA-binding protein subsites. *Biochemistry* 50, 8989–9001. doi: 10.1021/bi2006543

Noé, M. S., Ríos, A. C., and Tor, Y. (2012). Design, synthesis, and spectroscopic properties of extended and fused Pyrrolo-dC and Pyrrolo-C Analogs. *Org. Lett.* 14, 3150–3153. doi: 10.1021/ol3012327

Nordlund, T. M., Andersson, S., Nilsson, L., Rigler, R., Gräslund, A., and McLaughlin, L. W. (1989). Structure and dynamics of a fluorescent DNA oligomer containing the EcoRI recognition sequence: fluorescence, molecular dynamics, and NMR studies. *Biochemistry* 28, 9095–9103. doi: 10.1021/bi00449a021

Oesch, D., and Luedtke, N. W. (2015). Fluorescent chemosensors of carbohydrate triols exhibiting TICT emissions. *Chem. Commun.* 51, 12641–12644. doi: 10.1039/C5CC03857J

Ogasawara, S., and Maeda, M. (2008). Straightforward and reversible photoregulation of hybridization by using a photochromic nucleoside. *Angew. Chem. Int. Ed.* 47, 8839–8842. doi: 10.1002/anie.200803496

Okamoto, A. (2011). ECHO probes: a concept of fluorescence control for practical nucleic acid sensing. *Chem. Soc. Rev.* 40, 5815–5815. doi: 10.1039/c1cs15025a

Okamoto, A., Kanatani, K., and Saito, I. (2004). Pyrene-labeled base-discriminating fluorescent DNA probes for homogeneous SNP typing. *J. Am. Chem. Soc.* 126, 4820–4827. doi: 10.1021/ja039625y

Okamoto, A., Saito, Y., and Saito, I. (2005a). Design of base-discriminating fluorescent nucleosides. *J. Photochem. Photobiol. C* 6, 108–122. doi: 10.1016/j.jphotochemrev.2005.07.002

Okamoto, A., Tainaka, K., and Fujiwara, Y. (2006). Nile red nucleoside: design of a solvatofluorochromic nucleoside as an indicator of micropolarity around DNA. *J. Org. Chem.* 71, 3592–3598. doi: 10.1021/jo060168o

Okamoto, A., Tainaka, K., Nishiza, K.-I., and Saito, I. (2005b). Monitoring DNA structures by dual fluorescence of pyrene derivatives. *J. Am. Chem. Soc.* 127, 13128–13129. doi: 10.1021/ja053609e

Ono, T., Wang, S., Koo, C.-K., Engstrom, L., David, S. S., and Kool, E. T. (2012). Direct fluorescence monitoring of DNA base excision repair. *Angew. Chem. Int. Ed.* 51, 1689–1692. doi: 10.1002/anie.201108135

Østergaard, M. E., and Hrdlicka, P. J. (2011). Pyrene-functionalized oligonucleotides and locked nucleic acids (LNAs): Tools for fundamental research, diagnostics, and nanotechnology. *Chem. Soc. Rev.* 40, 5771–5718. doi: 10.1039/c1cs15014f

Ozers, M. S., Hill, J. J., Ervin, K., Wood, J. R., Nardulli, A. M., Royer, C. A., et al. (1997). Equilibrium binding of estrogen receptor with DNA using fluorescence anisotropy. *J. Biol. Chem.* 272, 30405–30411. doi: 10.1074/jbc.272.48.30405

Park, S., Otomo, H., Zheng, L., and Sugiyama, H. (2014). Highly emissive deoxyguanosine analogue capable of direct visualization of B-Z transition. *Chem. Commun.* 50, 1573–1575. doi: 10.1039/c3cc48297a

Psciuk, B. T., Lord, R. L., Munk, B. H., and Schlegel, H. B. (2012). Theoretical determination of one-electron oxidation potentials for nucleic acid bases. *J. Chem. Theory Comput.* 8, 5107–5123. doi: 10.1021/ct300550x

Ramreddy, T., Kombrabail, M., Krishnamoorthy, G., and Rao, B. J. (2009). Site-Specific Dynamics in TAT Triplex DNA as revealed by time-domain fluorescence of 2-Aminopurine. *J. Phys. Chem. B* 113, 6840–6846. doi: 10.1021/jp901216h

Ramreddy, T., Rao, and Krishnamoorthy, G. (2007). Site-specific dynamics of strands in ss- and dsDNA as revealed by time-domain fluorescence of 2-Aminopurine. *J. Phys. Chem. B* 111, 5757–5766. doi: 10.1021/jp068818f

Reha-Krantz, L. J., Hariharan, C., Subuddhi, U., Xia, S., Zhao, C., Beckman, J., et al. (2011). Structure of the 2-aminopurine-cytosine base pair formed in the polymerase active site of the RB69 Y567A-DNA polymerase. *Biochemistry* 50, 10136–10149. doi: 10.1021/bi2014618

Rehm, D., and Weller, A. (1970). Kinetics of fluorescence quenching by electron and H-Atom transfer. *Isr. J. Chem.* 8, 259–271. doi: 10.1002/ijch.197000029

Rettig, W. (1986). Charge separation in excited states of decoupled systems–TICT compounds and implications regarding the development of new laser dyes and the primary process of vision and photosynthesis. *Angew. Chem. Int. Ed.* 25, 971–988. doi: 10.1002/anie.198609711

Riedl, J., Ménová, P., Pohl, R., Orság, P., Fojta, M., and Hocek, M. (2012a). GFP-like fluorophores as DNA labels for studying DNA-protein interactions. *J. Org. Chem.* 77, 8287–8293. doi: 10.1021/jo301684b

Riedl, J., Pohl, R., Ernsting, N. P., Orság, P., Fojta, M., and Hocek, M. (2012b). Labelling of nucleosides and oligonucleotides by solvatochromic 4-aminophthalimide fluorophore for studying DNA-protein interactions. *Chem. Sci.* 3, 2797–2806. doi: 10.1039/c2sc20404e

Rist, M., Amann, N., and Wagenknecht, H.-A. (2003). Preparation of 1-Ethynylpyrene-modified DNA via sonogashira-type solid-phase couplings and characterization of the fluorescence properties for electron-transfer studies. *Eur. J. Org. Chem.* 2003, 2498–2504. doi: 10.1002/ejoc.200300125

Ryu, J. H., Seo, Y. J., Hwang, G. T., Lee, J. Y., and Kim, B. H. (2007). Triad base pairs containing fluorene unit for quencher-free SNP typing. *Tetrahedron* 63, 3538–3547. doi: 10.1016/j.tet.2006.10.091

Sabale, P. M., Tanpure, A. A., and Srivatsan, S. G. (2018). Probing the competition between duplex and G-quadruplex/i-motif structures using a conformation-sensitive fluorescent nucleoside probe. *Org. Biomol. Chem.* 16, 4141–4150. doi: 10.1039/C8OB00646F

Saito, Y., and Hudson, R. H. E. (2018). Base-modified fluorescent purine nucleosides and nucleotides for use in oligonucleotide probes. *J. Photochem. Photobiol. C: Photochem. Rev.* 36, 48–73. doi: 10.1016/j.jphotochemrev.2018.07.001

Saito, Y., Miyauchi, Y., Okamoto, A., and Saito, I. (2004). Base-Discriminating Fluorescent (BDF) nucleoside: distinction of thymine by fluorescence quenching. *Chem. Commun.* 7, 1704–1705. doi: 10.1039/b405832a

Sandin, P. (2005). Fluorescent properties of DNA base analogue tC upon incorporation into DNA — negligible influence of neighbouring bases on fluorescence quantum yield. *Nucl. Acids Res.* 33, 5019–5025. doi: 10.1093/nar/gki790

Sandin, P., Stengel, G., Ljungdahl, T., Börjesson, K., Macao, B., and Wilhelmsson, L. M. (2009). Highly efficient incorporation of the fluorescent nucleotide analogs tC and tCO by Klenow fragment. *Nucl. Acids Res.* 37, 3924–3933. doi: 10.1093/nar/gkp266

Schärer, O. D. (2003). Chemistry and biology of DNA repair. *Angew. Chem. Int. Ed.* 42, 2946–2974. doi: 10.1002/anie.200200523

Schweigert, C., Gaß, N., Wagenknecht, H.-A., and Unterreiner, A.-N. (2017). Significant fluorescence enhancement of N, N-dimethylaminobenzophenone after embedding as a C-nucleoside in DNA. *Chemphotochem* 2, 12–17. doi: 10.1002/cptc.201700183

Sedgwick, A. C., Wu, L., Han, H.-H., Bull, S. D., He, X.-P., James, T. D., et al. (2018). Excited-state intramolecular proton-transfer (ESIPT) based fluorescence sensors and imaging agents. *Chem. Soc. Rev.* 46, 7105–7139. doi: 10.1039/C8CS00185E

Seidel, C. A. M., Schulz, A., and Sauer, M. H. M. (1996). Nucleobase-specific quenching of fluorescent dyes. 1. Nucleobase one-electron redox potentials and their correlation with static and dynamic quenching efficiencies. *J. Phys. Chem.* 100, 5541–5553. doi: 10.1021/jp951507c

Seo, Y. J., and Kim, B. H. (2006). Probing the B-to-Z-DNA duplex transition using terminally stacking ethynyl pyrene-modified adenosine and uridine bases. *Chem. Commun.* 271, 150–152. doi: 10.1039/B514079J

Seo, Y. J., Ryu, J. H., and Kim, B. H. (2005). Quencher-free, end-stacking oligonucleotides for probing single-base mismatches in DNA. *Org. Lett.* 7, 4931–4933. doi: 10.1021/ol0518582

Shi, X., and Herschlag, D. (2009). "Fluorescence polarization anisotropy to measure RNA dynamics," in *Biophysical, Chemical, and Functional Probes of RNA Structure, Interactions and Folding: Part B Methods in Enzymology,* Vol. 469, ed D. Herschlag (Elsevier), 287–302.

Shin, D., Sinkeldam, R. W., and Tor, Y. (2011). Emissive RNA alphabet. *J. Am. Chem. Soc.* 133, 14912–14915. doi: 10.1021/ja206095a

Sholokh, M., Improta, R., Mori, M., Sharma, R., Kenfack, C., Shin, D., et al. (2016). Tautomers of a fluorescent g surrogate and their distinct photophysics provide additional information channels. *Angew. Chem. Int. Ed.* 55, 7974–7978. doi: 10.1002/anie.201601688

Sholokh, M., Sharma, R., Grytsyk, N., Zaghzi, L., Postupalenko, V. Y., Dziuba, D., et al. (2018). Environmentally sensitive fluorescent nucleoside analogues for surveying dynamic interconversions of nucleic acid structures. *Chem. Eur. J.* 5, 388–313. doi: 10.1002/chem.201802297

Sholokh, M., Sharma, R., Shin, D., Das, R., Zaporozhets, O. A., Tor, Y., et al. (2015a). Conquering 2-Aminopurine's deficiencies: highly emissive isomorphic guanosine surrogate faithfully monitors guanosine conformation and dynamics in DNA. *J. Am. Chem. Soc.* 137, 3185–3188. doi: 10.1021/ja513107r

Sholokh, M., Zamotaiev, O. M., Das, R., Postupalenko, V. Y., Richert, L., Dujardin, D., et al. (2015b). Fluorescent amino acid undergoing excited state intramolecular proton transfer for site-specific probing and imaging of peptide interactions. *J. Phys. Chem. B* 119, 2585–2595. doi: 10.1021/jp508748e

Sinkeldam, R. W., Greco, N. J., and Tor, Y. (2008). Polarity of major grooves explored by using an isosteric emissive nucleoside. *ChemBioChem* 9, 706–709. doi: 10.1002/cbic.200700714

Sinkeldam, R. W., Greco, N. J., and Tor, Y. (2010). Fluorescent analogs of biomolecular building blocks: design, properties, and applications. *Chem. Rev.* 110, 2579–2619. doi: 10.1021/cr900301e

Sinkeldam, R. W., Hopkins, P. A., and Tor, Y. (2012). Modified 6-Aza uridines: highly emissive pH-sensitive fluorescent nucleosides. *ChemPhysChem* 13, 3350–3356. doi: 10.1002/cphc.201200375

Sinkeldam, R. W., Wheat, A. J., Boyaci, H., and Tor, Y. (2011). Emissive nucleosides as molecular rotors. *ChemPhysChem* 12, 567–570. doi: 10.1002/cphc.201001002

Socher, E., and Seitz, O. (2008). FIT-probes in real-time PCR. *Methods Mol. Biol.* 429, 187–197. doi: 10.1007/978-1-60327-040-3_13

Somsen, O. J. G., Hoek, V. A., and Amerongen, V. H. (2005). Fluorescence quenching of 2-aminopurine in dinucleotides. *Chem. Phys. Lett.* 402, 61–65. doi: 10.1016/j.cplett.2004.11.122

Sowers, L. C., Fazakerley, G. V., Eritja, R., Kaplan, B. E., and Goodman, M. F. (1986). Base pairing and mutagenesis: observation of a protonated base pair

between 2-aminopurine and cytosine in an oligonucleotide by proton NMR. *Proc. Natl. Acad. Sci. U.S.A.* 83, 5434–5438. doi: 10.1073/pnas.83.15.5434

Srivatsan, S. G., Greco, N. J., and Tor, Y. (2008a). A highly emissive fluorescent nucleoside that signals the activity of toxic ribosome-inactivating proteins. *Angew. Chem. Int. Ed.* 47, 6661–6665. doi: 10.1002/anie.200802199

Srivatsan, S. G., and Sawant, A. A. (2011). Fluorescent ribonucleoside analogues as probes for investigating RNA structure and function. *Pure Appl. Chem.* 83, 213–232. doi: 10.1351/PAC-CON-10-09-16

Srivatsan, S. G., and Tor, Y. (2007a). Fluorescent pyrimidine ribonucleotide: synthesis, enzymatic incorporation, and utilization. *J. Am. Chem. Soc.* 129, 2044–2053. doi: 10.1021/ja066455r

Srivatsan, S. G., and Tor, Y. (2007b). Using an emissive uridine analogue for assembling fluorescent HIV-1 TAR constructs. *Tetrahedron* 63, 3601–3607. doi: 10.1016/j.tet.2007.01.074

Srivatsan, S. G., Weizman, H., and Tor, Y. (2008b). A highly fluorescent nucleoside analog based on thieno[3,4- *d*]pyrimidine senses mismatched pairing. *Org. Biomol. Chem.* 6, 1334–1335. doi: 10.1039/b801054d

Stanley, R. J., Hou, Z., Yang, A., and Hawkins, M. E. (2005). The two-photon excitation cross section of 6MAP, a fluorescent adenine analogue. *J. Phys. Chem. B* 109, 3690–3695. doi: 10.1021/jp0455982

Stivers, J. T., Pankiewicz, K. W., and Watanabe, K. A. (1999). Kinetic mechanism of damage site recognition and uracil flipping by escherichiacoliUracil DNA Glycosylase†. *Biochemistry* 38, 952–963. doi: 10.1021/bi9818669

Strobel, E. J., Yu, A. M., and Lucks, J. B. (2018). High-throughput determination of RNA structures. *Nat. Rev. Genet.* 19, 615–634. doi: 10.1038/s41576-018-0034-x

Su, X., Xiao, X., Zhang, C., and Zhao, M. (2012). Nucleic acid fluorescent probes for biological sensing. *Appl. Spectrosc.* 66, 1249–1262. doi: 10.1366/12-06803

Suzuki, A., Nemoto, N., Saito, I., and Saito, Y. (2014). Design of an environmentally sensitive fluorescent 8-aza-7-deaza-2′-deoxyadenosine derivative with dual fluorescence for the specific detection of thymine†. *Org. Biomol. Chem.* 12, 660–666. doi: 10.1039/C3OB41757C

Tainaka, K., Tanaka, K., Ikeda, S., Nishiza, K.-I., Unzai, T., Fujiwara, Y., et al. (2007). PRODAN-conjugated DNA: synthesis and photochemical properties. *J. Am. Chem. Soc.* 129, 4776–4784. doi: 10.1021/ja069156a

Tatikolov, A. S. (2012). Polymethine dyes as spectral-fluorescent probes for biomacromolecules. *J. Photochem. Photobiol. C* 13, 55–90. doi: 10.1016/j.jphotochemrev.2011.11.001

Técher, H., Koundrioukoff, S., Nicolas, A., and Debatisse, M. (2017). The impact of replication stress on replication dynamics and DNA damage in vertebrate cells. *Nat. Rev. Genet.* 18, 535–550. doi: 10.1038/nrg.2017.46

Teo, Y. N., and Kool, E. T. (2012). DNA-multichromophore systems. *Chem. Rev.* 112, 4221–4245. doi: 10.1021/cr100351g

Tomin, V. I., Demchenko, A. P., and Chou, P.-T. (2015). Thermodynamic vs. kinetic control of excited-state proton transfer reactions. *J. Photochem. Photobiol. C* 22, 1–18. doi: 10.1016/j.jphotochemrev.2014.09.005

Torimura, M., Kurata, S., Yamada, K., Yokomaku, T., Kamagata, Y., Kanagawa, T., et al. (2001). Fluorescence-quenching phenomenon by photoinduced electron transfer between a fluorescent dye and a nucleotide base. *Anal. Sci.* 17, 155–160. doi: 10.2116/analsci.17.155

Varghese, R., and Wagenknecht, H.-A. (2009). DNA as a supramolecular framework for the helical arrangements of chromophores: towards photoactive DNA-based nanomaterials. *Chem. Commun.* 2615–2624. doi: 10.1039/b821728a

Wahba, A. S., Esmaeili, A., Damha, M. J., and Hudson, R. H. E. (2010). A single-label phenylpyrrolocytidine provides a molecular beacon-like response reporting HIV-1 RT RNase H activity. *Nucl. Acids Res.* 38, 1048–1056. doi: 10.1093/nar/gkp1022

Ward, D. C., Reich, E., and Stryer, L. (1969). Fluorescence studies of nucleotides and polynucleotides. I. Formycin, 2-aminopurine riboside, 2,6-diaminopurine riboside, and their derivatives. *J. Biol. Chem.* 244, 1228–1237.

Weinberger, M., Berndt, F., Mahrwald, R., Ernsting, N. P., and Wagenknecht, H.-A. (2013). Synthesis of 4-aminophthalimide and 2,4-diaminopyrimidine C-nucleosides as isosteric fluorescent DNA base substitutes. *J. Org. Chem.* 78, 2589–2599. doi: 10.1021/jo302768f

White, S. J., and Cantsilieris, S. (eds.). (2017). *Genotyping: Methods and Protocols*. New York, NY: Humana Press, Springer Protocols.

Wilhelmsson, L. M. (2010). Fluorescent nucleic acid base analogues. *Q. Rev. Biophys.* 43, 159–183. doi: 10.1017/S0033583510000090

Wilhelmsson, L. M., Holmén, A., Lincoln, P., Nielsen, P. E., and Nordén, B. (2001). A highly fluorescent DNA base analogue that forms Watson-Crick base pairs with Guanine. *J. Am. Chem. Soc.* 123, 2434–2435. doi: 10.1021/ja0025797

Wilhelmsson, L. M., and Tor, Y. (eds.). (2016). *Fluorescent Analogs of Biomolecular Building Blocks: Design and Applications*. Hoboken, NJ: John Wiley & Sons Inc.

Wilson, D. L., Beharry, A. A., Srivastava, A., O'Connor, T. R., and Kool, E. T. (2018). Fluorescence probes for ALKBH2 Allow the measurement of DNA alkylation repair and drug resistance responses. *Angew. Chem. Int. Ed.* 57, 12896–12900. doi: 10.1002/anie.201807593

Wilson, J. N., and Kool, E. T. (2006). Fluorescent DNA base replacements: reporters and sensors for biological systems. *Org. Biomol. Chem.* 4:4265. doi: 10.1039/b612284c

Wu, J., Liu, W., Ge, J., Zhang, H., and Wang, P. (2011). New sensing mechanisms for design of fluorescent chemosensors emerging in recent years. *Chem. Soc. Rev.* 40, 3483–3413. doi: 10.1039/c0cs00224k

Xia, T. (2008). Taking femtosecond snapshots of RNA conformational dynamics and complexity. *Curr. Opin. Chem. Biol.* 12, 604–611. doi: 10.1016/j.cbpa.2008.08.033

Xu, D., Evans, K. O., and Nordlund, T. M. (1994). Melting and premelting transitions of an oligomer measured by DNA base fluorescence and absorption. *Biochemistry* 33, 9592–9599. doi: 10.1021/bi00198a027

Xu, W., Chan, K. M., and Kool, E. T. (2017). Fluorescent nucleobases as tools for studying DNA and RNA. *Nat. Chem.* 9, 1043–1055. doi: 10.1038/nchem.2859

Zamotaiev, O. M., Postupalenko, V. Y., Shvadchak, V. V., Pivovarenko, V. G., Klymchenko, A. S., and Mély, Y. (2014). Monitoring penetratin interactions with lipid membranes and cell internalization using a new hydration-sensitive fluorescent probe. *Org. Biomol. Chem.* 12, 7036–7044. doi: 10.1039/C4OB01242A

Zargarian, L., Ben Imeddourene, A., Gavvala, K., Barthes, N. P. F., Michel, B. Y., Kenfack, C. A., et al. (2017). Structural and dynamical impact of a universal fluorescent nucleoside analogue inserted into a DNA duplex. *J. Phys. Chem. B* 121, 11249–11261. doi: 10.1021/acs.jpcb.7b08825

Zhao, J., Ji, S., Chen, Y., Guo, H., and Yang, P. (2012). Excited state intramolecular proton transfer (ESIPT): from principal photophysics to the development of new chromophores and applications in fluorescent molecular probes and luminescent materials. *Phys. Chem. Chem. Phys.* 14, 8803–8817. doi: 10.1039/C2CP23144A

Zhao, L., and Xia, T. (2009). Probing RNA conformational dynamics and heterogeneity using femtosecond time-resolved fluorescence spectroscopy. *Methods* 49, 128–135. doi: 10.1016/j.ymeth.2009.04.001

Zhao, Z.-Y., San, M., Duprey, J.-L. H. A., Arrand, J. R., Vyle, J. S., and Tucker, J. H. R. (2012). Detection of single nucleotide polymorphisms within a sequence of a gene associated with prostate cancer using a fluorophore-tagged DNA probe. *Bioorg. Med. Chem. Lett.* 22, 129–132. doi: 10.1016/j.bmcl.2011.11.053

Zou, M., Chen, Y., Xu, X., Huang, H., Liu, F., and Li, N. (2012). The homogeneous fluorescence anisotropic sensing of salivary lysozyme using the 6-carboxyfluorescein-labeled DNA aptamer. *Biosens. Bioelectron.* 32, 148–154. doi: 10.1016/j.bios.2011.11.052

Conflict of Interest: The authors declare that the research was conducted in the absence of any commercial or financial relationships that could be construed as a potential conflict of interest.

frontiers in Chemistry

ORIGINAL RESEARCH
published: 12 May 2020
doi: 10.3389/fchem.2020.00381

Direct Detection and Discrimination of Nucleotide Polymorphisms Using Anthraquinone Labeled DNA Probes

Sarah A. Goodchild[1,2]*, *Rachel Gao*[2], *Daniel P. Shenton*[1], *Alastair J. S. McIntosh*[3], *Tom Brown*[4] *and Philip N. Bartlett*[1]*

[1] Defence Science and Technology Laboratory, Salisbury, United Kingdom, [2] University of Southampton, Southampton, United Kingdom, [3] Department for Transport, Great Minster House, London, United Kingdom, [4] Chemistry Research Laboratory, University of Oxford, Oxford, United Kingdom

A novel electrochemical detection approach using DNA probes labeled with Anthraquinone (AQ) as a reporter moiety has been successfully exploited as a method for the direct detection of DNA targets. This assay uses simple voltammetry techniques (Differential Pulse Voltammetry) to exploit the unique responsiveness of AQ to its chemical environments within oxygenated aqueous buffers, providing a specific detection mechanism as a result of DNA hybridization. This measurement is based on a cathodic shift of the reduction potential of the AQ tag and the concurrent reduction in peak current upon DNA binding. The further utility of this approach for discrimination of closely related DNA targets is demonstrated using DNA strands specific to *B. anthracis* and closely related bacillus species. DNA targets were designed to the *rpo*B gene incorporating nucleotide polymorphisms associated with different bacillus species. This assay was used to demonstrate that the shift in reduction potential is directly related to the homology of the target DNA. The discriminatory mechanism is dependent on the presence of oxygen in the measurement buffer and is strongly linked to the position of the nucleotide polymorphisms; with homology at the terminus carrying the AQ functionalised nucleotide critical to achieving accurate discrimination. This understanding of assay design was used to demonstrate an optimized assay capable of discriminating between *Yersinia pestis* (the causative agent of plague) and closely related species based on the *gro*EL gene. This method is attractive as it can not only detect DNA binding, but can also discriminate between multiple Single Nucleotide Polymorphisms (SNPs) within that DNA without the need for any additional reagents, reporters, or processes such as melting of DNA strands. This indicates that this approach may have great potential to be exploited within novel biosensors for detection and diagnosis of infectious disease in future Point of Care (PoC) devices.

Keywords: DNA hybridization, redox reporter, anthraquinone, nucleotide polymorphisms, diagnostics, environmental surveillance

OPEN ACCESS

Edited by:
James Tucker,
University of Birmingham,
United Kingdom

Reviewed by:
Qiuyu Gong,
Independent Researcher, Singapore, Singapore
Marcel Hollenstein,
Institut Pasteur, France

***Correspondence:**
Sarah A. Goodchild
sagoodchild@dstl.gov.uk
Philip N. Bartlett
P.N.Bartlett@soton.ac.uk

Specialty section:
This article was submitted to Supramolecular Chemistry, a section of the journal Frontiers in Chemistry

Received: *08 November 2019*
Accepted: *14 April 2020*
Published: *12 May 2020*

Citation:
Goodchild SA, Gao R, Shenton DP, McIntosh AJS, Brown T and Bartlett PN (2020) Direct Detection and Discrimination of Nucleotide Polymorphisms Using Anthraquinone Labeled DNA Probes. Front. Chem. 8:381. doi: 10.3389/fchem.2020.00381

INTRODUCTION

Technologies capable of providing rapid, agile detection and identification of a range of infectious organisms are desirable to support the development of Point of Care (PoC) devices. Detection of nucleic acids from organisms of interest using DNA amplification techniques such as Polymerase Chain Reaction (PCR) is an established and mature approach for identification of bacterial species

of interest (Rachwal et al., 2012; Weller et al., 2012, 2016). A wide variety of platforms exist for DNA amplification and detection, and highly integrated technologies (including direct sample to answer) technologies e.g., FilmArray can provide a robust and sensitive capability for screening panels of agents (Poritz et al., 2011). Current PCR technologies have developed to a point where they are well-accepted as a standard tool in clinical laboratories. However, the breadth of information that is generated by current PCR platforms remains limited by the requirement to design specific assays for each agent. Therefore, the capability to screen large panels of organisms requires a large number of assays or the ability to take a multiplexed approach, at the increasing cost of reagents, throughput, and time. Further limitations of PCR platforms lie in the inability to provide detailed species/strain level information in cases where pathogenic and non-pathogenic species of organisms are highly similar in DNA sequence and cannot be discriminated based on PCR amplification alone. This type of information can be provided by rapidly developing sequencing technologies (Dijk et al., 2018; Chiu and Miller, 2019), but the exploitation of these platforms in routine clinical diagnostics is currently challenged by the sample preparation and computational burdens that are challenging in clinical microbiology laboratories (Greninger and Greninger, 2018).

Lower burden options that provide a bridge between these two technology areas include DNA-hybridization based biosensors (Huyghe et al., 2009). Simple DNA hybridization techniques can be coupled to generic PCR amplification of genetic markers conserved across multiple microbial species, such as 16s RNA or *rpo*B, to provide breadth of assay coverage to panels of organisms of interest while including key Nucleotide Polymorphisms that can be mapped back to specific organisms (Wang et al., 2002; Adékambi et al., 2009; Klindworth et al., 2013). This amplification step is then followed by the determination of the homology of the DNA to specific sequences through hybridization to probes within a biosensor to provide identification of the causative pathogen. DNA hybridization can be detected using a range of approaches, including a number of optical techniques such as colorimetric, fluorescent, luminescent, and Raman spectroscopy (Järvinen et al., 2009; Tomlinson et al., 2014; Papadopoulou et al., 2015; Stulz, 2015; Boynton et al., 2017; Nano et al., 2017; Duprey et al., 2018).

Alternatively, electrochemical techniques, which convert a biological recognition event into a digital electrical signal, have also been widely demonstrated for the detection of DNA hybridization. Electrochemical techniques have particular advantages, including the low cost and portability of the associated measurement platforms and can be readily incorporated into devices to produce inexpensive, sensitive, and accurate instruments for diagnostic applications (Blair and Corrigan, 2019; Yáñez-Sedeño et al., 2019). As a consequence, development of novel electrochemically driven approaches for DNA hybridization remains an area of widespread focus for the development of diagnostic devices and *in-situ* environmental detection of clinically important or hazardous microorganisms.

Electrochemically-linked DNA hybridization assays most commonly employ single stranded hybridization probes of DNA or synthetic nucleic acid analogs such as Peptide Nucleic Acid (PNA), which are then immobilized on an electrode or other conductive substrate. The binding of DNA target molecules to these probes can then be measured using a variety of techniques [extensively reviewed in (Gorodetsky et al., 2008; Kang et al., 2009; Hvastkovs and Buttry, 2010; Tosar et al., 2010; Liu et al., 2012; Sontz et al., 2012; Ferapontova, 2018)]. Binding of complementary strands of DNA can act as a barrier to the movement of dissolved electrochemically active species as indirect measurements of DNA binding through the use of techniques such as Electrochemical Impedance Spectroscopy. Alternatively, the formation of a double stranded DNA complex can be reported by exploiting the ability of some metallo or organic intercalators (such as methylene blue, ruthenium, or derivatives of quinone and ferrocene), to bind differentially to single-stranded or double-stranded DNA thus allowing hybridization to be quantified. DNA probes may also be modified by covalent incorporation of electroactive reporters. Careful placement of the electroactive moiety within the DNA structure can then be used to detect not only DNA hybridization, but also the presence of mismatches within that DNA. This could be based on electron transfer through the DNA, or retardation of the flexibility of that DNA probe, impeding transfer of electrons to the electrode surface (Inouye et al., 2005; Pheeney and Barton, 2013; Zwang et al., 2018; Dauphin-ducharme et al., 2019).

DNA hybridization assays using anthraquinone (AQ) as the electroactive reporter are well-described in the literature. AQ is able to act as a selective intercalator into double stranded DNA (Mcknight et al., 2004; Gholivand et al., 2012). As such addition of aqueous soluble derivatives such as anthraquinonemonosulfonic acid (AQMS) has been extensively studied as a reporter for DNA duplex formation demonstrating the ability to discriminate between fully complementary DNA and DNA targets harboring nucleotide polymorphisms (Wong and Gooding, 2006; Batchelor-McAuley et al., 2010; Kowalczyk et al., 2010; Salvatore et al., 2013; Lin et al., 2016). A number of methods for covalently integrating nucleotides modified with AQ groups into DNA probes have also been developed (Yamana et al., 1996; Whittemore et al., 1999; Connors et al., 2003; Narayanan et al., 2004; Orino et al., 2005; Zhao et al., 2007; Abou-Elkhair et al., 2009; Ben Gaied et al., 2009; Balintová et al., 2011). DNA probes carrying these modifications at 3′ and 5′ termini, and within the DNA strand, have been demonstrated to be capable of specific and selective detection of DNA hybridization and discrimination of nucleotide polymorphisms (Yamana et al., 1996, 2001, 2003; Whittemore et al., 1999; Orino et al., 2005; Kumamoto et al., 2008; Balintová et al., 2011; Pheeney and Barton, 2013; Kongpeth et al., 2016).

While AQ is an attractive electrochemical reporter, it has proven less popular than others, such as methylene blue. One of the reasons for this is that the redox potentials of AQ can be influenced by its environment particularly the presence of protons and thus is heavily influenced by pH (Batchelor-McAuley et al., 2010; Guin et al., 2011). In addition, the interaction of quinones with cationic species is well-researched by supramolecular chemists, where host-guest interactions of cations with quinone ionophore groups affecting redox potentials

have been exploited in chemical sensing applications (Beer et al., 1994, 1999; Choi et al., 1995). As such, cationic species can have impact on the redox potentials of AQ in aqueous buffers (Li et al., 2011). Furthermore, AQ is able to self-mediate oxygen reduction in oxygenated buffers generating a catalytic reduction peak in electrochemical experiments in the presence of dissolved oxygen (Armitage et al., 1994; Li et al., 2011). Hence the majority of DNA hybridization assays using AQ require use of deoxygenated buffers (Whittemore et al., 1999; Yamana et al., 2001; Wong and Gooding, 2006; Kumamoto et al., 2008; Balintová et al., 2011; Pheeney and Barton, 2013; Salvatore et al., 2013; Lin et al., 2016). This requirement to remove background oxygen limits the easy exploitation of AQ in simple PoC devices. In addition, their discriminatory capabilities are limited to single nucleotide polymorphisms, reducing their exploitation potential for multiple closely related organisms (Kumamoto et al., 2008; Pheeney and Barton, 2013).

When dissolved oxygen is present in the buffer solution analysis is limited to the AQ reduction peak, due to the innate oxygen reduction properties of AQ. Previous studies have demonstrated that the reduction peak is affected by DNA hybridization to non-immobilized PNA probes with a covalently linked AQ reporter or as a intercalator to immobilized DNA probes resulting in reduction of peak current upon DNA hybridization (Kowalczyk et al., 2010; Kongpeth et al., 2016). This effect has not however been studied in surface immobilized DNA probes covalently labeled with AQ and warrants further investigation. In this study we therefore utilize immobilized DNA probes with covalent AQ reporters and demonstrate that this catalytic self-oxidation mechanism can be used as a simple direct reporter of DNA hybridization. We further demonstrate that this innate functionality of AQ is able to facilitate discrimination between multiple nucleotide polymorphisms within the target DNA offering a new simple approach for discriminating multiple species within a single, simple assay.

MATERIALS AND METHODS

All chemicals were sourced and used without further purification from Sigma Aldrich (UK) unless otherwise stated. All solutions were prepared using ultrapure Milli-Q water (18 MΩ cm^{-1}) according to concentrations stated. All AQ-modified DNA probes were synthesized by ATD Bio, Southampton, UK. Each probe included a 5′ three dithiol immobilization tag and a hexaethylene glycol (HEG) spacer between the thiol groups and the DNA sequence (Mahajan et al., 2008). An anthraquinone moiety was attached to the 3′ terminus, which would be distal to the electrode surface according to previously published methods (Zhao et al., 2007; Mahajan et al., 2009). Target DNA (24 bp) specific to each chosen species was synthesized by Sigma Genosys using standard methods.

Design of DNA Probes and Target DNA for the *rpo*B Gene of *Bacillus* Species

DNA sequences for the *rpo*B gene were taken from *Bacillus anthracis* Ames (accession number NC_003997.3), *Bacillus cereus* AH187 (NC_011658.1), *B. cereus* B4264 (NC_011725.1), *Bacillus thuringiensis* Al Hakam (NC_008600.1), and *Bacillus weihenstephanensis* KBAB4 (NC_010184.1). Alignments of the *rpo*B genes were performed (Clustal W) to identify areas of variability. A 24 base pair (bp) region of *rpo*B was selected between positions 1,061 and 1,085 (referenced to the *B. anthracis* genome) of the *rpo*B gene. This region was used for the design of probes BA-1, which was fully homologous with *B. anthracis* but contained between 1 and 7 bp mismatch with the other bacillus species (**Table 1**).

TABLE 1 | Sequences of anthraquinone modified DNA probes and target DNA for the *rpo*B gene target of Bacillus species.

DNA PROBES	
BA-1	XXX-HEG-5′-ACATTAATTACGCGCTCGCCTTCT-3′-AQ
BA-2	XXX-HEG-5′-ACATTAATTACGCGCTCGCCTTCG-3′-AQ
TARGET DNA	
B. anthracis; BA	5′-AGAAGGCGAGCGCGTAATTAATGT-3′
B. cereus AH187; BC1	5′-AGAAGGCGAGCGCGTAATTAA**C**GT-3′
B. cereus B4264; BC2	5′-AGAAGGCGA**A**CG**T**GTAATTAATGT-3′
B. thuringiensis Al Hakam; BC3	5′-**G**GAAGGCGA**A**CGCGTAATTAATGT-3′
B. weihenstephanensis; BWK	5′-AGAAGGCGA**A**CG**ATCT**AT**A**AA**C**GT-3′
ALL-BC	5′-**G**GAAGGCGA**A**CG**T**GTAATTAA**C**GT-3′
3′Terminus	5′-GGAAGGCGAGCGCGTAATTAATGT-3′
NA	5′-**T**GAA**AT**C**ACTTAGCT**T**CGCGTC**GT-3′

Underlined bases in target DNA sequences denote mismatches to probe BA-1. XXX indicates three dithiol linker and HEG is hexaethylene glycol.

Design of DNA Probes and Target DNA for the *groEL* Gene of *Yersinia* Species

DNA probes (24 bp) for the *gro*EL gene of *Yersinia pestis* were designed to be fully complementary to the genome sequence of *Y. pestis* Nepal516 (accession number gb_CP000305.1). Homologous regions containing nucleotide polymorphisms within these regions were selected from the genomes of the related bacterial species *Y. pseudotuberculosis* (gb_CP000950.1) and *Y. enterocolitica* (emb_AM286415.1) based on previously published work (Papadopoulou et al., 2015). Sequences of probes and target DNA used for each of the *gro*EL (YP1) assays shown in **Table 2**.

Preparation of DNA Functionalised Electrode Surfaces

Two millimeter diameter gold electrodes (CH Instruments) were mechanically polished using a polishing pad (Buehler) and sequential polishing using alumina powder of 0.3 μm then 0.05 μm followed by polishing with a bare polishing pad. In between each polishing stage, electrodes were cleaned by sonication in ultrapure (Milli-Q) water for 10 min. After the mechanical polishing was completed each electrode was further electrochemically cleaned by cycling in 0.5 M H_2SO_4 between

TABLE 2 | Sequences of anthraquinone modified DNA probe and target DNA for the *gro*EL gene target of *Y. pestis*.

DNA PROBE	
YP1	XXX-HEG-5′-GTACCGTCACCCGCAGCATCATTT-3′-AQ
TARGET DNA	
Y. pestis	5′-AAATGATGCTGCGGGTGACGGTAC-3′
Y. pseudotuberculosis	5′-**G**AATGA**C**GCTGCGGGTGACGGTAC-3′
Y. enterolytica	5′-**G**AA**C**GA**C**GCTGCGGGTGACGGTAC-3′

Underlined bases in target DNA sequences denote mismatches to probe YP. XXX indicates three dithiol linker and HEG is hexaethylene glycol.

−0.1 and 1.5 V vs. Saturated Calomel Electrode (SCE) for 60 cycles at 50 mV s^{-1}. Immediately after cleaning, electrodes were washed in ultrapure (Milli-Q) water, dried then soaked in probe solutions at a concentration of 1 μM in 10 mM Tris HCl buffer pH 7.5 containing 0.5 M NaCl for 16 h. The electrode surfaces were washed in buffer to remove excess DNA, then soaked in 1 mM mercaptohexanol in 10 mM Tris HCl buffer pH 7.5 containing 0.5 M NaCl for a further 2 h to ensure a passivated surface and a good presentation of the DNA probe in an upright position (Lee et al., 2006). Electrodes were washed in buffer (10 mM Tris HCl pH 7.5 containing 0.5 M NaCl) prior to use. For each experiment, three replicate electrodes were used for each target DNA to ensure that results were consistent for each target DNA product.

Electrochemical Measurements

All electrochemical measurements were performed using an Autolab PGSTAT302N (Metrohm Ltd). Electrochemical measurements were performed using a standard three electrode cell using bulk gold working electrodes of 2 mm diameter, a saturated calomel (SCE) reference electrode [both from CHI instruments (IJ Cambria)] with a homemade platinum mesh counter electrode (Goodfellow, 0.25 mm wire with 20 × 20 mm mesh).

Quantification of DNA Immobilized on Electrode Surfaces

The typical immobilization density achieved using probes BA-1 and BA-2 was calculated using the chronocoulometry method of Steel et al. (1998). Initially Q_{dl} for DNA functionalised surfaces in buffer containing no $[Ru(NH_3)_6]^{3+}$ was determined using a 500 ms reductive pulse from an initial potential of −0.1 V (equilibrated for 60 s) to −0.4 V in 10 mM Tris HCl buffer pH 7.5. $[Ru(NH_3)_6]^{3+}$ was then added to the buffer to a final concentration of 50 μM and allowed to equilibrate to the DNA for 10 min. The charge resulting from the presence of the $[Ru(NH_3)_6]^{3+}$ was then determined using the same chronoamperometry cycle and used to solve the integrated Cottrell equation (Equation 1; where Q is total charge, t is the time, n is the number of electrons transferred, F is the Faraday constant, A is the area of the electrode, D_o is diffusion coefficient and C_o^* the bulk concentration of $[Ru(NH_3)_6]^{3+}$ Q_{dl} is the double layer charge, and Γ_0 is the surface coverage of bound $[Ru(NH_3)_6]^{3+}$).

$$Q = \frac{2nFAD_o^{1/2}C_o^*}{\pi^{1/2}}t^{1/2} + Q_{dl} + nFA\Gamma_0 \quad (1)$$

A plot of Q relative to time for each electrode in the presence or absence of $[Ru(NH_3)_6]^{3+}$ was used to calculate the quantity of cation constrained at the electrode surface. This was used to calculate the quantity of immobilized DNA using Equation 2 where Γ_{DNA} is the probe surface density in molecules/cm^2, m is the number of bases in the probe DNA, z is the charge of the redox molecule, and N_A is Avogadro's number.

$$\Gamma_{DNA} = \Gamma_0 \left(\frac{z}{m}\right) N_A \quad (2)$$

All buffers were purged for at least 30 min with argon prior to use and all experiments were conducted under a blanket of argon. Electrodes were allowed to equilibrate for 10 min under argon purging after the addition of $[Ru(NH_3)_6]^{3+}$.

Direct Measurement of DNA Hybridisation on Anthraquinone Labeled DNA Probes

Electrodes functionalised with DNA were placed in 10 mM Tris HCl pH 8.0 containing 0.5 M NaCl. This buffer was used for the majority of DNA hybridization experiments with the exception of those to investigate the impact of pH on the electrochemical characteristics of the anthraquinone tag where Tris buffers of pH 9.0 and pH 7.0 were also used. In general, the electrochemical experiments were performed in the presence of oxygen. Where removal of oxygen was required, the measurement buffer was purged with argon for 30 min prior to performing any readings, and experiments were conducted under a blanket of argon.

Initial baseline measurements for each functionalised electrode were taken by Cyclic Voltammetry (CV) and Differential Pulse Voltammetry (DPV). CV experiments with probe BA-1 used a starting applied potential of −0.4 moving to −0.7 V at a scan rate of 50 mV s^{-1} (forward scan) followed by a reverse scan from −0.7 to −0.4 V at the same rate. Four repeats of the forward and reverse scans were performed in each measurement. For probe BA-2 the conditions used for CV were identical to BA-1 with the exception of a slightly more negative starting and finishing potential of −0.5 and −0.75 V respectively. For DPV, a starting applied potential of −0.4 V moving to −0.75 V at a scan rate of 50 mV s^{-1} was used throughout. After initial CV and DPV readings had been taken, target DNA was then added to each electrode at a concentration of 1 μM and incubated for 1 h at room temperature to allow hybridization to occur. Non-complementary DNA was added to additional probes as a negative control. CV and DPV measurements were then repeated to determine the effects of DNA hybridization.

Data Analysis

DPV scans were baseline subtracted using a polynomial multipoint fitting function (OriginPro 9.1, OriginLab, US). The position of the peak was then identified for each scan. The difference between the peak position before, and after,

hybridization of target DNA for each electrode was then calculated. Three replicate data points for each condition and for each target DNA on separate electrodes were combined for all *B. anthracis* assays to produce an average shift for each target DNA strand ($n = 3$). For assays using probe YP1 three replicate experiments each containing four replicate electrode surfaces were included ($n = 12$), 95% confidence intervals were calculated from the replicate data sets to show significant differences ($p \leq 0.05$).

RESULTS

Direct Detection of DNA Hybridisation Using AQ Modified DNA

DNA probe BA-1 was designed to be specific to a variable region of *B. anthracis rpo*B gene, overlapping SNPs known to exist in other closely related Bacillus species (**Table 1**). This probe was immobilized on the gold electrode surface via six thiol groups at the 5′ terminus with the 3′ anthraquinone positioned distal to the electrode surface (**Figure 1**). The density of the probe DNA was measured using chronocoulometry and determined to be 1.17 $\times$ 10^{12} (+/– 3.88 $\times$ 10^{10}) molecules cm^{-2} on average across three identical electrodes. This immobilization density achieved in high salt concentrations is of the level expected for this type of probe based on previous published reports using the same immobilization methods (Mahajan et al., 2008, 2009).

The electrochemical characteristics of the anthraquinone functionalized DNA probe BA-1 were subsequently measured using CV. This analysis was undertaken after purging the measurement buffer with argon for 30 min to remove oxygen and also in the presence of ambient concentrations of dissolved oxygen. Clear differences were observed between CVs taken from the same electrode in the presence and absence of oxygen in the solution (**Figure 2**). In the absence of oxygen, both the oxidation and reduction peaks of the AQ tag, are visible on the CV (**Figure 2A**). This result provides confirmation that DNA has bound to the electrode surface and that the AQ moiety has remained electrochemically functional. The positions of the oxidation and reduction peaks are also broadly in line with observed potentials from comparable AQ labeled probes being slightly higher than that observed with attachment of AQ to surfaces by self-assembled monolayer (SAM) based immobilization (Nagata et al., 2008) and similar to that observed by other AQ bearing DNA strands using internal and terminal labeling (Yamana et al., 2001; Kumamoto et al., 2008; Pheeney and Barton, 2013).

Conversely when the same electrode was examined in the presence of oxygen (**Figure 2B**), a change in shape of the CV was clearly observed. In the presence of oxygen a large reduction peak is obvious, but the oxidation peak is missing. This is due to the oxygen reduction capabilities of AQ in oxygenated buffers resulting in a catalytic reduction peak ∼10 fold higher than that observed in conditions containing no oxygen. This peak was observed again on the reverse scan suggesting that some structural reorganization of the flexible single stranded DNA probe occurs upon reduction of the AQ tag. Since the AQ tag showed a clear electrochemical response in CV experiments further work was undertaken to understand the impact of the binding of the complementary strand of DNA on the AQ tag.

Fully complementary 24 bp DNA (BA; **Table 1**) was then allowed to hybridize to DNA probes. Repeat measurements of the CV for the AQ were then taken to understand the impact of the binding event on the electrochemical signature. DPV was also used to interrogate impact of binding specifically on the reduction process of the AQ moiety (**Figure 3**). The signal from the AQ probe in deoxygenated buffer after hybridization is similar to the pre-hybridization signal. Little effect is observed when comparing CVs measured either before or after DNA hybridization (**Figure 3A**). When using DPV a slight reduction in the current produced was observed (**Figure 3B**) and is consistent with published data (Whittemore et al., 1999; Yamana et al., 2001; Kumamoto et al., 2008; Balintová et al., 2011; Pheeney and Barton, 2013). Conversely, with oxygen present in the electrolyte, hybridization of the complementary DNA strand resulted in a large shift in the position of the reduction peak. This shift (53 mV) was clearly observed in both the CV and the DPV (**Figures 3C,D**, respectively). This was consistently correlated with a drop in the peak current observed (reduction in peak amplitude) observed in the DPV. This is consistent with the signatures observed by Kongpeth et al., when using PNA-AQ functionalised probes in solution (Kongpeth et al., 2016). The CV also showed the appearance of a minor oxidation peak, which was not present prior to hybridization. The combination of these characteristics indicate that the hybridization of the DNA at the probe surface impedes the self-oxidation of AQ and thus slows the electron transfer kinetics of this process which can be observed using these simple electrochemical methods. This exploitation of the native self-oxidation characteristics of AQ offers a new simple methodology. As such, all subsequent measurements using the AQ probes were performed in the presence of dissolved oxygen to target this novel method of detecting DNA/DNA hybridization events. In addition, DPV was used as the simplest measurement technique focusing in on the reduction peak of the AQ probe, exploring effects of DNA hybridization on current output, and peak position.

The involvement of two protons per full electrochemical cycle of the AQ group (**Figure 1**) means that the pH of the measurement buffer will have a substantial impact on the electrochemistry of the AQ tag. It was therefore considered pertinent to define the impact pH had on the detection of DNA hybridization. DPV analysis of BA-1 was undertaken at pH 7, 8, and 9. Measurements were taken before and after DNA hybridization and the resulting drop in current and reduction potentials compared under each condition (**Figure 4**). This analysis demonstrated that the presence of excess protons at lower pHs results in a more positive initial redox potential, as well as lowest initial current output. After hybridization of the target DNA, two peaks are observed from the AQ probe at pH 7. The negative shift associated with one of these peaks is extremely large (90.9 mV +/– 0.66 mV) but the presence of an additional peak is a confounding factor in assay output. The reason for two separate peaks has not been further investigated in this work, but was consistently observed at lower pH using

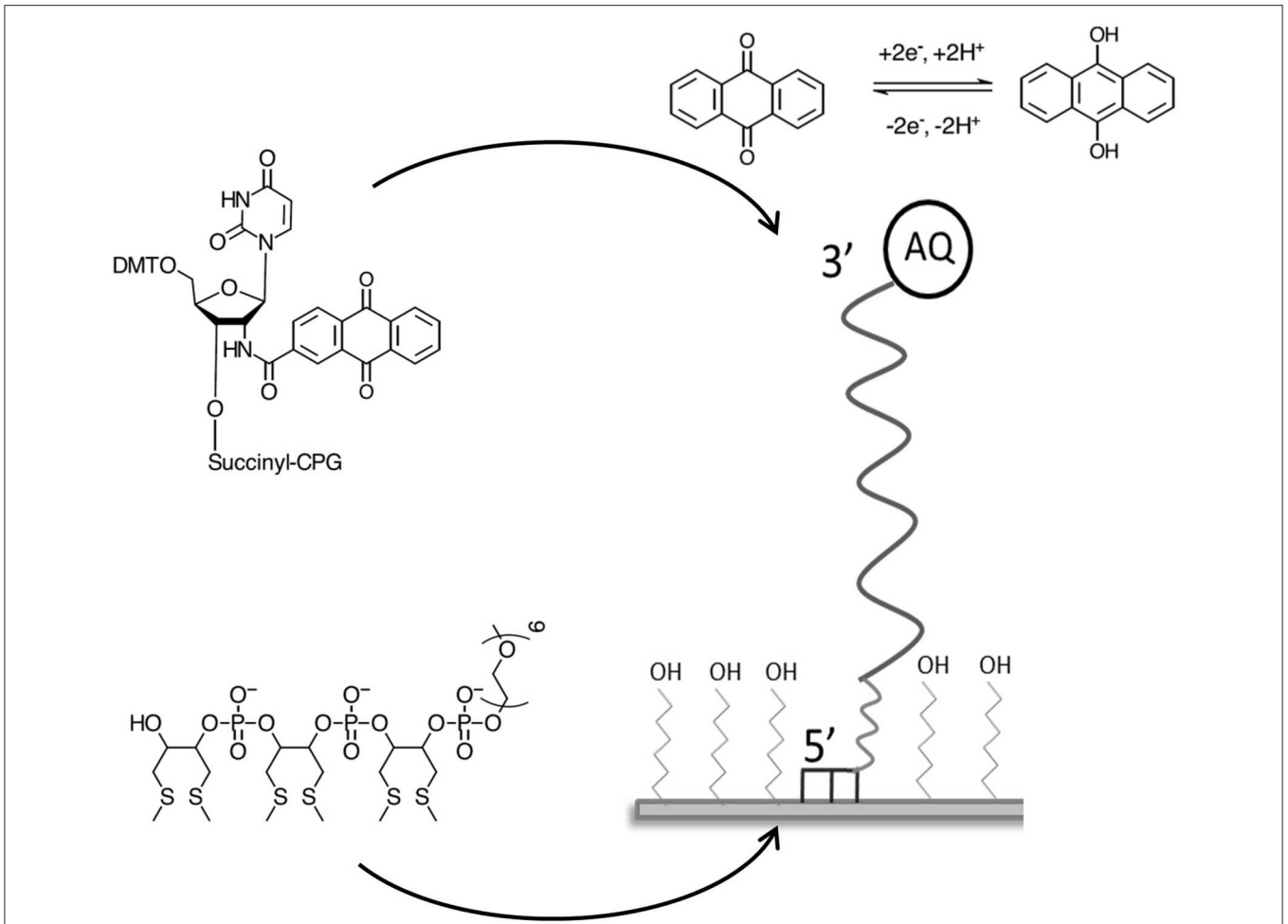

FIGURE 1 | Schematic illustrating the design and format of the AQ DNA hybridization sensor.

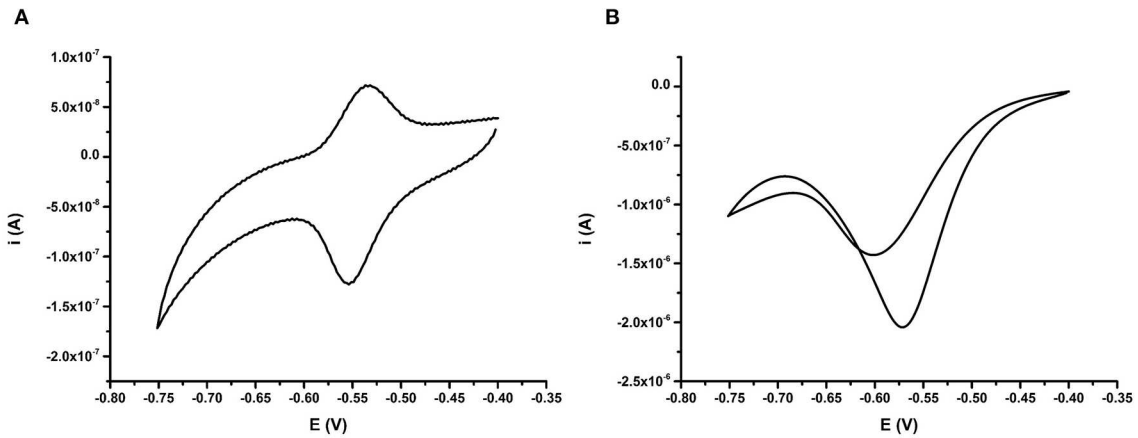

FIGURE 2 | (A) Behavior of AQ probe BA-1 deoxygenated (oxygen purged) conditions achieved by purging the electrolyte with argon for 30 min, and **(B)** oxygenated (oxygen present) conditions. Electrochemical scans are representative of $n = 3$ repeat electrodes, and were performed at 50 mV s^{-1} vs. SCE.

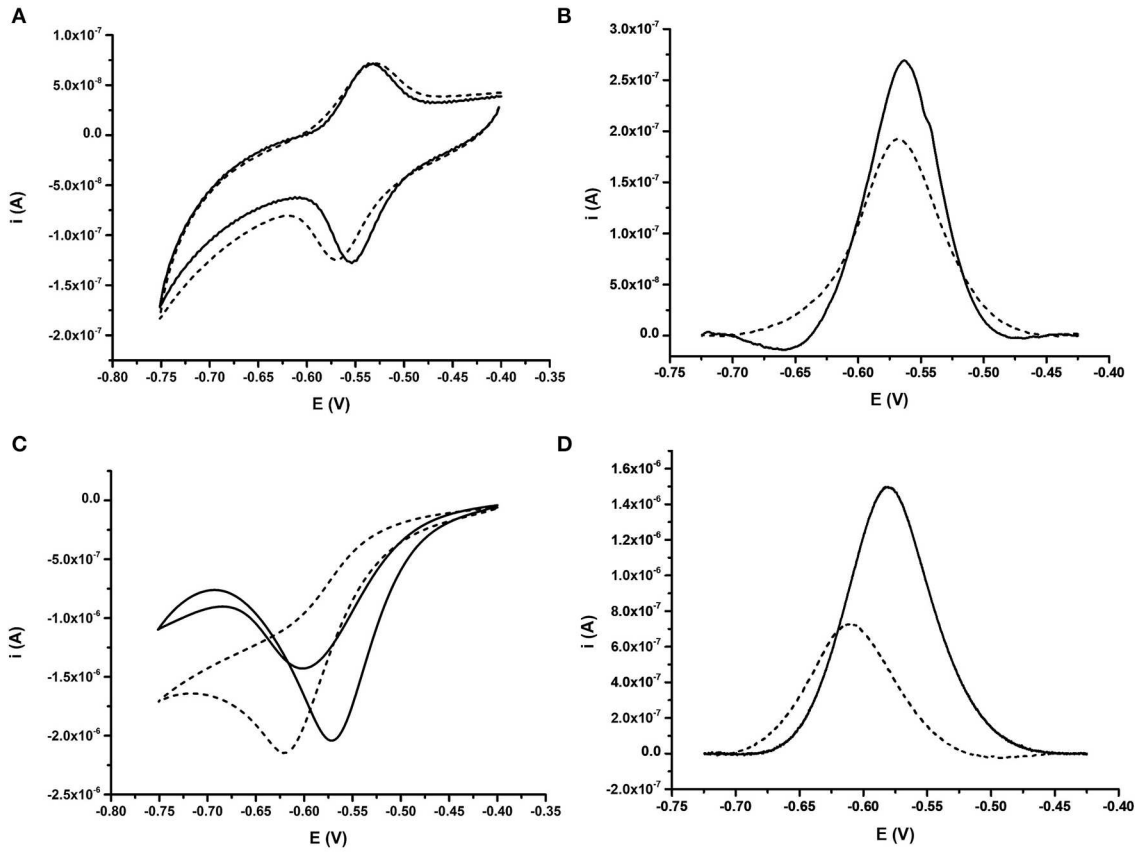

FIGURE 3 | Comparative behavior of probe BA-1 in response to fully complementary DNA under oxygenated and deoxygenated conditions. **(A)** CV and **(B)** DPV for probe under deoxygenated conditions; achieved by purging the electrolyte (10 mM Tris pH 8.0 containing 0.5 M NaCl) with argon for 30 min prior to analysis. **(C)** CV and **(D)** DPV for probe in buffer containing oxygen. In each case the signal from the ssDNA probe modified with AQ is shown as a solid line while the response after hybridization of fully complementary DNA is shown with a dashed line. The response of the same electrode under all conditions is shown. Electrochemical scans were performed at 50 mV s^{-1} vs. SCE.

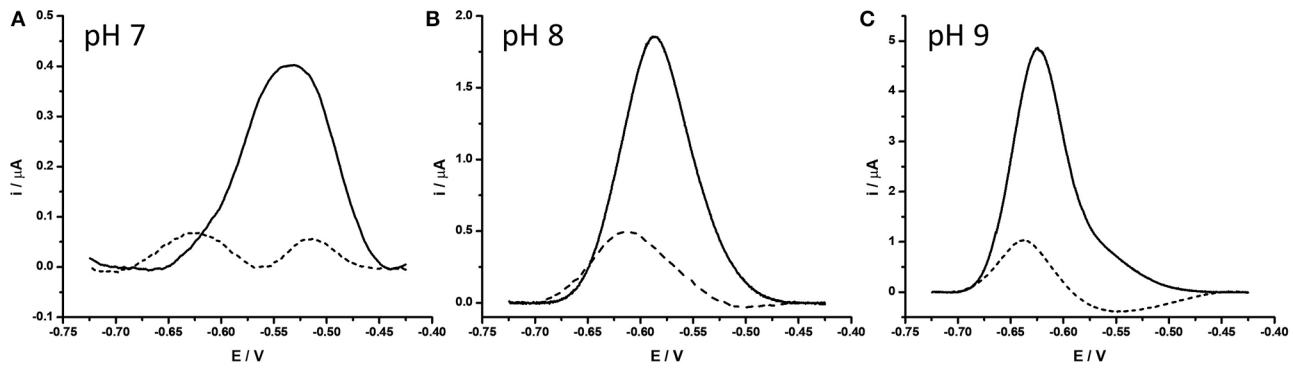

ΔE	90.9 mV (+/- 0.66 mV)
Δi	0.332 µA (+/- 0.102 µA)

ΔE	28.38 mV (+/- 1.7 mV)
Δi	1.22 µA (+/- 0.1 µA)

ΔE	14.3 mV (+/- 0.7 mV)
Δi	3.86 µA (+/- 0.65 µA)

FIGURE 4 | Effect of complementary DNA binding to probe BA-1 at **(A)** pH 7, **(B)** pH 8, **(C)** pH 9. In each case, AQ labeled probe BA-1 was measured as single stranded DNA using DPV (scan −0.4 V to −0.75 V; 50 mV s^{-1} vs. SCE) under oxygenated conditions in measurement buffer 10 mM Tris pH 8, containing 0.5 M NaCl (solid line) prior to hybridization to fully complementary DNA (dashed line). The response of the same electrode under all conditions is shown and is representative of the three electrodes tested under the same conditions.

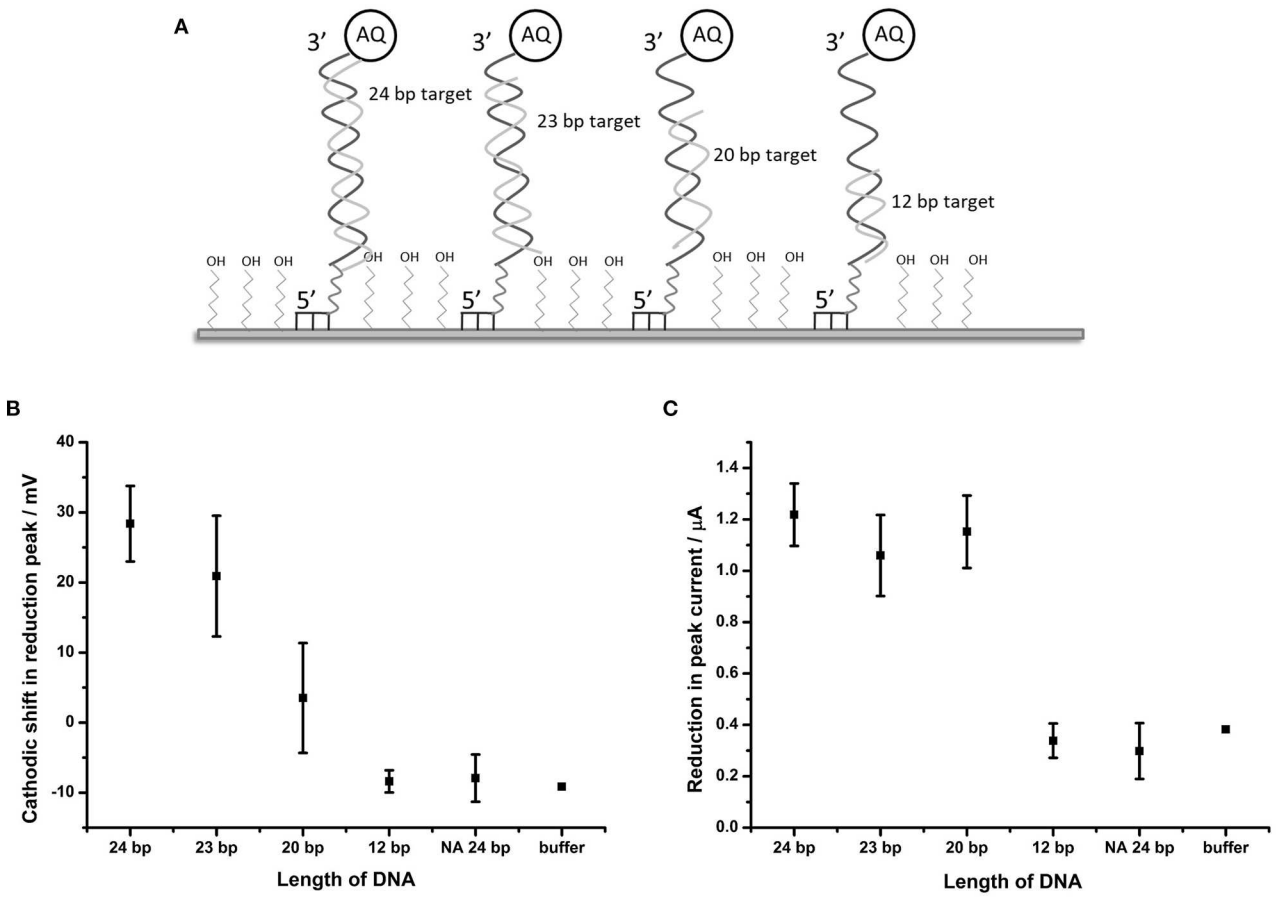

FIGURE 5 | Distance dependent effects of binding complementary DNA to probe BA-1. **(A)** Schematic description of the experimental design showing the position of binding of the shortened DNA strands in relation to the AQ tag. **(B)** Plot showing shift in the potential of the reduction peak and **(C)** plot of the change in peak current in response to hybridization of complementary DNA of different lengths. Points represent an average of the responses shown by three replicate electrodes (error bars indicate 95% confidence limits).

AQ labeled probes. We hypothesize this effect to be due to position effects of the DNA relative to the electrode surface at lower pH, which may be more complex in proton rich conditions that offset the natural negative charge of the DNA probe strands and could lead to secondary structures forming within the DNA probe, or less efficient binding of the target DNA to the high density DNA probes at neutral pH (Zhang et al., 2012). At pH 8 this complex effect is removed with a consistent single peak before and after DNA hybridization (28.4 mV +/– 1.7 mV, in this assay system). Current drop was also consistently observed as previously demonstrated.

At pH 9 the initial peak position was the most negative of the three conditions and had the highest current output (x10 relative to that at pH 7). After DNA binding occurred the current drop associated with the binding event was clearly observed, but the shift in position of the reduction peak was minimal (14.3 mV +/– 0.7 mV) reducing the dynamic nature of the signals observed. On the basis of this investigation the decision was taken to perform all future experiments at pH 8, as this condition demonstrated the best balance of current drop, and reduction potential shift.

Distance Dependence of Binding Event Relative to Current Drop and Reduction Potential Shift

It was considered likely that the effect on the catalytic self-oxidation of the AQ tag would be distance-related i.e. will be reliant on a close interaction of the hybridizing DNA strand to the AQ tag, resulting in occlusion of the AQ tag from oxygenated solvent. To further investigate this hypothesis, DNA targets of 23, 20, and 12 bp were synthesized (these were identical in sequence to BA target DNA described in **Table 1**, but truncated at the 5′ terminus). Use of these targets would result in complexes where the top of the hybridized strand would be 1, 4, and 12 bp distant from the AQ tag, respectively (**Figure 5A**).

DPV measurements from BA-1 probe were made in oxygenated buffer before and after hybridization of the target

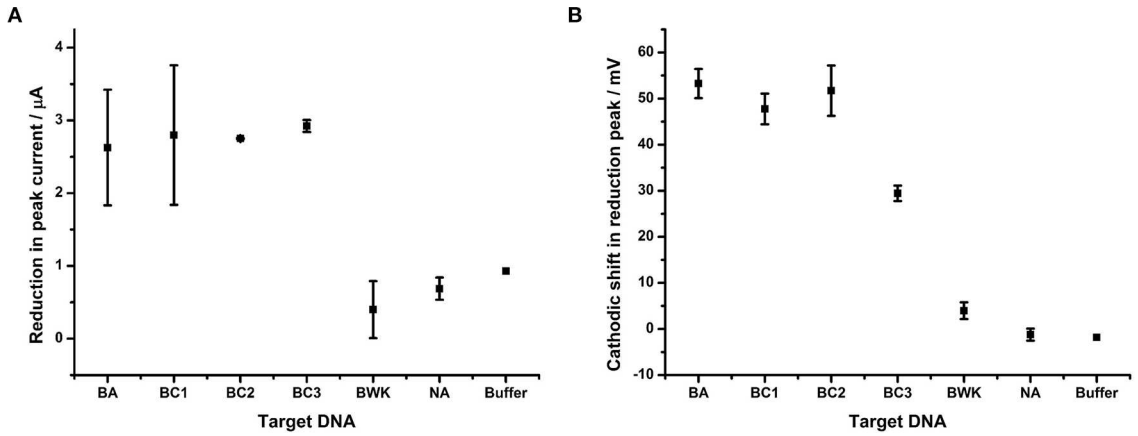

FIGURE 6 | Impact of DNA hybridization on peak current under oxygenated conditions in comparison to reduction peak shift. Probe BA-1 was hybridized to 24 bp DNA strands that were either fully complementary (BA) or contained 1 (BC1), 2 (BC3, BC2), 7 (BWK) nucleotide changes respectively. The response in terms of **(A)** showing reduction in peak current and **(B)** the shift in the potential of the reduction peak, respectively. All measurements were made by DPV (scan −0.4 V to −0.75 V; 50 mV s^{-1}) vs. SCE in 10 mM Tris buffer pH 8, 0.5 M NaCl. Points represent an average of the responses shown by three replicate electrodes (error bars are 95% confidence limits from this mean).

DNA strands. The peak shift and current drop observed after hybridization of each of the probes ($n = 3$) were measured (**Figures 5B,C**). The maximum shift (28.4 mV) in the reduction peak was observed for a 24 base target which produces a fully double-stranded DNA molecule at the electrode. Smaller changes in the reduction peak were observed for DNA targets of shorter length (19.3 and 5.2 mV for the 23 and 20 bp targets, respectively), which move the proximity of the double stranded DNA away from the AQ tag. A DNA target of 12 bases has no effect on the reduction peak of AQ. A binary response was seen with respect to the peak current (observable as peak height) upon binding DNA targets of different lengths. Targets of 20 bases and longer caused a reduction in peak height of around 1.1 μA, but 12 base targets had the same effect as an entirely non-complementary (i.e., non-binding) 24 bp target or buffer control.

This data suggests that the electron transfer between the electrode and AQ tag is indeed obstructed by the adjacent formation of the DNA double strand. This effect is reduced as the formation of the double strand is withdrawn from the AQ tag. The observations made in this experiment suggest that the electrochemical characteristics of the AQ tag are, as expected, heavily dependent on its environment, specifically in its relationship to hybridized DNA.

Discrimination Between DNA Targets From Different Bacillus Species Using Probe BA-1

Having demonstrated robust detection of simple DNA hybridization events using an immobilized AQ functionalised probe, attempts were made to define whether the same process could be used to both detect and further discriminate between fully matched DNA sequences and those containing nucleotide polymorphisms. In order to investigate this relationship, an experiment was designed to evaluate the potential application of this methodology to the detection and discrimination of closely related Bacillus species, based on the differences in the conserved gene target *rpo*B.

The impact of hybridizing each of a series of closely related DNA sequences, given in **Table 1**, to the probe BA-1 on the reduction of the AQ tag was determined (**Figure 6**). This experiment demonstrated that peak current appears to be a binary detection signature of DNA binding; i.e., the binding of any target DNA affects the peak current to the same degree irrespective of target homology (**Figure 6A**). It therefore offers a useful corroborative measurement of overall DNA binding, but does not correlate with homology in this work.

The shift in reduction peak on hybridization of DNA targets does however differ depending on the homology of the target DNA (**Figure 6B**). DNA corresponding to BC1, from *B. cereus* AH187 (a single nucleotide change) demonstrates a 47.8 mV shift and BC2, from *B. cereus* B4264 (two nucleotide changes) also shows a 51.7 mV cathodic shift in reduction potential. Both of these are indistinguishable from that of *B. anthracis*, BA (53.3 mV, fully complementary). Conversely, hybridization with DNA target from *B. weihenstephanensis* (seven nucleotide changes) produced little effect on the reduction peak with only a 4.0 mV shift. Most interestingly however, hybridization with BC3, *B. thuringiensis*, which like BC2, has two nucleotide mismatches was significantly different from the fully complementary BA target, as the reduction peak is shifted by only 29.5 mV.

The difference in the reduction shift between BC2 and BC3 DNA targets, both of which have two nucleotide changes, presents the possibility that the position, or type of DNA mismatch, can affect the extent of the change in the reduction shift. This would be expected as terminal mismatches would be expected to lead to fraying of the DNA strands close to the AQ and thus have greater effect on solvent accessibility than internal

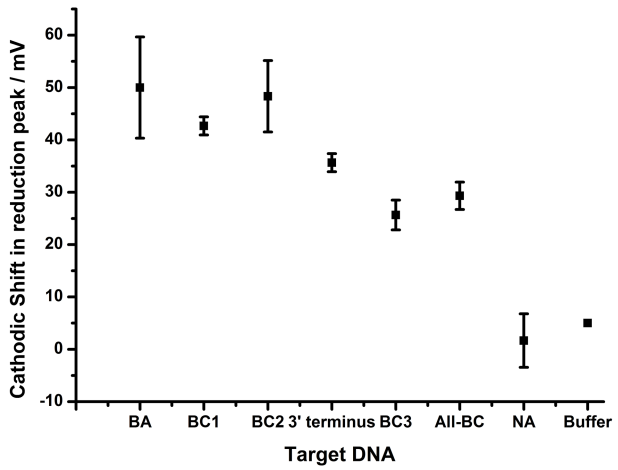

FIGURE 7 | Impact of terminal nucleotide on ability to distinguish base pair changes. Probe BA-1 was hybridized to target DNA that was fully homologous (BA) or contained 1 bp mutation toward the 5′ terminus of probe BA-1 (BC1), 2 bp mutations internal to the BA-1 probe (BC2), single base pair mutation at the 3′ terminus directly associated with the AQ tag (3′terminus), two bp mutations including AQ terminal bp (BC2), a combination of all BC mutations (4 bp mutations All-BC), in comparison to controls NA and buffer only. All measurements were made by DPV (scan −0.4 V to −0.75 V; 50 mV s^{-1}) vs. SCE in 10 mM Tris buffer pH 8 containing 0.5 M NaCl. Points represent an average of the responses shown by three replicate electrodes (error bars are 95% confidence limits from this mean).

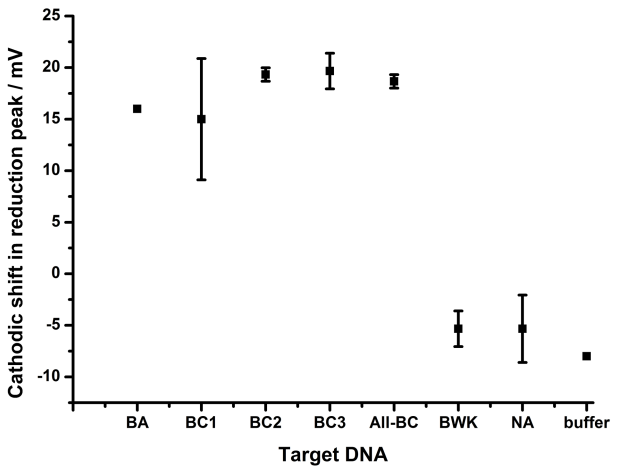

FIGURE 8 | The effect of DNA hybridization to probe BA-2. In each case the 3′ terminal nucleotide carrying the AQ tag is not homologous to any of the target DNA strands. In addition to the terminal mismatch, additional internal mutations were present within target DNA BC1, BC3 (1 bp), BC2 (2 bp), All-BC (3 bp), and BWK (7 bp). All measurements were made by DPV (scan −0.4 V to −0.75 V; 50 mV s^{-1}) vs. SCE in 10 mM Tris buffer pH 8 containing 0.5 M NaCl. Points represent an average of the responses shown by three replicate electrodes (error bars are 95% confidence limits from this mean).

mismatches. Further experiments were therefore designed in order to explore this hypothesis and a DNA target termed "3- terminus" containing a single terminal G:T mismatch at the 3′ end of the target DNA was therefore designed and hybridized to probe BA-1 (**Figure 7**).

The DPV data shows that the shift in the reduction peak for the AQ tag was reduced by 35.7 mV when the terminally mismatched DNA target was hybridized (3′-terminus), in comparison to 50.0 mV for the fully complementary target (BA). When a target containing a terminal mismatch plus one other in the DNA sequence (BC3) was analyzed, a shift in 25.7 mV was observed. This data indicates that the hybridization of DNA target with a single nucleotide change is distinguishable from a fully complementary target if that mismatch is adjacent to the AQ tag. Further nucleotide changes promoting mismatches elsewhere in the double stranded DNA were observed to have an additive effect. This result highlights the potential for this methodology in the robust detection of SNPs when assay design is constrained to include a terminal nucleotide mismatch.

The extent of the effect of the terminal mismatch on the electrochemical characteristics of the AQ tag was investigated through the use of an alternative probe, BA-2, which is identical to BA-1 with the exception of the 3′terminal nucleotide which is mismatched to all target DNA used in the previous experiments (**Figure 8**). This DNA probe deposits on gold electrodes with a similar density to BA-1 at 6.4 $\times$ 10^{11} molecules cm^{-2}. The data shows that hybridization of all targets produced a similar shift in the reduction peak of the AQ tag (15–20 mV) and that differentiation of the different targets is not observed. This suggests the nature of the terminal mismatch is critical to the mechanism which allows the differentiation of DNA targets observed in previous experiments.

Assay to Differentiate Between Yersinia Species

Based on the impact of mismatches on the performance of the AQ reporter assay for the *rpo*B target in Bacillus species, a set of design rules were established for assay optimization. Design criteria centered on inclusion of a terminal mismatch between probe and non-homologous targets. Furthermore, additional mismatches were clustered close to the AQ tag where they were expected to have greatest impact on the stability of the DNA complex and thus greatest discriminatory capability. These design rules were used to produce a further optimized assay designed to discriminate between closely related species of the *Yersinia* genus using the *gro*EL housekeeping gene (**Table 2**).

To evaluate the performance of the *gro*EL assay the YP-1 probe was hybridized to the surface of the gold electrodes as described above and hybridized to target DNA from *Y. pestis* (fully complementary), *Y. pseudotuberculosis* (two nucleotide mismatches), and *Y. enterolytica* (three nucleotide mismatches) (**Figure 9**). When the fully complementary DNA sequence from *Y. pestis* was applied to the electrode surface, a shift in the reduction potential of 55.8 mV +/− 2 mV was observed. This is consistent with that achieved in the Bacillus *rpo*B assay with fully complementary DNA. The extent of the shift is

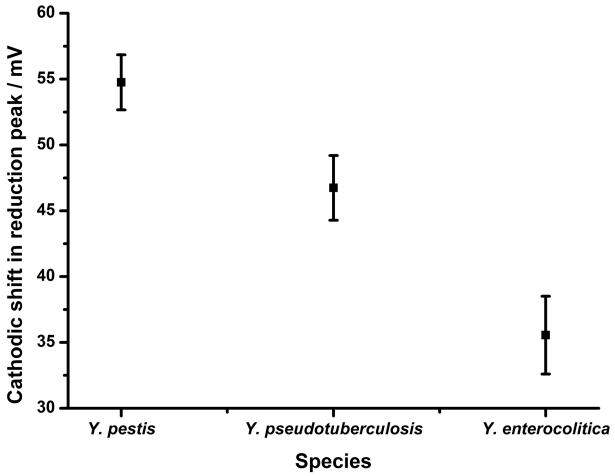

FIGURE 9 | Application of assay design to discriminate between *Yersinia* serovars. Probe YP1 was hybridized to 24 bp strands that were either fully complementary (*Y. pestis*) or containing 2 (*Y. pseudotuberculosis*) or 3 (*Y. enterocolitica*) nucleotide changes respectively. The response in terms of reduction potential shift is shown. All measurements were made by DPV (scan −0.4 V to −0.75 V: 50 mV s^{-1}) vs. SCE in 10 mM Tris buffer pH 8, 0.5 M NaCl. Points represent an average of the responses shown by 12 replicate electrodes across three independent experiments ($n = 4$ within each replicate) and error bars are 95% confidence limits.

reduced in line with the reducing complementarity of the DNA targets taken from *Y. pseudotuberculosis* (46.7 mV +/– 2.4 mV) and *Y. enterocolitica* (35.6 mV +/– 2.9 mV). This data suggest that the design rules established using the *B. anthracis* assay could be applied in this assay to discriminate between closely related DNA targets, as differentiation between Yersinia species is achieved depending on the extent of complementarity with the probe sequence. Furthermore, these results are highly reproducible, demonstrating the same response across replicates within the same experiment ($n = 4$) and across three separate experiments, implying this methodology is robust and reliable.

DISCUSSION

The native oxygen reduction of AQ in aqueous buffers has, to date, led to this tag proving a challenge to exploit as a reporter moiety in DNA hybridization assay requiring purging of electrolyte solutions to gather robust data (Whittemore et al., 1999; Yamana et al., 2001; Wong and Gooding, 2006; Kumamoto et al., 2008; Balintová et al., 2011; Pheeney and Barton, 2013; Salvatore et al., 2013; Lin et al., 2016). Recent reports have however indicated that AQ has the potential to be used as an electrochemical reporter moiety for DNA hybridization assays undertaken in oxygenated electrolytes (Kowalczyk et al., 2010; Kongpeth et al., 2016). The mechanism by which the AQ informs on DNA hybridization in oxygenated buffers, and how this could be applied to both detection and discrimination of nucleotide polymorphisms, has however not been fully investigated in surface immobilized DNA probes.

In this work we have characterized how the formation of DNA duplexes impacts on the electrochemical characteristics of an AQ tag in oxygenated buffers. The AQ tag used in this work is placed as a pendant to the terminus of the DNA probe, using a short linker and therefore is not designed to undergo π stacking into the DNA duplex (Liu and Barton, 2005; Gorodetsky et al., 2007; Pheeney and Barton, 2013). It is therefore unlikely that the signaling mechanism observed is based on electron tunneling through DNA strands. Instead, observations on the effects of DNA targets of different lengths, and the impact of terminal mismatches on AQ reduction potentials, indicates that DNA hybridization affects the innate oxygen reduction of AQ. Thus detection of DNA duplex formation is a combination of solvent occlusion of the AQ tag as a result of the presence of the complementary DNA strand, in addition to likely retardation of electron transfer from the AQ to the surface electrode as a result of the increased rigidity of the DNA duplex over the single stranded probe (Uzawa et al., 2010; Dauphin-ducharme et al., 2019). This mechanism has been demonstrated to be a robust and direct measurement of DNA hybridization.

A detailed study of the effect of terminal DNA mismatches and the additive effects of internal mismatches was undertaken using a model assay designed according to the *rpo*B gene from *B. anthracis*. These observations were used to establish design rules of how to exploit the AQ reporting mechanism to optimal effect. This enabled, bespoke design of an AQ detection assay capable of robustly distinguishing between *Y. pestis*, *Y. enterocolitica,* and *Y. pseudotuberculosis* using a single AQ labeled DNA probe.

This work has established that electrochemically based DNA probes carrying an AQ tag can be used as a sensor to provide highly discriminatory confirmation of binding events. Data indicates that the redox sensitivity of the AQ tag to its immediate environment can be exploited to provide high resolution information regarding the nature of DNA targets. This ability to discriminate between highly conserved DNA targets can be used to differentiate between closely related bacterial species, providing high confidence output to identify infectious agents of interest with the potential for onward development as a diagnostic technology. Further work will therefore be directed to understanding the performance of this method in terms of sensitivity and specificity against a broader range of targets. In addition, the application of this method to direct detection of DNA from complex sample types to include longer DNA targets produced by PCR assays will be undertaken. This will focus the development of novel technologies exploiting the methodologies identified here.

DATA AVAILABILITY STATEMENT

The raw data supporting the conclusions of this article will be made available by the authors, without undue reservation, to any qualified researcher.

AUTHOR CONTRIBUTIONS

SG and PB devised and designed the study. TB contributed to the DNA design aspects of the study. SG, DS, RG, and AM undertook experimental work. All authors contributed to writing and editing of the manuscript.

FUNDING

This work was funded by Dstl on behalf of the MoD including contract DSTLX1000061240 (University of Southampton). PB acknowledges receipt of a Royal Society Wolfson research merit award.

REFERENCES

Abou-Elkhair, R. A. I., Dixon, D. W., and Netzel, T. L. (2009). Synthesis and electrochemical evaluation of conjugates between 2'-deoxyadenosine and modified anthraquinone: probes for hole-transfer studies in DNA. *J. Org. Chem.* 74, 4712–4719. doi: 10.1021/jo900306g

Adékambi, T., Drancourt, M., and Raoult, D. (2009). The rpoB gene as a tool for clinical microbiologists. *Trends Microbiol.* 17, 37–45. doi: 10.1016/j.tim.2008.09.008

Armitage, B., Yu, C., Devadoss, C., and Schuster, G. B. (1994). Cationic anthraquinone derivatives as catalytic DNA photonucleases: mechanisms for DNA damage and quinone recycling. *J. Am. Chem. Soc.* 116, 9847–9859. doi: 10.1021/ja00101a005

Balintová, J., Pohl, R., Horáková, P., Vidláková, P., Havran, L., Fojta, M., et al. (2011). Anthraquinone as a redox label for DNA: synthesis, enzymatic incorporation, and electrochemistry of anthraquinone-modified nucleosides, nucleotides, and DNA. *Chemistry* 17, 14063–14073. doi: 10.1002/chem.201101883

Batchelor-McAuley, C., Li, Q., Dapin, S. M., and Compton, R. G. (2010). Voltammetric characterization of DNA intercalators across the full pH range: anthraquinone-2,6-disulfonate and anthraquinone-2-sulfonate. *J. Phys. Chem. B* 114, 4094–4100. doi: 10.1021/jp1008187

Beer, P. D., Gale, P. A., and Chen, G. Z. (1999). Electrochemical molecular recognition: pathways between complexation and signalling. *J. Chem. Soc. Dalt. Trans.* 1897–1910. doi: 10.1039/a901462d

Beer, P. D., Zheng, C., and Gale, P. A. (1994). Diester-calix[4]arenediquinone complexation and electrochemical recognition of group 1 and 2, ammonium and alkyl ammonium guest cations. *Tetrahedron* 50, 931–940. doi: 10.1016/S0040-4020(01)80807-3

Ben Gaied, N., Zhao, Z., Gerrard, S. R., Fox, K. R., and Brown, T. (2009). Potent triple helix stabilization by 5',3'-modified triplex-forming oligonucleotides. *ChemBioChem.* 10, 1839–1851. doi: 10.1002/cbic.200900232

Blair, E. O., and Corrigan, D. K. (2019). Biosensors and bioelectronics a review of microfabricated electrochemical biosensors for DNA detection. *Biosens. Bioelectron.* 134, 57–67. doi: 10.1016/j.bios.2019.03.055

Boynton, A. N., Marce, L., Mcconnell, A. J., and Barton, J. K. (2017). A ruthenium(II) complex as a luminescent probe for DNA mismatches and abasic sites. *Inorg. Chem.* 56, 8381–8389. doi: 10.1021/acs.inorgchem.7b01037

Chiu, C. Y., and Miller, S. A. (2019). Clinical metagenomics. *Nat. Rev. Genet.* 20, 341–355. doi: 10.1038/s41576-019-0113-7

Choi, D., Chung, T. D., Kang, S. K., Lee, S. K., Kim, T., Chang, S. K., et al. (1995). Electrochemical recognition of ammonium and alkali metal cations with calix[4]arenediquinone. *J. Electroanal. Chem.* 387, 133–134. doi: 10.1016/0022-0728(95)03946-E

Connors, W. H., Narayanan, S., Kryatova, O. P., and Richert, C. (2003). Synthesis of oligonucleotides with a 2'-cap at the 3'-terminus via reversed phosphoramidites. *Org. Lett.* 5, 247–250. doi: 10.1021/ol020212w

Dauphin-ducharme, P., Plaxco, K. W., States, U., Barbara, S., States, U., Sciences, M., et al. (2019). High-precision electrochemical measurements of the guanine-, mismatch-, and length-dependence of electron transfer from electrode-bound DNA are consistent with a contact-mediated mechanism. *J. Am. Chem. Soc.* 141, 1304–1311. doi: 10.1021/jacs.8b11341.Details

Dijk, E. L., Van, J. Y., Naquin, D., and Thermes, C. (2018). The third revolution in sequencing technology. *Trends Genet.* 34, 666–681. doi: 10.1016/j.tig.2018.05.008

Duprey, J. H. A., Bassani, D. M., Hyde, E. I., Jonusauskas, G., Ludwig, C., Rodger, A., et al. (2018). Biomolecular chemistry rationalisation of a mechanism for sensing single point variants in target DNA using anthracene- tagged base discriminating probes†. *Org. Biomol. Chem.* 16, 6576–6585. doi: 10.1039/c8ob01710g

Ferapontova, E. E. (2018). DNA electrochemistry and electrochemical sensors for nucleic acids. *Annu. Rev. Anal. Chem.* 11, 197–218. doi: 10.1146/annurev-anchem-061417-125811

Gholivand, M. B., Kashanian, S., and Peyman, H. (2012). DNA-binding, DNA cleavage and cytotoxicity studies of two anthraquinone derivatives. *Spectrochim. Acta A Mol. Biomol. Spectrosc.* 87, 232–240. doi: 10.1016/j.saa.2011.11.045

Gorodetsky, A., Buzzeo, M., and Barton, J. (2008). DNA-mediated electrochemistry. *Bioconjug. Chem.* 19, 2285–2296. doi: 10.1021/bc8003149.DNA-Mediated

Gorodetsky, A. A., Green, O., Yavin, E., and Barton, J. K. (2007). Coupling into the base pair stack is necessary for DNA-mediated electrochemistry. *Bioconjug. Chem.* 18, 1434–1441. doi: 10.1021/bc0700483

Greninger, A. L., and Greninger, A. L. (2018). Expert review of molecular diagnostics the challenge of diagnostic metagenomics the challenge of diagnostic metagenomics. *Expert Rev. Mol. Diagn.* 18, 605–615. doi: 10.1080/14737159.2018.1487292

Guin, P. S., Das, S., and Mandal, P. C. (2011). Electrochemical reduction of quinones in different media: a review. *Int. J. Electrochem.* 2011:816202. doi: 10.4061/2011/816202

Huyghe, A., Francois, P., and Schrenzel, J. (2009). Characterization of microbial pathogens by DNA microarrays. *Infect. Genet. Evol.* 9, 987–995. doi: 10.1016/j.meegid.2008.10.016

Hvastkovs, E. G., and Buttry, D. A. (2010). Recent advances in electrochemical DNA hybridization sensors. *Analyst* 135, 1817–1829. doi: 10.1039/c0an00113a

Inouye, M., Ikeda, R., Takase, M., Tsuri, T., and Chiba, J. (2005). Single-nucleotide polymorphism detection with "wire-like" DNA probes that display quasi "on-off" digital action. *Proc. Natl. Acad. Sci. U.S.A.* 102, 11606–11610. doi: 10.1073/pnas.0502078102

Järvinen, A., Laakso, S., Piiparinen, P., Aittakorpi, A., Lindfors, M., Huopaniemi, L., et al. (2009). Microarray-based assay. *BMC Microbiol.* 9:161. doi: 10.1186/1471-2180-9-161

Kang, D., Zuo, X., Yang, R., Xia, F., Plaxco, K. W., and White, R. J. (2009). Comparing the properties of electrochemical-based DNA sensors employing different redox tags. *Anal. Chem.* 81, 9109–9113. doi: 10.1021/ac901811n

Klindworth, A., Pruesse, E., Schweer, T., Peplies, J., Quast, C., Horn, M., et al. (2013). Evaluation of general 16S ribosomal RNA gene PCR primers for classical and next-generation sequencing-based diversity studies. *Nucleic Acids Res.* 41, 1–11. doi: 10.1093/nar/gks808

Kongpeth, J., Jampasa, S., Chaumpluk, P., Chailapakul, O., and Vilaivan, T. (2016). Immobilization-free electrochemical DNA detection with anthraquinone-labeled pyrrolidinyl peptide nucleic acid probe. *Talanta* 146, 318–325. doi: 10.1016/j.talanta.2015.08.059

Kowalczyk, A., Nowicka, M., Jurczakowski, R., Niedzialkowski, P., and Ossowski, T. (2010). New anthraquinone derivatives as electrochemical redox indicators for the visualization of the DNA hybridization process. *Electroanalysis* 22, 49–59. doi: 10.1002/elan.200900389

Kumamoto, S., Watanabe, M., Kawakami, N., Nakamura, M., and Yamana, K. (2008). 2'-anthraquinone-conjugated oligonucleotide as an electrochemical probe for DNA mismatch. *Bioconjug. Chem.* 19, 65–69. doi: 10.1021/bc070097f

Lee, C.-Y., Gong, P., Harbers, G. M., Grainger, D. W., Castner, D. G., and Gamble, L. J. (2006). Surface coverage and structure of mixed DNA/alkylthiol monolayers on gold: characterization by XPS, NEXAFS, and fluorescence intensity measurements. *Anal. Chem.* 78, 3316–3325. doi: 10.1021/ac052137j

Li, Q., Batchelor-Mcauley, C., Lawrence, N. S., Hartshorne, R. S., and Compton, R. G. (2011). Electrolyte tuning of electrode potentials: the one electron vs.

two electron reduction of anthraquinone-2-sulfonate in aqueous media. *Chem. Commun.* 47, 11426–11428. doi: 10.1039/c1cc14191k

Lin, Y.-J., Wu, Y.-C., Mani, V., Huang, S.-T., Huang, C.-H., Hu, Y.-C., et al. (2016). Designing anthraquinone–pyrrole redox intercalating probes for electrochemical gene detection. *Biosens. Bioelectron.* 79, 294–299. doi: 10.1016/j.bios.2015.12.042

Liu, A., Wang, K., Weng, S., Lei, Y., Lin, L., Chen, W., et al. (2012). Development of electrochemical DNA biosensors. *TrAC Trends Anal. Chem.* 37, 101–111. doi: 10.1016/j.trac.2012.03.008

Liu, T., and Barton, J. K. (2005). DNA electrochemistry through the base pairs not the sugar-phosphate backbone. *J. Am. Chem. Soc.* 127, 10160–10161. doi: 10.1021/ja053025c

Mahajan, S., Richardson, J., Brown, T., and Bartlett, P. N. (2008). SERS-melting: a new method for discriminating mutations in DNA sequences. *J. Am. Chem. Soc.* 130, 15589–15601. doi: 10.1021/ja805517q

Mahajan, S., Richardson, J., Gaied, N. B., Zhao, Z., Brown, T., and Bartlett, P. N. (2009). The use of an electroactive marker as a SERS label in an E -melting mutation discrimination assay. *Electroanalysis* 21, 2190–2197. doi: 10.1002/elan.200904681

Mcknight, R. E., Zhang, J., and Dixon, D. W. (2004). Binding of a homologous series of anthraquinones to DNA. *Bioorg. Med. Chem. Lett.* 14, 401–404. doi: 10.1016/j.bmcl.2003.10.054

Nagata, M., Kondo, M., Suemori, Y., Ochiai, T., Dewa, T., Ohtsuka, T., et al. (2008). Electron transfer of quinone self-assembled monolayers on a gold electrode. *Colloids Surf. B Biointerfaces* 64, 16–21. doi: 10.1016/j.colsurfb.2007.12.017

Nano, A., Boynton, A. N., Barton, J. K., and States, U. (2017). A rhodium-cyanine fluorescent probe: detection and signaling of mismatches in DNA. *J. Am. Chem. Soc.* 139, 17301–17304. doi: 10.1021/jacs.7b10639.A

Narayanan, S., Gall, J., and Richert, C. (2004). Clamping down on weak terminal base pairs: oligonucleotides with molecular caps as fidelity-enhancing elements at the 5'- and 3'-terminal residues. *Nucleic Acids Res.* 32, 2901–2911. doi: 10.1093/nar/gkh600

Orino, N., Kumamoto, S., Nakamura, M., and Yamana, K. (2005). Electrochemical detection of single base mismatches in DNA using redox modified oligonucleotides. *Nucleic Acids Symp. Ser.* 49, 139–140. doi: 10.1093/nass/49.1.139

Papadopoulou, E., Goodchild, S. A., Cleary, D. W., Weller, S. A., Gale, N., Stubberfield, M. R., et al. (2015). Using surface-enhanced raman spectroscopy and electrochemically driven melting to discriminate yersinia pestis from Y. Pseudotuberculosis based on single nucleotide polymorphisms within unpuri fi ed polymerase chain reaction amplicons. *Anal. Chem.* 87, 1605–1612. doi: 10.1021/ac503063c

Pheeney, C. G., and Barton, J. K. (2013). Intraduplex DNA-mediated electrochemistry of covalently tethered redox-active reporters. *J. Am. Chem. Soc.* 135, 14944–14947. doi: 10.1021/ja408135g

Poritz, M. A., Blaschke, A. J., Byington, C. L., Meyers, L., Nilsson, K., David, E., et al. (2011). FilmArray, an automated nested multiplex PCR system for multi-pathogen detection : development and application to respiratory tract infection. *PLoS ONE* 6:e26047. doi: 10.1371/journal.pone.0026047

Rachwal, P. A., Rose, H. L., Cox, V., Lukaszewski, R. A., Murch, A. L., and Weller, S. A. (2012). The potential of taqman array cards for detection of multiple biological agents by real-time PCR. *PLoS ONE* 7:e35971. doi: 10.1371/journal.pone.0035971

Salvatore, P., Zeng, D., Karlsen, K. K., Chi, Q., and Wengel, J. (2013). Electrochemistry of single metalloprotein and DNA-based molecules at au (111) electrode surfaces. *Chem. Phys. Chem.* 14, 2101–2111. doi: 10.1002/cphc.201300299

Sontz, P. A., Muren, N. B., and Barton, J. K. (2012). DNA charge transport for sensing and signaling. *Acc. Chem. Res.* 45, 1792–1800. doi: 10.1021/ar3001298.DNA

Steel, A. B., Herne, T. M., and Tarlov, M. J. (1998). Electrochemical quantitation of DNA immobilized on gold. *Anal. Chem.* 70, 4670–4677.

Stulz, E. (2015). Porphyrin-modified DNA as construction material in supramolecular chemistry and Nano-architectonics. *Chimia* 69, 678–683. doi: 10.2533/chimia.2015.678

Tomlinson, J., Harrison, C., Boonham, N., Goodchild, S. A., and Weller, S. A. (2014). Influence of the length of target DNA overhang proximal to the array surface on discrimination of single-base mismatches on a 25-mer oligonucleotide array. *BMC Res. Notes* 7:251. doi: 10.1186/1756-0500-7-251

Tosar, J. P., Brañas, G., and Laíz, J. (2010). Electrochemical DNA hybridization sensors applied to real and complex biological samples. *Biosens. Bioelectron.* 26, 1205–1217. doi: 10.1016/j.bios.2010.08.053

Uzawa, T., Cheng, R. R., White, R. J., Makarov, D. E., and Plaxco, K. W. (2010). A mechanistic study of electron transfer from the distal termini of electrode-bound, single-stranded DNAs. *J. Am. Chem. Soc.* 132, 16120–16126. doi: 10.1021/ja106345d

Wang, D., Coscoy, L., Zylberberg, M., Avila, P. C., Boushey, H. A., Ganem, D., et al. (2002). Microarray-based detection and genotyping of viral pathogens. *Proc. Natl. Acad. Sci.U.S.A.* 99, 15687–15692. doi: 10.1073/pnas.242579699

Weller, S. A., Bailey, D., Matthews, S., Lumley, S., Sweed, A., Ready, D., et al. (2016). Identification of ebola virus disease in heat-treated blood samples obtained in Sierra Leone and the United Kingdom. *J. Clin. Microbiol.* 54, 114–119. doi: 10.1128/JCM.02287-15.Editor

Weller, S. A., Cox, V., Essex-lopresti, A., Hartley, M. G., Parsons, T. M., Rachwal, P. A., et al. (2012). Evaluation of two multiplex real-time PCR screening capabilities for the detection of *Bacillus anthracis*, *Francisella tularensis* and *Yersinia pestis* in blood samples generated from murine infection models. *J. Med. Microbiol.* 61, 1546–1555. doi: 10.1099/jmm.0.049007-0

Whittemore, N. A., Mullenix, A. N., Inamati, G. B., Manoharan, M., Cook, P. D., and Tuinman, A. A., et al. (1999). Synthesis and electrochemistry of anthraquinone-oligodeoxynucleotide conjugates. *Bioconjug. Chem.* 10, 261–270. doi: 10.1021/bc980095i

Wong, E. L. S., and Gooding, J. J. (2006). Charge transfer through DNA : a selective electrochemical DNA biosensor. *Anal. Chem.* 78, 2138–2144. doi: 10.1021/ac0509096

Yamana, K., Kawakami, N., Ohtsuka, T., Sugie, Y., Nakano, H., and Saito, I. (2003). Electrochemical detection of single-base mismatches in DNA by a redox-active intercalator conjugated oligonucleotide. *Nucleic Acids Res. Suppl.* 2003, 89–90. doi: 10.1093/nass/3.1.89

Yamana, K., Kumamoto, S., Nakano, H., and Sugie, Y. (2001). Electrochemistry of DNA duplex containing an anthraquinonylmethyl group at the 2'-sugar position. *Nucleic Acids Res. Suppl.* 1, 35–6. doi: 10.1093/nass/1.1.35

Yamana, K., Mitsui, T., Yoshioka, J., Isuno, T., and Nakano, H. (1996). Incorporation of two anthraquinonylmethyl groups into the 2'-O-positions of oligonucleotides: increased affinity and sequence specificity of anthraquinone-modified oligonucleotides in hybrid formation with DNA and RNA. *Bioconjug. Chem.* 7, 715–720. doi: 10.1021/bc960064s

Yáñez-Sedeño, P., Campuzanoa, S., and Pingarrón, J. M. (2019). Pushing the limits of electrochemistry toward challenging applications in clinical diagnosis, prognosis, and therapeutic action. *Chem. Commun.* 55, 2563–2592. doi: 10.1039/c8cc08815b

Zhang, J., Lang, H. P., Yoshikawa, G., and Gerber, C. (2012). Optimization of DNA hybridization efficiency by pH-driven nanomechanical bending. *Langmuir* 28, 6494–6501. doi: 10.1021/la205066h

Zhao, Z., Peng, G., Michels, J., Fox, K. R., and Brown, T. (2007). Synthesis of anthraquinone oligonucleotides for triplex stabilization. *Nucleosides Nucleotides Nucleic Acids* 26, 921–925. doi: 10.1080/15257770701506491

Zwang, T. J., Tse, E. C. M., Barton, J. K., and States, U. (2018). Sensing DNA through DNA charge transport theodore. *ACS Chem. Biol.* 13, 1799–1809. doi: 10.1021/acschembio.8b00347.Sensing

Conflict of Interest: The authors declare that the research was conducted in the absence of any commercial or financial relationships that could be construed as a potential conflict of interest.

Advantages of publishing in Frontiers

OPEN ACCESS
Articles are free to read for greatest visibility and readership

FAST PUBLICATION
Around 90 days from submission to decision

HIGH QUALITY PEER-REVIEW
Rigorous, collaborative, and constructive peer-review

TRANSPARENT PEER-REVIEW
Editors and reviewers acknowledged by name on published articles

Frontiers
Avenue du Tribunal-Fédéral 34
1005 Lausanne | Switzerland

Visit us: www.frontiersin.org
Contact us: info@frontiersin.org | +41 21 510 17 00

REPRODUCIBILITY OF RESEARCH
Support open data and methods to enhance research reproducibility

DIGITAL PUBLISHING
Articles designed for optimal readership across devices

FOLLOW US
@frontiersin

IMPACT METRICS
Advanced article metrics track visibility across digital media

EXTENSIVE PROMOTION
Marketing and promotion of impactful research

LOOP RESEARCH NETWORK
Our network increases your article's readership